Soils and Rocks

Volume 40, N. 2

2017

ISSN 1980-9743

Soils and Rocks

Soils and Rocks

An International Journal of Geotechnical and Geoenvironmental Engineering

ABMS

G

Volume 40, N. 2
May-August 2017

Soils and Rocks is an International Journal of Geotechnical and Geoenvironmental Engineering published by

ABMS - Brazilian Association for Soil Mechanics and Geotechnical Engineering
Av. Queiroz Filho, 1700 – Torre A Sky, Sala 106 – Vila Hamburguesa
05319-000, São Paulo, SP
Brazil

SPG – Portuguese Geotechnical Society
LNEC, Avenida do Brasil, 101
1700-066 Lisboa
Portugal

Issue Date: *August 2017*

Issue: *400 copies and 800 online-distributed copies*

Manuscript Submission: *For review criteria and manuscript submission information, see Instructions for Authors at the end.*

SOILS and ROCKS

An International Journal of Geotechnical and Geoenvironmental Engineering

Editor Paulo Scarano Hemsi - Aeronautics Institute of Technology, Brazil

Co-editor José Couto Marques - University of Porto, Portugal

“Ad hoc” Reviewers

Soils and Rocks is indebted to all “ad hoc” reviewers.
A complete list of reviewers that contributed to the current volume of *Soils and Rocks* will be published here in the December issue.

Soils and Rocks publishes papers in English in the broad fields of Geotechnical Engineering, Engineering Geology and Geoenvironmental Engineering. The Journal is published in April, August and December. Subscription price is US$ 90.00 per year. The journal, with the name “Solos e Rochas”, was first published in 1978 by the Graduate School of Engineering, Federal University of Rio de Janeiro (COPPE-UFRJ). In 1980 it became the official magazine of the Brazilian Association for Soil Mechanics and Geotechnical Engineering (ABMS), acquiring the national character that had been the intention of its founders. In 1986 it also became the official Journal of the Brazilian Association for Engineering Geology and the Environment (ABGE) and in 1999 became the Latin American Geotechnical Journal, following the support of Latin-American representatives gathered for the Pan-American Conference of Guadalajara (1996). In 2007 the journal acquired the status of an international journal under the name of Soils and Rocks, published by the Brazilian Association for Soil Mechanics and Geotechnical Engineering (ABMS), Brazilian Association for Engineering Geology and the Environment (ABGE) and Portuguese Geotechnical Society (SPG). In 2010, ABGE decided to publish its own journal and left the partnership.

Soils and Rocks

1978,	1 (1, 2)
1979,	1 (3), 2 (1,2)
1980-1983,	3-6 (1, 2, 3)
1984,	7 (single number)
1985-1987,	8-10 (1, 2, 3)
1988-1990,	11-13 (single number)
1991-1992,	14-15 (1, 2)
1993,	16 (1, 2, 3, 4)
1994-2010,	17-33 (1, 2, 3)
2011,	34 (1, 2, 3, 4)
2012-2016,	35-39 (1, 2, 3)
2017,	**40 (1, 2,**

ISSN 1980-9743 CDU 624.131.1

ISSN 1980-9743

SOILS and ROCKS

An International Journal of Geotechnical and Geoenvironmental Engineering

Publication of

ABMS - Brazilian Association for Soil Mechanics and Geotechnical Engineering

SPG - Portuguese Geotechnical Society

Volume 40, N. 2, May-August 2017

Table of Contents

Articles

Energy Ratio (E_R) for the Standard Penetration Test Based on Measured Field Tests

J.A. Lukiantchuki, G.P. Bernardes, E.R. Esquivel

Abstract. The Standard Penetration Test (SPT) is often used to estimate the soil parameters for geotechnical design projects, using the N_{SPT} index. However, these estimates are performed based on empirical correlations without any scientific basis. Moreover, the test has a large inherent results dispersion due to the use of different types of equipment and execution procedures. Since the N_{SPT} index depends on the amount of energy that is effectively transmitted to the sampler during the hammer fall, it is fundamental to be able to estimate this energy. Given the importance of estimating the energy that reaches the SPT sampler, an instrumented subassembly was developed in order to simultaneously assess the amount of energy transmitted to the drill rods, at sections just above the sampler and just below the anvil. This paper presents a series of SPT experimental results carried out in two different sites located in the State of São Paulo, using two different equipment set-ups (with manual and automatic tripping mechanisms), enabling the assessment of the top and bottom energy ratio under different conditions. Results show that for *hand lifting hammer* and *automatic trip hammer* systems the difference in the energy ratio is not significant. However, the dispersion of the results for the *hand lifting hammer* system is more pronounced due to execution procedures, equipment and operators.

Keywords: penetration test, SPT test, energy, energy ratio, dynamic instrumentation, foundations.

1. Introduction

Despite criticism, the Standard Penetration Test (SPT) continues to be widely used for geotechnical designs, using the N_{SPT} index as an indicator of soil properties (shear strength, compressibility and undrained shear strength of soils). The criticism is related to results dispersion attributable to the variability inherent in SPT tests. Standard penetration tests are performed using different types of equipment (hammers, drill rod, borehole fluids, sampling tubes, among others), execution procedures and operators. Consequently, the N_{SPT} index, which is often used to estimate geotechnical soil parameters, is broadly variable and its consistency has been questioned. In addition, these estimates are performed based on empirical correlations without any scientific basis. Researchers and practitioners highlight that it is possible to increase the N_{SPT} index accuracy by observing recommended standards and using a more skilled and experienced field crew (Schnaid *et al.*, 2009; Reading *et al.*, 2010).

The estimation of soil properties is performed through empirical correlations using the N_{SPT} index, which corresponds to the number of blows required for the sampler to penetrate 300 mm into to the soil after an initial seating drive of 150 mm. The N_{SPT} index does not represent physical soil resistance but is an indicator of soil resistance, which depends not only on the soil properties but also on the equipment characteristics. The N_{SPT} index is also strongly dependent on the amount of energy delivered to the drill rods (Schmertmann & Palacios, 1979) and to the SPT sampler during hammer impact (Aoki & Cintra, 2000). For each hammer drop there is a corresponding nominal potential energy (*PE*) that is theoretically equal to 474.5 J (ASTM, 2008). According to the Brazilian standard, the corresponding nominal potential energy for SPT is equal to 478.2 J (ABNT, 2001).

The amount of energy that is initially delivered to the top of the drill rods, and subsequently transmitted to the sampler, can be significantly influenced by many factors, including the type and shape of hammer, drop height, equipment conditions, the length and mass of the drill rods, secondary impacts, soil conditions, verticality of the test, condition of the trip mechanism, among other variables (Schmertmann & Palacios, 1979; Belincanta & Cintra; 1998; Aoki & Cintra; 2000; Tsai *et al.*, 2004; Odebrecht *et al.*, 2005; Sancio & Bray, 2005; Aoki *et al.*, 2007; Youd *et al.*, 2008; Lee *et al.*, 2010; Reading *et al.*, 2010).

Due to the energy losses in the different mechanical components of the hammer release system and other sources of dissipation, the energy delivered to the rods and sampler is not equal to the nominal potential energy (Schmertmann & Palacios, 1979; Aoki & Cintra, 2000; Odebrecht *et al.*, 2005; Cavalcante *et al.*, 2008; Lukiantchuki, 2012, Santana *et al.*, 2012; Lukiantchuki *et al.*, 2015). Thus, the energy ratio of the SPT setup (E_R) (Eq. 1) is

Juliana Azoia Lukiantchuki, Ph.D., Associate Professor, Departamento de Engenharia Civil, Universidade Estadual de Maringá, Maringá, PR, Brazil. e-mail: jazoia@yahoo.com.br.
George de Paula Bernardes, Ph.D., Associate Professor, Departamento de Engenharia Civil, Universidade Estadual Paulista, Guaratinguetá, SP, Brazil. e-mail: gpb@feg.unesp.br.
Edmundo Rogerio Esquivel, Ph.D., Associate Professor, Departamento de Geotecnia, Universidade de São Paulo, São Carlos, SP, Brazil. e-mail: esquivel@sc.usp.br.
Submitted on June 20, 2016; Final Acceptance on May 10, 2017; Discussion open until December 29, 2017.

usually defined as the ratio of the amount of energy transferred to the drill rods (Force-Velocity Method, referred to as *EFV*), to the nominal potential energy (*PE*) (ASTM, 2010). The *EFV* is calculated by integrating the force multiplied by the velocity over time. The use of the *EFV* method in estimating SPT energy is considered to be the most reliable and accurate method for estimating SPT energy during wave propagation (Sy & Campanella, 1991; Howie *et al.*, 2003; Youd *et al.*, 2008).

$$E_R = \frac{EFV}{PE} = \frac{\int_{t=0}^{t=\infty} F(t) \times v(t)\,dt}{PE} \quad (1)$$

where $F(t)$ = the normal force, during the wave propagation, at a specific section, and $v(t)$ = the particle velocity.

The energy ratio (E_R) should be evaluated for the system when the N_{SPT} index is used to estimate soil properties for geotechnical designs or for comparing results. However, different types of equipment are used to perform SPT tests, resulting in variable energy ratio values and N_{SPT} indexes. Therefore, researchers and practitioners recommend that the N_{SPT} index should be normalized (Kovacs & Salomone, 1982; Robertson *et al.*, 1983; Seed *et al.*, 1985; Skempton, 1986) to a reference energy ratio of 60% (N_{60}) (ISSMFE, 1989) (Eq. 2).

$$N_{60} = \frac{E_R}{E_{60}} \times N_{SPT} \quad (2)$$

where N_{SPT} = is the blow count; E_R = is the energy ratio of the specific SPT set up; E_{60} = 60% of the international reference of nominal potential energy (≅ 474 J); N_{60} = N_{SPT} index corrected to 60% of the international reference for nominal potential energy.

In conventional methods, energy is measured just below the anvil through an instrumented subassembly installed at the top of the drill rods. However, Aoki & Cintra (2000) suggested redefining the SPT energy ratio as the ratio of the maximum amount of energy transferred to the soil sampler system to the nominal potential energy. According to these authors, the energy ratio above the sampler is inversely proportional to the drill rod length (Fig. 1) and the energy ratio would be related to the work done during sampler penetration into the soil and not to the available kinetic energy.

Some researchers (Cavalcante *et al.*, 2008; Odebrecht *et al.*, 2005; Santana *et al.*, 2012; Lukiantchuki *et al.*, 2015) have measured energy in a section just above the sampler. However, little data is available due to the difficulty in placing the instrumentation inside the borehole. The assessment of the amount of energy transmitted to the string of rods, simultaneously at a section just below the anvil and a section just above the sampler, allows for estimating energy losses over the rod (e_4) (Eq. 3) (Danziger *et al.*, 2008).

$$E_s = e_1 \times e_2 \times e_3 \times e_4 \times PE \quad (3)$$

where E_s = is the amount of energy that reaches the sampler; e_1 = is the correction factor which relates the energy just before the impact to the free fall energy; e_2 = is the ratio between the energy just below the anvil and the kinetic energy just before the impact; e_3 = is a factor related to the drill rod length and e_4 = is the factor which relates the energy loss over the drill rod length.

Considering the importance of estimating the energy that reaches the SPT sampler, an instrumented subassembly, capable of reading acceleration and force signals just above the sampler, was developed. This paper presents the results of a series of SPT experimental tests performed using two instrumented subassemblies, one placed just below the anvil and the other just above the sampler. This instrumentation allowed the simultaneous assessment of the amount of energy transmitted to the drill rods at sections just above the sampler and just below the anvil. Additionally, the SPT tests were conducted using different hammer types (hand lifting pin weight and automatic trip hammer). Results allow for estimation of the energy ratio at the top (anvil) and at the bottom (sampler) of drill rods, for two different equipment set-ups.

2. Instrumentation

In this research, two instrumented subassemblies were built, similar to the one developed by Odebrecht *et al.* (2005). Each instrumented subassembly consists of one segment of rod, to which a pair of accelerometers and one load cell have been installed (Fig. 2a). The load cell is composed of four double strain gauges (350 Ω each), from a Wheatstone bridge circuit, assembled 90° apart (Fig. 2b).

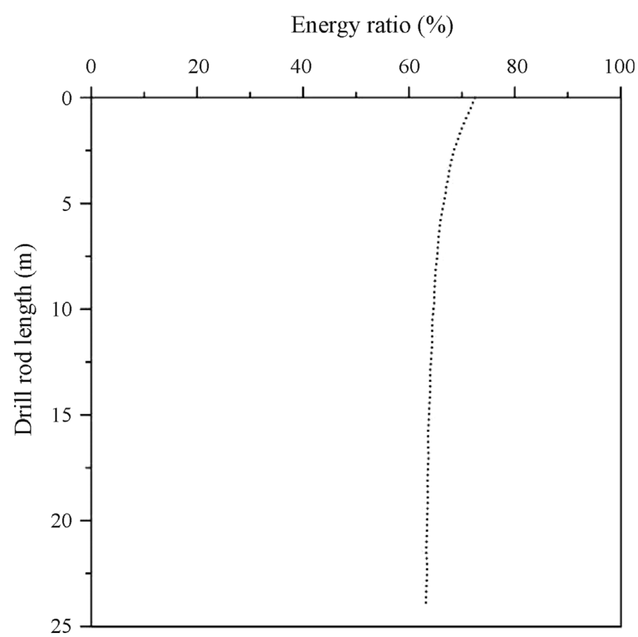

Figure 1 - Energy ratio above the sampler *vs.* drill rod length (Aoki & Cintra, 2000).

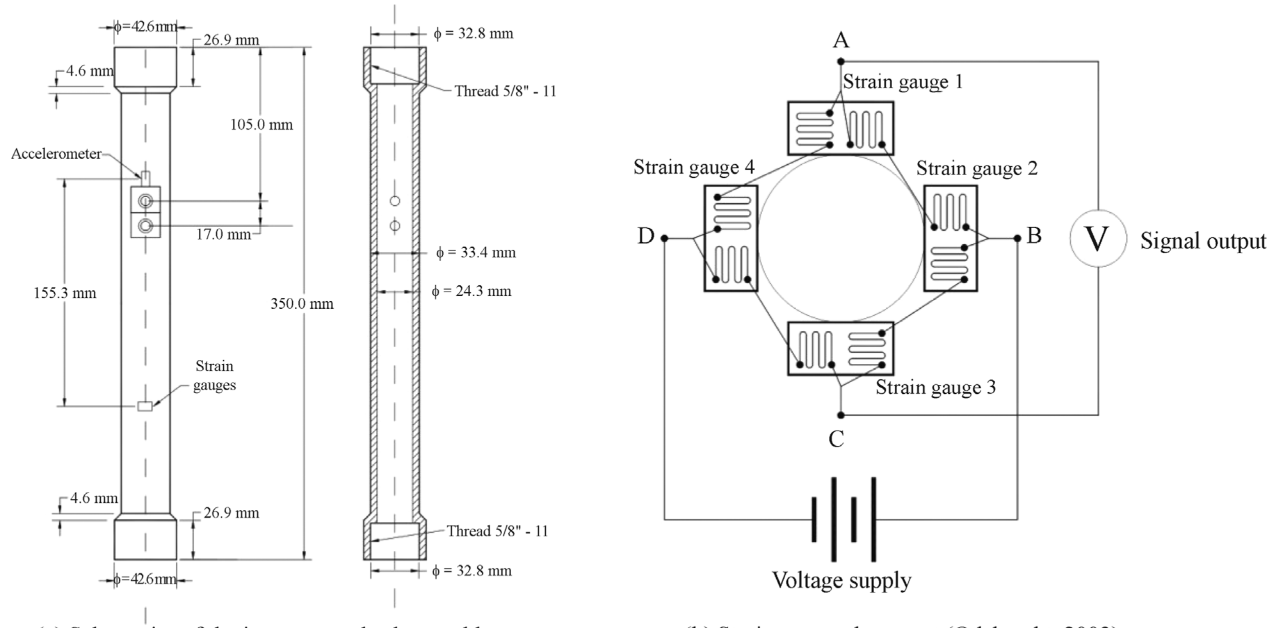

(a) Schematics of the instrumented subassembly (b) Strain gauge placement (Odebrecht, 2003)

Figure 2 - Instrumentation developed (Lukiantchuki, 2012).

A pair of PCB Piezotronics piezoeletric accelerometers was rigidly mounted on each instrumented subassembly by means of an aluminum support. A suitable support geometry was defined through dynamic tests with different support geometries (Lukiantchuki, 2012).

Laboratory test results yielded the accelerometer support shown in Fig. 3a as the most suitable for field tests. This support presented the lowest resonance and anti-resonance effects. It was possible to collect data with frequencies up to 14,000 Hz, with low amplitude variations.

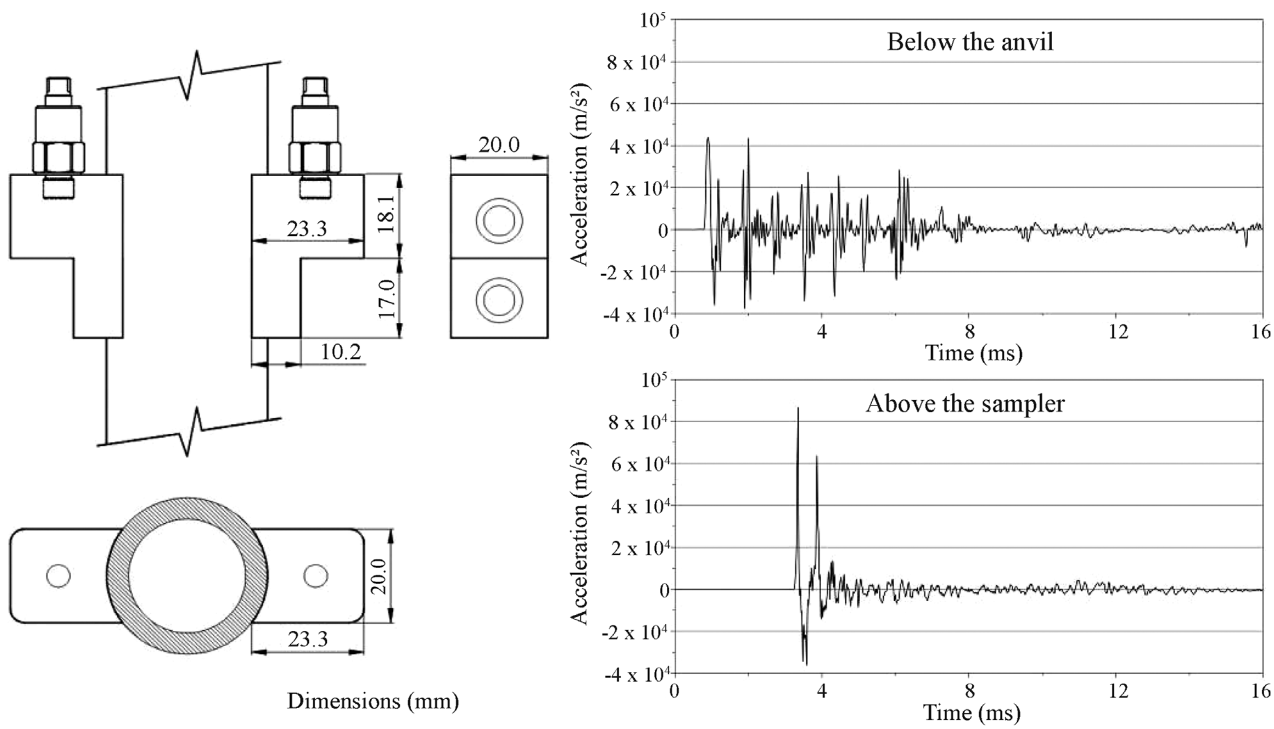

(a) (b)

Figure 3 - (a) Accelerometer supports, (b) comparison between acceleration magnitudes measured at sections just below the anvil and just above the sampler.

For recording accelerations at the section just below the anvil, accelerometers capable of measuring accelerations up to 5000 g, in the 0.4-10,000 Hz frequency range (model 350B04) were used. The experimental test results show that accelerations at the section just above the sampler are higher than those at the section just below the anvil (Fig. 3b). For this reason, accelerometers capable of measuring accelerations up to 20,000 g in the 1-15,000 Hz frequency range (model 350M77) were necessary.

Lukiantchuki *et al.* (2011) argue that the tip of the sampler be free (tip resistance is very low) for the first blow in SPT tests, allowing the tip to move downward. This tip movement generates a reflected tensile wave, which doubles the particle velocity at the tip of the sampler (Skov, 1982). When the instrumentation is placed just above the sampler, the time interval between the incoming compressive wave and the reflected tensile wave is very short. This time interval is equal to $2L'/c$, where L' is the distance from the accelerometer position to the sampler and c is wave propagation velocity (Fig. 4). Due to the particle velocity superposition, the accelerations are summed. This is the reason for the need to use accelerometers with higher capacity (20,000 g).

To record the signal data, an HBM data acquisition system, model MX410, was used. This four-channel portable data acquisition system is suitable for analyzing high frequency dynamic events. Field tests were conducted at a 96-kHz sampling rate per channel. Additionally, a trigger, a pre-trigger and a low-pass filter (anti-aliasing) corresponding to 15% of the selected sampling rate was used.

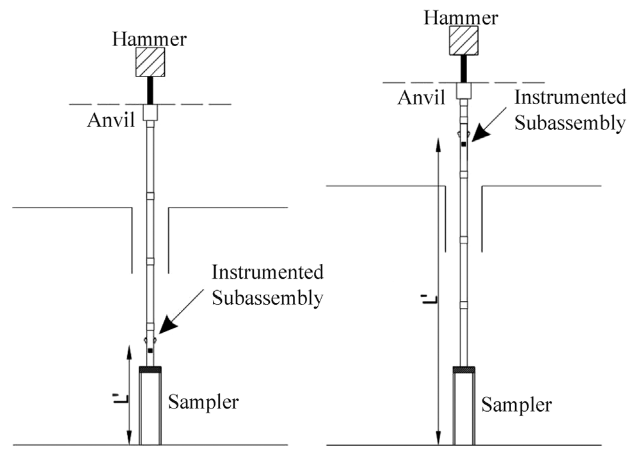

Figure 4 - Distance between the subassembly and the sampler tip (L') (Lukiantchuki *et al.*, 2011).

3. Experimental Set-Up

The SPT field tests, performed according to the Brazilian Standard (ABNT, 2001), were carried out at the Experimental Research Site of São Paulo State University (UNESP) in the city of Bauru and at a field site in the city of São Carlos, both cities located in the state of São Paulo, Brazil. The experimental sites, which are geologically similar, are composed of a thick layer of lateritic silty fine sand. This unsaturated, very porous and collapsible layer presents low bearing capacity, with an N_{SPT} index varying from 1 to 30 blows, for depths in the range from 1 m to 30 m. The only difference between the Bauru and São Carlos sites is that the average water level is 30 m and 12 m below the surface, respectively (Figs. 5 and 6).

The field tests were performed using both a *hand lifting pin weight hammer* and an *automatic trip hammer system* (Table 1). The *hand lifting pin weight hammer system* will be referred to hereafter as a *hand lifting system*. This system uses a pin weight hammer (65 kg) (Fig. 7a) with a manual tripping mechanism. The *automatic trip hammer system* uses a hammer (61.75 kg) with an automatic tripping mechanism (Fig. 7b). The SPT tests used Brazilian Standard drill rods, which have a cross-section area of around 4.2×10^{-4} m^2, a weight of 32 N/m each and the rod joints have a cross-section area of around 8.4×10^{-4} m^2.

4. Calculation and Procedures

The amount of energy (*EFV*) transmitted to the drill rods can be both theoretically and experimentally estimated. Experimentally, the energy can be calculated using the *EFV* method, by integrating the product of normal force (F) multiplied by the particle velocity (v) with respect to time, as in Eq. 1. The integration initial instant (t_i) corresponds to the beginning of the event, that is, when the force signal becomes different from zero. The integration final instant (t_f) is when the force and velocity signal become zero and no additional energy transfer occurs. At the final instant, the energy transferred to the drill rods reaches a maximum value. The *EFV* method provides accurate energy values even when the proportionality between force and velocity is lost (Sy & Campanella, 1991; Howie *et al.*, 2003).

Table 1 - SPT hammer systems.

SPT Hammer	Hammer mass (kg)	Wood cushion	Drop heigth (mm)	Overall mass (kg)	Lifting system	Rod (weight/meter)	Rope
Hand lifted pin weight hammer	65.00	YES	750	65	Hand lifted	32 N/m	Flexible sisal rope
Automatic trigger trip hammer	61.75	NO	750	95	Mechanized lifted	32 N/m	Steel cable

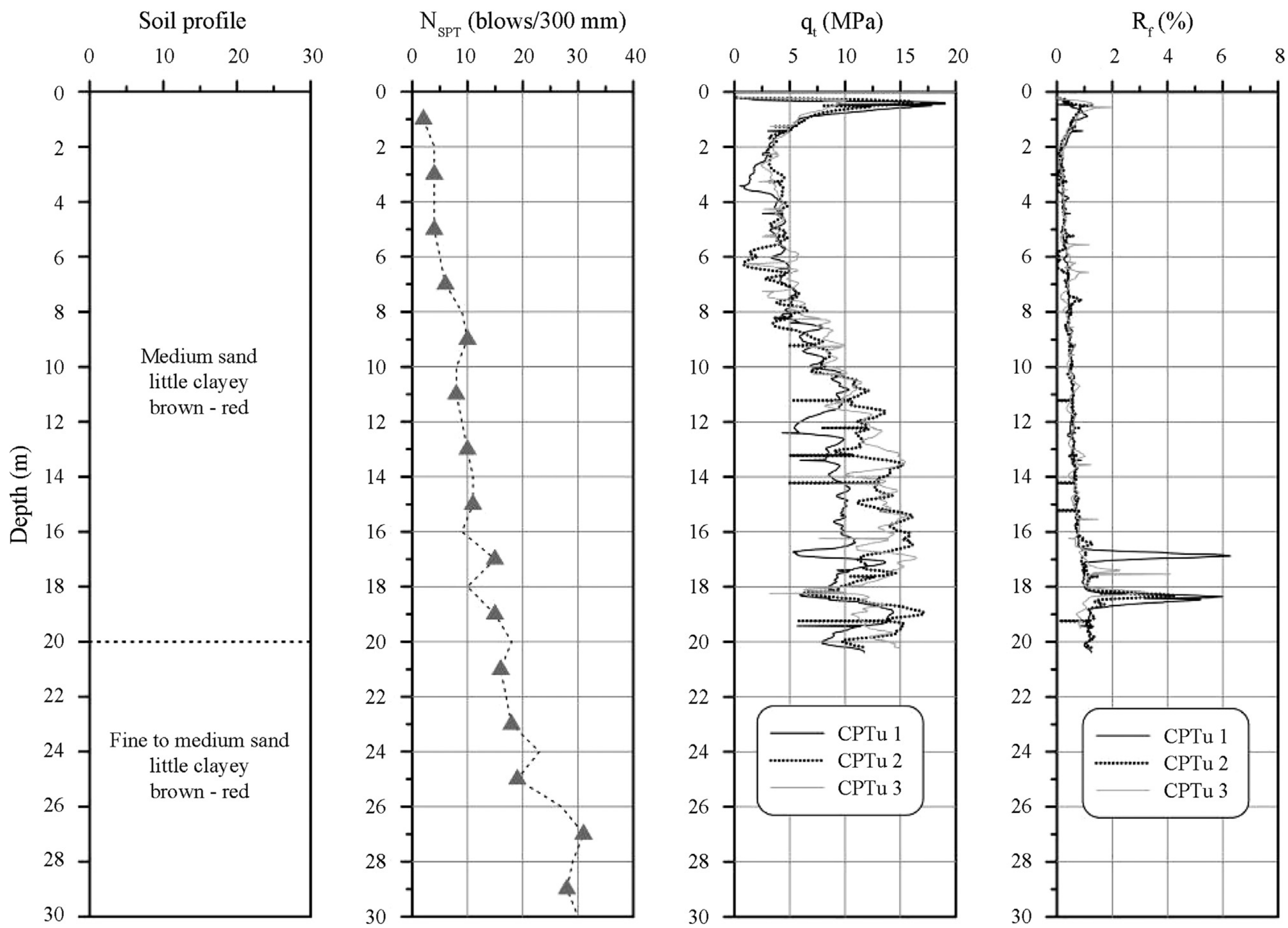

Figure 5 - Bauru site soil profile.

The velocity trace was obtained by integrating the acceleration signal measurements. In this procedure, it was assumed that at the initial instant, the acceleration was equal to zero. Likewise, the initial computed velocity was corrected, setting it to zero. In addition, the displacement trace was obtained by integrating the velocity signals. Then, the maximum displacement value was compared with the SPT sampler penetration measured in the field. The performance of the developed instrumentation can be observed in Fig. 8, in which the maximum top and bottom displacements appear to be very close to the measured sampler penetration. The energy curves are consistent, indicating an energy loss of about 38 J for a depth of 4 m.

The product of velocity and rod impedance (Z) has the same dimension of force (Eq. 4):

$$F(t) = \frac{a \times E}{c} \times v(t) = Z \times v(t) \tag{4}$$

where a = area of the rod cross-section (4.2×10^{-4} m^2); E = modulus of elasticity of the rod (206840 MPa); c = theoretical wave propagation velocity = $(E/\rho_R)^{0.5} \cong 5120$ m/s; ρ_R = mass density of the rod (7880 kg/m^3); v = particle velocity; Z = rod impedance (Sancio and Bray, 2005).

In order to verify the suitability of the developed equipment, the force traces (F) and velocity traces (v) multiplied by the rod impedance (Z) were compared. These traces should be proportional in the time interval between the initial instant (t_i) and the instant ($t_i + 2L'/c$), where L' is the distance between the accelerometer and the sampler tip. Due to wave reflections, this trace superposition does not occur after the instant ($t_i + 2L'/c$).

Figure 9 shows a typical record of F and vZ comparisons for the instrumentation placed below the anvil. This test was performed at an initial depth of 10.0 m, the total length of the drill rod (from anvil to sampler) was 10.73 m, so that L' was about 10.43 m. As the N_{SPT} index was 18 blows/0.29 m, each blow by the hammer caused an average sampler penetration of about 0.016 m into the soil.

The F and vZ records begin at point O (t = 4.65 ms) and rise sharply to a maximum value of approximately 60 kN. After the initial peak, the force and velocity magnitudes decrease and tensile wave reflections caused by loose joints appear. At point 6 a compression wave reflection can be observed due to an increase of impedance at the sampler head. At point A the curves are separated due to downward and upward wave effects.

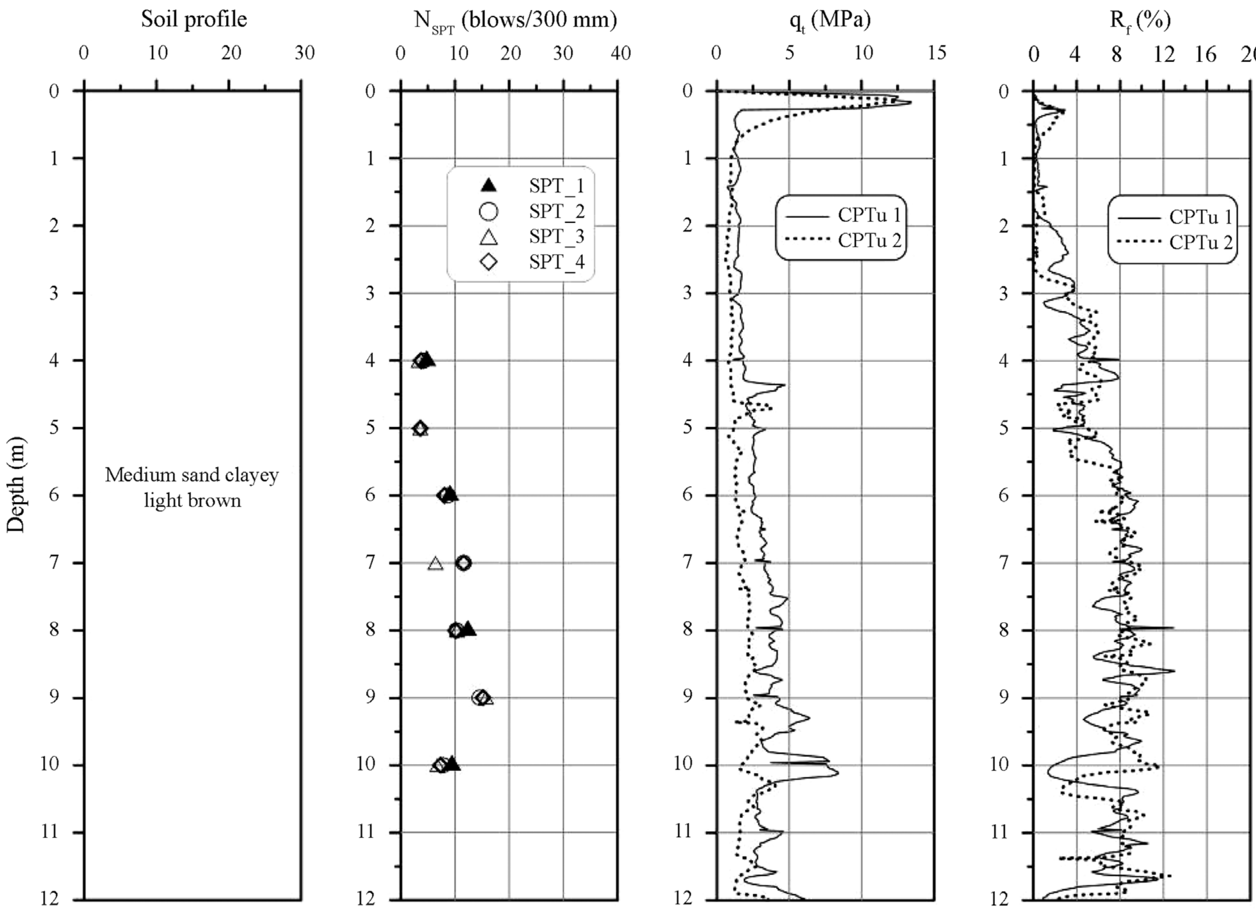

Figure 6 - São Carlos site soil profile.

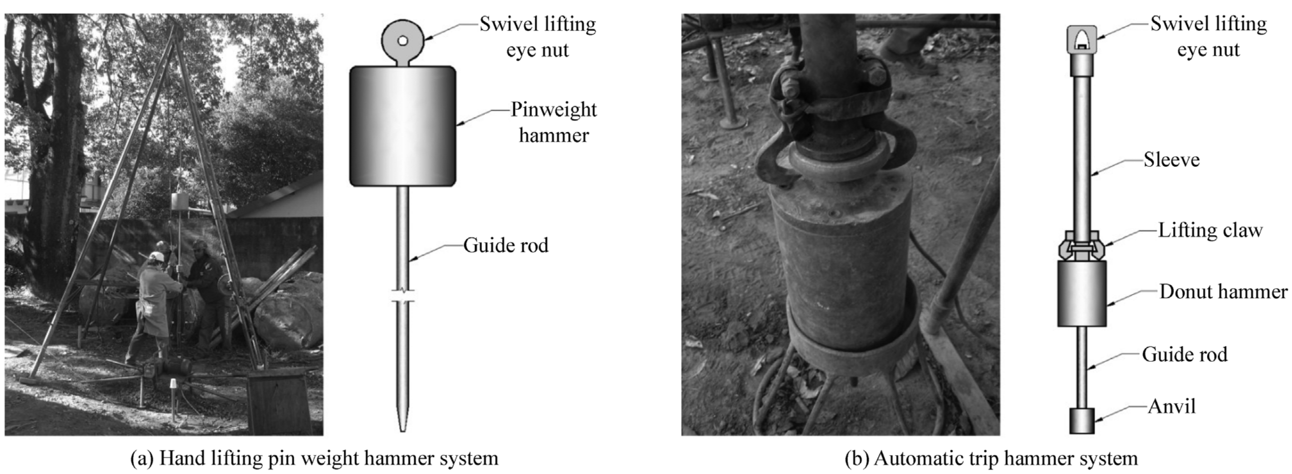

Figure 7 - Hammer systems.

5. Energy Measurements

5.1. Suitability of the developed instrumentation

In order to ensure the suitability of instrumented blow data, the sampler displacement was measured for each blow and compared to the calculated displacement. As can be observed, independently of the positioning of the instrumentation, the sampler measured and calculated displacements show good agreement (Figs. 10 and 11). This makes sense since the displacement that occurs at the top and bottom of the drill rods is the same. Therefore, the developed instrumentation is adequate for estimating the energy transmitted during wave propagation.

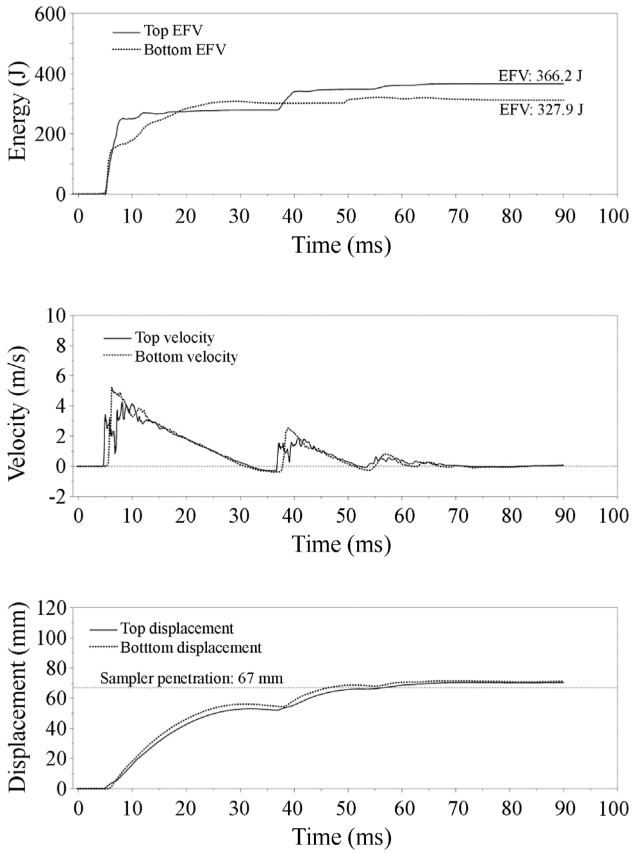

Figure 8 - Energy, velocity and displacement traces (third blow at the depth of 4 m – São Carlos site – *automatic trip hammer system*).

5.2. Energy ratio (E_R)

The results and conclusions, presented below, are derived from the analysis of 185 instrumented blows. The instrumentation allowed for the simultaneous assessment of the amount of energy transmitted to the drill rods at sections just below the anvil and a section just above the sampler. It was therefore possible to estimate the energy ratio in both sections and analyze the energy loss during the sampler penetration.

For the present analysis, the energy ratio was divided into 8 groups (G*i*) considering different ranges (Table 2).

Figures 12 and 13 show the energy ratio (E_R) histogram for the *hand lifting* and *automatic trip hammer systems*, which represent the E_R values for a section immedi-

Table 2 - Groups and energy ratio ranges adopted.

Group	Energy ratio range (%)
G1	$E_R \le 30$
G2	$30 < E_R \le 40$
G3	$40 < E_R \le 50$
G4	$50 < E_R \le 60$
G5	$60 < E_R \le 70$
G6	$70 < E_R \le 80$
G7	$80 < E_R \le 90$
G8	$E_R > 90$

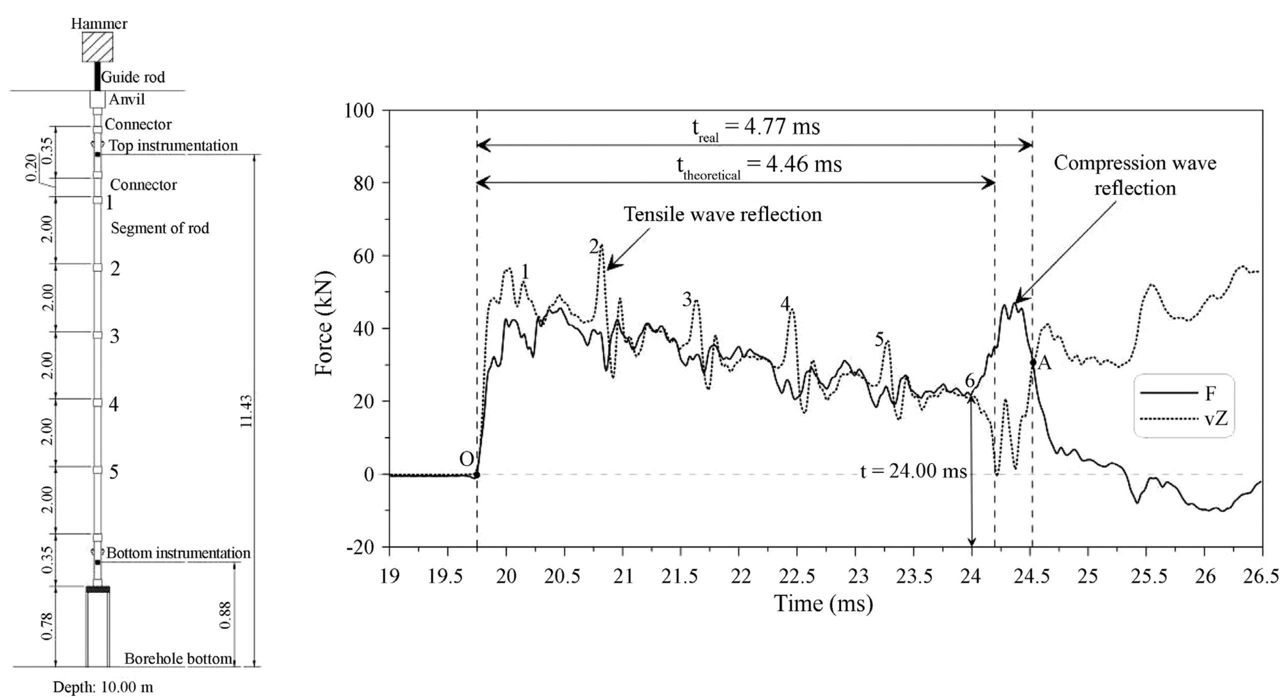

(a) Instrumentation position

(b) Force signal comparison

Figure 9 - Comparison of F and vZ signals for instrumentation placed below the anvil.

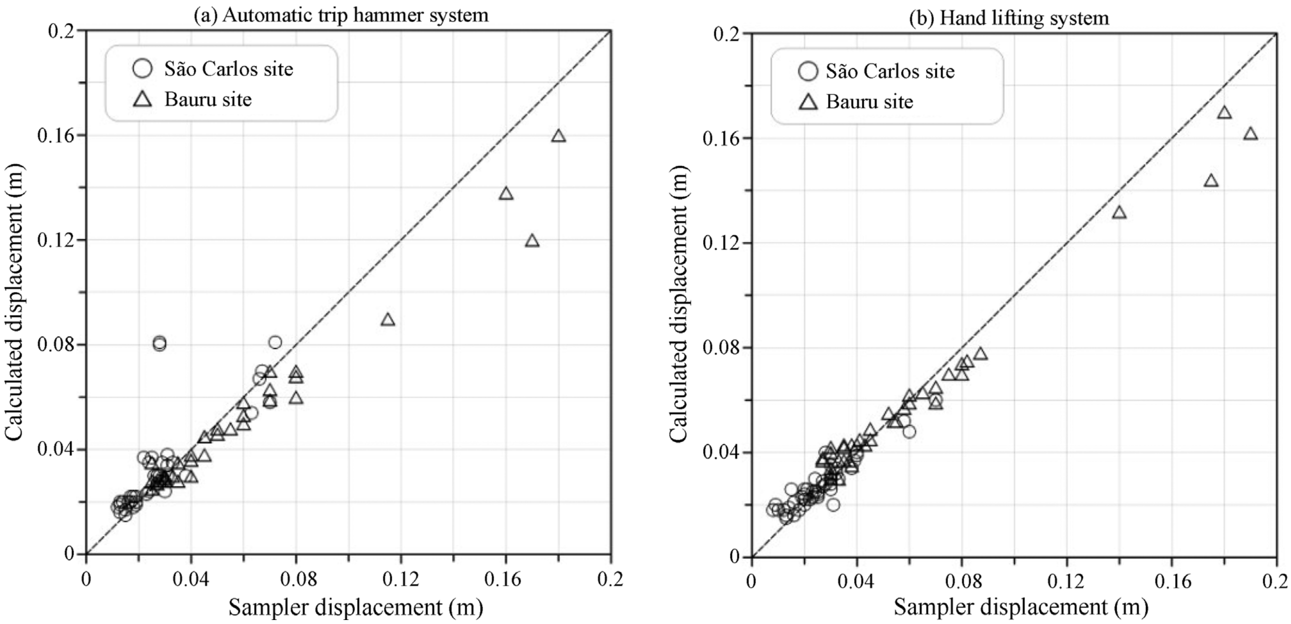

Figure 10 - Comparison of sampler displacement and calculated displacement for instrumentation placed below the anvil.

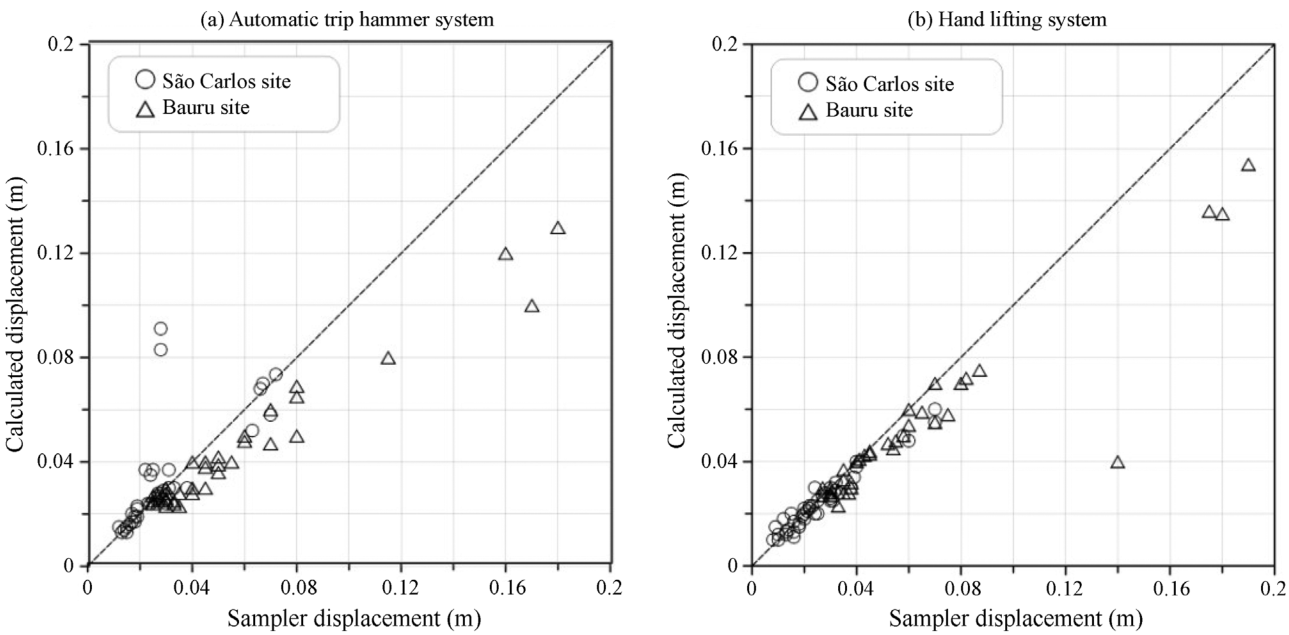

Figure 11 - Comparison of sampler displacement and calculated displacement for instrumentation placed above the sampler.

ately below the anvil. The data indicate that most of the E_R values for the *hand lifting system* are in group G6, which corresponds to energy ratios between 70% and 80%, whereas most of the values for the *automatic trip hammer system* are in group *G*7, corresponding to energy ratios between 80% and 90%. In general, results show that the energy ratio corresponding to the *automatic trip hammer system* is slightly higher than those corresponding to the *hand lifting system*. This behavior is consistent with the work of Reading *et al.* (2010), especially because the execution procedures for an *automatic trip hammer system* with an automatic tripping mechanism are less influenced by operators. In addition, for *hand lifting system*, buckling of the drill rods occurs during the hammer fall due to the eccentricity of the blow and consequently a higher amount of energy is lost.

Figures 14 and 15 show the energy ratio (E_R) histogram for *hand lifting* and *automatic trip hammer systems*, which represent the E_R values for a section immediately above the sampler. Results indicate that energy measured above the sampler is more variable than energy measured below the anvil.

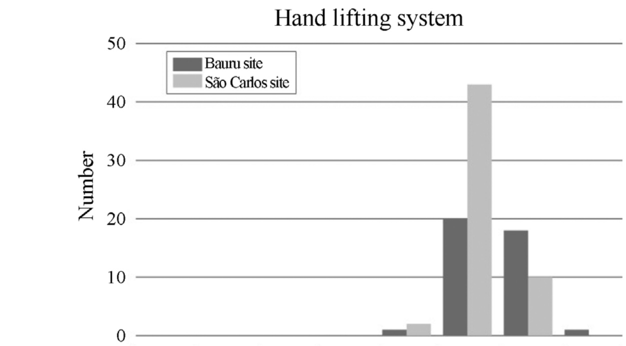

	G1	G2	G3	G4	G5	G6	G7	G8
Bauru site	0	0	0	0	1	20	18	1
São Carlos site	0	0	0	0	2	43	10	0

Figure 12 - Energy ratio (E_R) histogram for *hand lifting system* (instrumentation placed below the anvil).

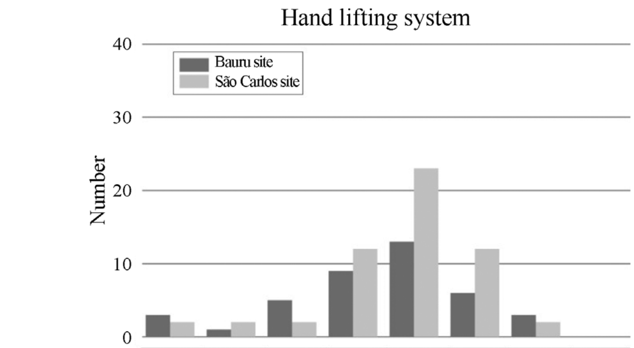

	G1	G2	G3	G4	G5	G6	G7	G8
Bauru site	3	1	5	9	13	6	3	0
São Carlos site	2	2	2	12	23	12	2	0

Figure 14 - Energy ratio (E_R) histogram for *hand lifting system* (instrumentation placed above the sampler).

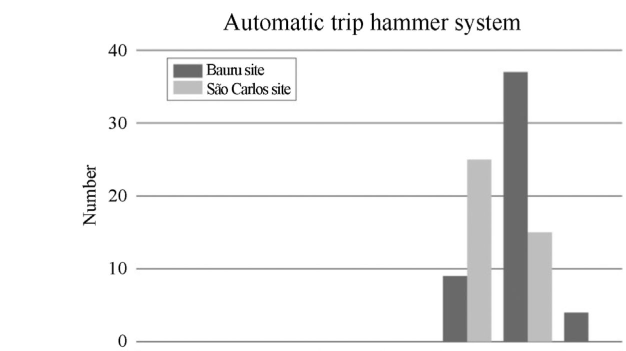

	G1	G2	G3	G4	G5	G6	G7	G8
Bauru site	0	0	0	0	0	9	37	4
São Carlos site	0	0	0	0	0	25	15	0

Figure 13 - Energy ratio (E_R) histogram for *automatic trip hammer system* (instrumentation placed below the anvil).

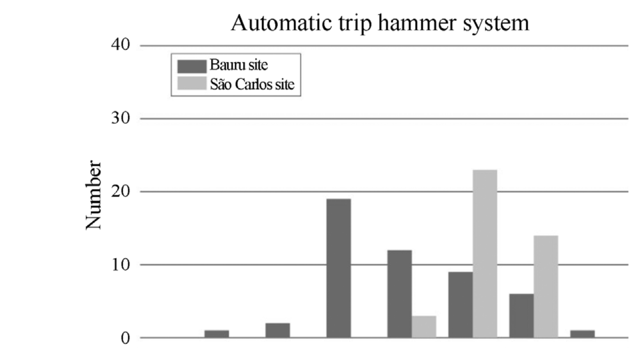

	G1	G2	G3	G4	G5	G6	G7	G8
Bauru site	0	1	2	19	12	9	6	1
São Carlos site	0	0	0	0	3	23	14	0

Figure 15 - Energy ratio (E_R) histogram for *automatic trip hammer system* (instrumentation placed above the sampler).

The data indicate that most of the E_R values for the *hand lifting system* are in group G5, which corresponds to energy ratios between 60% and 70%. For the *automatic trip hammer system* values are in group G4, for the Bauru site, and in group G6, for the São Carlos site, which corresponds to energy ratios between 50-60% and 70-80%, respectively.

The values of energy ratio as a function of the depth for Bauru and São Carlos sites, considering the different set-ups, are presented in Figs. 16 and 17. The behavior of the data shows that the energy transferred to the anvil is not influenced by the rod length (Fig. 16). Santana *et al.* (2014) observed this same behavior using drill rod lengths varying from 10.80 m to 25.70 m. In the present study, drill rod lengths varying from 2.95 m to 12.95 m were used, due to the limitation of the cable length for the instrumentation placed above the sampler.

Results show that it is possible to use an average value for E_R in a section just below the anvil. The coefficient of variation (*CV*) was about 5% (Table 3), which is a very small value considering geotechnical tests. Phoon & Ching (2012) mentioned that the availability of multiple test data in a typical site investigation can contribute to the coefficient of variation reduction. Additionally, Phoon & Kulhawy (1999) demonstrated that a CV from 25% to 50% can be expected for N_{SPT} index estimation. However, the data presented in this paper, demonstrate that the energy variation can be controlled by following recommended execution procedures, consequently the estimation of N_{SPT} index can be made more reliable.

On the other hand, results also show that E_R values in a section just above the sampler are highly variable (Fig. 17). The data indicates that the energy transference to the sampler does not have a defined behavior and it is not possible to use an average value to represent E_R in a section just above the sampler.

The energy ratio values measured just below the anvil are less variable than the values measured above the sampler, probably because most of the energy is transferred during the first impact (Fig. 18). On the other hand, the energy before reaching the sampler is dissipated during the wave propagation through the drill rods, connected by somewhat loose rod joints, making it highly variable.

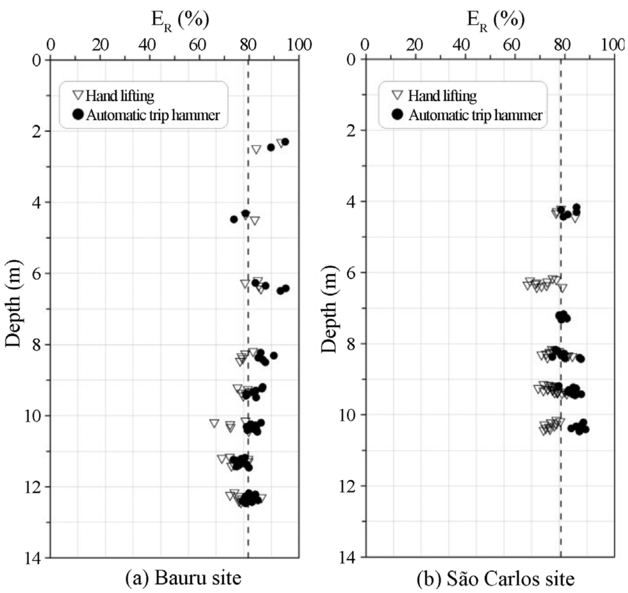

Figure 16 - Depth *vs.* energy ratio (instrumentation placed below the anvil).

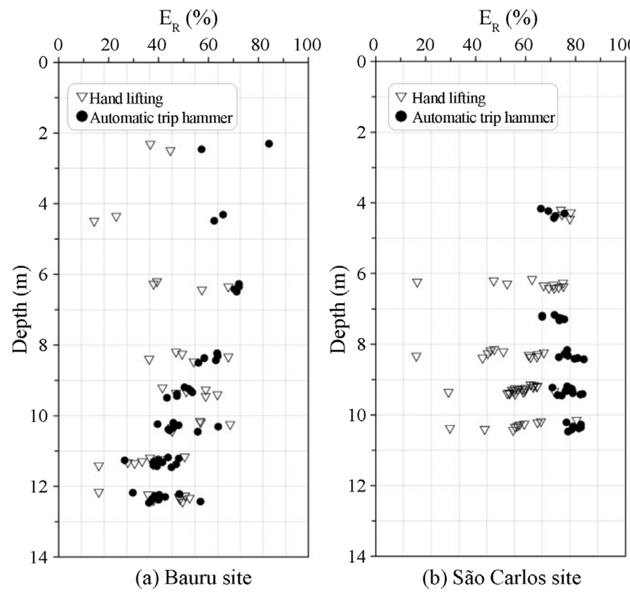

Figure 17 - Depth *vs.* energy ratio (instrumentation placed above the sampler).

Table 3 shows the E_R average values, standard deviation (*SD*) and the coefficient of variation (*CV*) for the experimental data. Results indicate that the E_R for the *hand lifting system* is about 79% when the instrumentation is placed below the anvil. Santana *et al.* (2014) estimated values ranging from 67% to 115%. However, the authors observed that the hammer drop height may vary due to operator execution procedures. In the present work, the hammer drop height was strictly controlled and maintained the standard value of 0.75 m. Therefore, E_R values higher than 100% can be justified by the additional potential energy of the hammer and rods due to the sampler penetration into the soil (Odebrecht *et al.*, 2005).

Results also show that for the *automatic trip hammer system* the E_R is about 84%, which is 5% higher than the E_R value estimated for the *hand lifting system*. This behavior makes sense because the automatic tripping mechanism is less influenced by operators. Additionally, the blow is more centric and buckling of the drill rods is minimized.

The energy values measured above the sampler were highly variable (Table 3), except for the *automatic trip hammer system* at the São Carlos site. Generally, results show the difficulty of measuring the energy in this section, which is probably because wave reflections and buckling of the drill rods occur during the wave propagation.

Table 3 - Statistical results.

Bauru site				
Parameters	Automatic trip hammer system system set-up		Hand lifting system	
	Anvil	Sampler	Anvil	Sampler
E_R average (%)	83.4	64.7	79.9	59.0
SD	4.4	13.6	4.3	15.1
CV (%)	5.2	21.0	5.4	25.6
São Carlos site				
Parameters	Automatic trip hammer system		Hand lifting system	
	Anvil	Sampler	Anvil	Sampler
E_R average (%)	83.8	78.3	77.3	62.7
SD	3.1	4.0	3.5	12.3
CV (%)	3.7	5.1	4.6	19.7

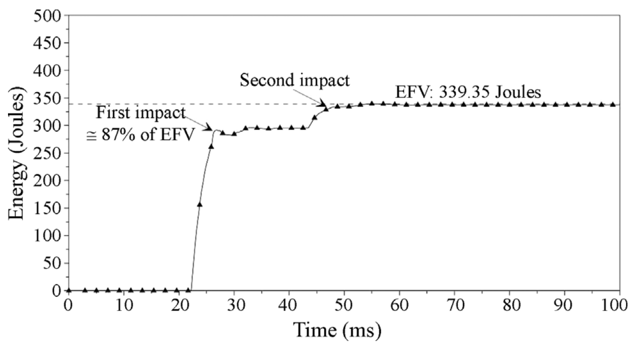

Figure 18 - Mechanism of energy transfer to the drill rods (below the anvil).

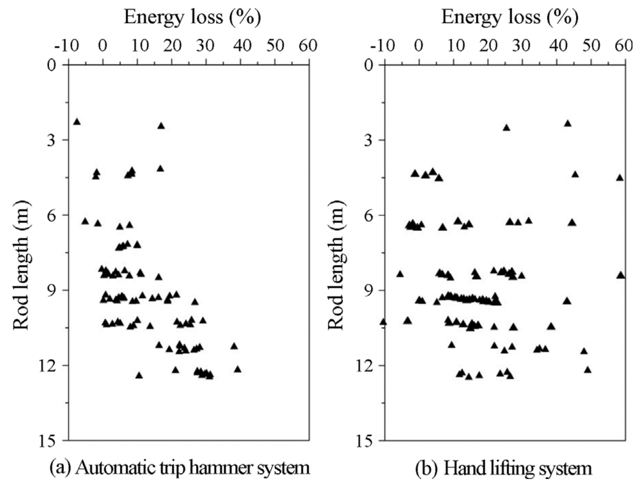

Figure 20 - Energy losses over the rod.

The acceleration signals allowed observing the behavior differences between the manual and automatic hammers, following hammer impact (Fig. 19). The acceleration records show that acceleration becomes different from zero at the instant that the hammer hits the anvil (hammer impact). It can be noted that for the automatic hammer, the signals corresponding to both accelerometers installed in the subassembly agree during the impact until the instant of 0.14 ms (Fig. 19a). This indicates that during the hammer impact there was no eccentricity effect. However, for the manual hammer, the acceleration signals are not in agreement during the hammer impact (Fig. 19b). It can be noted that the acceleration signals are not in agreement, most likely due to the blow eccentricity effect. This effect is more frequent for the manual tripping mechanism because the free fall of the hammer is strongly dependent on the operators at the instant they release the hammer.

5.3. Energy losses over the rod

The energy losses over the rod were evaluated by comparing energy values calculated in sections just below the anvil and just above the sampler. Figure 20 shows the energy losses over the rod for the *hand lifting* and *automatic trip hammer systems*. As it can be observed, results show a significant loss of energy. For the *automatic trip hammer system*, the data indicates a trend of increasing loss of energy with the length of rods. Results show a loss of energy of about 40% for 12 m of rod length. However, for the *hand lifting system* the loss of energy shows a dispersion of values and consequently there is no trend to be observed.

Odebrecht (2003) and Johnsen and Jagello (2007), identified a trend of increasing energy loss with increasing rod length. Odebrecht *et al.* (2005) performed instrumented SPT tests in a calibration chamber. However, in field tests, due to the different boundary conditions, different behavior should be expected. Johnsen & Jagello (2007) found a scatter behavior of energy loss using several different SPT systems. However, the increase of energy loss with the increase of rod length is a consensus among researchers.

In the present work, the dispersion of results can be explained by the soil conditions and execution procedures. For shallow depths and soft soil, the energy transfer occurs through multiple impacts (secondary impacts). During the energy transference, the buckling of the drill rod causes significant energy losses. Therefore, the energy loss is highly variable.

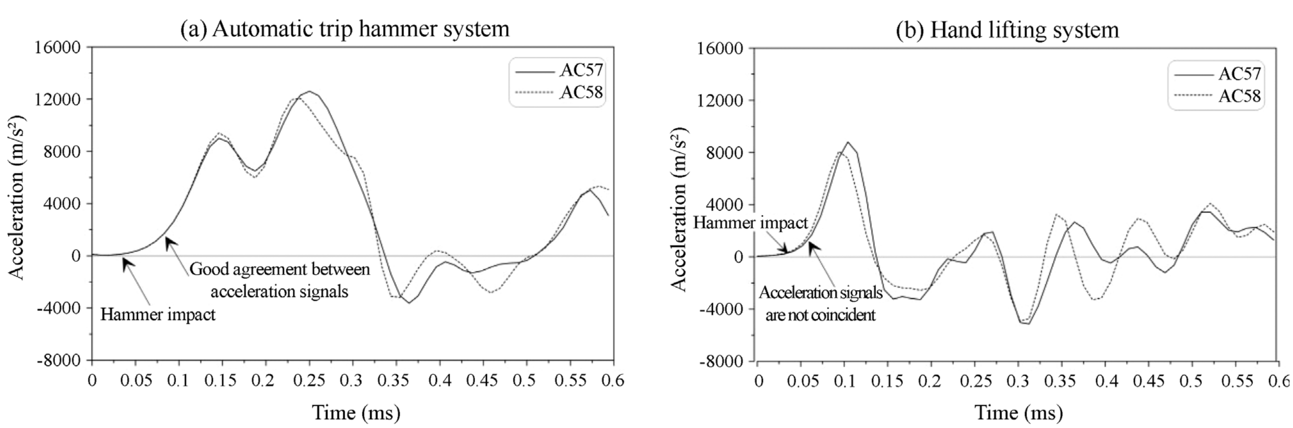

Figure 19 - Comparison between acceleration signals for different hammer systems.

5.4. The implications of the N_{SPT} index corrections

The energy ratio values have a significant effect on the N_{SPT} index, so that this index should be adjusted to a reference energy ratio of 60% (N_{60}) (Eq. 2). For set-ups with different energy ratios, the N_{SPT} index may vary significantly (Reading *et al.*, 2010), making this correction a necessity.

Figures 21 and 22 show the comparison of the N_{SPT} index for energy ratio values estimated in the present work. For both *hand lifting* and *automatic trip hammer systems*, results from the Bauru site (Fig. 21) show that the N_{SPT} index does not vary significantly because the E_R values are very similar (Table 3). In this figure, N_{80} and N_{83} are the N_{SPT} indexes estimated for energy ratios of 80% and 83%, respectively. Consequently, the comparison between the N_{SPT} indexes for different energy ratio indicates that N_{60} is about 36% higher than N_{80} or N_{83}.

Figure 22 shows results from São Carlos. In this figure, N_{77} and N_{84} are the N_{SPT} indexes estimated for energy ratios of 77% and 84%, respectively. The difference between the energy ratios of the hammer systems is about 7%. The comparison between the N_{SPT} indexes for different energy ratios indicates that N_{60} is about 28% and 40% higher than N_{77} or N_{84}, respectively. However, Reading *et al.* (2010) demonstrated that for larger differences the N_{SPT} index may vary by about 90%. Therefore, the application of the N_{SPT} correction based on energy ratio, estimated from energy measurements during SPT tests, would give a consistent N_{SPT} index for any kind of equipment set-up.

The European Standard (ISO, 2005) requires that a certificate of calibration including the E_R value be available and provides a recommended method for estimating energy ratios and reporting the results. Additionally, the calibrations should be carried out every six months because the hammer may become damaged.

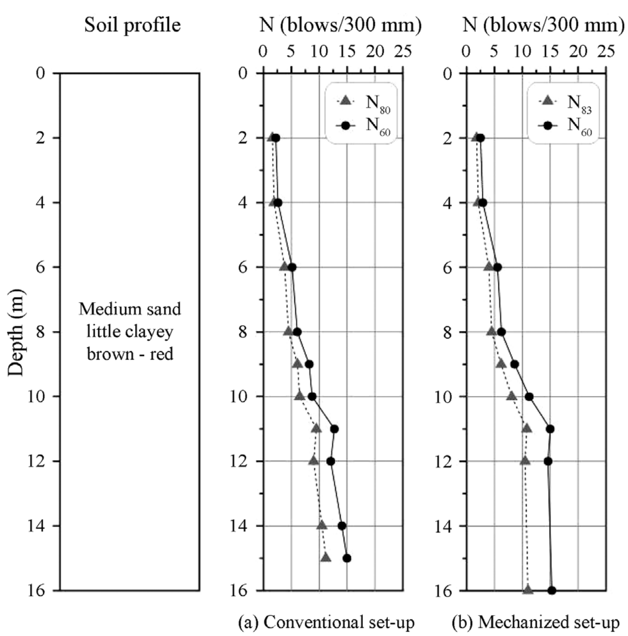

Figure 21 - N_{SPT} index for different energy ratios (Bauru site).

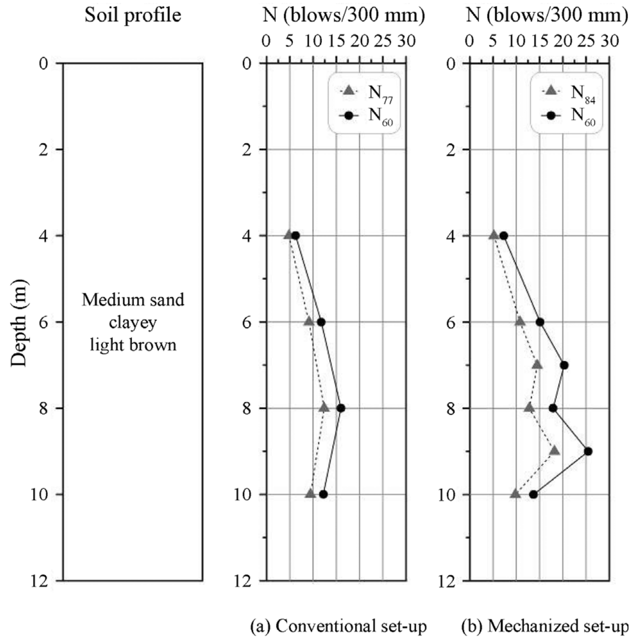

Figure 22 - N_{SPT} index for different energy ratios (São Carlos site).

6. Conclusions

This paper presents the results of SPT tests performed with two instrumented subassemblies, one placed at the top and the other at the bottom of the string of rods. This instrumentation allowed for the assessment of the amount of energy transmitted to the drill rods, at sections just below the anvil and just above the sampler, for two different equipment set-ups, with both a *hand lifting* and an *automatic trip hammer system*. The energy ratio was also estimated and compared. The following conclusions can be stated concerning the energy in SPT tests.

1. The developed instrumentation allowed for the simultaneous assessment of energy transmitted to the drill rods at sections just above the sampler and just below the anvil. The comparison between measured and calculated sampler displacement showed good agreement. Therefore, the developed instrumentation is adequate for estimating the energy transmitted during wave propagation.
2. Experimental in-situ results show that the top energy ratio (E_R) values corresponding to the *hand lifting system* are between 70% and 80%, whereas the values corresponding to the *automatic trip hammer system* are between 80% and 90%. Results show that the top energy ratio for the *automatic trip hammer system* is slightly higher than the *hand lifting system*. This behavior makes sense because the *automatic trip hammer system* has an automatic tripping mechanism and conse-

quently the execution procedures are less influenced by operators. Also, for the *hand lifting system* (manual tripping mechanism), buckling of the drill rods occurs during the hammer fall, due to the eccentricity of the blow and consequently additional energy is consumed. The same effect does not occur for the *automatic trip hammer system*, because the blow is more centric.

3. Experimental in-situ results also show that the bottom energy ratio values for both equipment systems are more variable than the energy values measured below the anvil.
4. Results indicate that the energy values assessed just below the anvil are less variable than the values estimated above the sampler, probably because most of the energy is transferred during the first impact. The energy is dissipated during the wave propagation over the drill rods and the amount that reaches the sampler is highly variable.
5. The data shows that the energy transferred to the anvil is not influenced by its length. Additionally, results show that it is possible to use an average value for E_R in a section just below the anvil. The coefficient of variation (*CV*) was about 5%, which is considered a very small value for geotechnical problems. On the other hand, results also show that E_R values in a section just above the sampler are highly variable. The data indicates that the energy transferred to the sampler does not have a defined behavior and it is not possible to use an average value to represent E_R in a section just above the sampler.
6. Acceleration records indicate that during the hammer impact, eccentricity effects are more frequent for the manual tripping mechanism. For this tripping mechanism, the free fall of the hammer is strongly dependent on the operators at the instant they release the hammer.
7. Experimental results show a significant loss of energy over the drill rod. For the *automatic trip hammer system*, the behavior of data indicates a trend of increasing energy loss with the length of rods. However, for the *hand lifting system* the energy loss also shows wide dispersion that cannot be easily explained. A loss of energy of about 40% for a 12-m rod was observed, which can be explained by the soft soil and the buckling of the drill rods during the energy transference, which causes significant energy losses.
8. For the Bauru site, results show that the N_{SPT} indexes are very similar for both equipment set-ups. Thus, the comparison between the N_{SPT} indexes for different energy ratios shows that N_{60} is about 36% higher than N_{80} or N_{83}. Results for the São Carlos site also indicated that the N_{SPT} index does not vary for *hand lifting* and *automatic trip hammer systems*. The comparison between the N_{SPT} indexes for different energy ratios indicates that N_{60} is about 28% and 40% higher than N_{77} or N_{84}, respectively. The N_{SPT} index correction based on energy ratios estimated from energy measurements during SPT tests would give a consistent N_{SPT} index for any kind of equipment set-up.

The SPT test results of this research indicate that the variability of the amount of the energy that reaches the anvil can be minimized by controlling execution procedures. Additionally, equipment set-up using an automatic tripping mechanism yields lower results dispersion. Results also show that difficulties may arise in measuring and interpreting the amount of energy that reaches the sampler. The variability of results is widely variable in terms of energy and loss of energy, whose explanation is not very clear.

Acknowledgments

The authors are thankful to FAPESP (Grant No. 2008/08268-4) and CNPq (Grant No. 479001/2009-0) for the financial support. Furthermore, the first author is thankful to CAPES for granting the scholarship that made the development of this research possible both in Brazil and Canada.

References

ABNT (2001). Standard Penetration Test (SPT). NBR 6484, Rio de Janeiro, 17 p. (in Portuguese).

Aoki, N. & Cintra, J.C.A. (2000). The application of energy conservation Hamilton's principle to the determination of energy efficiency in SPT test. Proc. 6th International Conference on the Application of Stress-Wave Theory to Piles, São Paulo, pp. 457-460.

Aoki, N.; Esquivel, E.R.; Neves, L.F.S. & Cintra, J.C.A. (2007). The impact efficiency obtained from static load test performed on the SPT sampler. Soils and Foundations, 47(6):1045-1052.

ASTM (2008). Standard test method for standard penetration test (SPT) and Split-Barrel Sampling of Soils. D1586-08a. ASTM International, West Conshohocken, PA.

ASTM (2010). Standard test method for energy measurement for dynamic penetrometers. D4633. ASTM International, West Conshohocken, PA.

Belincanta, A. & Cintra, J.C.A. (1998). Evaluation of intervenient factors on the ABNT method to SPT execution. Soils and Rocks, 21(3):119-133.

Cavalcante, E.H.; Danziger, B.R. & Danziger, F.A.B. (2008). On the energy reaching the sampler during SPT. Proc. 8th International Conference on the Application of Stress-Wave Theory to Piles, Lisbon, pp. 737-742.

Danziger, F.A.B.; Danziger, B.R. & Cavalcante, E.H. (2008). Energy and meaning of the N value in SPT in special cases. Proc. XIV COBRAMSEG, Buzios, pp. 2214-2224 (in Portuguese).

Howie, J.A.; Daniel, C.R.; Jackson, R.S. & Walker, B. (2003). Comparison of energy measurement methods in the standard penetration test. Report prepared for the

U.S. Bureau of Reclamation, Geotechnical Research Group, Department of Civil Engineering, The University of British Columbia, Vancouver, Canada.

ISO (2005). Geotechnical Investigation and Testing - Field Testing. Part 3: Standard Penetration Test. ISO 22476-3, Switzerland, 22 p.

ISSMFE (1989). Report of ISSMFE - Technical Committee on Penetration Testing of Soils - TC 16 with reference test procedures - CPT-SPT-DP-WST. International Reference Test Procedure for the Standard Penetration Test (SPT), p. 17-19.

Johnsen, L.F. & Jagello, J.J. (2007). Discussion of energy efficiency for standard penetration test. Journal of Geotechnical and Geoenvironmental Engineering, 133(4):486-487.

Kovacs, W.D. & Salomone, L.A. (1982). SPT hammer energy measurement. Journal of the Soil Mechanics and Foundation Division, ASCE, 108(GT4):599-620.

Lee, C.; Lee, J.S.; An, S. & Lee, W. (2010). Effect of secondary impacts on SPT rod energy and sampler penetration. Journal of Geotechnical and Geoenvironmental Engineering, 136(3):522-526.

Lukiantchuki, J.A.; Bernardes, G.P. & Esquivel, E.R. (2015). Efficiency in Standard Penetration Test. Proc. XVI ECSMGE Geotechnical Engineering for Infrastructure and Development, Edinburgh, p. 2981-2985.

Lukiantchuki, J.A.; Esquivel, E.R. & Bernardes, G.P. (2011). Interpretation of force and accelerations signals during hammer impact in SPT tests. Proc. Pan-Am CGS Geotechnical Conference, Toronto, Canada, 8p.

Lukiantchuki, J.A. (2012). Interpretation of SPT Test Results Based on Dynamic Instrumentation. Doctoral Thesis, University of São Paulo, São Carlos, 326 p. (in Portuguese).

Odebrecht, E.; Schnaid, F.; Rocha, M.M. & Bernardes, G. (2005). Energy efficiency for standard penetration tests. Journal of Geotechnical and Geoenvironmental Engineering, 131(10):1252-1263.

Odebrecht, E. (2003). SPT Energy Measures. Doctoral Thesis, Federal University of Rio Grande do Sul, Porto Alegre, 230 p. (in Portuguese).

Phoon, K.K. & Ching, J. (2012). Beyond coefficient of variation for statistical characterization of geotechnical parameters. Proc. 4th Geotechnical and Geophysical Site Characterization, Porto de Galinhas, p. 113-130.

Phoon, K.K. & Kulhawy, F.H. (1999). Characterization of geotechnical variability. Canadian Geotechnical Journal, 36(4):612-624.

Reading, P.; Lovell, J.; Spires, K. & Powell, J. (2010). The implications of the measurement of energy ratio (Er) for the Standard Penetration Test. Ground Engineering, Technical Note, available at https://www.geplus.co.uk/ downloaded on May 4th 2016..

Robertson, P.K.; Campanella, R.G. & Wightman, A. (1983). SPT-CPT correlations. Journal of Geotechnical Engineering, ASCE, 109(11):1449-1459.

Sancio, R.B. & Bray, J.D. (2005). An assessment of the effect of rod length on SPT energy calculations based on measured field data. Geotechnical Testing Journal, 28(1):1-9.

Santana, C.M.; Danziger, F.A.B. & Danziger, B.R. (2012). The measurement of energy reaching the sampler in SPT. Proc. 4th Geotechnical and Geophysical Site Characterization, Porto de Galinhas, p. 921-926.

Santana, C.M.; Danziger, F.A.B. & Danziger, B.R. (2014). Energy measurement in the Brazilian SPT system. Soils and Rocks, 37(3):243-255.

Schmertmann, J.H. & Palacios, A. (1979). Energy dynamics of SPT. Journal of the Geotechnical Engineering Division, ASCE, 105(GT8):909-926.

Schnaid, F.; Odebrecht, E.; Rocha, M.M. & Bernardes, G. (2009). Prediction of soil properties from the concepts of energy transfer in dynamics penetration test. Journal of Geotechnical and Geoenvironmental Engineering, 135(8):1092-1100.

Seed, H.B.; Tokimatsu, K.; Harder, L.F. & Chung, R.M. (1985). Influence of SPT procedures in soil liquefaction resistance evaluations. Journal of Geotechnical Engineering Division, ASCE, 111(12):1425-1445.

Skempton, A.W. (1986). Standard penetration test procedures and the effects in sands of overburden pressure relative density, particle size, ageing and overconsolidation. Geotechnique, 36(3):425-447.

Skov, R. (1982). Evaluation of Stress Wave Measurements. DMT, Grumdungstechnik, Hamburg, Germany.

Sy, A. & Campanella, R.G. (1991). An alternative method of measuring SPT energy. Proc. 2nd International Conference on Recent Advances in Geotechnical Earthquake Engineering and Soil Dynamics, St. Louis, p. 499-505.

Tsai, J.S.; Liou, Y.J.; Liu, F.C. & Chen, C.H. (2004). Effect of hammer shape on energy transfer measurement in the standard penetration test. Soils and Foundations, 44(3):103-114.

Youd, T.L.; Bartholomew, H.W. & Steidl, J.H. (2008). SPT hammer energy ratio *vs.* drop height. Journal of Geotechnical and Geoenvironmental Engineering, 134(3):397-400.

List of Symbols

SPT: Standard Penetration Test
N_{SPT}: blow count
PE: nominal potential energy
E_R: energy ratio of the specific SPT set up
EFV: force-velocity method
$F(t)$: the normal force, during the wave propagation, at a specific section
$v(t)$: the particle velocity

N_{60}: N_{SPT} index corrected to 60% of the international reference for nominal potential energy E_{60}: 60% of the international reference of nominal potential energy
E_s: amount of energy that reaches the sampler
e_1: correction factor which relates the energy just before the impact to the free fall energy
e_2: ratio between the energy just below the anvil and the kinetic energy just before the impact
e_3: factor related to the drill rod length
q_t: tip resistance after correction for pore pressure effects
R_f: friction ratio
t_i: the integration initial instant
t_f: the integration final instant
Z: rod impedance
a: area of the rod cross-section
E: modulus of elasticity of the rod
c: theoretical wave propagation velocity
ρ_R: mass density of the rod
L': distance between the accelerometer and the sampler tip
g: gravitational acceleration

Resistivity Piezocone in the Conceptual Site Model Definition

M.T. Riyis, H.L. Giacheti

Abstract. The management and remediation of contaminated sites are strongly dependent on the diagnosis process during the site characterization program. A Conceptual Site Model (CSM) elaborated by use of high-resolution site characterization (HRSC) tools allows for a detailed diagnosis of geo-environmental issues. The piezocone (CPTu) test is a high-resolution tool that allows several specific sensors to be attached, such as the resistivity module. This hybrid device is called the resistivity piezocone (RCPTu). A simulated geo-environmental site characterization program was performed on a Brazilian erosion site using several tools (direct-push soil samplers, hollow stem auger and RCPTu) to develop the CSM for a site similar to the Brazilian conditions. The aim was to elaborate a detailed stratigraphical profile and verify the applicability of this tool at the studied site. It was noted that the RCPTu data interpretation was consistent with the data from traditional methods, with much more details. Better results were achieved when decision-making occurred on site. It was concluded that the RCPTu is a very useful tool in elaborating a suitable hydrogeological conceptual site model, even for Brazilian conditions, especially in an approach that prioritizes high-resolution geo-environmental characterization.

Keywords: site characterization, in situ testing, stratigraphical logging, soil sampling, RCPTu.

1. Introduction

A deficient site characterization program is the major cause of inadequate remediation of contaminated sites. It has been noted, in several cases, that it fails at the very first step, when the site diagnosis is elaborated or, more precisely, during Conceptual Site Model (CSM) development.

In Brazil, efforts aimed at proper geo-environmental site characterization are still in an early phase. Two major legal instruments were recently published: CETESB - The São Paulo State Law # 13577/2009 and the CONAMA - The Federal Resolution # 420/2009, valid throughout the Brazilian territory.

The person or company that caused the contamination, or earned financial gain through it, or the site owner is liable for the remediation of a contaminated site in Brazil. They have the legal obligation to investigate and to recover the site. The "Legally Responsible Person" currently hires a "Technical Manager" to do the job. This manager subcontracts certain outsourced services (chemical analysis laboratories, drilling companies, soil, groundwater and vapor sampling, monitoring well installations, among others) trying to optimize project-cost reduction. Typically, this manager just strictly complies with the Brazilian requirements. In most cases, the site is not properly characterized; therefore, it is not suitably remediated.

The goal of the "Legally Responsible Person" in the U.S. approach (USEPA, 2004) is to rehabilitate the site as effectively as possible, considering the project globally. Significant investments have been made in research and technologies, tools and equipment for site assessment, investigation and diagnosis of contaminated sites to achieve this goal.

A number of North American companies implemented the Triad Approach and Expedite Site Assessment to achieve this goal, based on three basic principles:

- Prompt and on-site decision-making;
- The CSM must be continuously reviewed and, at the end of the diagnostic job on site, it should have the lowest possible degree of uncertainties, which must be manageable (Aquino Neto, 2009; Killinbeck, 2012; Quinnan, 2012);
- Dense and high-resolution data must be collected within a short timeframe (Cleary, 2009; Martin & St Germain, 2008).

The piezocone (CPTu) and the resistivity piezocone (RCPTu) and their accessories are frequently used for the characterization of contaminated sites in the U.S. (Vienken *et al.*, 2012). They are very useful tools since:

- They collect a high density of data very quickly (Lee *et al.*, 2008; Killinbeck, 2012; Welty, 2012);
- They provide a high resolution profile at relatively low cost (Giacheti *et al.*, 2006; De Mio & Giacheti, 2007, Lee *et al.*, 2008; Quinnan, 2012; Shinn III, 2004);
- Decision-making can occur on site;
- It provides a very good understanding of the geology, a most critical variable in CSM elaboration (Cleary, 1989; Killinbeck, 2012; Quinnan, 2012; Welty, 2012);
- They provide the development of a very good hydrostratigraphical profile (Cleary, 2009; Quinnan *et al.*, 2010; Vienken *et al.*, 2012);

Marcos Tanaka Riyis, M.Sc., Technical Director, ECD Sondagens Ambientais Ltda., Sorocaba, SP, Brazil. e-mail: marcos@ecdambiental.com.br.
Heraldo Luiz Giacheti, D.Sc., Full Professor, Departamento de Engenharia Civil e Ambiental, Universidade Estadual Paulista, Bauru, SP, Brazil. e-mail: giacheti@feb.unesp.br.
Submitted on July 29, 2016; Final Acceptance on June 21, 2017; Discussion open until December 29, 2017.

- They allow soil and groundwater data to be collected, which would be very difficult (or impossible) to obtain in certain specific sites.

Site characterization campaigns were currently carried out to assess contaminated sites in regular jobs in Brazil to follow an outdated approach. They end up incomplete and raise many uncertainties. Reasons that contribute to this are the fact that decisions are not made on site and the traditional site characterization methods use low-resolution tools. In addition, traditional methods are usually not adequately employed, resulting in inefficient remediation projects with extremely long periods and at very high costs for the "Legally Responsible Person" and for society as a whole, often making it impossible to properly revitalize the site.

A case study is presented where RCPTu were used as the major tool to simulate proper site characterization with a low degree of uncertainty, as should be done in a contaminated site following the US EPA approach. The objective is to develop a solid CSM in a simulated geo-environmental site characterization and discuss the advantages and limitations of this approach in terms of our current conditions in Brazil.

2. Studied Site

The studied site is an erosion process in the city of Bauru, in the central region of São Paulo State, Brazil. The city is settled in a natural amphitheater with a radius of about 5 km, modeled by several streams at the headwaters of the Bauru River. The regional relief presents wide and gentle hills, and the rocks are sandstones of the Marília and Adamantina Formations. The typical soils are residual from sandstone of the Marília, Adamantina and Cenozoic Formations, with a sandy texture and small portion of clay. Soil formation in tropical climates, marked by the alternation of rainy seasons and droughts, intensifies leaching in the thin surface horizon, producing a porous and permeable structure, usually with a deep groundwater table.

This erosion process is located nearby the São Paulo State University (Unesp) campus and along the Água Comprida Creek (Fig. 1). It originated from the collapse of the rainwater dissipation system, poor design, poor construction and lack of infrastructure and maintenance, as described by Ide *et al.* (2010). The process reached a huge dimension with the installation of land allotment for housing (the residential condominiums Jardim Colonial and Jardim Niceia) in an area highly susceptible to erosion.

The rapid evolution of the erosion process was due to several heavy rainfalls, typical in this region, which struck and destroyed the water dissipating system. Figure 2 shows one of the branches of the erosion process in the studied site. According to Ide *et al.* (2010), a revitalization project was elaborated to rectify the bed of the stream due to the rapid evolution of the erosion process. However, the lack of maintenance is contributing to slope instability, and minor erosions are still taking place at the site.

Several site characterization campaigns, including field observation, laboratory and in situ tests were carried out at the site to better understand and explain the erosion process (Campos, 2014; Ide *et al.*, 2010).

3. Site Characterization

Ide (2009) previously carried out five SPT at the studied site. They were used to elaborate a preliminary Conceptual Site Model (CSM). After this, soil sampling, four monitoring well installation using the hollow stem auger drilling and ten resistivity piezocone tests were carried out at the site by Riyis (2012) to simulate proper site characterization as it should be undertaken in a contaminated site, following the US EPA approach.

3.1. Soil sampling

Soil samples were collected using the single tube direct-push soil sampler (DPT) at 9 locations every 1 m depth interval. It consists of a pushing tubular steel sampler, 1.40 m-long, with a 55 mm outer diameter and 46 mm inner diameter. This sampler contains a liner (1.20 m-long with an outer diameter of 44 mm), a transparent polymer (HDPE or PVC) tube with soil samples retrieved and stored after spiking and removing the set of direct-push tools.

The DPT (Fig. 3) was pushed into the ground using percussion. The equipment was an SB-50 Atlas Copco hydraulic hammer coupled to a truck-mounted hydraulic rig. Besides the sampler, the DPT has extending rods and adapters. Once the pushing process is complete, the DPT is retrieved and the liner is removed and sealed with two HDPE plastic caps. The DPT is reassembled and replaced in the borehole, with an extending rod to sample 1.0 m deeper, as represented in Fig. 3.

The choice for a single tube, direct-push soil sampler rather than another type, like the dual tube or the piston sampler, was made because it is faster and more widely used in Brazil. The other two types are only used in Brazil in exceptional cases (Riyis, 2012).

In cases where the borehole collapses, casing is necessary. In such cases, soil sampling is carried out with hollow stem auger (HSA) drilling. In the present study, the HSA tools were installed using a rig mounted on a VW 9150 truck. This equipment allows for the application of a maximum torque of 5 kN.m.

The DPT set is pushed into the ground and then removed and dismantled and the liner is removed from inside the sampler for tactile-visual soil identification. Then, HSA drilling is carried out to the previous sample depth. When this depth is reached, the DPT set inside the HSA is taken out and the DPT is replaced with a direct-push soil sampler inside the hollow boreholes. The DPT is hammered one more meter, and the sampling procedure is repeated (Fig. 4).

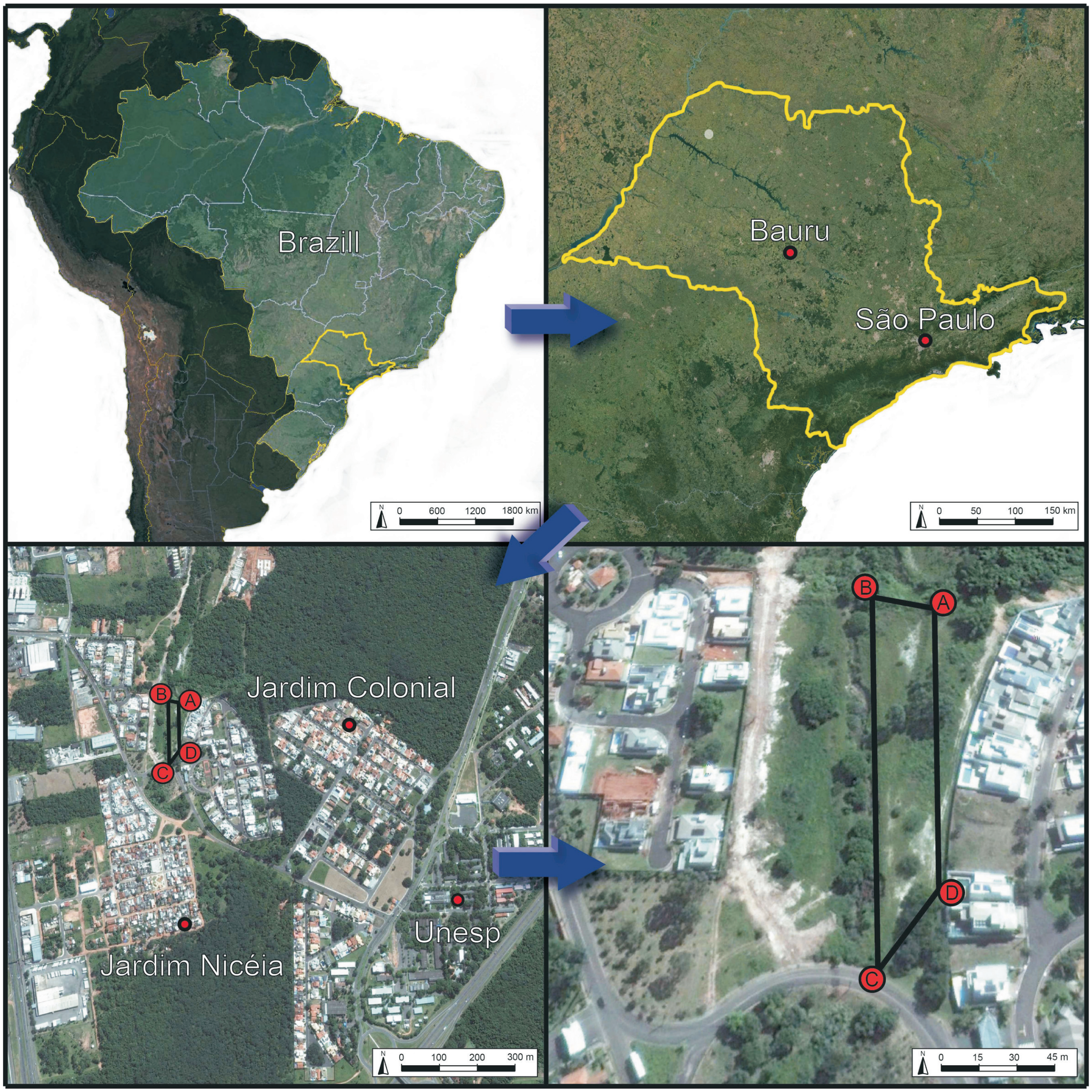

Figure 1 - Site location and aerial view of the studied site (adapted from Google Maps).

3.2. RCPTu

The piezocone is an instrumented probe that is pushed into the ground vertically at a standard rate of 20 mm/s. Measurements of tip resistance (q_c), sleeve friction (f_s) and pore pressure (u) at up to three locations are typically recorded every 10, 20, 25 or 50 mm depth intervals.

Due to the "inner" geometry of a cone penetrometer the ambient pore water pressure will act on the shoulder area behind the cone and on the ends of the friction sleeve, and this effect is often referred as "the unequal area effect" (a) and influences the total stress determined from the cone and friction sleeve (Lunne *et al.*, 1997). The corrected cone resistance (q_t) is given by Eq. 1:

$$q_t = q_c + u_2(1-a) \quad (1)$$

Changes in the friction ratio ($R_f = f_s / q_t \cdot 100\%$) are often used to identify changes in the soil profile based on soil behavior classification charts. Pore pressure records provide information about the response of the ground to the probe during the pushing and the consequent migration of fluids. A pressure transducer inside the piezocone takes the pore pressure measurement. The traditional procedure to

Figure 2 - A branch of the erosion process (Ide *et al.*, 2010).

measure pore pressure is by saturating the porous element with water or glycerin. Larsson (1995) and Elmgren (1995) suggested the use of a slot filter filled with grease as an alternative procedure.

The slot filter filled with grease is easier to prepare and handle than the porous piezo-element saturated with glycerin. It has a better application for deep groundwater level (Mondelli *et al.*, 2009). Mondelli *et al.* (2010) have used this technique in tropical soils. The pore pressure transducer inside the piezocone is brought into stiff contact with the pore water in the soil by filling the inner cavity with water and pressing the grease into the cavities inside the cone tip.

The RCPTu is like any other CPTu. The additional procedure is to add a signal generator to the data acquisition system to control the current level and frequency for the electrical bulk soil resistivity (or conductivity) measurements.

Figure 5 presents a Wenner-type resistivity piezocone with an array of four electrodes. Bulk soil resistivity (ρ_b) measurements are taken with the inner electrodes, and the current is applied through outer electrodes. These measurements are added to all other standard piezocone data (q_c, f_s and u).

The used CPTu probe was produced by Geotech AB (Sweden), NOVA acoustic model (wireless). The position to measure pore pressure is standard (u_2) and according to international practice. A slot filter filled with grease was used to measure pore pressure. The equipment has a ratio of unequal areas (a) equal to 0.84. This hybrid probe has a resistivity (or conductivity) module, which was also produced by Geotech AB. This module provides bulk soil resistivity data, also using the NOVA acoustic wireless system. Wireless data transfer and acquisition were performed with a microphone, which is part of this system.

The pushing equipment was anchored using double helicoids of 180 mm in diameter and extended rods with square coupling. Ten RCPTu were carried out using a hydraulic system attached to a tractor to perform the test.

The CPTu procedure followed the Brazilian Standards (ABNT-MB 3406/1990), like the ASTM D3441 standard. The hydraulic system was positioned, leveled and

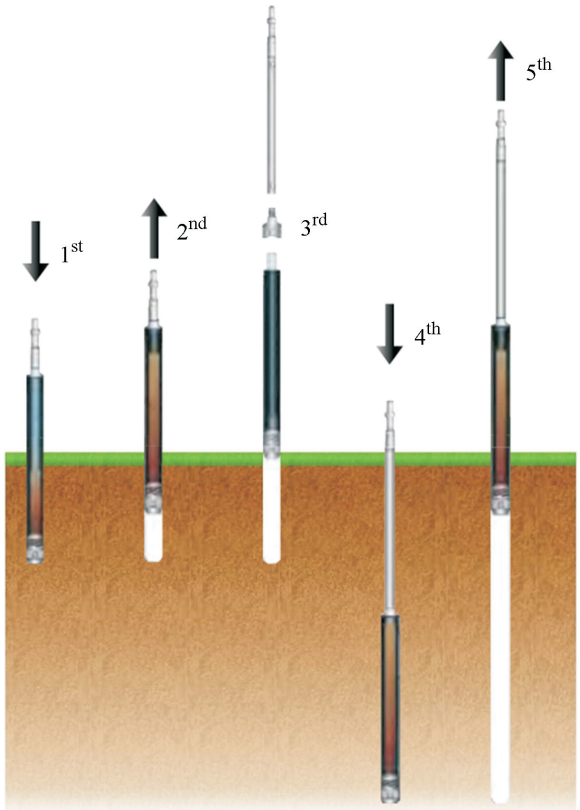

Figure 3 - Single tube sampling (adapted from AMS, 2012).

Figure 4 - Hollow stem auger drilling in use.

anchored (Fig. 6). Next, the baseline was taken and the RCPTu was carried out at a constant rate, interrupted only to connect extra rods.

The data were recorded at regular 20 mm depth intervals and displayed in real time on a computer connected to an acoustic data transmission system. Thus, the following data were recorded: tip resistance (q_c), lateral friction (f_s), pore pressure (u_2) and bulk soil resistivity (ρ_b).

The piezocone data interpretation for stratigraphical logging can be done using a classification chart as the one proposed by Robertson *et al.* (1986), which correlates the corrected point resistance (q_t) and the friction ratio (R_f), as presented in Fig. 7.

Besides the soil classification, this chart also shows the tendency of variation for relative density (*Dr*), stress history (*OCR*), sensitivity (S_t) and void ratio (*e*). The piezocone also allows classifying the soil based on the pore pressure data, by using the pore pressure index (B_q), whose formula is presented inside the B_q *vs.* q_t chart from Fig. 7. This approach is best applicable in soft soils, where the point resistance is low and the generated pore pressure is usually high. As discussed by Lunne *et al.* (1997), the classification charts do not classify the soil based on the grain size distribution or plasticity but they provide an information about the soil behavior.

Recently Robertson (2009) updated the Unified Approach, in which the soil is classified based on the I_c index calculated by Eq. 2 for qualitative analysis of the soil behavior. The soil behavior type (SBT) is function of a range of I_c values and the position in the proposed classification chart. The interpretation of CPT data via this specific approach considers the soil in terms of its behavior. For example, it is not appropriate to say that a soil is a sand, but that behaves in the same way as a sand-like material.

$$I_c = \left[(3.47 - \log Q_{tn})^2 + (\log F_r + 1.22)^2\right]^{0.5} \tag{2}$$

where:

$$Q_{tn} = \left(\frac{q_t - \sigma_v}{p_a}\right) \times \left(\frac{p_a}{\sigma'_{vo}}\right)^n \tag{3}$$

$$F_r = \left(\frac{f_s}{q_t - \sigma_{vo}}\right) \times 100\% \tag{4}$$

q_t = CPT corrected total cone resistance

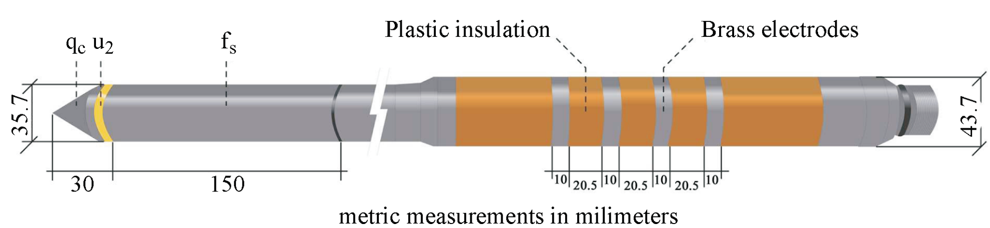

Figure 5 - Resistivity piezocone (RCPTu) probe with a four-electrode array (adapted from Mondelli *et al.*, 2007).

f_s = CPT sleeve friction
σ_{vo} = pre-insertion in-situ total vertical stress
σ'_{vo} = pre-insertion in-situ effective vertical stress
$(q_t - \sigma_v)/p_a$ = dimensionless net cone resistance, and,
$(p_a / \sigma'_{vo})^n$ = stress normalization factor
n = stress exponent that varies with SBT
p_a = atmospheric pressure in same units as q_t, σ_v and σ_{vo}

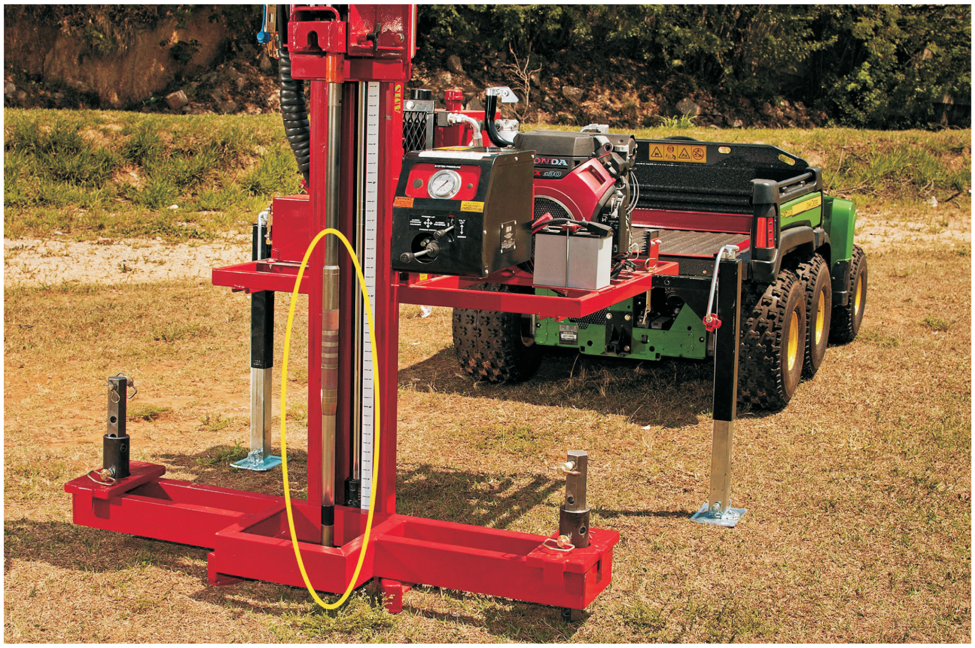

Figure 6 - Pushing rig and the RCPTu probe highlighted in the figure ready for the test.

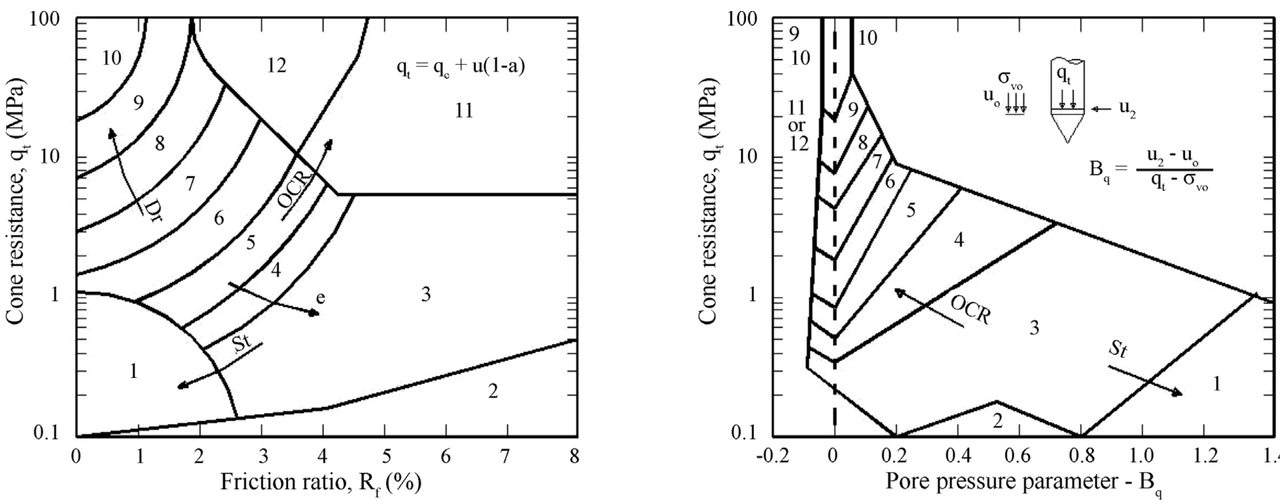

SBT	Soil behavior type
1	Sensitive fine grained
2	Organic material
3	Clay
4	Silty clay to clay
5	Clayey silt to silty clay
6	Sandy silt to clayey silt

SBT	Soil behavior type
7	Silty sand to sandy silt
8	Sand to silty sand
9	Sand
10	Gravelly sand to sand
11	Very stiff fine grained*
12	Sand to clayey sand*

* Overconsolidated or cemented

Figure 7 - Soil classification chart for CPTu interpretation proposed by Robertson *et al.* (1986).

The hydraulic conductivity (k) profile is an interesting information for a proper hydro-stratigraphical interpretation, which is very useful for the geo-environmental site characterization. Robertson (2010) proposed relationships between soil permeability (k) and I_c represented by:

$$k = 10^{(0.952 - 3.04 I_c)} \text{ m/s} \quad \text{for} \quad 1.00 < I_c \leq 3.27 \qquad (5)$$

$$k = 10^{(-4.52 - 1.37 I_c)} \text{ m/s} \quad \text{for} \quad 3.27 < I_c < 4.00 \qquad (6)$$

Robertson (2010) says that the Eq. 5 and Eq. 6 can be used to provide an approximate estimate of soil permeability (k) and to show the variation of soil permeability with depth from a CPT sounding. The author also states that the normalized CPT parameters (Q_{tn} and F_r) respond to the mechanical behavior of the soil and depend on many soil variables; the suggested relationship between k and Ic is approximate and should only be used as a guide.

4. Testing Data and Discussion

4.1. Previous data

Five SPT carried out on the studied site by Ide (2010) were used for site characterization of the erosion process to establish the preliminary CSM represented in Fig. 8. Based on this information, a predominantly heterogeneous sandy soil profile was expected. Presence of clayey lenses or other fine materials with diverse thickness at various locations of the soil profile could be typical at the site. The expected groundwater level was shallow (between 4 to 5 m depth), indicating the presence of several layers with different hydraulic conductivities.

According to this preliminary model, a free aquifer was predominantly associated to a sandy formation with high hydraulic conductivity. It formed the preferential flow for eventual contamination. Another important aquifer could be found close to the bedrock (expected at 12 to 15 m depth), confined by one or more aquitard layers with unknown thicknesses. This confined aquifer may also have a high hydraulic conductivity. Some vertical flow was also expected, demonstrating that there are, in fact, different aquifers. There were several uncertainties associated to this preliminary model since the SPTs were far away from one another (around 75 m) for the scale to which the appropriate CSM was intended to be defined.

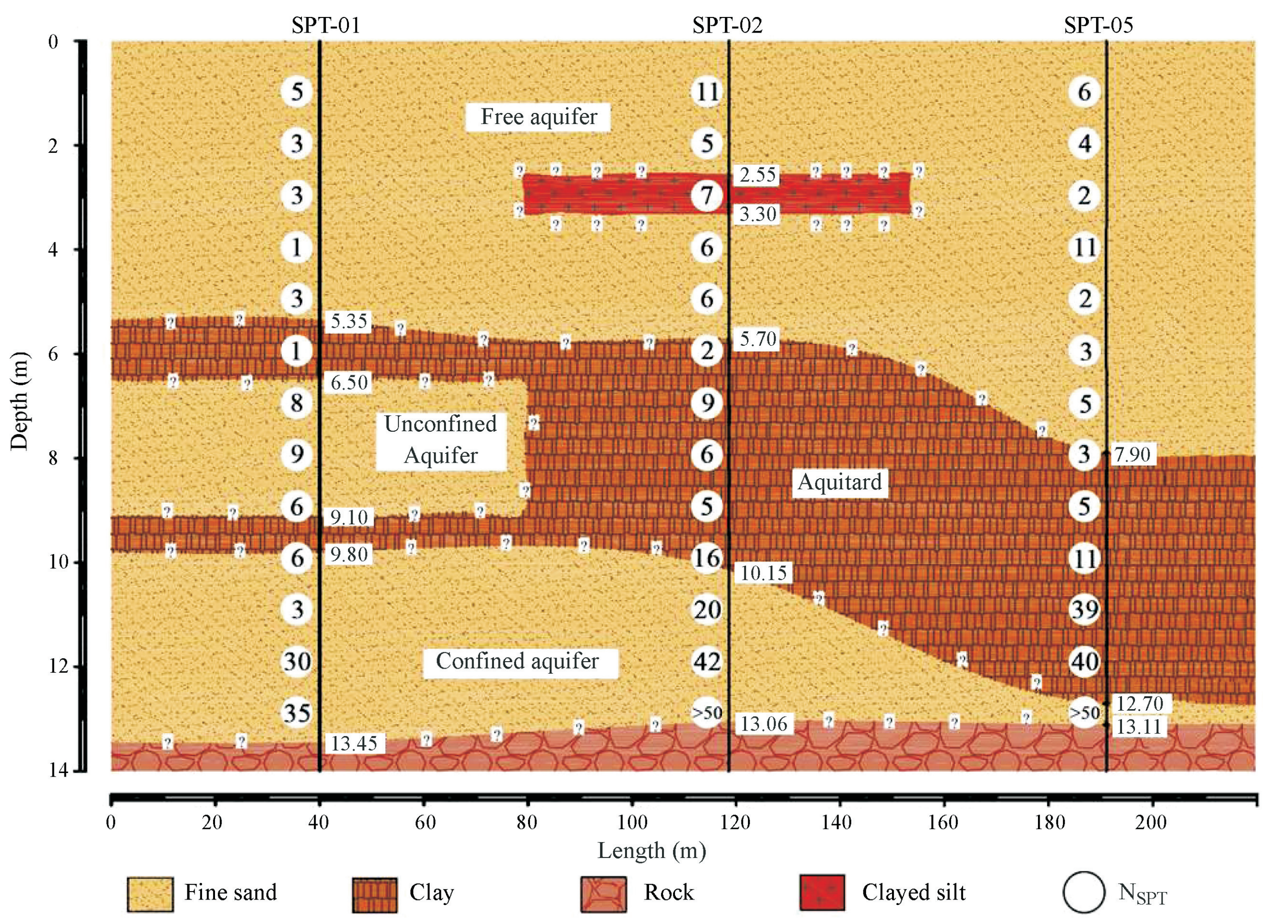

Figure 8 - Preliminary CSM interpreted for the studied site based on SPT data from Ide (2010).

4.2. Soil sampling

A site investigation campaign started with soil sampling with DPT, a technique recommended by US EPA and, in São Paulo State, by State Basic Sanitation Engineering Company (CETESB). It has been recognized as the best technique for soil sampling for contaminated site investigations (CETESB, 1999). A single tube was chosen as the DPT type for an initial sampling strategy. A cross section parallel to the creek and perpendicular to the direction of the studied site was established by Ide *et al.* (2010) to identify the site stratigraphical profile. In this section, 20 m distance was established between each sampling point as the default for the initial data collection (Fig. 9).

Ten soil-sampling points (DP-01 to DP-10) were taken with the single tube DPT. The samples were collected in liners at depth intervals of one meter, and they were described on site by the visual-tactile identification method.

Certain limitations were noted during sampling when attempting to establish an accurate CSM with the required resolution for proper characterization of this site. They were: collapse of the borehole wall requiring the use of casing; the hydraulic pressure loading material into the casing; and recovery of saturated sandy soil samples. These limitations are discussed as follow.

4.2.1. Borehole wall collapse

The collapse of the borehole wall occurred at the first sample point (DP-01). After retrieving the fifth sample (from 4.0 to 5.0 m depth), when the DPT was relocated into the borehole, it was noticed that the bottom of the sampling pit was about 4.7 m depth, instead of 5.0 m as expected. This means that at least 0.3 m of material fell to the bottom of the borehole and the following sample, which would be 5.0 to 6.0 m depth, was contaminated with material that did not belong to this layer. As such, the following two samples (5.0 to 6.0 and 6.0 to 7.0 m depth) were collected this way, and the soil from the bottom part of the liner was discharged.

The same procedure was adopted at the sample point DP-05; however, due to the need for extra information at this site location, the sample was recollected; *i.e.*, after collecting the sample from 5.0 to 6.0 m depth, the DPT was taken out, and the probe was inserted once again, 1 m away from the previous one. HSA rotary drilling was used up to a 5.0 m depth and then soil sampling from 5.0 to 6.0 m was performed inside the hollow augers. After sampling, HSA drilling was continued up to a depth of 6.0 m, and the soil sample was collected inside the hollow auger for the depth from 6.0 to 7.0 m. When the sample from 5.0 to 6.0 m depth was recollected, a layer of about 0.2 m of plastic gray clay with sand grains was noted, which had not been detected in the previous sampling (with no casing). This was certainly due to contamination of the sample material from the upper layers. The procedure was repeated up to 8.0 m depth, but the samples below 6.0 m depth were not representative due to another factor: the hydraulic pressure have loaded material into the hollow augers, which will be discussed below.

4.2.2. Hydraulic pressure

Some samples were not representative due to sample contamination with material beneath the casing caused by the hollow augers, as previously described. The material inlet occurs because of the hydraulic pressure associated with friable and non-cohesive soils (fine sand characteristics). If the hydrostatic pressure is high enough (estimated to be 30 kPa), the soil tends to enter in the hollow augers and block the retrieval of representative samples. There are tools to minimize this problem, like the Piston Sampler from AMS Inc., for example. However, they were not widely available in Brazil in 2012.

4.2.3. Recovering samples

Another problem occurred during the sampling at the point DP-06: excessive volumes of water in the sandy soil sample. Consequently, the sampler penetrated the ground with casing (HSA), but when it was removed from the bore-

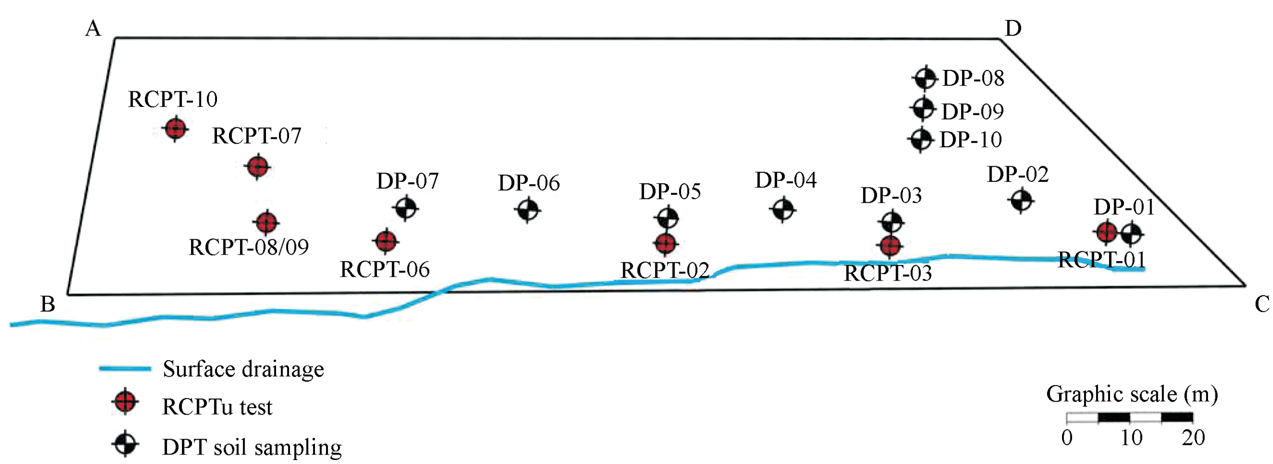

Figure 9 - DPT and RCPTu locations at the studied site.

hole, there was almost no recovered sample because it escaped from the DPT sampler due to the large amount of water coming out of it. There are other tools to minimize this effect, like the core catcher. Unfortunately, it was not used in Brazil in 2012.

4.2.4. Discussion

The soil profile interpreted via samples collected with the DPT at each investigation point is shown in Fig. 10. The refined CSM elaborated based on this information is represented in Fig. 11.

During the DPT data interpolation to elaborate the cross section presented on Fig. 11, it was decided to consider the Clayed Fine Sand and Silty Fine Sand just as a Fine Sand because it is very difficult to distinguish these soil types on site by tactile-visual identification. It was also considered during the interpolation process that there was no substantial difference in terms of flux and storage zones for both soils and they were defined as aquifers.

The three factors previously discussed restricted the elaboration of refined CSM in the vertical direction using just the DPT data. On the other hand, just the five SPT from Ide (2010) provided more information below a 6.0 m depth than DPT. The DPT data provided a more detailed soil profile at the shallow depths, where the free aquifer was expected and a better conceptual model at the horizontal direction was elaborated.

It is also clear that the CSM elaborated using the DPT leads to several uncertainties. They arose mainly from the limitation of data collection as well as the limitations in how to interpret the data, since tactile-visual soil identification depends on the technician who is performing it. Variations of two orders of magnitude are usual (Ahlers, 2012) and the scale on which samples can be described is inappropriate to identify the necessary differences in hydraulic conductivity.

4.3. RCPTu

RCPTu was carried out as the next step for CSM elaboration on the studied site. The goals of using this tool were:

- to define detailed profiles at the selected key site locations;
- to refine the CSM;
- to check the accuracy and limitations of this tool compared to the SPT and DPT;
- to perform a detailed check of the position at the soil profile for any minimal lenses of clay that may act as an aquitard; and
- to confirm the presence of a deeper aquifer.

Ten RCPTu were carried out at the same section where the soil samples were collected (Fig. 9), most of them right beside the DPT. The RCPT-04 was not used since it presented some communication problems between the probe and the data acquisition system probably caused by low battery at the very beginning of the test. The same happened during the RCPT-08 when it reached 4.72 m depth. After changing the batteries, a new test (RCPT-09) was carried out at the same position. So the interpretation logging for this point was identified as RCPT-08/09 up to 9.58 m depth.

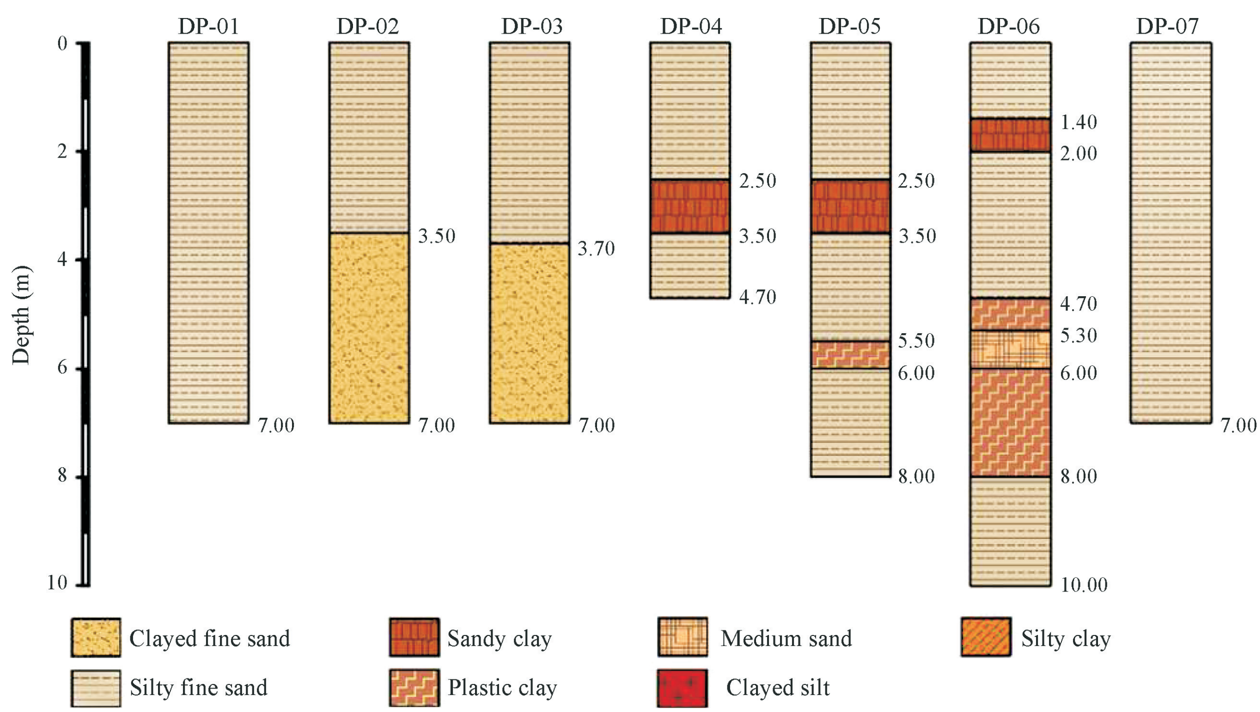

Figure 10 - Interpretation of all DPT logging from one of the longitudinal cross sections for the studied site.

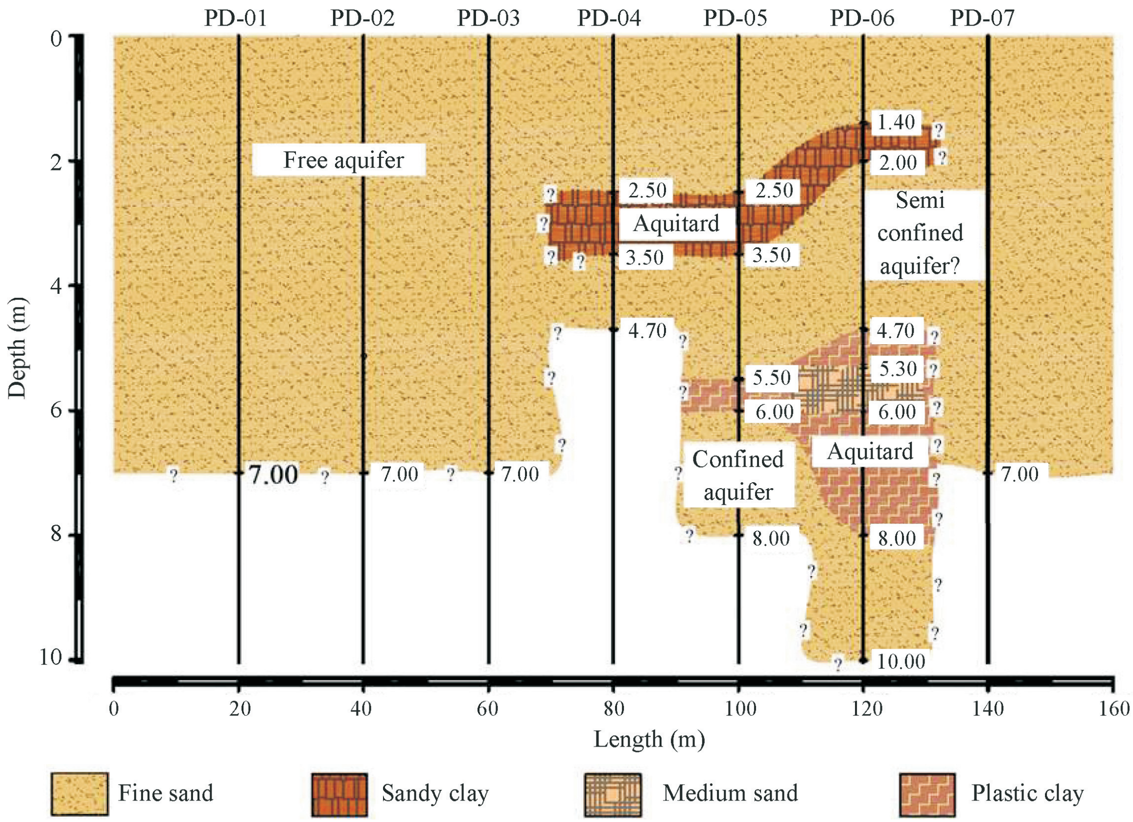

Figure 11 - Refined CSM for one cross section based on the DPT logging profiles.

A typical RCPTu data and the interpreted stratigraphical profile is presented in Fig. 12 for the RCPT-02. The identification of the soil profile is presented on the laptop screen during the test, allowing for refining the CSM right after every test. The soil type was identified by using Robertson *et al.* (1986) classification chart as a reference. They were confirmed and adjusted based on the samples retrieved with the DPT. Of note is the fact of how well the resistivity sensor complements the piezocone data (q_t, f_s and u), and it provides information more suited to the scale that investigation of a contaminated site needs. In the studied site, the soil bulk resistivity (ρ_b) profile was also useful to help define the groundwater level (GWL) with a big drop on the ρ_b value at 3.8 m depth (Fig. 12). This information was confirmed by the monitoring well installed beside this test location. It was also observed that variation in bulk resistivity (Fig. 12) occurred together with the other variations on three CPTu parameters (q_t, f_s and u) as the soil behavior changed (higher ρ_b in sandy lenses and lower ρ_b in clayey lenses), indicating that there is no sign of contamination on the studied site, since the ρ_b value is much affected by the fluid present in the pores of soil. This is one of the main applications of the resistivity data.

Since the bulk resistivity (ρ_b) data is more affected by the fluid present in the pores of soil, which can be contaminated, this extra information is quite important for geo-environmental site characterization using the piezocone technology, as discussed by Lunne *et al.* (1977). Daniel *et al.* (2003) discuss the applicability of resistivity piezocone for site characterization and they state that the RCPTu has proven to be a simple and useful screening tool mainly for delineating plumes of contaminated groundwater. De Mio *et al.* (2005) also illustrate the advantage of using the RCPTu to detect saltwater intrusion into a surficial sedimentary aquifer at the Paranaguá harbor, Paraná State, in Brazil. According to these authors, a high chloride concentration contaminated shallow water wells to supply water for local industries. Figure 13 shows two RCPTu of the tests carried out at the site guided by the dipole-dipole electrical profiling. One test (RCPTu B) intercepted the salt intrusion zone between 5.0 and 8.0 m depth. The other (RCPTu A) was positioned at a location with no evidence of contamination to get the ρ_b background values. This example points out the advantage of using this hybrid test to detect contaminated groundwater as well as to select the target for water sampling.

Performing the data interpretation for the studied site, it is was confirmed that the RCPTu provided much more details in the vertical direction and presented far fewer limitations than the DPT, as shown in Fig. 10 (for DPT) and Fig. 14 (for RCPTu). The interpretation of each RCPTu logging profile considers Robertson *et al.* (1986) chart to-

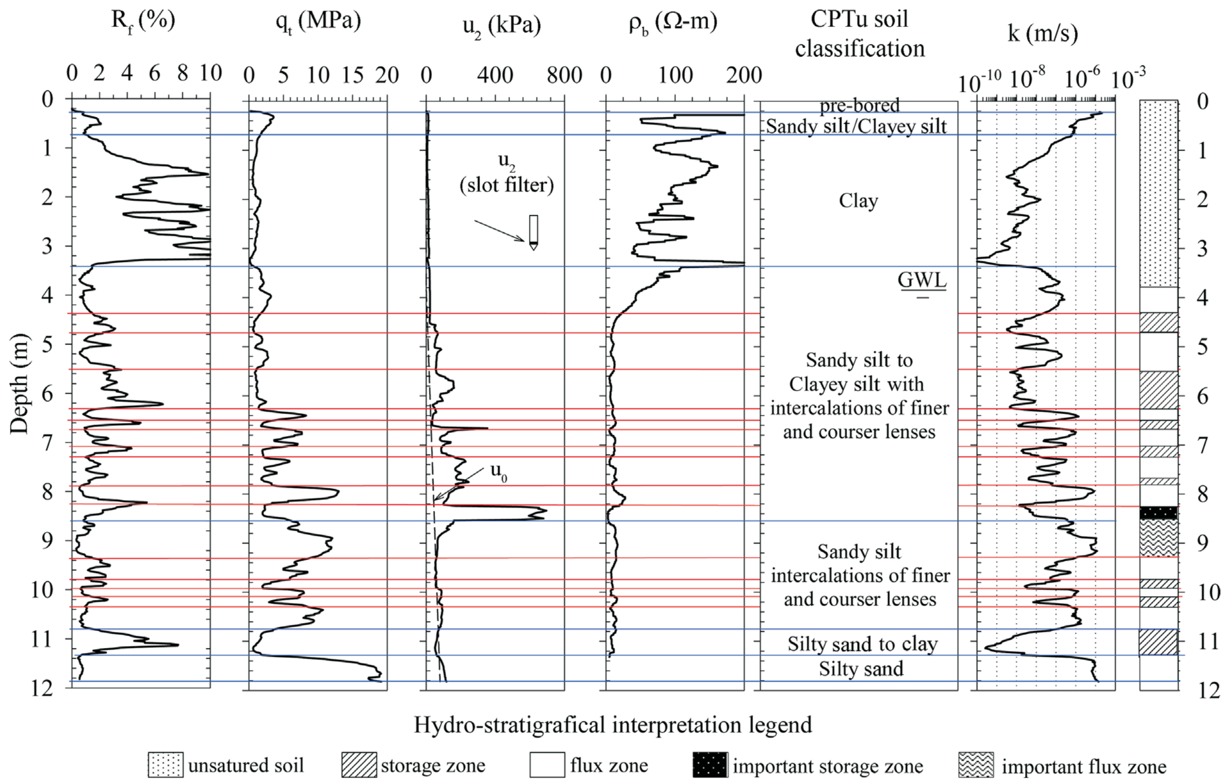

Figure 12 - Typical resistivity piezocone data (RCPT-02) and soil profile identified with Robertson *et al.* (1986) classification chart and hydro-stratigraphical profile considering estimated *k* profile.

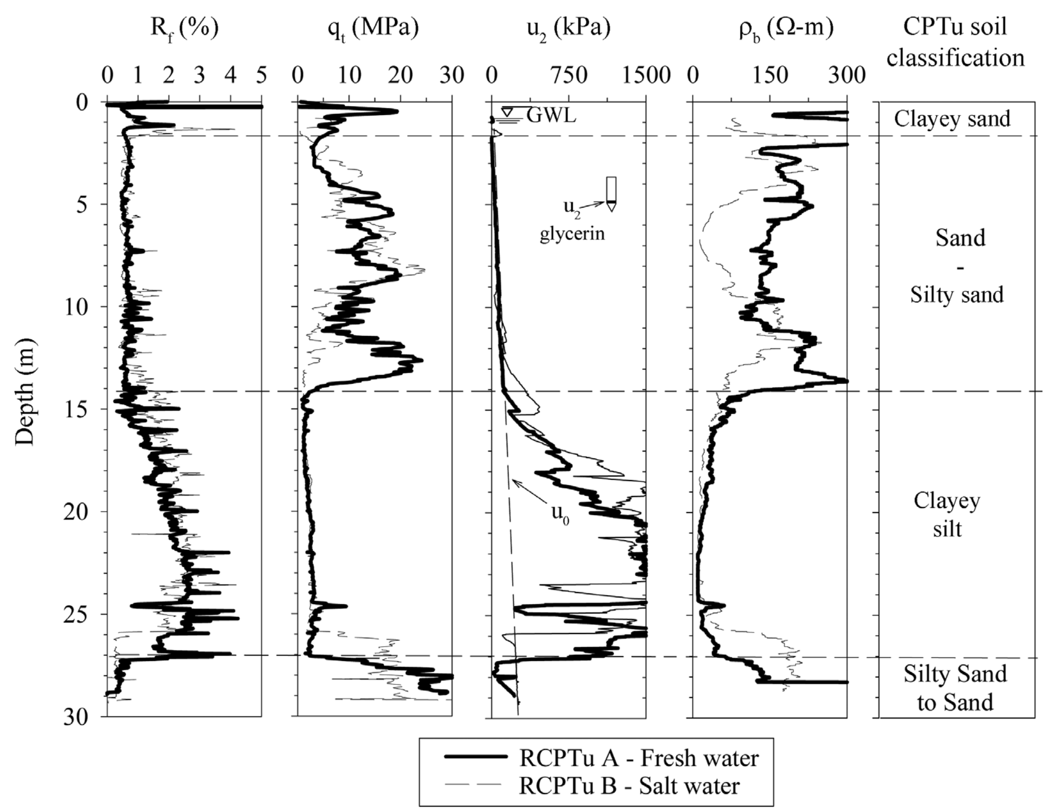

Figure 13 - Two resistivity piezocones (RCPTu A e RCPTu B) and the soil profile identified with Robertson *et al.* (1986) classification chart in a site with salt intrusion into the groundwater (adapted from De Mio *et al.*, 2005).

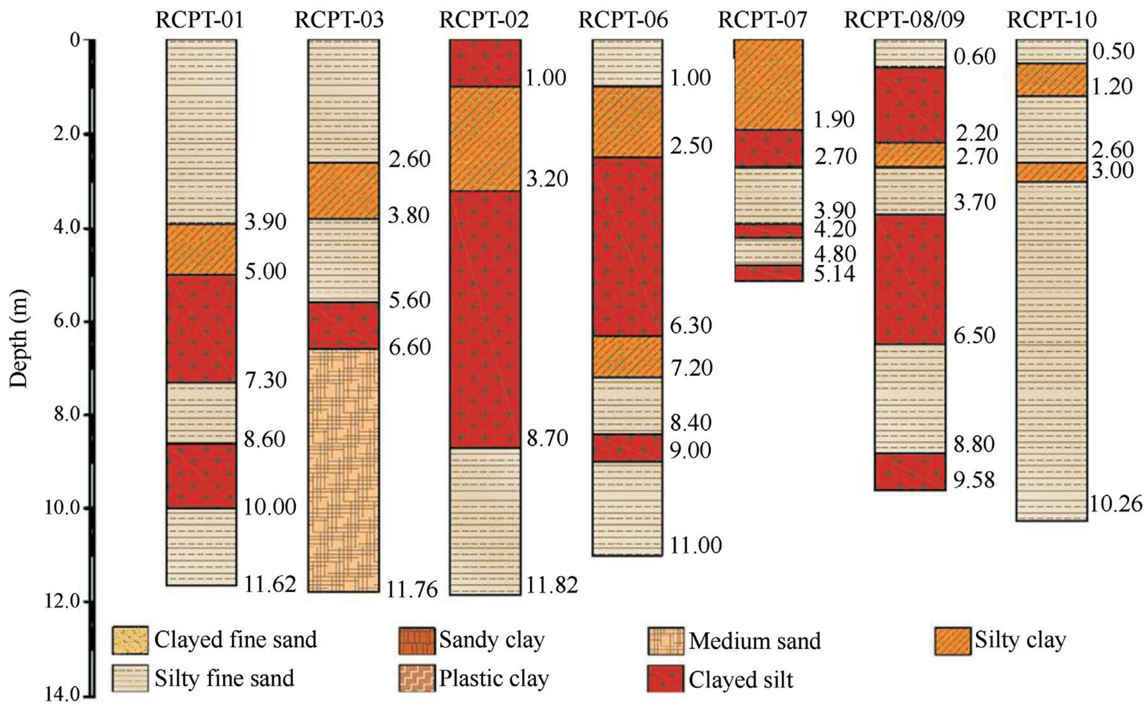

Figure 14 - Interpretation of all RCPTu for stratigraphic logging for one longitudinal cross section.

gether with the resistivity profile, as represented in Fig. 12. For each testing position, interpreted soil logging provided a better representation of soil variability in a more appropriate resolution for geo-environmental applications. It is also important to point out that these tests reached a greater depth than DPT, with great precision and high repeatability. Based on these test data, it was clearly possible to observe the existence of clayey and sandy lenses with variable thickness in all test points, and there is certainly a confined aquifer at the lower portion of the soil profile.

After the interpretation of all the RCPTu data and considering the position of each test, it was possible to refine the CSM previously presented. The cross-section profile is represented in Fig. 15.

It is also important to point out that the refined CSM based on RCPTu data showed the detection of some clayey (or fine material) and some sandy (or coarser material) lenses, and permitted the identification of the storage and flux zones following the approach suggested by Quinan *et al.* (2010) and Quinan (2012). The estimated k profile calculated based on the CPTu data (Eq. 5 and Eq. 6), as suggested by Robertson (2010) was used and it was useful to help identifying clayey lenses (storage zones), as shown in Fig. 12 in a detailed interpretation of the RCPT-02 test. All these lenses were detected by the four (q_t, f_s, u and ρ_b) RCPTu sensors. The elaboration of a figure like this is the first step in the interpretation of the hydro-stratigraphical profile, and it can be conducted on site. A closer look at the hydrogeological heterogeneities on a detailed scale revealed the presence of several storage zones, and two major layers: an important flux zone and an important store zone, as shown in Fig. 12. These heterogeneities are very important to CSM elaboration and to future remediation projects on a site, as discussed by Welty (2012) and Cleary (2009).

The CSM was significantly improved on site after the RCPTu campaign. It was also possible to define the exact position of the monitoring wells sampling screens. The position of the monitoring well sampling screen for the studied site would be the important flux zone with a window size equal to the thickness of the important flux zone indicated in Fig. 12. This procedure is carried out as the next step of geo-environmental site characterization.

The installation of monitoring wells is considered the best approach in Brazil for conducting hydrogeological site characterization. It must be preceded by a consistent CSM with the highest accuracy, resolution and detail as possible. If a consistent CSM does not exist, and the only information is the drilling itself for well installation, the uncertainties associated with the installation process, and the region where this well is effectively monitored, become so questionable that they can derail any accurate decision.

The major limitation of the RCPTu and all pushing accessories is the fact that their penetration is difficult at sites with dense soils, large boulders, rock or cemented layers. Another limitation in countries like Brazil is that the equipment used by the local contractors is imported. It makes the purchase, maintenance, calibration and repairing more expensive and time consuming.

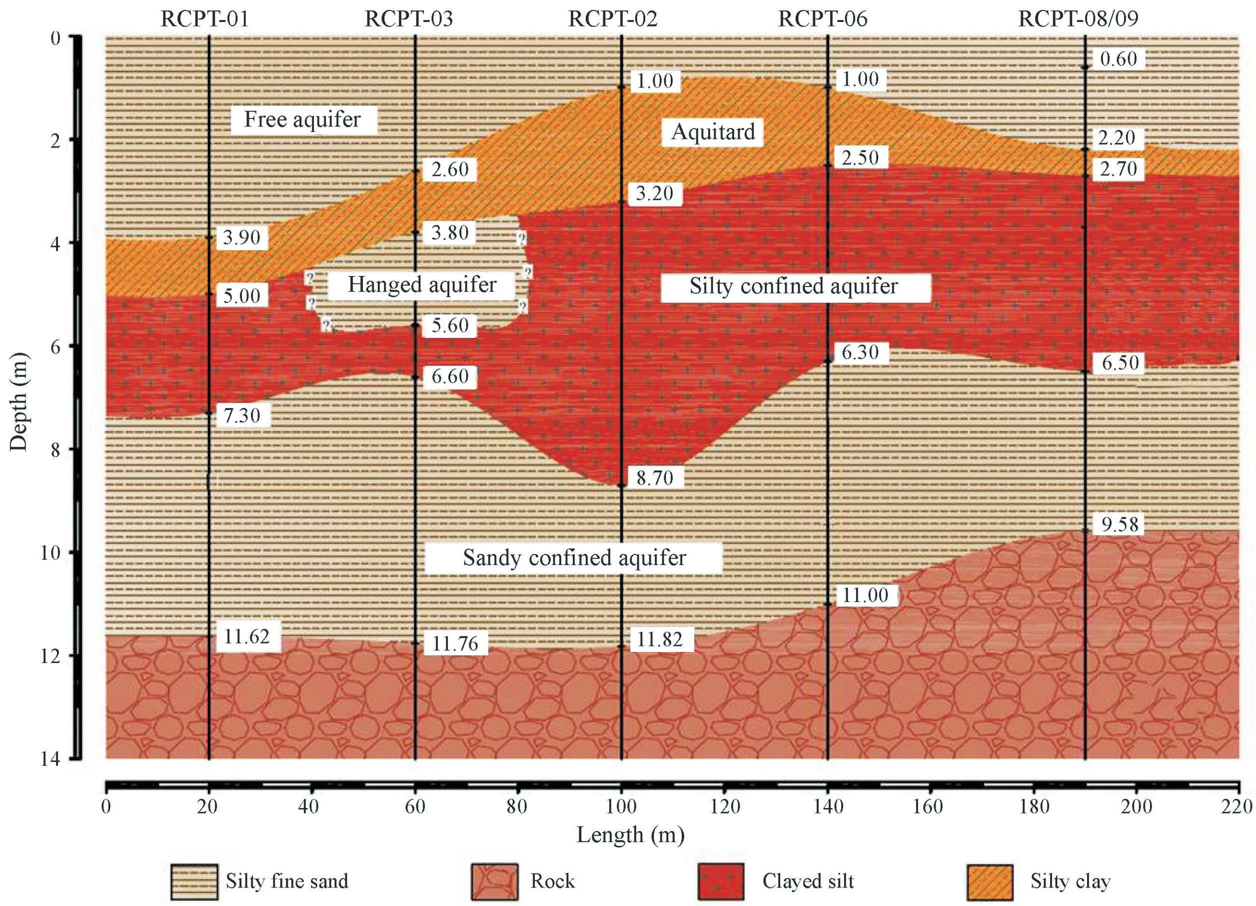

Figure 15 - Refined CSM for one cross section based on the RCPTu logging profiles.

5. Conclusions

The interpretation of RCPTu data was consistent for refining the conceptual site model elaboration at the studied site. This test can be used in an analogous way to the traditional ones (direct-push sampling and hollow stem auger drilling) since the achieved results were at least equivalent. They were faster and provided a greater level of detail than the traditional method. Geological and hydrogeological heterogeneities were detected within centimeter accuracy, which is not possible with DPT sampling and monitoring well installation.

The RCPTu presented fewer limitations than the traditional methods in the studied site, chiefly so when compared to the DPT. They reached greater depths and were more reliable, especially in cases where DPT presented limitations.

The bulk resistivity (ρ_b) complemented q_t, f_s and u data and it was useful to detail the stratigraphical profile and to help define the groundwater level for the studied site. The RCPTu data for delineating plumes of contaminated groundwater, as presented by De Mio *et al.* (2005), is not applicable in the studied site since there was no sign of contamination.

The RCPTu was a very useful tool to elaborate a suitable hydro-stratigraphical conceptual site model, especially in an approach that prioritizes high-density data collection in a high-resolution site investigation. The data were more consistent, and this hybrid tool was very useful in supporting a proper site investigation and diagnosis. It was also observed that site investigation achieves a better result when decision-making is made in real time, on site.

Acknowledgments

The authors gratefully acknowledge São Paulo Research Foundation - FAPESP (Grant # 2010/50650-3) and National Council for Scientific and Technological Development - CNPq (Grants # 481752/2010-2 and # 310867/2012-6).

References

ABNT Brazilian Association of Technical Standards (1990). MB 3406/1990: Soil - In situ Cone Penetration Test (CPT). ABNT, Rio de Janeiro, Rio de Janeiro, Brazil, 10 p (in Portuguese).

Ahlers, R. (2012). NAPL theory. Proc. North Amer Env Field Conf and Exposit, Nielsen Environmental Field School, Tampa, Mach 2012.

AMS (2012). Piston sampling system. American Falls, Idaho, USA, available at https://www.ams-samplers.com/.

Aquino Neto, V. (2009). Guideline for execution of detailed investigation and intervention plan in gas station and gas retailers available at http://www.cetesb.sp.gov.br (in Portuguese).

ASTM (1988). Standard Test Method for Deep, Quasi-Static, Cone and Friction-Cone Penetration Tests of Soil - D3441. ASTM International, West Conshohocken, Pennsylvania, USA, 8 p.

Campos, C.J.M. (2014). Erodibility Assessment by the Inderbitzen method in Unsaturated Soil From Bauru-SP Region. Master Thesis, Bauru College of Engineering, São Paulo State University, Bauru, 140 p (in Portuguese).

CETESB State Basic Sanitation Engineering Company (1999). Contaminated site management manual. CETESB, Project CETESB-GTZ. Technical Cooperation Brazil-Germany. 2nd Edition. CETESB, São Paulo, available at http://www.cetesb.sp.gov.br/ (in Portuguese).

Cleary, R. (1989). Groundwater. Brazilian Association of Water Resources (ABRH), Porto Alegre, 117 p. available at http://www.clean.com.br/Menu_Artigos/cleary.pdf (in Portuguese).

Cleary R. (2009). Why the majority of the remediation systems fails? Proc 1st Int Conf. of Underground Env. (CIMAS). Brazilian Association of Groundwater, São Paulo (in Portuguese).

CONAMA National Council of Environment (2009). Resolution # 420/09, from December 28 2009. Regulates the criteria and the soil quality guiding values about the presence of chemical substances and set the guidelines for the environmental management of contaminated sites caused by anthropic activities, Brazilian Federal Law. Official Gazette of the Federal Executive nº 249, Brasília, DF, Brazil, p. 81-84 (in Portuguese).

Daniel, C.R.; Campanella, R.G.; Howie, J.A. & Giacheti, H.L. (2003). Specific depth cone resistivity measurements to determine soil-engineering properties. Journal of Env. & Eng. Geophysics, 8(1):15-22.

De Mio, G. & Giacheti, H.L. (2007). The use of piezocone tests for high-resolution stratigraphy of quaternary sediment sequences in the Brazilian coast. Anais da Academia Brasileira de Ciências, 79(1):153-170.

De Mio, G.; Giacheti, H.L.; Stevanato, R.; Góis, J.R. & Ferreira, F.J.F. (2005). Investigation of salt-water intrusion in surficial aquifer based on electrical resistivity measurements. Solos e Rochas, 28(3):249-260. (in Portuguese)

Elmgren, K. (1995). Slot-type pore pressure CPT-u filters: behavior of different filling media. Proc. of the Int. Sym. on Cone Penetration Test. CPT'95. Swedish Geotechnical Society, Linkoping, v. 2, pp. 9-12.

Giacheti, H.L.; Peixoto, A.S.P.; Mondelli, G. & De Mio, G. (2006). Resistivity piezocone for geo-environmental site characterization of soils: Two case histories from Brazil. Proc. 5th Int. Congr. on Env. Geotech.: Opport., Challeng. and Responsib. for Env. Geotech., Int. Soc. of Soil Mech. and Geotech Eng, ISSMGE, Thomas Telford, v. 1, pp. 453-460.

Ide, D.M. (2009). Geotechnical Site Characterization and Study of an Erosion Process Caused by Urban Setting. Master Thesis, São Carlos School of Engineering, São Paulo State University, São Carlos, 129 p. (in Portuguese).

Ide, D.M.; Silva, R.A.; Corghi, F.N. & Giacheti, H.L. (2010). Erosion process caused by an urban setting in Brazil. Proc. of 6th Int. Congr. on Env. Geotech., Tata McGraw Hill Education Private, New Delhi, pp. 1273-1278.

Killenbeck, E. (2012). Depositional systems: why is geology important? North Am. Env. Field Conf. and Exposit., Nielsen Environmental Field School, Tampa, Mach 2012.

Larsson, R. (1995). Use of a thin slot as filter in piezocone tests. Proc. of the Int. Sym. on Cone Penetration Test. CPT'95. Swedish Geotechnical Society, Linkoping, v. 2, pp. 35-40.

Lee, D.S.; Elsworth, D. & Hryciw, R. (2008). Hydraulic conductivity measurement from on-the-fly uCPT sounding and from VisCPT. Journal of Geotechnical and Geo-Environmental Engineering, 134(12):1720-1729.

Lunne, T.; Robertson, P.K. & Powell, J.J.M. (1997). Cone Penetration Testing in Geotechnical Practice. Taylor & Francis, London, 312 p.

Martin, T. & St Germain, R. (2008). Direct push site characterization, direct push of NAPL with Laser-Induced Fluorescence (LIF). North Am. Env. Field Conf. and Exposit., Nielsen Environmental Field School, Tampa, Mach 2012.

Mondelli, G.; Giacheti, H.L.; Boscov, M.E.G.; Elis, V.R. & Hamada, J. (2007). Geoenvironmental site investigation using different techniques in a municipal solid waste disposal site in Brazil. Environmental Geology, 52(5):871-887.

Mondelli, G.; De Mio, G.; Giacheti, H.L. & Howie, J.A. (2009). The use of slot filter in piezocone tests for site characterization of tropical soil. Proc of the 17th Int. Conf. on Soil Mech. and Geotech. Eng.: The Acad. and Pract. of Geotech. Eng. Millpress Science, Alexandria, v. 2, pp. 973-976.

Mondelli, G.; Giacheti, H.L. & Howie, J.A. (2010). Interpretation of resistivity piezocone tests in a contaminated municipal solid waste disposal site. Geotechnical Testing Journal, 33(2):123-136.

Quinnan, J.A. (2012). Real-time high-resolution LNAPL and DNAPL characterization - Part 1: Philosophy and background. Proc. North Am. Env. Field Conf. and Exposit., Nielsen Environmental Field School, Tampa, Mach 2012.

Quinnan, J.A.; Welty, N.R.H. & Killinbeck, E. (2010). Hydro-stratigraphic and permeability profiling for groundwater remediation projects. Proc. of the 2nd Int. Sym. on Cone Penetration Test. (CPT'10), Int. Soc. for Soil Mech. and Geotech. Eng., ISSMGE. Huntington Beach, Paper 3:33.

Riyis, M.T. (2012). Geo-Environmental Site Characterization with In Situ Decision-Making Using the Resistivity Piezocone as a High-Resolution Tool. Master Thesis, Bauru College of Engineering, São Paulo State University, Bauru, 159 p (in Portuguese).

Robertson, P.K. (2009). CPT interpretation - A unified approach. Canadian Geotechnical Journal, 46(11):1337-1355.

Robertson, P.K. (2010). Estimating in-situ soil permeability from CPT & CPTu. Proc. of the 2nd Int. Sym. on Cone Penetration Test. (CPT'10), Int. Soc. for Soil Mech. and Geotech. Eng., ISSMGE. Huntington Beach, Paper 2:51.

Robertson, P.K.; Campanella, R.G.; Gillespie, D. & Greig, J. (1986). Use of piezometer cone data, Proc. of ASCE Spec. Conf. In Situ 86: Use of In Situ Tests in Geotech. Eng., American Society of Engineers ASCE, Blacksburg, pp. 1263-1280.

São Paulo's Environment State Secretary (2009). State law # 13577/09, from July 8 2009. Regulates the guidelines and procedures for soil quality and management of contaminated sites and provides others correlated provisions. São Paulo State Law. Official Gazette of the State of Sao Paulo, São Paulo, Brazil, 119(127):1741. (in Portuguese)

Shinn III, J.D. (2004). Enhanced Access Penetration System (EAPS): Draft Final Technical Report. Applied Research Associates, Albuquerque, New Mexico, USA, Work Performed Under Contract: DE-AC26-01NT41187, pp. 1-51.

US EPA United States Environmental Protection Agency (2004). EPA removes love canal for superfund list. New York, New York, USA available at http://yosemite.epa.gov/opa/admpress.nsf/e34cbb5867df82a08525 7359003d480c/40a7e32b0bbe56018525712a006fca02 !OpenDocument.

Vienken, T.; Leven, C. & Dietrich, P. (2006), Use of CPT and other direct push methods for (hydro-) stratigraphic aquifer characterization - A field study. Canadian Geotech. Journal, 49(2):197-206.

Welty, N.R.H. (2012). Permeability mapping: strategies and methods. Proc. North Am. Env. Field Conf. and Exposit., Nielsen Environmental Field School, Tampa, Mach 2012.

Behavioral Evaluation of Small-Diameter Defective and Intact Bored Piles Subjected to Axial Compression

P.J.R. Albuquerque, J.R. Garcia, O. Freitas Neto, R.P. Cunha, O.F. Santos Junior

Abstract. Foundation engineering has continually sought to understand the behavior of piles subjected to loads and their influence on the overall structural behavior. Recently, more load tests are being performed in construction due to the recommendations of the NBR6122/2010 Brazilian code. The available literature offers few reports on pile behavior in a faulty foundation. Therefore, the present study assessed the behavior of a single pile with and without a defect: 5 m long, small-diameter (ϕ = 0.25 m) bored piles were embedded in diabase soil (porous, lateritic and unsaturated) at Experimental Site II (Unicamp). The piles behavior were compared by laboratory tests, numerical analysis using the finite element software LCPC Cesar v.4.07 and experimental results from slow maintained load (SML) tests. Strain gauge instruments were installed at the top and tip of each pile. As predicted by the numerical analyses, when subjected to the first stage of the pile load test, the defective region of the pile failed structurally; however, the pile was still able to resist or "absorb" loading. Factors related to the loading ratio of the foundation, the total and differential displacements and the rotation of the top block were examined. The results obtained in the two analyses (numerical and in situ) were satisfactory and showed significant agreement, providing greater understanding of the complex behavior of this foundation system.

Keywords: defective pile, bored pile, load test, instrumented piles

1. Introduction

One of the main topics of study in foundation engineering is the load capacity of a structural element embedded in the ground. Theoretical and semi-empirical methods are used to calculate the bearing capacity, and refined numerical tools are used to predict foundation behavior. However, the most reliable method for analyzing the bearing capacity and foundation behavior is to conduct load tests, that reduce the uncertainties and provide greater savings to the project. If none of the construction site piles experience installation problems, such as failures during the installation, use of low quality materials or poor performance evaluation, the project risk decreases. However, the risk may increase if some foundation piles have a defect that could compromise the load capacity of the pile group.

In addition to the interactions predicted by the relevant calculations and design methodologies, the behavior of a single pile-top block system with a defective pile was evaluated in this study. A pile defect can be considered to be a "hidden variable" from an analytical point of view because it is not included in the design. Therefore, in the general context, defects appear as a result of unknown uncertainties or negligence in installation. In addition to the technical difficulty of addressing such a problem, studies on this subject are faced with a lack of data and available information from the pile manufacturers and installers.

Several studies have been conducted on blocks with defective piles; however, these studies are exclusively theoretical, numerical or associated with experiments on reduced-scale models. Among the most significant studies are those of Makarchian & Poulos (1994), Abdrabbo (1997), Xu (2000), Prakoso & Kulhawy (2001), Petek *et al.* (2002), Kong & Zhang (2004), Novak *et al.* (2005), Zhang & Wong (2007), Cordeiro (2007), Cunha *et al.* (2007), Cunha *et al.* (2010), Chung *et al.* (2010), Leung *et al.* (2010), Omeman (2012) and Freitas Neto *et al.* (2013). Full-scale experimental studies are rare, especially those including pile defects.

Considering the lack of information available in the literature and the relevance of this subject, the present study assessed the behavior of a full-scale foundation with and without defective piles. The defective foundation element was sized and analyzed in the laboratory before it was installed and loaded in the field. The piles were installed at Experimental Site II of the University of Campinas (Universidade Estadual de Campinas – Unicamp). They were subjected to a slow maintained load (SML) test: intact pile (Garcia, 2015) and defective pile (Freitas Neto, 2013).

Paulo José Rocha de Albuquerque, Ph.D., Associate Professor, Faculdade de Engenharia Civil, Arquitetura e Urbanismo. Universidade Estadual de Campinas, Campinas, SP, Brazil. e-mail: pjra@fec.unicamp.br.
Jean Rodrigo Garcia, Ph.D., Associate Professor, Faculdade de Engenharia Civil, Universidade Federal de Uberlândia, Uberlândia, MG, Brazil. e-mail: jean.garcia@ufu.br.
Osvaldo Freitas Neto, Ph.D., Associate Professor, Departamento de Engenharia Civil, Universidade Federal do Rio Grande do Norte, Natal, RN, Brazil, e-mail: osvaldocivil@ct.ufrn.br.
Renato Pinto da Cunha, Ph.D., Associate Professor, Universidade de Brasília, Brasília, DF, Brazil. e-mail: rpcunha@unb.br.
Olavo Francisco dos Santos Junior, Ph.D., Full Professor, Departamento de Engenharia Civil, Universidade Federal do Rio Grande do Norte, Natal, RN, Brazil. e-mail: olavo@ct.ufrn.br.
Submitted on October 8, 2016; Final Acceptance on May 5, 2017; Discussion open until December 29, 2017.

2. Pile Foundation Pathologies

Pile defects may be of structural and/or geotechnical origin. Geotechnical defects arise due to problems resulting from poorly conceived projects, poor geological-geotechnical characterization and improper pile installation. The most commonly cited geotechnical problems are those associated with lower than expected tip and lateral bearing capacity due to, for example, the presence of compressible and low resistance soil layers (Poulos, 2005).

Structural bearing capacity, manufacturing and installation problems that affect pile performance are mainly due to discrepancies in size, concrete strength and other variables between the design values and the actual values on site (Poulos, 1997). These defects typically manifest as a sharp reduction in the pile cross section due to necking of cracked sections and damaged areas on the pile.

In the case of bored piles, the most common problems are low cement content in concrete mass, inappropriate mixing and inadequate pouring, which results in concrete segregation and setting delays. The collapse of unprotected excavation walls during concreting and a lack of pile continuity can result in a reduced cross section area, which compromises the pile performance.

Statistical data about pile defects are scarce and have rarely been published. Klingmüller & Kirsch (2004) presented a German study of low-strain pile integrity testing to analyze cast-in-place piles. The authors showed that 15% of the tested piles presented results that caused concern, while 5% indicated very clear problems that required intervention. The authors also mentioned that 30% of the defective piles presented poor concrete, 21% showed insufficient length, *i.e.*, the piles were shorter than predicted in design, 14% showed shaft strangulation (necking) and 35% showed problems related to structural cracking. According to these authors, 18% of pile integrity verification tests are usually performed due to suspicion of failure, 26% on grounds that present "special" behavior and 56% as part of routine checks.

This paper analyzes the effects of necking and the use of a low quality concrete in the same pile section and their influence on the foundation performance.

3. Experimental Area

The Unicamp Experimental Site II, is located close to the School of Civil Engineering, Architecture and Urban Design at Unicamp, in Campinas-SP, Brazil, in a region that includes the basic intrusive rocks of the Serra Geral Formation (Diabase) of the São Bento Group. Pedologically, soils of this region can be classified as purple latosols, mineralogically consisting of quartz, ilmenite, magnetite, kaolinite, gibbsite, iron oxides and hydroxides; this typical layer of soil may have a thickness ranging from 5 to 30 m (Zuquete, 1987), with an unsaturated, porous and collapsible upper zone close to the surface. Figure 1 shows the simplified geological-geotechnical profile of the experimental site obtained from laboratory tests performed by Gon (2011) as well as from standard penetration tests (SPTs) and cone penetration tests (CPTs) conducted by Rodriguez (2013).

4. Methodology

The objective of this study was to evaluate the behavior of a bored pile with and without a defect based on experiments and numerical analysis using the finite element method (FEM). In both the numerical analysis and experimental SML tests, information was obtained regarding the load capacity of the foundation, the total and differential settlements, and the rotation of the block as well as the load distribution along the pile shaft and at the pile tip.

4.1. Numerical analyses

Numerical analyses were performed using the LCPC-CESAR v.4.07 software, developed at the *Laboratoire Central des Ponts et Chaussées* (Road and Public Works Research Institute). This software is a 3D FEM (Finite Element Method) tool. To adequately balance the computational effort and the convergence of the obtained results, a quadratic pentahedral element consisting of 15 nodes was used.

The FEM program was useful in predicting the load *vs.* displacement behavior and the load transfer along the pile shaft. To ensure the reliability of the numerical analysis results, three verifications were performed before initiating the analyses:

a) Comparison with available published results;
b) A convergence test to ensure that the boundary conditions did not influence the analysis results; and
c) Comparison of the soil parameters used in the analysis with the experimental results.

A convergence test, which consists of verifying whether the boundary conditions provide results that are in accordance with the pre-established definitions, was performed in the preprocessing step to validate the half-space dimensions, *i.e.*, the model geometry. Comparisons with available results were made to ensure the applicability of the program to the problems addressed in this study.

After completing the steps outlined above, the finite element model was calibrated by comparing the results of a load test on a single pile (L = 5 m and ϕ = 0.25 m) that was evaluated by Schulze (2013) at the FEC-Unicamp experimental site for the same pile, using the properly adjusted soil parameters that were originally obtained by Gon (2011). The Mohr-Coulomb constitutive model was considered adequate for the soil behavior. The parabolic plastic model, which is available in the LCPC-CESAR v.4.07 software, was used for the concrete.

The numerical analyses performed in this study were subdivided into two stages. The first stage was the calibration of the geotechnical parameters in the Mohr-Coulomb

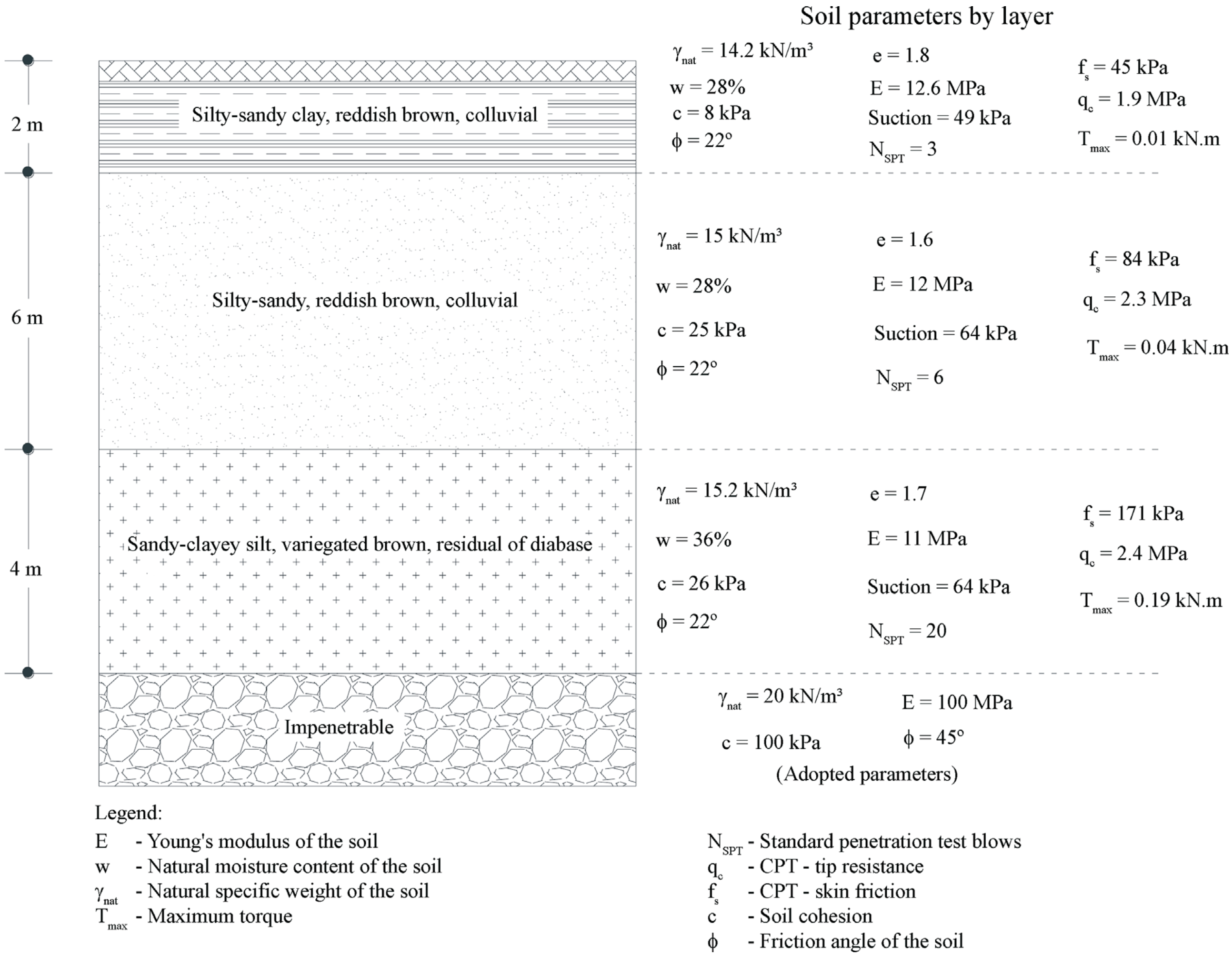

Figure 1 - Average parameters of the geological profile at the experimental site (Garcia, 2015).

constitutive model and the subsequent acquisition of the parameters used for the design and modeling of the defective pile area. The second stage a comprised numerical analysis of the intact pile.

4.1.1. Calibration of geotechnical parameters and the defect size

The numerical analysis showed that the geotechnical parameters obtained by Gon (2011) presented similar behavior to those obtained experimentally by Scallet (2011) and Schulze (2013) in load tests on isolated piles. Because these piles have the same geometric characteristics and the tests were performed in the same experimental field as those in the present study, the same geotechnical parameters obtained by Gon (2011) were used in all of the numerical analyses in this paper.

Several criteria were used to determine the conventional ultimate load. In this study, the criteria used to determine the conventional ultimate load were those from Décourt (1993), Décourt (1995) and the British Standard (BS 8004:2015), which indicates that the conventional ultimate load for precast and bored piles must be equivalent to a load corresponding to a settlement of nearly 10% of the nominal pile diameter. When applying this criterion to the load *vs.* displacement curves obtained by Scallet (2011) and those from Schulze (2013), the conventional ultimate loads were approximately 150 kN and 175 kN, respectively, at a displacement of 10% of the pile diameter, *i.e.*, 0.025 m.

The conventional ultimate load in the FEM numerical analysis conducted by Freitas Neto (2013) was approximately 163 kN. For that load at the pile head, the load ranged from 130 kN to 140 kN close to the faulty section, which occurred at a depth of 1.9 m and 2.5 m, respectively. Therefore, the average geotechnical ultimate load corresponding to the cross section with a defect was 135 kN. Thus, when applying a safety factor of two (2.0), an allowable structural load of approximately 68 kN was obtained. Thus, 68 kN was assumed to correspond to the load at which the defective zone of the pile would be compromised when subjected to an axial load in the field.

After determining the axial load under which the cross section would present a poor performance when subjected to loading, the defective section of the pile was modeled in the laboratory to simulate a structural defect on the pile. The defective section of the pile was molded with mortar at a cement-to-sand ratio of 1:9 and a water-to-cement ratio of 1.50. The intact cross section of the pile measured 25 cm in diameter; however, to simulate a reduction in the cross section, a hollow cylinder with an equivalent diameter of 18.4 cm was molded, *i.e.*, the cross section of the intact pile was decreased by 26.4%. Specimens with a diameter of 0.25 m and a height of 0.60 m, simulating the cross section of the pile, were subjected to compressive strength tests in the laboratory at full-scale.

4.1.2. Numerical analysis of the intact and defective piles

To obtain the parameters used to compare the foundations with and without defective piles, numerical analyses were performed on respective blocks with the intact and defective piles. Table 1 and Fig. 2 show the geometric characteristics used in the numerical analysis performed in this study, while Table 2 presents the material parameters used in the numerical analyses.

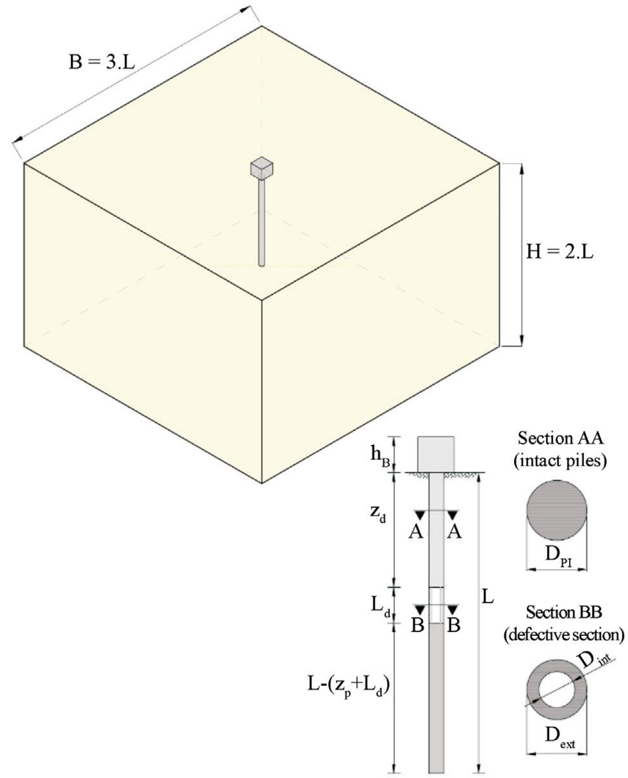

Figure 2 - Detail of the geometric dimensions (numerical analysis).

4.2. Pile construction and static load tests

Figure 3 shows the cross section and dimensions of the piles under the block as well as the dimensions and position of the defect. This figure also shows the positions of the instrumentation, with strain gauges installed at the top and tip of the pile.

Two bored test piles were constructed with lengths of 5 m and diameters of 0.25 m. The intact pile was fully reinforced along its shaft with four CA-50A steel bars (ϕ = 10 mm) and spiral stirrups of CA-50 steel (ϕ = 6.3 mm). In the defective pile, the longitudinal reinforcement was divided into two segments of 2.5 m, and a segment of 0.6 m was removed from the upper half of the reinforcement. This stirrup section removed from the reinforcement corresponds to the position of the defect.

The construction sequence of the defective pile was as follows: positioning the reinforcement for the lower section at the bottom of the bored hole, pouring concrete in the lower 2.5 m section of the pile, installing the precast hollow cylinder mortar to form the defect on top of the poured concrete (with sealed ends on the cylinder), installing the reinforcement of the upper section of the pile and final pouring of concrete (Fig. 4).

Table 1 - Geometric dimensions.

D_{PI} (m)	D_{PD} (m)	A_{PI} (m^2)	A_{PD} (m^2)	B (m)	L (m)	L_d (m)	z_d (m)	H (m)	s/D_{PI}
0.25	0.185	0.049	0.027	15	5.0	0.60	1.90	10	5.0

D_{PI} – Diameter of the intact piles; D_{PD} – Equivalent diameter of the defective pile cross sections; A_{PI} – Area of the intact cross section of the piles; A_{PD} – Area of the defective cross section of the piles; B – Horizontal dimension; L – Length of the pile; L_d – Length of the defective zone; z_d – Depth of the defect; H – Vertical dimension; and s/D_{PI} – Relative spacing.

Table 2 - Material properties.

$E_P = E_R$ (GPa)	E_{PD} (GPa)	E_S (MPa)	ν_c	ν_S	f_{ck} (MPa)	f_{ct} (MPa)
28.5	5.9	Figure 1	0.20	0.45	25	2.5

$E_P = E_R$ – Young's modulus of the concrete piles; E_{PD} – Young's modulus of the defective material; ν_c – Poisson's ratio of the concrete; ν_s – Poisson's ratio of the soil; f_{ck} – Compressive characteristic strength of the concrete; f_{ct} – Tensile characteristic strength of the concrete.

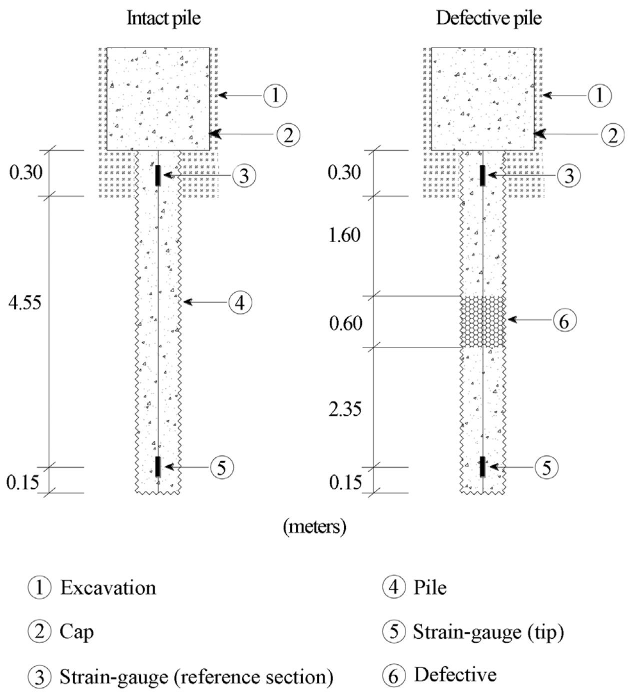

Figure 3 - Positions of the instrumentation and the Defect.

Instrumentation on the pile was placed along the reinforcement axis at the top and tip of the pile. Furthermore, before positioning the block reinforcement, the instrumentation wires were properly protected by running them through PVC tubes.

4.3. Load tests

SML tests were conducted according to the NBR 12.131 (ABNT, 2006) procedure. The reaction scheme consisted of bored piles (ϕ = 0.6 m and L = 9.0 m) that were designed to resist the tensile stresses caused by the reaction system during the load tests. The piles were reinforced with 10 CA-50 steel bars (ϕ = 10 mm) and CA-50 steel spiral stirrups (ϕ = 6.3 mm). This reinforcement was completed by installing a Dywidag tie rod with a 9.2 m length and diameter of 32 mm. The reaction beam used in the load tests was 5.3 m long and was formed by the union of two I-beams capable of resisting up to 2 MN (Fig. 5).

A load cell with a maximum capacity of 2 MN was used for the load measurement at the top block. Displacement readings were obtained via four displacement transducers with a range of 100 mm.

5. Results and Discussion

This section presents and discusses the results of foundation blocks on an intact single pile and a defective single pile obtained experimentally ($SD_{1(EXP)}$ and $CD_{1(EXP)}$) from two static load tests and the results obtained numerically from three-dimensional finite element modeling with the LCPC-CESAR software ($SD_{1(NUM)}$ and $CD_{1(NUM)}$). Further-

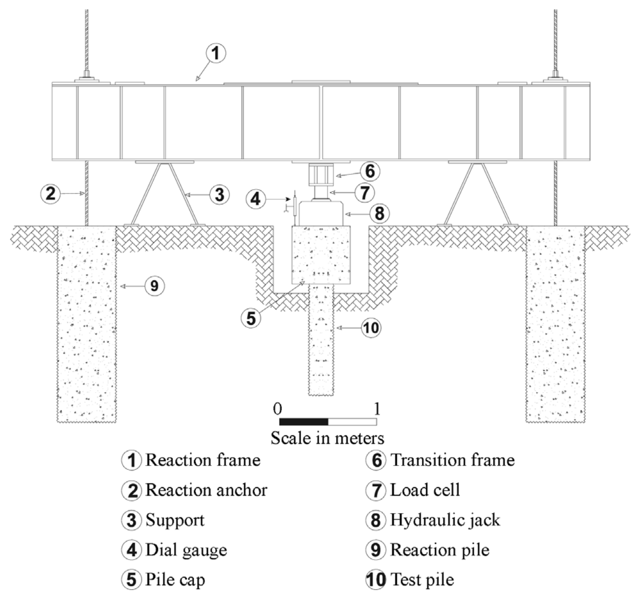

Figure 5 - Front view sketch of the main reaction system (Garcia, 2015).

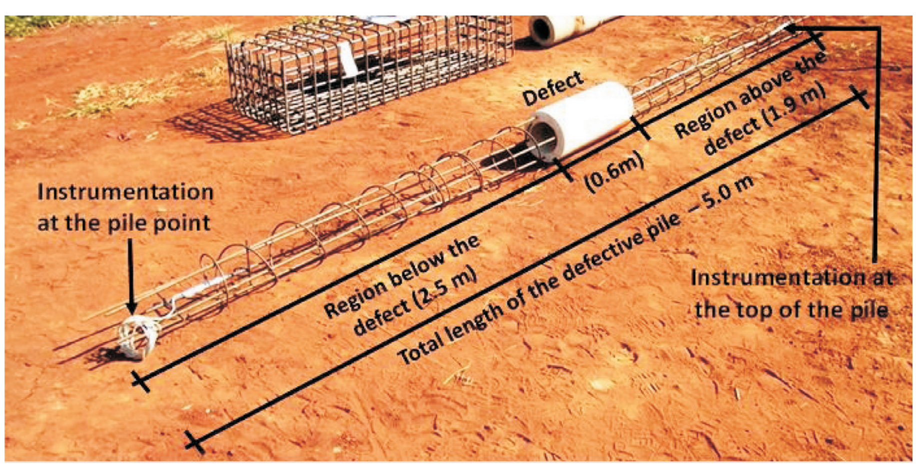

Figure 4 - Longitudinal diagram of the defective pile (Freitas Neto, 2013).

more, the behavior associated with the loading and displacement is discussed along with the load distribution between the block and the pile before and after structural failure.

5.1. Load *vs.* displacement curve

This section presents the results obtained experimentally and numerically for top loading the piles as well as analyses referring to the ratio between the applied load and the conventional ultimate load (Q/Q_{ult}) associated with top loading. Figure 6 correlates the load *vs.* displacement curves obtained numerically and experimentally. These curves show that the conventional ultimate loads were defined for 25 mm of settlement (10% of the nominal pile diameter). The curves in Fig. 6 clearly show that the experimental and numerical curves of the piles without defects exhibit similar behavior up to 50% of the ultimate load (1/2 Q_{ult}); after this point, the experimental curve showed less displacement for the same load. For the defective pile, different behavior was noted from the start of loading. The experimental curve for the defective pile was unaltered for low load values applied on top of the block (Q < 60 kN). The displacements of the curve obtained from numerical simulation were higher than those observed experimentally; however, the experimental curve showed a sudden failure at 100 kN, while the results from the numerical simulation indicated that the pile continued to absorb load after this point.

Table 3 summarizes the conventional ultimate load values, the total displacement and maximum and average differential displacement obtained from both the numerical analysis and the static load test performed in the field.

Using the data in Table 3, an additional analysis was conducted using the ratio between the applied and ultimate load (Q/Q_{ult}) both numerically and experimentally. Figures 7 and 8 present these results in terms of the intact and the

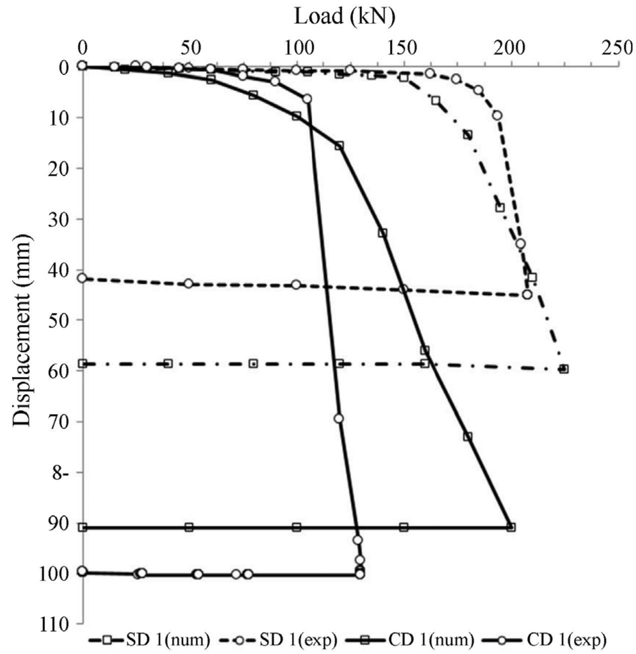

Figure 6 - Load *vs.* displacement curve.

Table 3 - Results obtained from the load test and numerical simulations.

Pile	ΔQ (kN)	Q_{ULT} (kN)	$\rho_{10\%D}$ (mm)	ρ_{MMAX} (mm)
$SD_{1(NUM)}$	15	225	25	59.8
$SD_{1(EXP)}$	15	208	25	45.1
$CD_{1(NUM)}$	20	200	25	91.0
$CD_{1(EXP)}$	15	130	25	~ 100.0

ΔQ – Load increase applied in each loading stage; Q_{RUPT} – Geotechnical ultimate load of the foundation; $\rho_{10\%D}$ – Displacement for a settlement of 10%D; and ρ_{MMAX} – Maximum displacement at the end of loading.

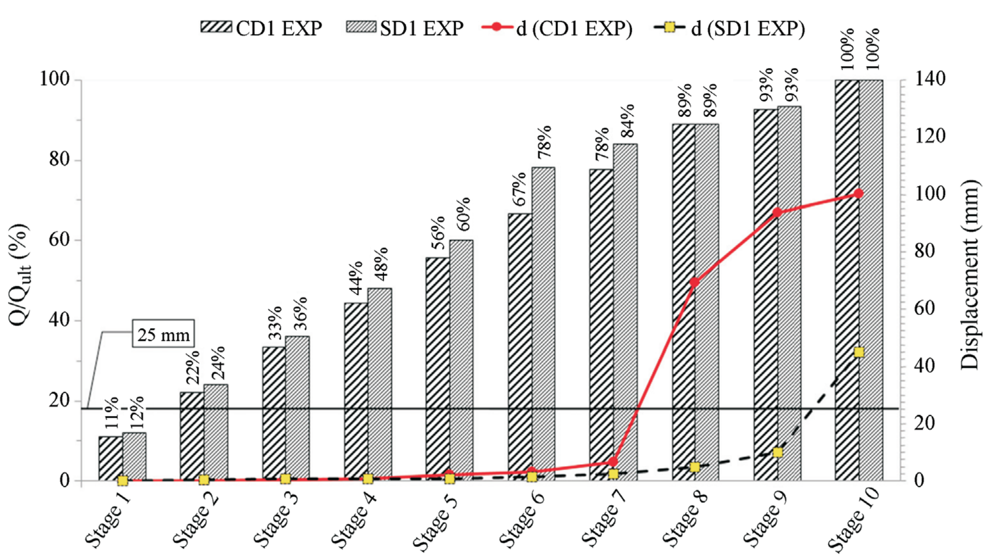

Figure 7 - Graph of the Q/Q_{ult} and displacement (experimental).

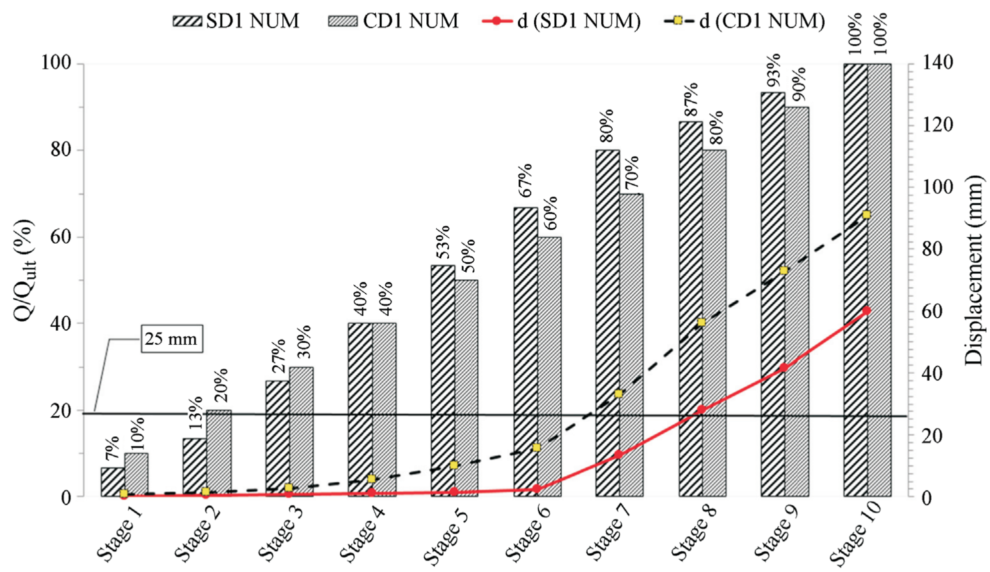

Figure 8 - Graph of the Q/Q_{ult} and displacement (numerical).

defective piles. For the defective pile, the experimental displacement was less than 5 mm up to the 7th stage (approximately 80% of the ultimate load), after which it abruptly increased to +80 mm at the ultimate load. In contrast, the displacement remained less than 10 mm up to the 9th stage for the intact pile. In both cases in the numerical simulations, the displacements remained low and approximately constant up to the 5th stage (120 kN). After that point, the defective pile sharply increased its displacement up to +80 mm at the ultimate load (200 kN), with similar behavior (but at a lower degree) for the intact pile.

The above results clearly indicate that the defective pile indeed failed earlier than expected: the experimental ultimate load of the intact pile (208 kN) was 43% higher than the equivalent ultimate load for the defective pile (135 kN). The Q/Q_{ult} ratio was also higher for the intact pile than for the defective one at the 25 mm displacement level. In terms of the final displacement at the ultimate load, it is clear that for any of the studied cases, the intact pile had a much smaller final displacement than the defective one. Directly comparing both the load and displacement results clearly indicate the contrasting characteristics of the defective and intact piles.

Figures 9 and 10 present the experimental results and the numerical results for the intact and defective piles, respectively.

Figure 9 shows the Q/Q_{ult} ratio for the intact pile obtained both numerically and experimentally. This figure shows that the displacements were similar up to the 6th stage, which represents approximately 70% of the ultimate

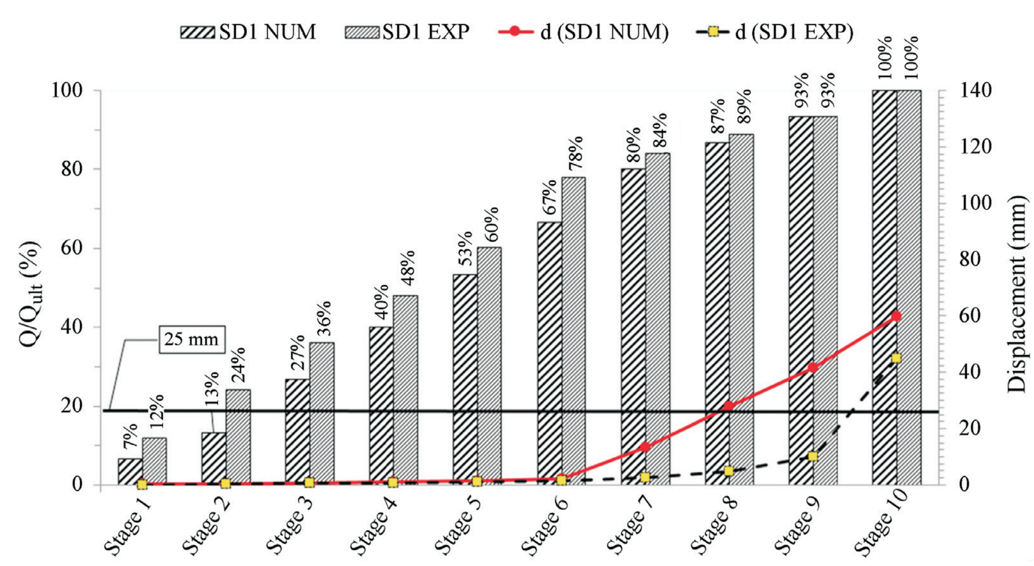

Figure 9 - Graph of the Q/Q_{ult} and displacement determined numerically and experimentally (intact pile).

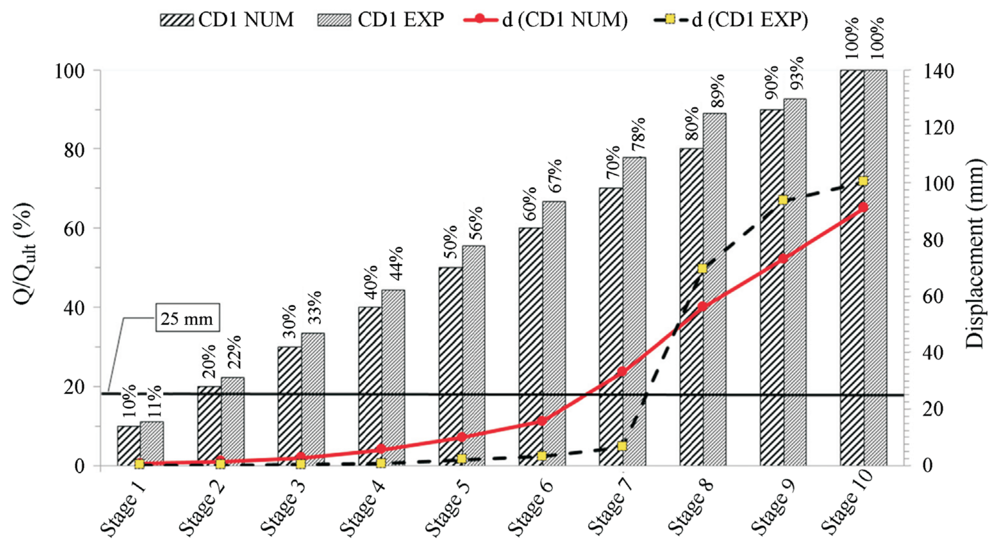

Figure 10 - Graph of the Q/Q_{ult} and displacement determined numerically and experimentally (defective pile).

load. After this point, the experimental displacements were consistently lower than those obtained numerically. At the ultimate load (10th stage), the differences between the numerical and experimental displacements sharply decreased, although the numerical value was approximately +30% higher than the experimental value. At the 25 mm reference displacement, both the numerical and experimental loads were approximately similar; however, the Q/Q_{ult} ratio differed drastically (95% for the experimental case compared to 87% for the numerical case).

Figure 10 expands the analysis for the defective pile; this figure illustrates that the defective pile showed distinct behavior (compared to the previous figure) when comparing the numerical and experimental results. At the 25 mm reference displacement, the numerical and experimental loads were quite different (65% of the ultimate load for the numerical case and 78% for the experimental case). Moreover, for the same Q/Q_{ult} (> 80%), unlike Fig. 9, the experimental displacements were consistently larger than the numerical values.

5.2. Tip and lateral loads

This section analyzes the data related to the load transfer along the depth and the mobilized skin friction. Figures 11 and 12 present the graphs of the average axial load transfer in the piles along their depth as obtained in the load tests. The axial load on the piles was assumed to vary linearly with depth, and the presented loads correspond to those obtained directly at the top of the piles. Mobilization of skin friction occurs from the 1st to 6th stage coupled with a small participation of tip resistance. Skin friction depletion occurs after the 6th stage, as evidenced by the parallel straight lines, concurrent with the mobilization of tip resistance, registering the maximum value of this resistance in the 11th stage (208 kN). Figure 12 shows the load distribution for the defective pile, indicating that the tip resistance

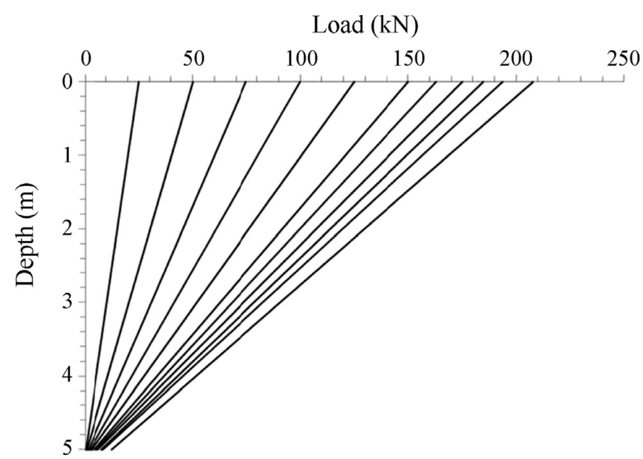

Figure 11 - Load transfer in the intact pile (experimental) (Garcia, 2015).

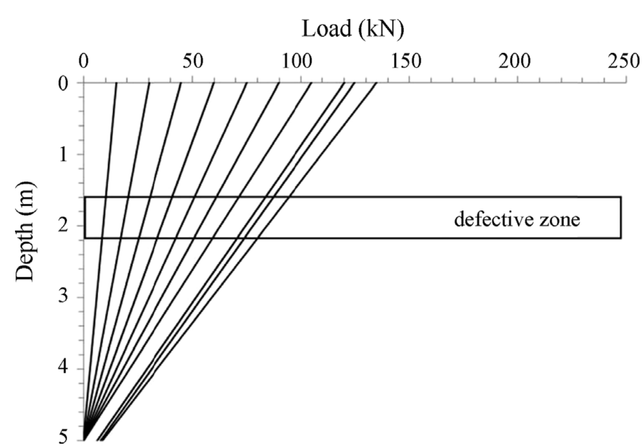

Figure 12 - Load transfer in the defective pile (experimental) (Freitas Neto, 2013).

was mobilized after the 7th stage (105 kN); from this point on, a depletion of skin friction was observed, as verified by the parallel straight lines of the load transfer. The defective pile structurally failed when its internal load reached a level close to 105 kN, and naturally, from this point on, there was no proportionality anymore between applied load on top of the pile and measured load on its tip. Nevertheless (and surprisingly), the defective pile did continue to “absorb” applied loads from the block, beyond its structural failure, indicating that even “failed” it continued somehow to accomplish its primary function of receiving and delivering superstructure loads to underlying more competent soil layers.

Figures 13 and 14 show the load distribution along the depth obtained from the numerical analysis. For the intact pile, the tip load was mobilized from the start of loading but at a low magnitude. Similarly, the defective pile presented lower tip mobilization than that obtained for the intact pile.

Figures 15 and 16 presents the total load at the top and lateral loads *vs.* displacement obtained from the load tests

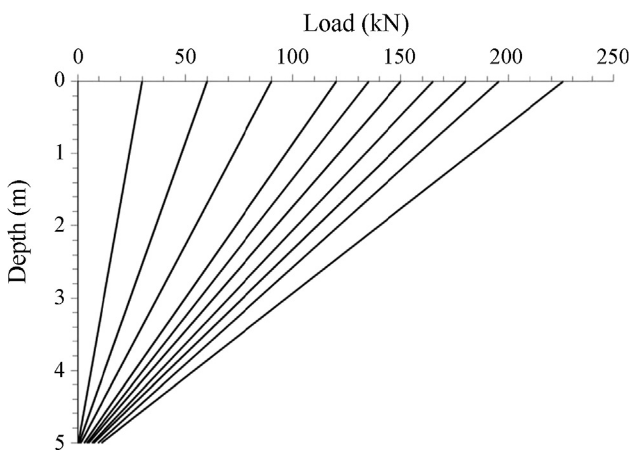

Figure 13 - Load transfer in the intact pile (numerical) (Freitas Neto, 2013).

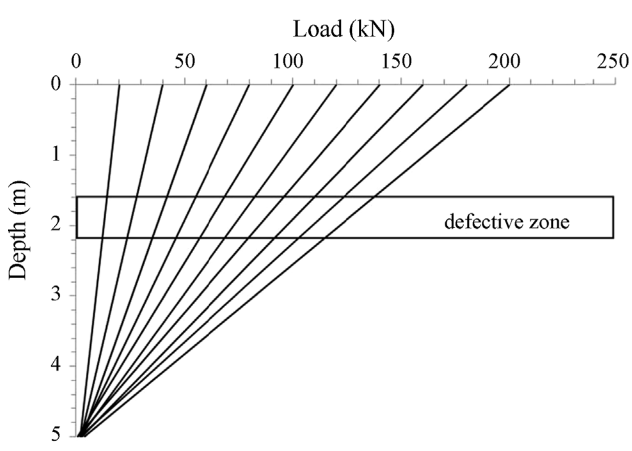

Figure 14 - Load transfer in the defective pile (numerical) (Freitas Neto, 2013).

and the numerical models. Skin friction was responsible for most of the load absorbed by the piles. For the values obtained experimentally, small displacements were required for complete mobilization of skin friction, maintaining the tendency for friction stabilization after its depletion (Fig. 15). This phenomenon was not observed in the numerically obtained results; the lateral load did not present a clear definition of depletion, considering the load increase

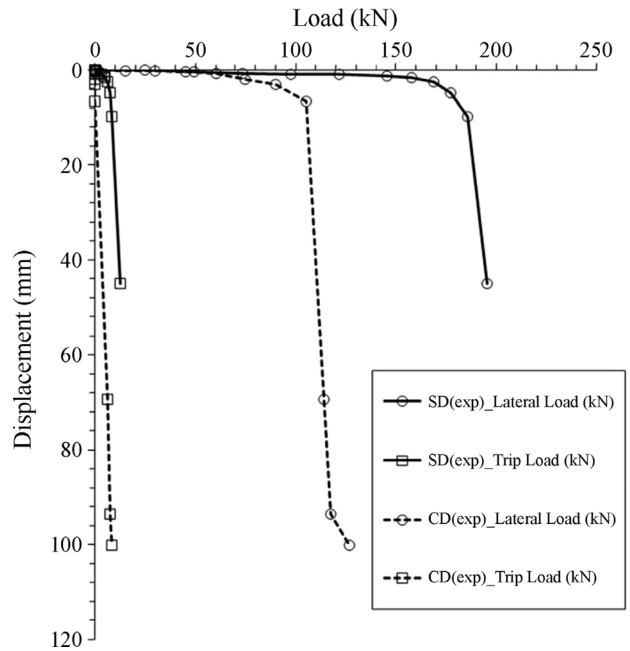

Figure 15 - Curves of top and lateral loads *vs.* displacement (experimental).

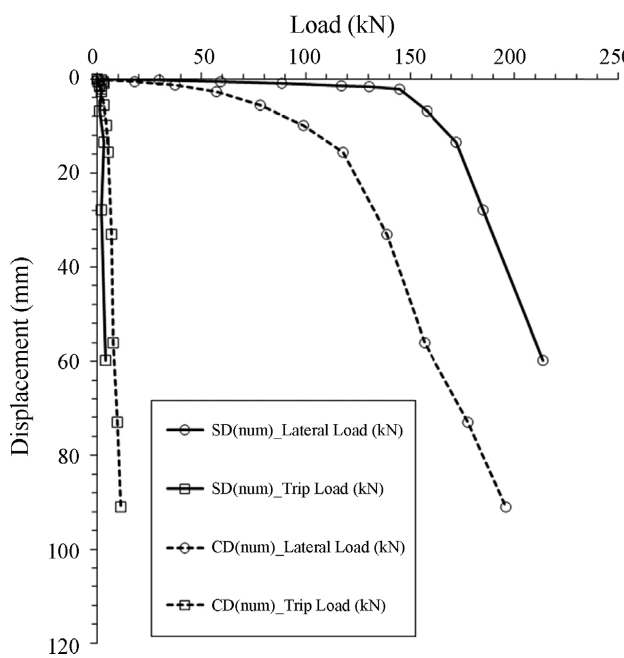

Figure 16 - Curves of top and lateral loads *vs.* displacement (numerical).

after the inflection point in the lateral load *vs.* displacement graph (Fig. 16).

For the intact pile, the skin friction at the maximum load of the load test (208 kN) was on the order of 50 kPa (Fig. 15). This value is close to the value obtained by Albuquerque (2001) from instrumented load tests on bored piles at Experimental Field I – Unicamp, which is close to the location of the tests in this study. For the defective pile, the skin friction for the maximum load (135 kN) was approximately 32 kPa. This value is 36% lower than that obtained for the intact pile. However, observing the friction value of the intact pile associated with the ultimate load of the defective pile (135 kN), the value was approximately 31 kPa. This result indicates that before the defect manifests, the friction of the defective pile is very similar to that of the intact pile.

The same skin friction trend was observed in the numerical analysis for both ultimate loads (Q_{ult}) and working (half of ultimate) loads ($Q_{ult/2}$), indicating that the modeling results were similar to the experimental data (Figs. 17 and 18).

5.3. Evaluation of differential displacements at the top of the defective pile

This section analyzes the influence of the defect on the behavior at the top of the pile during the loading tests. The differential displacements obtained experimentally may be due to a potential eccentricity of the faulty pile, *i.e.*, the construction and interference of the defect resulted in the imbalance of the pile/block assembly because it was not laterally confined. Figure 19 shows the settlement values recorded by each of the linear variable differential transformers (LVDTs). The maximum settlements were registered by LVDT 1 and LVDT 2. The maximum differential settlement recorded at the end of the load test on this block was 25.6 mm between LVDTs 1 and 3.

Figure 19 shows the values of angular rotation on top of the block for each level of applied load. This figure dem-

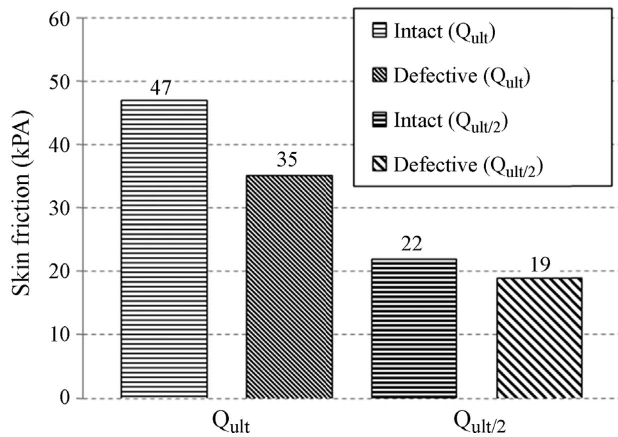

Figure 17 - Graph of skin friction (experimental).

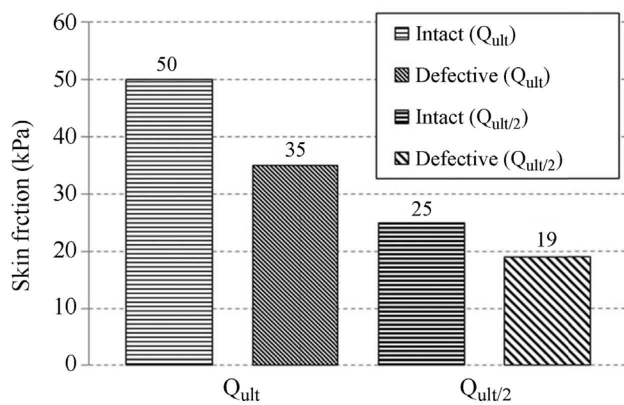

Figure 18 - Graph of skin friction (numerical).

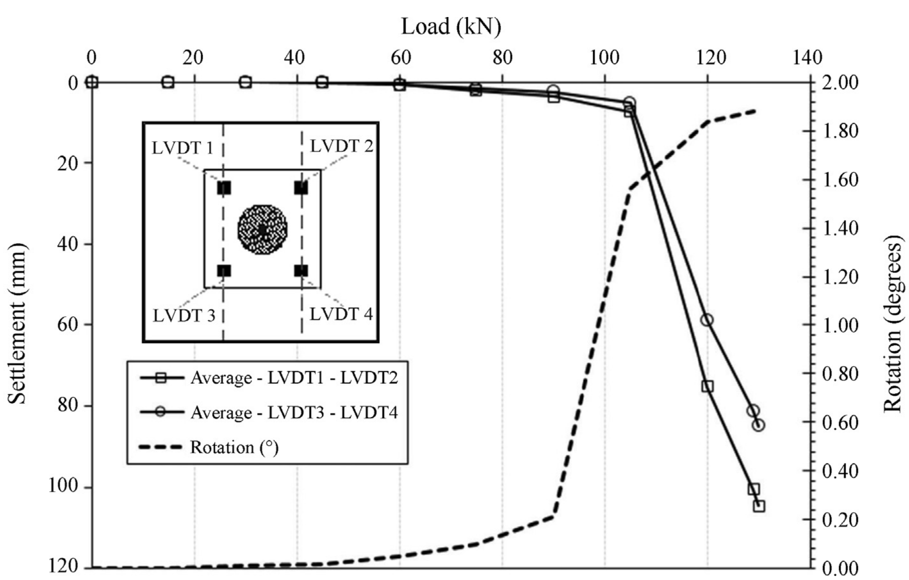

Figure 19 - Block rotation and average settlement with each load increase (CD 1).

onstrates that the $CD_{1(EXP)}$ pile began to exhibit significant rotations after 60 kN of applied load, reaching approximately 1.9° when approaching the conventional ultimate load stage (110 kN). In absolute terms, this rotation angle is equivalent to a vertical displacement in the order of 20 mm at the extremities of the top block. So, besides bearing capacity concerns on the design of the foundation, excessive differential settlements (*i.e.*, rotations) seem to be the major design issue when having defective piles in a vertically loaded deep foundation.

5.4. Evaluation of the defect (*in situ*)

After conducting the load tests, a 3.0 m deep and 0.90 m in diameter excavation was dug adjacent to the defective pile to verify whether the defective cross section of the pile had failed after the loading test. Figures 20 and 21 show the success in predicting the behavior of the defective pile region; the defect was in fact mobilized when the load tests were performed. The failure mode of the defective zone of the pile was similar in the laboratory (Fig. 22) and in the field.

6. Conclusions

Based on the results and analyses, the following conclusions were made:

- The load tests performed on the piles with and without a defect showed varying behaviors when subjected to different loads. The defect was responsible for an approximately 50% reduction in the ultimate load. This result proves, as expected, that a defect in the pile may compromise the stability of a group of piles, thus demonstrating the need to identify anomalies in piles.
- The pile defect was located at approximately 1.9 m below the block and clearly influenced the load capacity of the pile and therefore affected the rotation of the pile block system. This behavior would perhaps differ if the defect was located at another section or depth, although

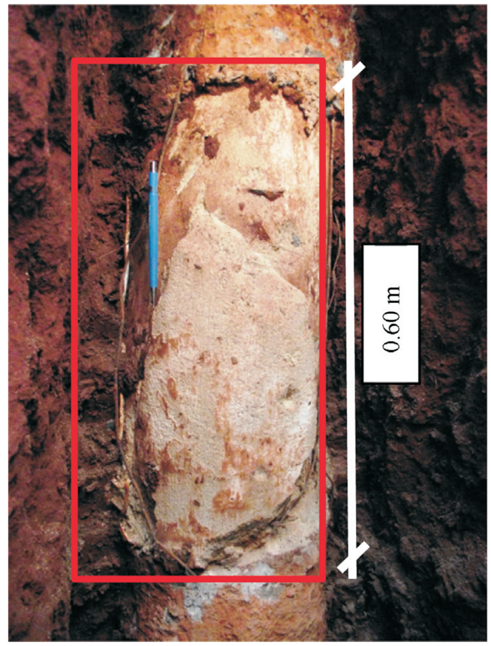

Figure 20 - Defective zone of the pile mobilized after performing the load test on block $CD_{1(EXP)}$.

Figure 21 - Detail of the defect after performing the load test on block $CD_{1(EXP)}$.

Figure 22 - Sample after failure stage (laboratory test).

this was not tested in this study. In this case, the defect would be expected to have less influence on the system behavior if it was located closer to the pile's tip. However, more research is needed on this topic.

- The results obtained from numerical modeling using the LCPC-Cesar v.4.07 software with the geotechnical parameters determined by Gon (2011) satisfactorily predicted the behavior of the piles with and without a defect. The difference with respect to the experimental data was related to the behavior of the load *vs.* settlement curve. The numerical analyses presented higher displacements than the experimental results for the same load.
- Foundations are designed according to the load obtained after applying a safety factor of two (working load), which generally corresponds to half of the ultimate load of an intact foundation. For the intact pile, the working load was equivalent to 85 kN, exceeding the 55 kN working load of the defective pile. Therefore, it is important to highlight the significant rotation at the top of the pile, even if it is almost equivalent to the working load of the foundation. If this pile was designed for loads equivalent to the working load (85 kN), it would probably not fail during the foundation's lifetime but would probably suffer excessive total and differential settlements.
- In general, the piles worked mainly through skin friction, which was responsible for approximately 95% of the load applied to the top. This result was indeed expected for the bored piles installed in this type of soil (porous, laterite and unsaturated). The friction values obtained both numerically and experimentally were similar, indicating that the numerical model provided satisfactory results.
- The load friction of the piles obtained numerically did not show decreasing skin friction with increasing loading. With increasing top load, the lateral load and displacements increased, showing a different behavior than that of the experimental data.
- The experimental mobilization of tip resistance of the piles was generally a function of the load level or the level of settlement of the pile, showing the need for considerable displacements for mobilization. The same behavior was shown by the numerical analysis, but the tip load obtained from the numerical analysis for the defective pile was higher than that obtained for the intact pile.
- Strain gauges were adequate for determining the loads on the top and tip of the piles, acquiring information on the load transfer. This information is considered essential to understanding the overall pile behavior.
- Defects in the piles manifest as a function of the load magnitude; therefore, it is suggested that an integrity evaluation of the piles should be performed soon after installing the piles because at this time, the piles are not yet subjected to loading from the superstructure. If necessary, the foundation can be reinforced by either changing the block geometry or installing new piles to minimize the impact on construction progress. This evaluation may be performed using the integrity test (PIT) and can be subsequently complemented with static load tests and dynamic loading tests, as recommended by the standard NBR 6122 (ABNT/2010).

Acknowledgments

The authors thank the São Paulo Research Foundation (Fundação de Amparo à Pesquisa no Estado de São Paulo – FAPESP), the National Council for Scientific and Technological Development (Conselho Nacional de Desenvolvimento Científico e Tecnológico - CNPq) and the Foundation for Research and Extension Support (Fundação de Apoio ao Ensino, Pesquisa e Extensão – FAEPEX - Unicamp) for the financial support necessary for research development. The authors also thank the Dywidag company for donating the rods used in the tests.

References

Abdrabbo, F.M. (1997). Misuse of soils and foundation causes disaster. Proc. Int. Conf. on Foundation Failures, Singapore, p. 121-130.

ABNT – Associação Brasileira de Normas Técnicas (2006). NBR 12.131: Estacas – Prova de Carga Estática. Rio de Janeiro, Brazil, 8 p.

ABNT – Associação Brasileira de Normas Técnicas (2010). NBR 6122: Projeto e Execução de Fundações. Rio de Janeiro, Brazil, 91 p.

Albuquerque, P.J.R. (2001). Estacas Escavadas, Hélice Contínua e Ômega Estudo do Comportamento à Compressão em Solo Residual de Diabásio, Através de Provas de Carga Instrumentadas em Profundidade. Tese de Doutorado em Engenharia, Escola Politécnica, Universidade de São Paulo, São Paulo, 272 p.

BSI – The British Standard Institution (2015). BS 8004: Code of Practice for Foundations. London, United Kingdom, 115 p.

Chung, D.N.; Kim, D. & Jo, S. (2010). Settlement of piled rafts with different pile arrangement schemes via centrifuge tests. Journal of Geotechnical and Geoenvironmental Engineering, 139(10):1690-1698.

Cordeiro, A.F. (2007). Avaliação Numérica de Reforço de Grupo de Estacas pela Introdução de Estacas Adicionais. Dissertação de Mestrado, Publicação G. Dm-155/07, Departamento de Engenharia Civil e Ambiental, Universidade de Brasília, Brasília, 118 p.

Cunha, R.P.; Cordeiro, A.F.; Sales, M.M. & Small, J.C. (2007). Parametric analyses of pile groups with defective piles: Observed numerical behaviour and remediation. Proc. 10th Australia - New Zealand Conference on Geomechanics, Brisbane, v. 1, pp. 454-459.

Cunha, R.P.; Cordeiro, A.F.B. & Sales, M.M. (2010). Numerical assessment of an imperfect pile group with defective pile both at initial and reinforced conditions. Soils and Rocks, 33(2):81-93.

Décourt, L. (1993). Predicted and measured behavior of non-displacement piles in residual soils. Proc. of BAP II, Deep Foundations on Bored and Auger Piles, Ghent, pp. 369-376.

Décourt, L. (1995). On the load-settlement behavior of piles. III Conferência Odair Grillo. Solos e Rochas, 18(2):93-112.

Freitas Neto, O.; Cunha, R.P.; Santos Júnior, O.F.; Albuquerque, P.J.R. & Garcia J.R. (2013). Comparison of numerical methods for piled raft foundations. Advanced Materials Research (Online), 838-841:334-341.

Freitas Neto, O. (2013). Avaliação Experimental e Numérica de Radiers Estaqueados com Estacas Defeituosas em Solo Tropical do Brasil. Tese de Doutorado, Publicação G.TD-088/2013, Departamento de Engenharia Civil e Ambiental, Universidade de Brasília, Brasília, 253 p.

Garcia, J.R. (2015). Análise Experimental e Numérica de Radiers Estaqueados Executados em Solo da Região de Campinas/SP. Tese de Doutorado, Faculdade de Engenharia Civil, Arquitetura e Urbanismo da Universidade Estadual de Campinas, Campinas, 359 p.

Gon, F.S. (2011). Caracterização Geotécnica Através de Ensaios de Laboratório de um Solo de Diabásio da Região de Campinas/SP. Dissertação de Mestrado, Faculdade de Engenharia Civil, Arquitetura e Urbanismo da Universidade Estadual de Campinas, Campinas, 153 p.

Klingmüller, O. & Kirsch, F. (2004). A Quality and safety issue for cast-in-place: 25 years of experience with low-strain integrity testing in Germany – From scientific peculiarity today-today practice. Proc. Current Practices and future trends in deep foundations, ASCE, Geotechnical Special Publication, Reston, n. 125, p. 202-221.

Kong, L. & Zhang, L. (2004). Lateral or torsional failure modes in vertically loaded defective pile groups. Journal Geotechnical Special Publication, 124:625-636.

Leung, Y.F.; Klar, A. & Soga, K. (2010). Theoretical study on pile length optimization of pile groups and piled rafts. Journal of Geotechnical and Geoenvironmental Engineering. ASCE. 136(2):319-330.

Makarchian, M. & Poulos, H.G. (1994). Underpinning by piles: a numerical Study. Proc. 13th International Conference on Soil Mechanics and Foundation Engineering, New Delhi, v. 4, pp. 1467-1470.

Novak, J.L.; Reese, L.C. & Wang, S.T. (2005). Analysis of Pile-Raft Foundations with 3D Finite-Element Method. Proceedings of the Structures Congress, New York, pp. 12.

Omeman, Z.M. (2012). Load Sharing of Piled-Raft Foundations in Sand Subjected to Vertical Loads. Ph.D. Thesis in the Department of Building, Civil and Environmental Concordia University. Montreal, Quebec, 131 p.

Petek, K.; Felice, C.W. & Holtz, R.D. (2002). Capacity analysis of drilled shafts with defects. Deep Foundations, Geot. Spec. Pub. ASCE, 2(116):1120-1135.

Poulos, H.G. (1997). Behaviour of pile groups with defective piles. Proc. 14th Int. Conf. Soil Mechanics Foundation Engineering, Hamburg, pp. 871-876.

Poulos, H.G. (2005). Pile behavior – Consequences of geological and construction imperfections. J. Geotech. and Geoenvir. Eng., ASCE, 131(5):538-563.

Prakoso, W.A. & Kulhawy, F.H. (2001). Contribution to piled raft foundation design. Journal of Geotechnical and Geoenvironmental Engineering, 127(1):17-24.

Rodriguez, T.G. (2013). Caracterização Geotécnica de um Solo de Diabásio por Meio de Ensaios SPT e CPT. Dissertação de Mestrado, Faculdade de Engenharia Civil, Arquitetura e Urbanismo da Universidade Estadual de Campinas, Campinas, 134 p.

Scallet, M.M. (2011). Comportamento de Estacas Escavadas de Pequeno Diâmetro em Solo Laterítico e Colapsível da Região de Campinas/SP. Dissertação de Mestrado, Faculdade de Engenharia Civil, Arquitetura e Urbanismo da Universidade Estadual de Campinas, Campinas, 166 p.

Schulze, T. (2013). Análise da Capacidade de Carga de Estaca Escavada Instrumentada de Pequeno Diâmetro por Meio de Métodos Semi Empíricos. Dissertação de Mestrado, Faculdade de Engenharia Civil, Arquitetura e Urbanismo da Universidade Estadual de Campinas, Campinas, 136 p.

Xu, K. (2000). General Analysis of Pile Foundations and Application to Defective Piles. Ph.D. Thesis, University of Sydney, 404 p.

Zhang, L. & Wong, E. (2007). Centrifuge modeling of large-diameter bored pile groups with defects. Journal of Geotechnical and Geoenvironmental Engineering ASCE, 133(9):1091-1101.

Zuquete, L.V. (1987). Análise Crítica da Cartografia Geotécnica e Proposta Metodológica para Condições Brasileiras. Tese de Doutorado, Escola de Engenharia de São Carlos, Universidade de São Paulo, São Carlos, 637 p.

Deterioration Characteristic of Mudstone Due to Freeze-Thaw Action Using Electrical Impedance Spectroscopy

J.C. Hu, H.F. Wang, J. Zhao

Abstract. Determining the damage of rocks after freeze-thaw cycles is an important subject for natural building rocks used in cold regions. Freeze-thaw test is an important method for determining the deteriorations of stones due to freeze-thaw action. To understand the mechanisms of rock deterioration in cold regions, the electrical impedance spectroscopy technique can be utilized to investigate the mechanical properties of mudstone because of freeze-thaw test. Firstly, the initial rock properties including mineral composition, microstructure, water absorbing capacity and the thermogravimetric properties are measured for assessing damage characteristic of mudstone duo to freeze-thaw action. Then, an instrument is designed for measurement electrical impedance spectroscopy of the specimens during freeze-thaw test. Finally, the capacitance, resistance and the parameter indicating dispersive effect φ are analyzed from Nyquist curve of electrical impedance spectroscopy of mudstone specimens. The variation of above parameters abides by the law which their values changes at 12 of freeze-thaw cycles. The results show the specimen crack occurs obviously at 12 of freeze-thaw cycles. It proved the electrical impedance spectroscopy is a useful method to research rock cracking due to freeze-thaw action.

Keywords: mudstone, freeze-thaw test, electrical impedance spectroscopy, capacitance, resistance, constant phase element.

1. Introduction

Rock deterioration is a topic of concern in many fields such as geologic materials and cultural/historical sculptures and monuments. In cold regions, rocks are subjected to freeze-thaw action and therefore deteriorate more quickly. Rock weathering is promoted by repeated freezing and thawing of water in the voids of rock, and its damage depends on the temperature, rock type and moisture content in cold regions (Matsuoka, 1990). Chen *et al.* (2004) have subjected to freeze-thaw tests rock specimens prepared from welded tuff with a degree of saturation from 0% to 95%. When the initial degree of saturation exceeded 70%, the rock was damaged significantly, and the degree of saturation in the surface layer was higher than that in the center of the frozen specimen (Chen *et al.*, 2004). Rock deterioration is the result of the number of freeze-thaw cycles, temperature, rock type, applied stress and moisture content in cold regions (Chen *et al.*, 2004; Tan *et al.*, 2011). A statistical model was developed for predicting the percentage loss values in uniaxial compression strength from intact tests of impact strength, modulus of elasticity and water absorption (Bayram, 2012). The changes of the mass and volume ultrasonic velocities, the complete stress-strain curves, uniaxial compressive strengths, frost resisting coefficient, weathering degree, dynamic elastic modulus and acoustic emission parameters for marble specimens were obtained before and after freeze-thaw action. The main physical and mechanical characteristics of marble were summed up under cycles of freeze-thaw test (Wu *et al.*, 2006). Of course, except for above-mentioned details, the researchers use many methods to investigate rock deterioration during freeze-thaw cycles, such as CT scanning test (Yang & Pu, 2002), gloss test (Ozcelik *et al.*, 2012), ultrasound propagation speed test (Iñigo *et al.*, 2013). However, little information of rock damage was obtained in real-time during the freeze-thaw test. In the present paper, rock deterioration duo to freeze-thaw test was investigated with electrical impedance spectroscopy.

Electrical impedance spectroscopy (EIS) has been used extensively to characterize the electrical properties of materials as a function of frequency (Gersing, 1998; Pan *et al.*, 2003; Prabakar & Rao, 2007; Li, 2003). The EIS results are used to interpret impedance spectra in terms of resistance and capacitance associated with the physicochemical properties of the sample under test (Zhang *et al.*, 1990; Zhang & Willison, 1991; Bhatt & Nagaraju, 2009). Many researchers (Olson *et al.*, 1995; Perron & Beaudoin, 2002; Hu *et al.*, 2007) have used EIS to estimate the physical state of various porous solid samples. The EIS was used to measure physical-mechanical properties of rock including fault breccia, sandstone and limestone (Kahraman & Alber, 2006; Kahraman *et al.*, 2015; Saltas *et al.*, 2014; Su *et al.*, 2000), and also to monitor CO_2 or oil migration within saturated rock (Kirichek *et al.*, 2013; Liu *et al.*, 2015). For im-

Jiang Chun Hu, Ph.D., Associate Professor, School of Civil & Architecture Engineering, Zhongyuan University of Technology, Zhengzhou, China. e-mail: hujiangchun@163.com.
Hong Fang Wang, Ph.D., Associate Professor, School of Materials & Chemical Engineering, Zhongyuan University of Technology, Zhengzhou, China. e-mail: 52020135@163.com.
Jian Zhao, Ph.D., Lecturer, State Key Laboratory for Geomechanics and Deep Underground Engineering, China University of Mining and Technology, Beijing, China. e-mail: zhaojiancumtb@163.com.
Submitted on October 9, 2016; Final Acceptance on July 14, 2017; Discussion open until December 29, 2017.

pedance spectra, the qualitative interpretations are that the grain-interior response lies at highest frequency, the sample-electrode response at low frequency and the grain boundary response at the mid-frequencies, and the qualitative interpretations take parameters from the impedance spectra which can show some properties of rock (Kahraman & Alber, 2006; Kahraman *et al.*, 2015; Hu *et al.*, 2007; Huebner & Dillenburg, 1995).

The authors have developed a method for simultaneous measurement of rock deterioration and impedance characteristics of rock because of freezing and thawing. A feature of the impedance spectra, the frequency dispersion (or depression) angle, was found to contain information of pore structure and the related parameters of mass transfer of unfrozen water, pore blocking. The ultimate goal of this work is to provide useful information for the development of a frost resistance test based on electrical measurement methods.

2. Materials and Methods

2.1. Rock specimens

Test specimens were prepared from mudstone produced in Northern Liaoning province, China. The mudstone consists of quartz (32.9%), sodium feldspar (24.7%), clay mineral (42%) (including illite 23%, kaolinite 18%, chlorite 19%, illite smectite mixed layer 40%) and a small amount of calcite. The X-ray diffraction (XRD) tests are shown in Fig. 1 and 2, for the mudstone and clay minerals, respectively.

The mudstone, which has a relatively low strength, has been classified as a soft rock in civil engineering. It is a clay-bearing rock, and scanning electron microscope (SEM) images showing the microcharacteristics and microcracks of the specimen are given in Fig. 3 and Fig. 4, respectively. The figures show that the samples are compact. Fig. 3 includes some micropores whose size is 10-20 μm. In the sample picture in Fig. 4, which has an amplification of 1000 times, there are some fractures and their size is 5-10 μm.

2.2. Physical and mechanical properties

The porosity of a rock specimen was determined by two means, namely, water absorption capacity and water intrusion method. In the water saturation, specimens were immersed in two ways, one is saturated under certain pressure, and the other is saturated under natural conditions. The saturation velocity of specimen is very important regarding rock deterioration. Saturation velocity of specimen is described with water absorption content, water absorption velocity and the rate of change of water absorbing capacity with time.

The water absorption content, ω_t, was calculated from Eq. 1:

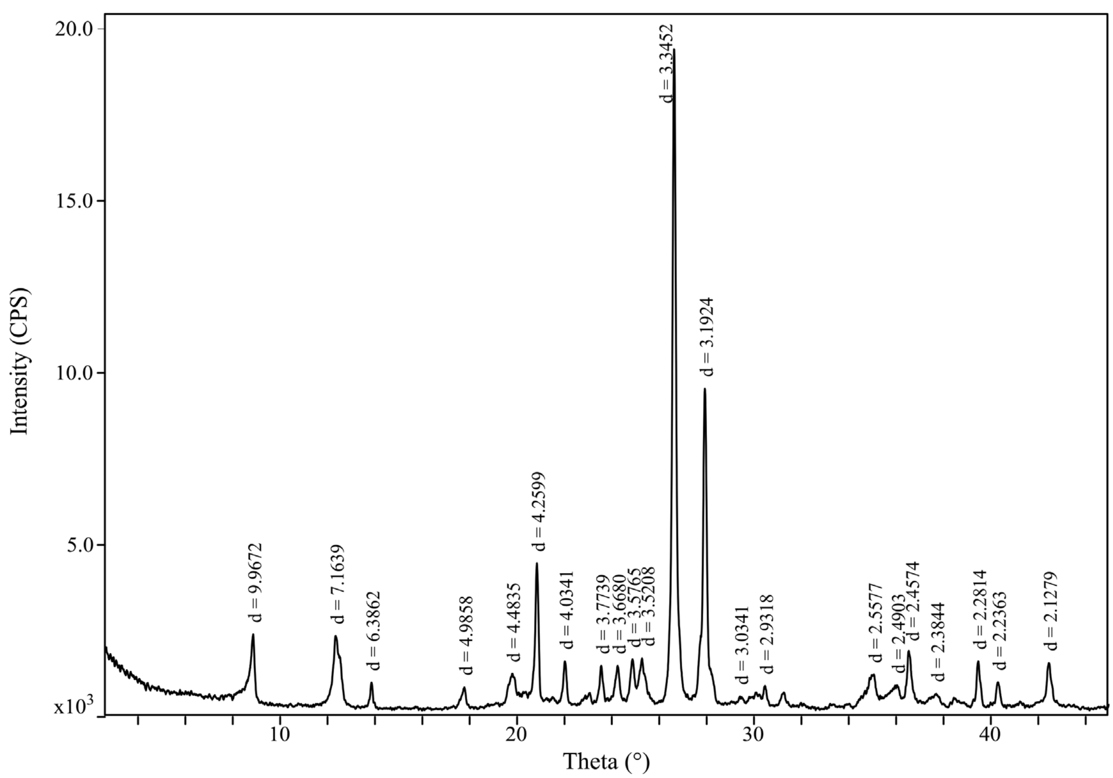

Figure 1 - XRD spectrum diagram showing the mineral compositions of specimen.

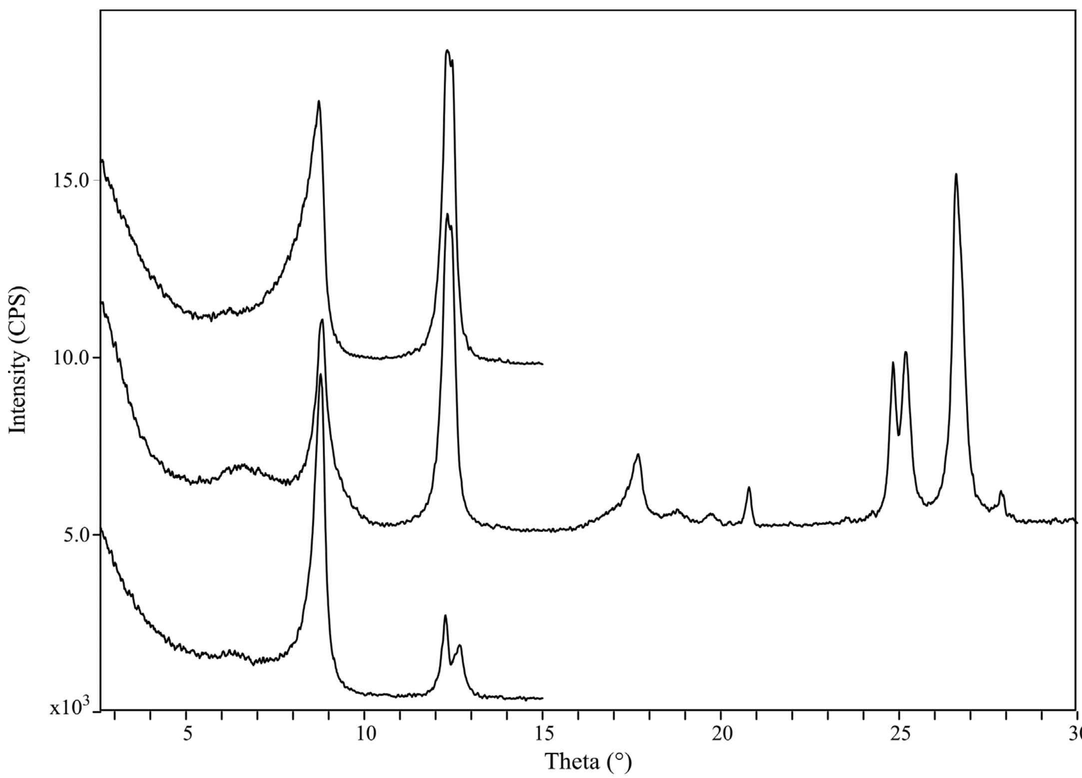

Figure 2 - XRD spectrum diagram showing the compositions of specimen clay mineral.

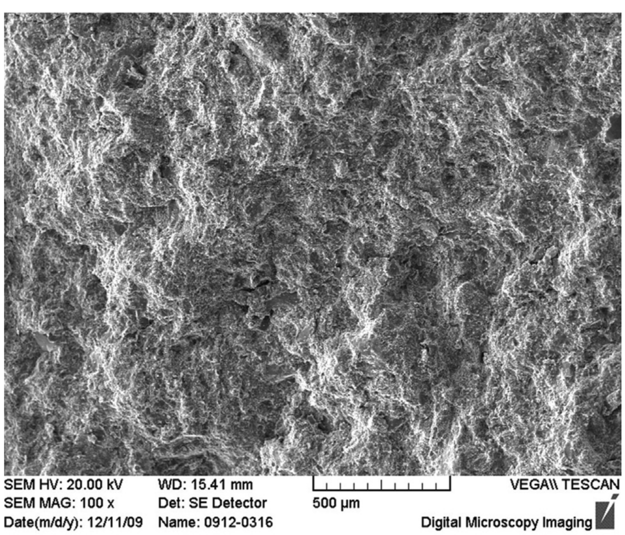

Figure 3 - SEM image showing the microcharacteristics of specimen (×100).

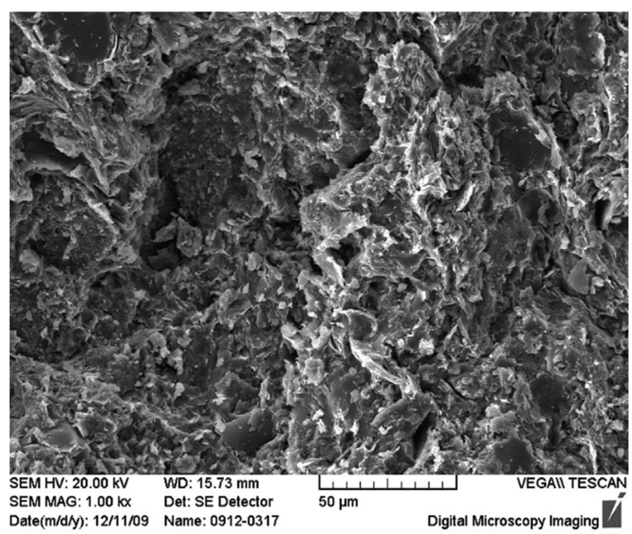

Figure 4 - SEM image showing the microcracks of specimen (×1,000).

$$\omega_t = \omega_0 + \frac{m_{wt}}{m_s} \tag{1}$$

where ω_0 is the water content of specimen in natural conditions; m_{wt} is the specimen weight after water absorption; m_s is the dry weight of specimen.

The change of water absorbing capacity with time is shown in Fig. 5.

In order to describe rock strength change with its water absorbing capacity, the strength softening coefficient $\eta(t)$ was used, which is calculated from Eq. 2:

$$\eta(t) = \frac{\sigma_{ti}}{\sigma_c} \tag{2}$$

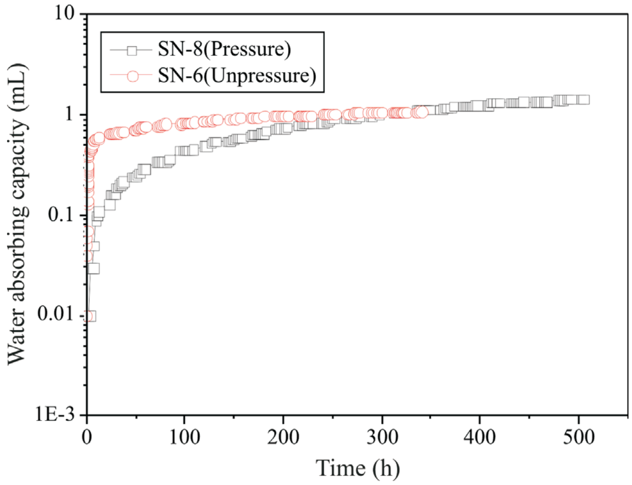

Figure 5 - Variation of water absorbing of specimen SN-6 and SN-8 with time.

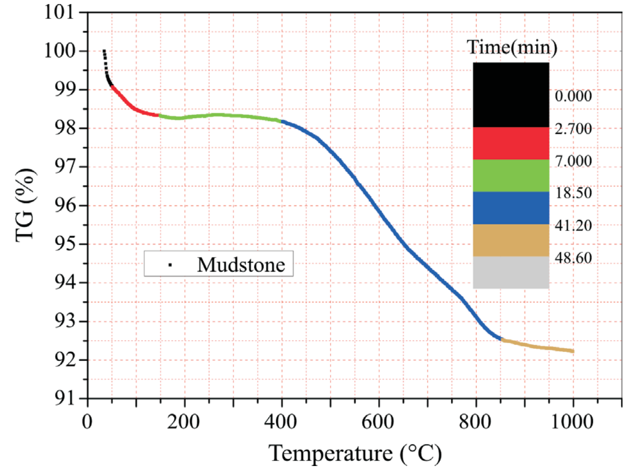

Figure 6 - Variation of the specimen weight with temperature.

where σ_{ti} is the uniaxial compression strength value with time; σ_c is the uniaxial compression strength standard value.

The uniaxial compression tests and the rock water content measurements were performed using standard methods. The summarizing values are shown as Table 1.

2.3. Thermal analysis test

In order to investigate the relation of mudstone physical properties and temperature, the weight change of specimen with temperature in Simultaneous Thermal Analysis (STA) was measured using the Ntzsch STA 409 PC/PG, and the result is given in Fig. 6. The result shows that the thermogravimetric (TG) properties of mudstone are more complex than those of the single minerals.

2.4. Freeze-thaw test

The freeze-thaw test was conducted in a temperature-controlled chamber, and before the test, specimens have been saturated. The freeze-thaw cycle occurred in distilled water from 12 °C to -20 °C. The temperature variation of the freeze-thaw cycle was done as shown in Fig. 7. In the temperature-controlled chamber, a special apparatus shown in Fig. 8 is prepared for the EIS measurement of specimen. Two containers were installed on both sides of the apparatus to ensure the specimen is always in the saturated state. Between the container and specimen, there are the electrodes which connect to the electrochemical workstation. The apparatus in the temperature-controlled chamber ensures specimen real-time monitoring during the freeze-thaw cycle. A freeze-thaw cycle took 4 h, about 2 h for freezing and 2 h for thawing.

2.5. Electrical impedance spectroscopy test

For evaluating the specimen damage degree because of freeze-thaw action, the EIS test was conducted after each freeze-thaw cycle till the specimen was clearly damaged. The Nyquist curves (Crossley, 1975) of EIS are shown in Fig. 9, where the symbol for impedance is, as usually, Z. In these figures, there are six Nyquist curves: before the freeze-thaw action, after six cycles, nine cycles, twelve cycles, fifteen cycles and eighteen cycles of the freeze-thaw action.

Table 1 - Summary of test results.

Name	Time (h)	Water absorbing capacity (mL)	Water content (%)	Uniaxial compression strength (MPa)	Strength softening coefficient
SN-1	/	/	0	68.31	1.07
SN-2	saturated	7.50	1.11	63.67	0.99
SN-3	0	0	1.09	64.07	1.00
SN-7	saturated	9.27	1.36	30.31	0.47
SN-4	181.186	0.84	0.94	/	/
SN-5	180.731	0.70	0.58	64.72	1.01
SN-6	340.340	1.09	2.28	51.59	0.81
SN-8	505.500	1.44	1.07	31.75	1.09

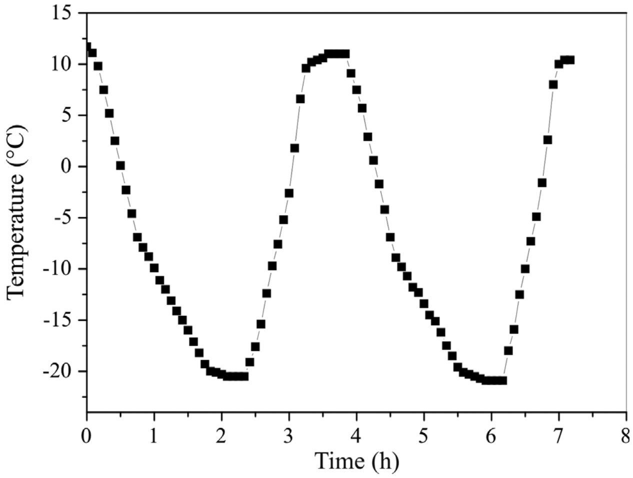

Figure 7 - Variation of temperature in every freeze-thaw cycle.

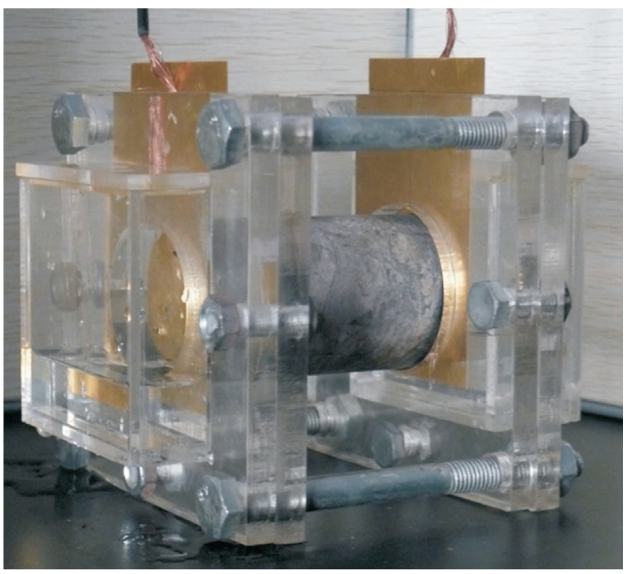

Figure 8 - The apparatus in the temperature-controlled chamber for the EIS measurement of specimen.

3. Results and Discussion

3.1. Initial rock properties

One of the factors influencing rock damage during freeze-thaw cycles is its minerals. Rock damage because of minerals has three mechanisms as follows. (1) Different thermal expansion coefficient of minerals in rock: when the temperature decreases from 12 °C to -20 °C, or increases from -20 °C to +12 °C, different expansion of minerals in rock will generate stress among minerals. When this stress exceeds the shear strength among them, damage occurs. (2) Minerals in rock are poor conductors of heat: during freeze-thaw cycle, the temperature gradient in rock is from the surface to the interior. So expansion degree from the surface to the interior has big differences, which will generate stress. The rock will be damaged when the stress exceeds the shear strength. (3) Some minerals can be deformed after absorbing water: the clay-bearing rocks such as shales, claystones, mudstones, and siltstones always contain clay minerals, especially montmorillonite, whose volume will expand when they are immersed in water. Expansion of clay minerals will generate pressure. When this pressure exceeds the tensile strength of rock, cracking occurs.

Another factor is pore water, which influences rock damage also through three mechanisms. (1) Expansion when water changes to ice: when the temperature decreases to below 0 °C, water begins to freeze in rock. If more than 90% of the pore volume is filled with water, expansion of water during freezing will generate pressure. When this pressure exceeds the tensile strength of the rock, cracking occurs. (2) Formation of ice lens or wedge: this is the persistent growth of a crystal large enough to disrupt the rock that contains enough water to feed further growth. A rock, such as mudstone, is a porous material in which pore water will not freeze immediately below 0 °C and can migrate during freezing. This phenomenon may be caused by the presence of dissolved chemicals and the relatively small sizes of the pores (Pigeon & Setier, 1997). (3) Hydraulic pressure: as ice grows in a pore or other space, owing to the expansion associated with freezing, unfrozen water is expelled from that space.

Before the freeze-thaw test, the mineral composition of specimens were obtained from the XRD test, as shown in Table 2 and Table 3. The specimen mainly contains quartz, sodium feldspar and clay mineral. Their thermal expansion coefficients are different, which will generate stress among minerals during freeze-thaw cycle and the specimen will be damaged. Simultaneously, the specimens will be damaged during freeze-thaw cycle because they are solids and minerals of their composition are poor conductors of heat. The mudstone contains 42% clay mineral. When specimens are immersed in water, part of clay mineral will contact with water and expand because of absorbing water. Expansion pressure can make the specimen crack open.

The water saturation method (Chen *et al.*, 2004) showed that the porosity of the specimens varied from 5.8% to 6.8%, with an average of 6.3%. Fig. 3 and Fig. 4 show that the specimens contain a few micropores and microfractures. The previous tests show that the mudstones have water absorbing capacity under natural or pressure state. The mudstone contains a certain amount of absorbed water, crystal water and constitutional water, zeolite water and interlayer water from TG test shown in Fig. 6. The properties above mentioned can create internal pressures during freeze-thaw test. The first is the action of the unfrozen water being pushed into smaller spaces (including micropores and microfractures) and the resistance to this flow increases the hydrostatic pressure. Secondly, freezing typically occurs first at the outer surface, forcing the remaining water

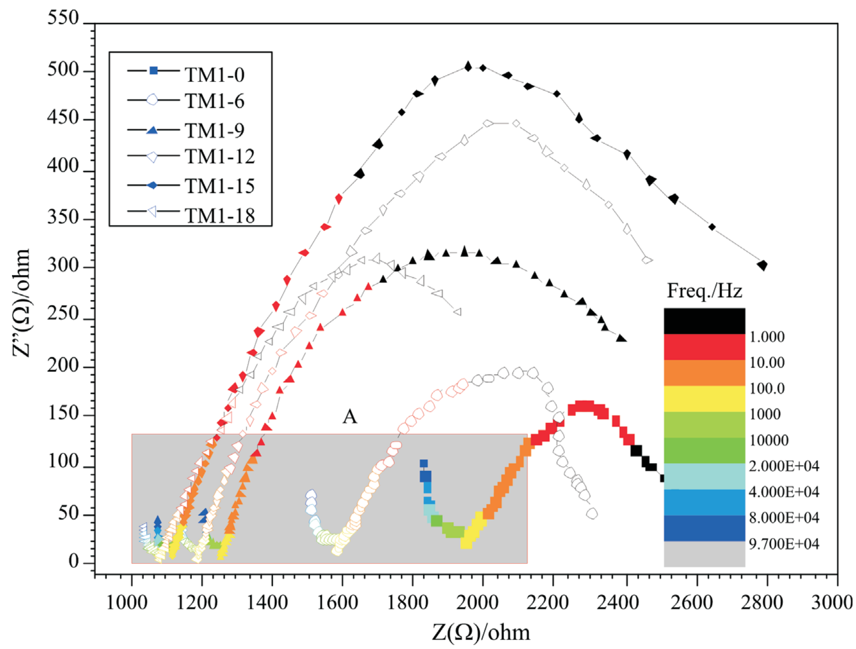

Figure 9 - The Nyquist curves of specimen after freeze-thaw cycles.

Table 2 - Specimen mineral composition.

Number	Kinds and percentage composition (%)							Clay mineral (%)
	Quartz	Potassium feldspar	Sodium feldspar	Anorthose	Calcite	Dolomite	Pyrite	
SN-1	32.9	/	24.7	/	0.4	/	/	42.0

Table 3 - Specimen clay mineral composition.

Number	Percentage composition (%)						Mixed-layer ratio (%)	
	Smectite	Illite/Smectite	Illite	Kaolinite	Chlorite	Chlorite/Smectite	Illite/Smectite	Kaolinite/Smectite
SN-1	/	40	23	18	19	/	30	/

inwards to create a saturated flow hydraulic pressure. Pressure is developed due to the resistance to the water flowing rapidly through the capillaries. The third involves saturated materials whereby an advancing ice front produces a hydrostatic compression that will create a tensile force within the constraining rock. Simultaneously, the heat transfers from the surface to the inner part of the specimen, or in the opposite direction. Because the minerals of specimen are poor conductors of heat and have different thermal expansion coefficient, stress will be generated among the minerals during freeze-thaw test. The water immersion also causes the clay minerals expansion.

3.2. EIS properties

Useful information is obtained from the data of EIS in the freeze-thaw test. However, the internal damage of rock during the freeze-thaw action can be expressed by the parameters from the data of EIS including capacitance properties, resistance properties, and constant phase element and so on.

3.2.1 Capacitance properties of Nyquist curves

The capacitance C_p of mudstone is calculated from its Nyquist curves taken for every freeze-thaw cycle using Eq. 4 (Bhatt & Nagaraju, 2009) and the obtained values are plotted in Fig. 9.

$$X_P = \frac{R^2 + X^2}{R} \tag{3}$$

$$C_P = \frac{1}{2\pi f X_P} \tag{4}$$

where R and X are values of real and imaginary components of Nyquist curve at a frequency f, the value of f is chosen such that these imaginary component values are nearly maximum on the high frequency asymptote (HFA) part on Nyquist curve (Hu *et al.*, 2007).

Fig. 10 shows that the change rate of capacitance up to 9 freeze-thaw cycles is lower than that from 12 to 18 freeze-thaw cycles. The middle line of the curve is flat. This indicates that the mudstone crack induces a higher change rate as the freeze-thaw cycles increase past 12.

3.2.2. Resistance properties of Nyquist curves

The resistance of mudstone is calculated from its Nyquist curves taken for every freeze-thaw cycle using Eq. 5 (Bhatt & Nagaraju, 2009) and the obtained values are plotted in Fig. 11.

$$R_P = \frac{R^2 + X^2}{X} \tag{5}$$

where R and X are values of real and imaginary components of Nyquist curves at a frequency f, the value of f being chosen such that these imaginary component values are nearly maximum on the HFA part on Nyquist curves (Hu *et al.*, 2007).

Fig. 11 shows that the rate of change of resistance is high at the starting point of freeze-thaw test. From 12 to 18 freeze-thaw cycles, the line becomes flat. It indicates that the specimen offers decreasing resistance till 12 times, which means the mudstone crack is extending steadily during 12 times freeze-thaw cycles. After 12 freeze-thaw cycles, the crack does not extend due to the freeze-thaw action, the value of the curve is mainly the resistance of the solution contained in the specimen.

3.2.3. Constant phase element of Nyquist curves

A dispersive, frequency-dependent element or so-called constant phase element (CPE) can be introduced to account for the shape of the depressed complex plot (Perron & Beaudoin, 2002). The impedance contribution of this element can be expressed as follows:

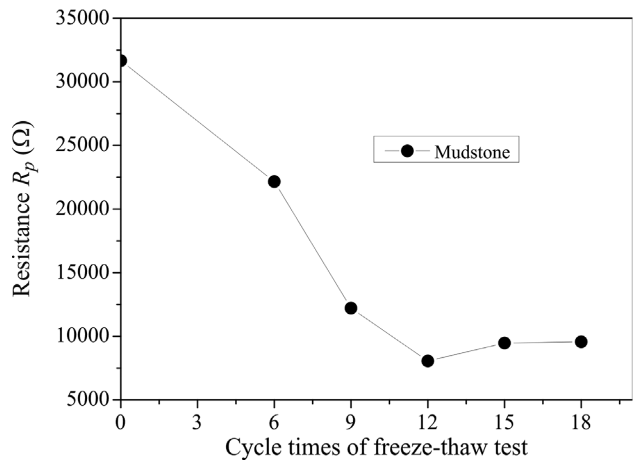

Figure 11 - Variation in resistance of specimen with cycle times.

$$Z(CPE) = A_0^{-1}(jw)^{-\varphi} \tag{6}$$

where $\varphi = 1 - 2/\pi(\alpha)$ and α is the depression angle.

Therefore, φ can be used to represent the degree of perfection of the capacitor and represents a measure of how far the arc is depressed below the real impedance axis.

Previous work indicates a dependence of φ on the characteristics of the material pore size distribution (Hu *et al.*, 2007). This work has suggested that a broad pore size distribution would result in a wide spread of relaxation times corresponding to a large dispersion angle. A narrow pore size distribution would result in a significantly reduced spread of relaxation times. The range of pore size distributions represented by the solution in specimen and porous conforms to these arguments (Perron & Beaudoin, 2002). The results of mudstone during freeze-thaw test are shown as Fig. 12, in which φ comes from the zone A of Fig. 9. The value of φ is increasing up till 12 freeze-thaw cycles. Then, the value starts to decrease from 12 to 18 freeze-thaw cycles. It indicates the uniformity of specimen

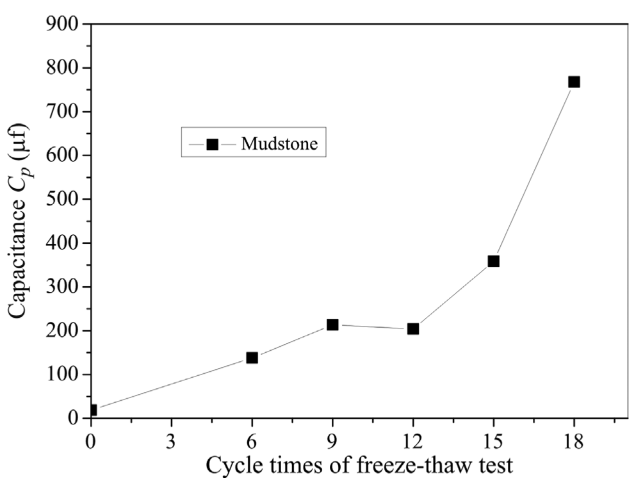

Figure 10 - Variation in capacitance of specimen with cycle times.

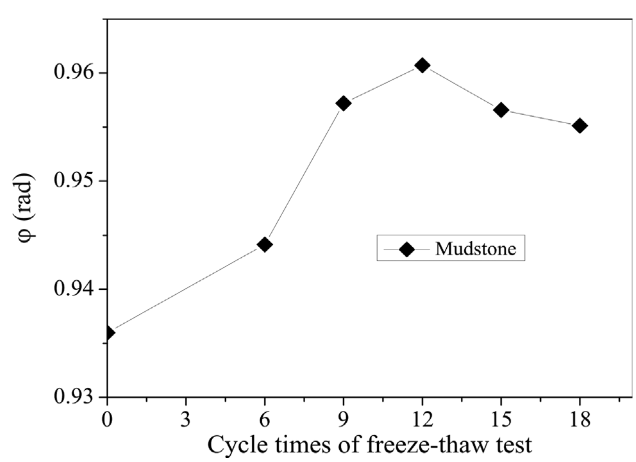

Figure 12 - Variation of φ (indicating dispersive effect) with cycle times.

getting better and better firstly, and uniform degree of pore size distribution variation becoming worse after 12 freeze-thaw cycles.

4. Conclusions

The designed instrument based on EIS is found quite suitable for rapid and nondestructive measurement of electrical properties of mudstone during freeze-thaw test. The designed instrument is also found quite suitable for the simultaneous measurement of capacitance and resistance of the specimen during freeze-thaw cycles. The change rate of capacitance showed the mudstone crack extending with the freeze-thaw cycles. The variation in resistance of mudstone specimen revealed that the mudstone crack extends steadily during 12 freeze-thaw cycles and from that time the crack connects the electrodes at both ends of the specimen. After 12 freeze-thaw cycles, the changes of resistance are smooth and steady, which shows that the crack does not extend due to the freeze-thaw action, the value of the curve being mainly the resistance of the solution contained in the specimen. The parameter indicating dispersive effect φ, which is increasing firstly and decreasing subsequently, shows the change rule of specimen crack at freeze-thaw test. Thus, the study of electrical properties of mudstone proved to be quite useful to study rock cracking during freeze-thaw test or other mechanical action.

Acknowledgments

The authors would like to acknowledge the financial support of the National Natural Science Foundation of China (51574296) and the Key Discipline and Open Laboratory for Deep Mine of Henan Province Colleges and Universities (Henan Polytechnic University) (2014KF-03). The authors also appreciate Prof. Zhibiao Guo for taking samples and the proposal about freeze-thaw test.

References

Bayram, F. (2012). Predicting mechanical strength loss of natural stones after freeze-thaw in cold regions. Cold Regions Science and Technology, 83-84:98-102.

Bhatt, C.M. & Nagaraju, J. (2009). Studies on glass transition and starch re-crystallization in wheat bread during staling using electrical impedance spectroscopy. Innovative Food Science and Emerging Technologies, 10(2):241-245.

Bona, N.; Rossi, E. & Capaccioli, S. (2001). Electrical measurements in the 100 Hz to 10 GHz frequency range for efficient rock wettability determination. Society of Petroleum Engineers, 6(1):80-88.

Chen, T.C.; Yeung, M.R. & Mori, N. (2004). Effect of water saturation on deterioration of welded tuff due to freeze-thaw action. Cold Regions Science and Technology, 38:127-136.

Crossley, T.R. (1975). Envelope curves to inverse Nyquist array diagrams. International Journal of Control, 22(1):57-63.

Gersing, E. (1998). Impedance spectroscopy on living tissue for determination of the state of organs. Bioelectrochemistry and Bioenergetics, 45:145-149.

Hu, J.C.; Wang, H.F.; He, M.C. & Sun, X.M. (2007). Impedance spectroscopy and application to test the microcrack of rock. Chinese Journal of Geotechnical Engineering, 29(6):853-856.

Huebner, J.S. & Dillenburg, R.G. (1995). Impedance spectra of hot dry silicate minerals and rock: Qualitative interpretation of spectra. American Mineralogist, 80:46-64.

Iñigo, A.C.; García-Talegón, J. & Vicente-Tavera, S. (2013). Colour and ultrasound propagation speed changes by different ageing of freezing thawing and cooling heating in granitic materials. Cold Regions Science and Technology, 85:71-78.

Kahraman, S. & Alber, M. (2006). Estimating the unconfined compressive strength and elastic modulus of a fault breccia mixture of weak rocks and strong matrix. International Journal of Rock Mechanics & Mining Sciences, 43:1277-1287.

Kahraman, S.; Alber, M.; Fener, M. & Gunaydin, O. (2015). An assessment on the indirect determination of volumetric block proportion of Misis-Fault Breccia (Adana, Turkey). Bulletin of Engineering Geology and the Environment , 74(3):899-907.

Kirichek, A.; Ghose, R. & Heller, K. (2013). Laboratory monitoring of CO_2 migration within brine-saturated reservoir rock though complex electrical impedance. Society of Exploration Geophysicists, 2742-2746.

Li, X.B. (2003). Impedance Spectroscopy for Manufacturing Control of Material Physical Properties. Master Thesis, Department of Electrical Engineering, University of Washington, pp. 62-75.

Liu, Y.; Xue, Z.Q. & Park, H. (2015). Measurement of electrical impedance of a Berea sandstone core during the displacement of saturated brine by oil and CO_2 injections. Journal of Applied Geophysics, 123:50-62.

Matsuoka, N. (1990). Mechanisms of rock breakdown by frost action: an experimental approach. Cold Regions Science and Technology, 17:253-270.

Olson, R.A.; Christensen, B.J.; Coverdale, R.T.; Ford, S.J.; Moss, G.M. & Jennings, H.M. (1995). Interpretation of the impedance spectroscopy of cement paste via computer modelling, part III microstructural analysis of frozen cement paste. Journal of Materials Science, 30:5078-5086.

Ozcelik, Y.; Careddu, N. & Yilmazkaya, E. (2012). The effects of freeze-thaw cycles on the gloss values of polished stone surfaces. Cold Regions Science and Technology, 82:49-55.

Pan, L.K.; Huang, H.T. & Sun, C.Q. (2003). Dielectric relaxation and transition of porous silicon. Journal of Applied Physics, 94(4):2695-2700.

Perron, S. & Beaudoin, J. J. (2002). Freezing of water in portland cement paste-an ac impedance spectroscopy study. Cement & Concrete Composites, 24:467-475.

Pigeon, M. & Setier, M. (1997). Action of frost and deicing chemicals: basic phenomena and testing. Rilem Proceedings 30. Freeze-thaw Durability of Concrete, pp. 1-22.

Prabakar, K. & Rao, S. P. (2007). Complex impedance spectroscopy studies on fatigued soft and hard PZT ceramics. Journal of Alloys and Compounds, 437(1-2):302-310.

Saltas, V.; Fitilis, I. & Vallianatos, F. (2014). A combined complex electrical impedance and acoustic emission study in limestone samples under uniaxial loading. Tectonophysics, 637:198-206.

Su, Q.X.; Feng, Q.N. & Shang, Z.Y. (2000). Electrical impedance variation with water saturation in rock. Geophysics, 65(1):68-75.

Tan, X.J.; Chen, W.Z.; Yang, J.P. & Cao, J.J. (2011). Laboratory investigations on the mechanical properties degradation of granite under freeze-thaw cycles. Cold Regions Science and Technology, 68:130-138.

Wu, G.; He, G.L. & Zhang, L. (2006). Experimental study on cycles of freeze-thaw of marble. Chinese Journal of Rock Mechanics and Engineering, 25:2930-2938.

Yang, G.S. & Pu, Y.B. (2002). Initial discussion on the damage propagation of rock under the frost and thaw condition. Journal of China Coal Society, 27:357-360.

Zhang, M.I.N.; Stout, D.G. & Willison, J.H.M. (1990). Electrical impedance analysis in plant tissues: Symplasmic resistance and membrane capacitance in the Hayden model. Journal of Experimental Botany, 41(3):371-380.

Zhang, M.I.N. & Willison, J.H.M. (1991) Electrical impedance analysis in plant tissues: A double shell model. Ibid, 42:1465-1476.

Influence of the Embedded Length on the Overall Stability of Single Anchored Retaining Walls

C.M. Santos Josefino, N.M.C. Guerra, A.N. Antão

Abstract. Urban excavations are frequently performed using anchored retaining walls. Overall stability is an important stability verification in such walls and is significantly influenced by geometrical and mechanical characteristics of the wall, of the anchors and of the soil. In the present work, particular emphasis is given to the role of the embedded length in reducing the needed anchor length to ensure the overall stability, for the case of single anchored retaining walls. The need to reduce the anchor length can be justified by economical and technical reasons. The problem is analysed using classic limit equilibrium methods and finite element calculations.

Keywords: overall stability, anchored retaining walls, urban excavations, embedded length.

1. Introduction

Overall stability is an important verification for the design of anchored retaining walls. The overall stability of anchored retaining walls depends on the anchor length and on other geometrical parameters such as anchor head depth, anchor inclination and the embedded length of the wall. In this work the influence of these parameters on the minimum anchor length needed to ensure overall stability is studied through a parametric analysis and by using Broms' (1968) classical limit equilibrium method for checking the overall stability of single anchored retaining walls.

The classical methods for overall stability are based on Kranz's (1953) method. This method was initially presented for single anchored retaining walls using plate or beam anchors. It was later extended by Jelinek & Ostermayer (1967) to walls with two or more horizontal plate or beam anchor levels and by Ranke & Ostermayer (1968) to cases involving two or more inclined grouted pre-stressed anchors. Broms (1968) presented an alternative method to Kranz's approach and applied it to single-anchored (grouted, pre-stressed and inclined) retaining walls. These methods are often cited in reference works, such as Hanna (1982), Matos Fernandes (1990) and Puller (1996), explaining how they can be used to check the overall stability, but systematic works showing the practical results on anchor length of the application of such methods could not be found in the literature. Recently, Santos Josefino *et al.* (2014) performed a parametric analysis of Broms' and Kranz's methods showing the influence of different approaches for safety verification on the needed anchor length of single-anchored retaining walls. Conclusions on the required location of the grouted anchor bond were presented. This approach was extended to retaining walls with two anchor levels by Guerra *et al.* (2016).

In the present paper this line of work is proceeded and particular attention is given to the role of the embedded length of single anchored retaining walls as a way of reducing the anchor length needed to ensure the overall equilibrium. The interest of such solution is justified by possible reasons of cost (for cases where the cost of increasing the embedded length of the wall could be compensated by the benefit of decreasing the anchor lengths) but also, most particularly, by geometrical difficulties in using long anchors due to possible proximity to the excavation of buried and/or sensitive structures, in an urban environment. For the analysis of this parameter a series of finite element calculations is performed, their results being presented and compared with the limit equilibrium approach.

2. Classical Limit Equilibrium Methods for the Analysis of Overall Stability

Kranz's (1953) and Broms' (1968) methods are two classical limit equilibrium methods for the analysis of overall stability (Fig. 1). As described by Guerra *et al.* (2016), there are three differences between the two methods: 1) location of point C; 2) definition of safety factor and 3) volume involved in the equilibrium.

Kranz's method and the ones directly derived from it, consider point *C* at the middle of the bond length. Broms' method considers the possibility of other locations for this point, but in the present paper point C will be assumed as in Kranz's method, at the center of the bond length. Therefore, the anchor length assumed in the calculations in Broms' method will be L_u, given by:

Cláudia S. Josefino, M.Sc, Ph.D. Student, Departamento de Engenharia Civil, Faculdade de Ciências e Tecnologia, Universidade Nova de Lisboa, Lisboa, Portugal. e-mail: claudiajosefino@hotmail.com.
Nuno M. da Costa Guerra, Ph.D., Associate Professor, UNIC, Departamento de Engenharia Civil, Faculdade de Ciências e Tecnologia, Universidade Nova de Lisboa, Lisboa, Portugal. e-mail: nguerra@fct.unl.pt.
Armando M.S. Nunes Antão, Ph.D., Associate Professor, UNIC, Departamento de Engenharia Civil, Faculdade de Ciências e Tecnologia, Universidade Nova de Lisboa, Lisboa, Portugal. e-mail: amna@fct.unl.pt.
Submitted on November 4, 2016; Final Acceptance on July 5, 2017; Discussion open until December 29, 2017.

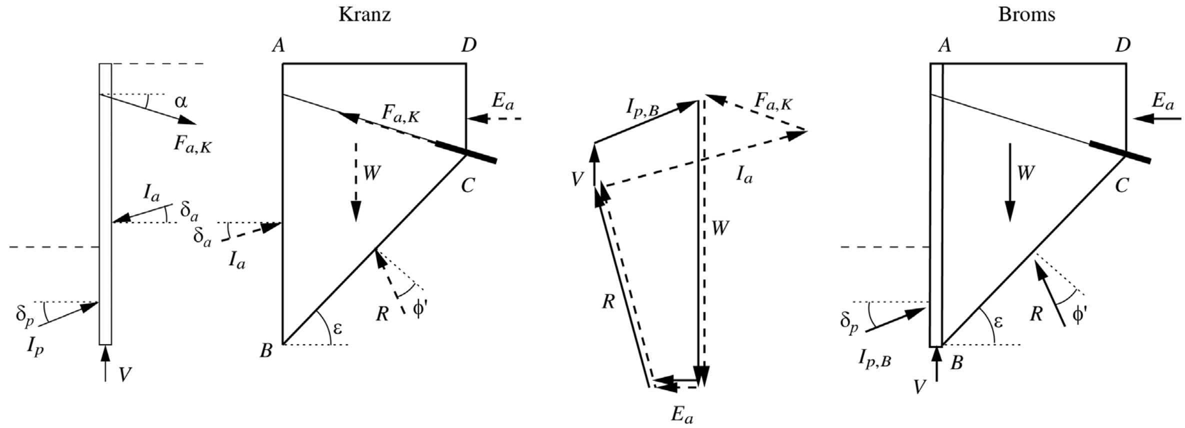

Figure 1 - Geometry of the case study.

$$L_u = L_f + \frac{L_b}{2} \quad (1)$$

where L_f is the free anchor length and L_b is the bond length (Fig. 2).

Safety factors were originally defined in different ways in the two methods. Kranz's method assumes the safety factor, FS_K, to be defined as:

$$FS_K = \frac{F_{a,K}}{F_a} \quad (2)$$

where $F_{a,K}$ is the allowed force on the anchor, determined from Kranz's method, and F_a is the force applied on the anchor. Broms' method considers the safety factor, FS_B, as:

$$FS_B = \frac{I_p}{I_{p,B}} \quad (3)$$

where I_p is the passive force that can be mobilized on the embedded length of the wall and $I_{p,B}$ is the passive force needed to ensure equilibrium, determined from Broms' method.

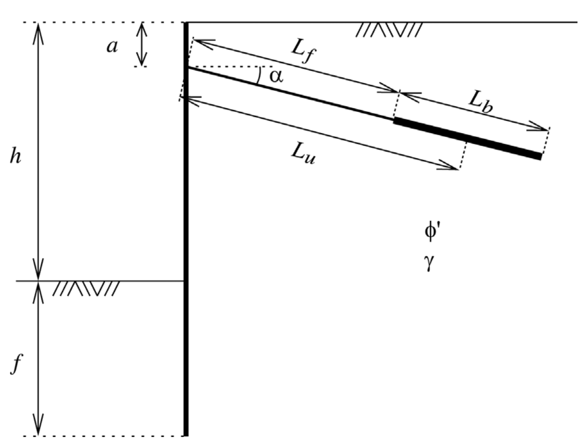

Figure 2 - Kranz's and Broms' methods (adapted from Guerra *et al.* (2016)). Forces for Kranz's method in the polygon are represented by dashed lines; forces for Broms' method are represented by solid lines.

Instead of using those global safety factors, design values of the soil and soil-wall interface properties can be used, and the two methods become equivalent from this perspective also.

Finally, in spite of the differences between these methods concerning the volume involved in equilibrium, they are equivalent. In fact, Broms' method considers the equilibrium of both wall and soil mass ABCD, whereas Kranz's method considers the equilibrium of the soil mass only (Fig. 1). The forces involved in Broms' method (solid lines in the polygon in Fig. 1) are: the passive force, $I_{p,B}$, the vertical force aplied to the toe of the wall, V, the weight of the soil mass *ABCD*, W, the active force, E_a, and the reaction, R. The wall weight was not considered in the present work (and in Fig. 1), but it could easily be included. Also, force V was considered equal to zero. This approch is conservative and the force is probably small in cases of steel sheet-piles or other walls with small cross section. Kranz's method considers equilibrium of the wall and of the soil mass *ABCD* separately. The equilibrium of the wall involves the anchor force, F_a, the active earth pressure, I_a, the passive earth pressure, $I_{p,B}$ and the vertical force aplied to the toe of the wall, V. The forces involved in the equilibrium of the soil mass *ABCD* (the ones involved in Kranz's method, represented by dashed lines in the polygon of Fig. 1) are: the active earth pressure, I_a, the weight of the soil mass, W, the active earth pressure developed along *CD*, E_a, the reaction, R and the anchor force, F_a. If all applied forces are in equilibrium (and, in particular, if the wall is in equilibrium), the two methods will be equivalent.

In the present paper, Brom's method is used.

3. Definition of the Case Study

A case study with the very simple geometry presented in Fig. 2 was considered. The retaining wall has one level of prestressed anchors and is suporting an excavation of depth

h in a homogeneous and dry soil with a friction angle ϕ' and unit weight γ, without surface loads on the supported soil. The anchors make an angle α with the horizontal plane. The embedded length of the wall is f and the depth of the anchor head is a; the soil-to-wall friction angle is δ.

Stability of this kind of structure is ensured by the passive earth pressure developed along the embedded length and by the anchor force. The embedded length and the anchor force were determined using the free-earth support method (Costet & Sanglerat, 1975). Full equilibrium of the wall (including vertical equilibrium) is ensured by using the methodology from Frank *et al.* (2004). This method uses an iterative procedure where full equilibrium is obtained by considering the possibility of the soil-to-wall friction angle not being fully mobilized on either the active side, with friction angle δ_a, or the passive side of the wall, with friction angle δ_p (Fig. 1). In the problem addressed in the present paper, it is the friction angle on the active side that needs adjustment (vertical equilibrium can only be obtained by decreasing δ_a; a decrease in δ_p would further unbalance vertical forces). Active earth pressure coefficients were determined using Coulomb's theory (Coulomb, 1776), through the equation of Müller-Breslau (1906); passive earth pressure coefficients were those from Kérisel & Absi (1990).

Equations of equilibrium of moments and of horizontal forces were used for a first iteration of the anchor force and of the embedded length. The equation of equilibrium of vertical forces was then used to determine the mobilized value of the soil-to-wall friction angle, δ_a, less or equal to δ, which ensured vertical equilibrium. This new value of the soil-to-wall friction angle was then used to perform a second iteration, with updated active earth pressure coefficients, again using equilibrium equations of moments and of horizontal forces. The procedure continued until full equilibrium was achieved for the desired margin of error.

For the simple case presented in Fig. 2, this procedure can be carried out in a dimensionless way, allowing the anchor force and the embedded length to be determined dimensionlessly - $F_d/(\gamma h^2)$ and f_0/h - as a function of ϕ', δ, α and a/h. Symbol f_0 represents the embedded length determined from the free-earth support method. In the present case f is equal to f_0; further in the paper cases where $f > f_0$ will be analysed.

The case study presented considered $\phi' = 30°$, $\delta = 20°$, $\alpha = 15°$ and $a/h = 0.2$. Calculations were performed using Design Approach 1 (combination 2) of Eurocode 7 (EN 1997-1, 2004), which uses a partial factor for the friction angles of 1.25, resulting in $\phi'_d = 24.8°$ and $\delta_d = 16.2°$ (d in subscript denotes design values). As in this example there are no variable actions, all other partial factors are equal to 1.0 (EN 1997-1, 2004).

Results of the iterative procedure are presented in Table 1. Final values obtained are $f_0/h = 0.3729 (\approx 0.37)$ and $F_{ad}/\gamma h^2 = 0.1184$.

4. Application of Broms' Method

4.1. Determination of the anchor length needed to ensure overall stability

The vertical equilibrium of the forces involved in Broms' method (Fig. 1) results on the following equation:

$$R = \frac{W - I_{p,B} \sin\delta_p}{\cos(\varepsilon - \phi')} \tag{4}$$

where angle ε (Fig. 1) is given by:

$$\varepsilon = \arctan\frac{h + f - a - L_u \sin\alpha}{L_u \cos\alpha} \tag{5}$$

The horizontal equilibrium results in:

$$I_{p,B} \cos\delta_p - E_a - R\sin(\varepsilon - \phi') = 0 \tag{6}$$

The equations presented above also allow the calculation of the value of L_u required for equilibrium and can be re-written in a dimensionless way (as shown in a different form by Schnabel Foundation Company (1996) and Elton & Whitbeck (1997)). In fact, the ratio L_u/h can be written as a function of other dimensionless parameters:

$$\frac{L_u}{h} = f\left(\phi'; \alpha; \frac{f}{h}; \frac{a}{h}\right) \tag{7}$$

These equations were programmed in Fortran 90 for the geometry of the case study shown in Fig. 2.

4.2. Case study results

The procedure described above was applied to the case presented in section 3 and considering the value of $f_0/h = 0.37$ determined in the same section. The result obtained for dimensionless length L_u/h is 1.245. This length is the minimum length needed to ensure the verification of safety according, again, to Design Approach 1, combination 2 of Eurocode 7. Figure 3 shows the mecanism involved in this calculation.

In this calculation the only safety factor involved is the one applied to the friction angles (equal to 1.25), and

Table 1 - Results of the iterative procedure for determining the embedded length and anchor force for the case study.

Iteration	δ_{ad} (°)	f_0/h	$F_{ad}/(\gamma h^2)$
1	16.2343	0.34895	0.1060
2	6.2996	0.37394	0.1189
3	6.6983	0.37286	0.1184
4	6.6859	0.37289	0.1184
5	6.6863	0.37289	0.1184

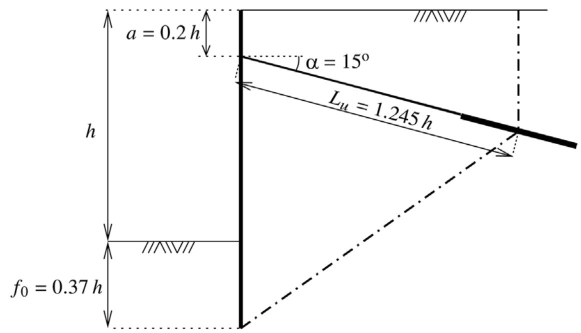

Figure 3 - Broms' mechanism obtained for the case study ($\phi'_d = 24.8°$, $\delta_d = 16.2°$).

therefore this result of the length L_u can be interpreted either as the value that ensures safety for $\phi' = 30°$ or as the value that corresponds to limit equilibrium situation for $\phi' = 24.8°(\approx 25°)$. So, in the following analyses the values of ϕ' can either be the characteristic values of the friction angle (and the results will be the limit equilibrium case) or the design values of the friction angle (and the results will be the minimum to verify safety, in an approach where safety is considered in this way).

4.3. Parametric analysis

4.3.1. Introduction

The main purpose of this paper is to analyse the influence of the embedded length of the wall on the overall stability and, particularly, on the possibility of using shorter ground anchors. However, results also depend significantly on other mechanical and geometrical parameters, such as the soil friction angle, the anchor inclination and the depth of the anchor head. The influence of these parameters will therefore be briefly analysed first. In all cases the soil-to-wall friction angle is assumed equal to 2/3 of the soil friction angle.

4.3.2. Influence of the soil friction angle

To study the influence of the soil friction angle, the previous calculations were repeated for different values of this parameter. Free-earth support method, using the procedure of Frank *et al.* (2004), to evaluate the embedded length and anchor force ratios, and Brom's method, to determine the anchor length ratio L_u/h, were used in the same way. Anchor inclination and depth ratio of anchor head were kept with the previous values of $\alpha = 15°$ and $a/h = 0.2$.

Results for f_0/h, L_u/h and L_u/f_0 are shown in Fig. 4 (in fact, Fig. 4 also presents results for other values of α but only the case of $\alpha = 15°$ is now commented).

Figure 4 shows that, as expected, the embedded length ratio of the wall f_0/h decreases significantly with the soil friction angle, as does the anchor length ratio L_u/h. The anchor ratio decreases less than the embedded length, as demonstrated by the values of L_u/f_0, which show a significant increase with the increase of the soil friction angle. These findings are not surprising. It is well-known that in the equilibrium of this type of retaining walls, the passive force plays an extremely important role, and this role is strongly influenced by the soil friction angle. The role of the friction angle on the overall stability is important, but not as vital as in the case of the wall equilibrium. In fact, the passive force does not play such a crucial part in the overall stability as it does in the wall equilibrium.

4.3.3. Influence of anchor inclination

The influence of anchor inclination was studied repeating previous analyses (performed for $\alpha = 15°$) for other values of angle α - 0, 30 and 45°. Results obtained are also

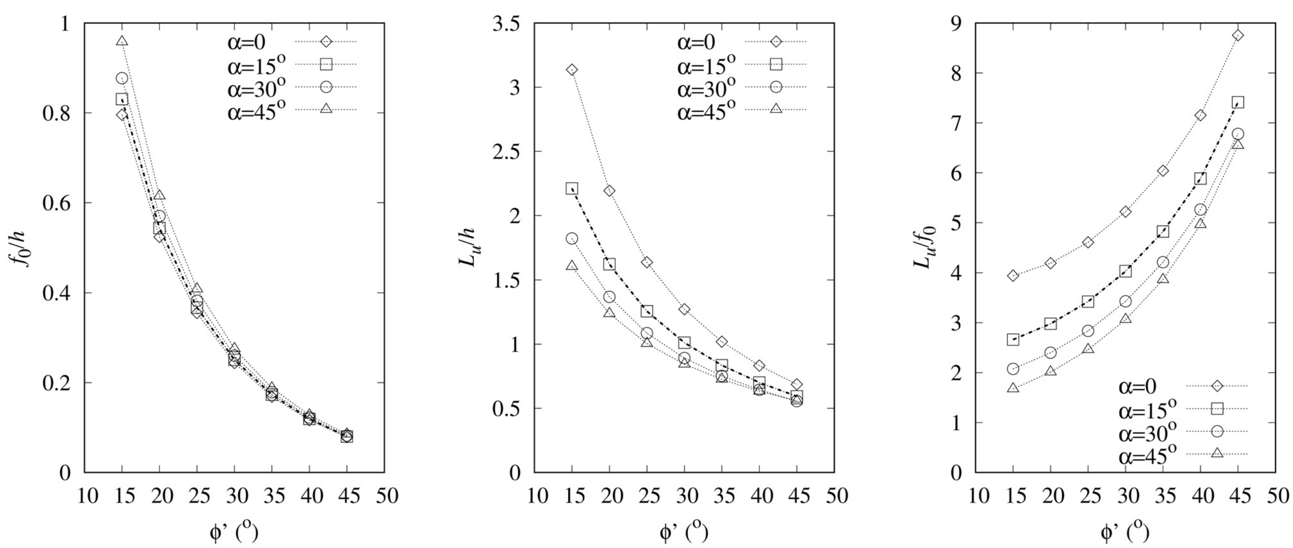

Figure 4 - Values of f_0/h, L_u/h and L_u/f_0 as a function of the soil friction angle for different anchor inclinations and for $a/h = 0.2$ and $\delta/\phi' = 2/3$.

presented in Fig. 4. Anchor inclination has some effect on the embedded length, although relatively small. Greater values of anchor inclination lead to greater embedded lengths, which is needed to ensure vertical equilibrium, as more inclined anchors apply larger vertical forces to the wall. The effect on the anchor length needed to ensure the overall stability is the oposite: greater anchor inclinations lead to shorter anchor lengths, which can be explained by the deeper mechanisms associated to more inclined anchors. Results of L_u/f_0 are therefore greater for less inclined anchors.

4.3.4. Influence of the depth of the anchor head

All previous results were obtained for the depth ratio of the anchor head, a/h, equal to 0.2. To analyse the influence of this depth, calculations were repeated for other values of a/h (0.4 and 0.6), for the case of α = 15° and for different soil friction angles. Results are shown in Fig. 5.

The figure shows that both f_0/h and L_u/h ratios decrease with the increase of a/h. The decrease of f_0/h is a consequence of the equilibrium of the wall, which involves a greater force on the anchor for greater values of a/h, and the decrease of L_u/h is caused by the deeper mechanisms involved for greater a/h (for the same anchor inclination) in a way similar to that observed in the previous section. Ratio L_u/f_0 is greater for greater a/h ratios and assumes the lowest values for the intermediate case of a/h = 0.4.

4.3.5. Influence of the embedded length

The influence of the embedded length is studied by initially considering the case ϕ' = 30°, α = 15° and a/h = 0.2, and repeating calculations using Broms' method for embedded length ratios f/h greater than f_0/h (or, in another way, considering different f/f_0 ratios). Results are presented by the points marked "ϕ' = 30°" in the left graphic (α = 15°) of Fig. 6; the other lines will be addressed next.

Graphics in Fig. 6 were prepared using the same scale horizontally and vertically. It can therefore be observed that a small increment in f/h results in a significant decrease in L_u/h. In fact, an increase in f/h of 0.05 results in a decrease in L_u/h of about 0.30, which shows the effectiveness in the overall stability of increasing the embedded length. Results also show that Broms' method gives no solution for L_u beyond a certain value of f/h. In fact, the point corresponding to the greatest value of f/h (and the lowest value of L_u/h) is the last for which Broms' method gives a solution and this corresponds to the situation where the anchor length is still outside the active wedge behind the wall (defined from the wall toe and also marked in Fig. 6). For embedded lengths beyond this case, there is no solution from Broms' method. This does not mean, however, that increasing the embedded length would not further reduce the required value of L_u/h; it only means that the ratio L_u/h can no longer be determined by Broms' method. This will be addressed in the next section.

Results for other friction angles of the soil are also presented in Fig. 6 and similar conclusions may be drawn. The active wedges limit the cases for which solutions from Broms' method can be found in the way previously described. Also, it can be concluded that the reduction in the needed anchor length by increasing the embedded length of the wall is more effective for lower values of the anchor inclination, due to the shallower mechanisms involved, and for lower values of the soil friction angle, due to the more inclined active wedges and therefore the narrower range for which Broms' method gives solution.

A different representation of the same type of results is shown in Fig. 7. The influence of the soil friction angle is

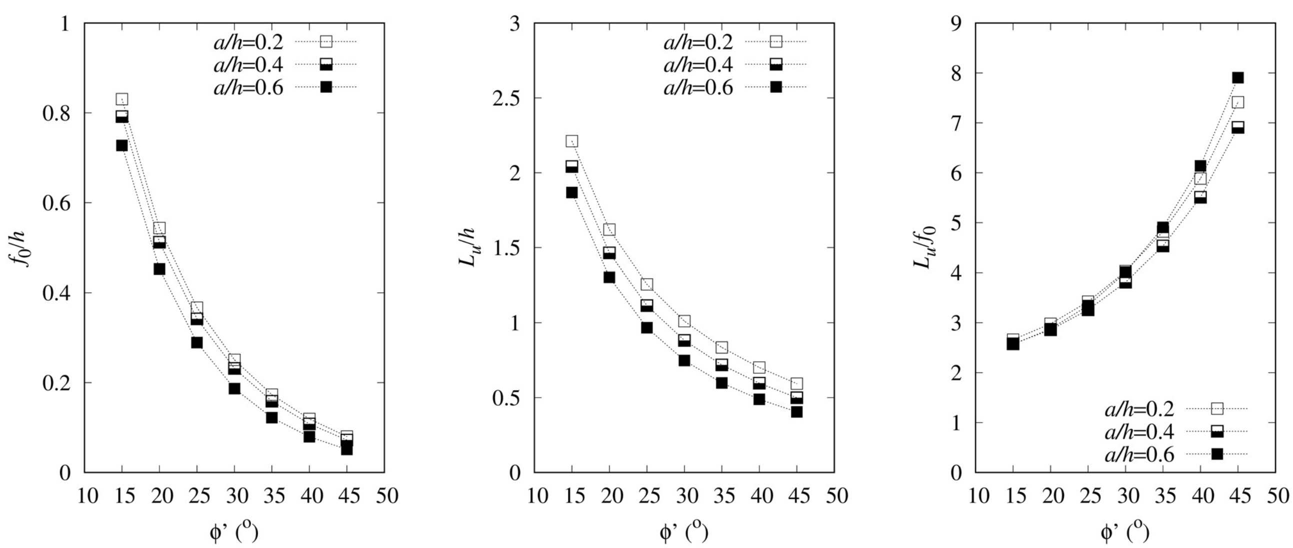

Figure 5 - Values of f_0/h, L_u/h and L_u/f_0 as a function of the soil friction angle for different depth ratios of the anchor head and for α = 15° and δ/ϕ' = 2/3.

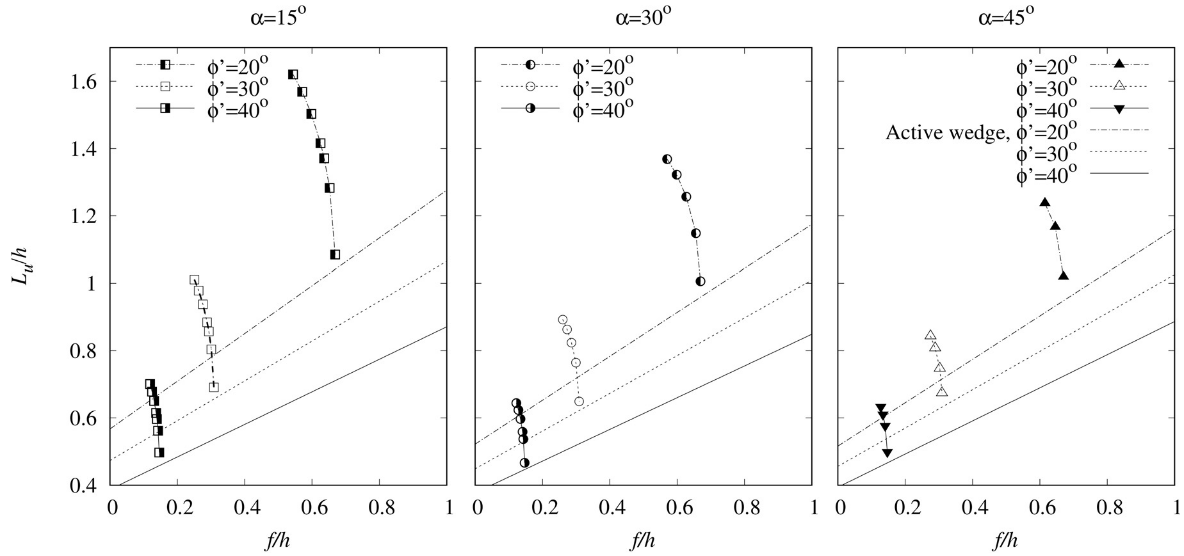

Figure 6 - Values of L_u/h as a function of the embedded length ratio, *f/h*, for different soil friction angles and anchor inclinations, for *a/h* = 0.2 and δ/φ' = 2/3.

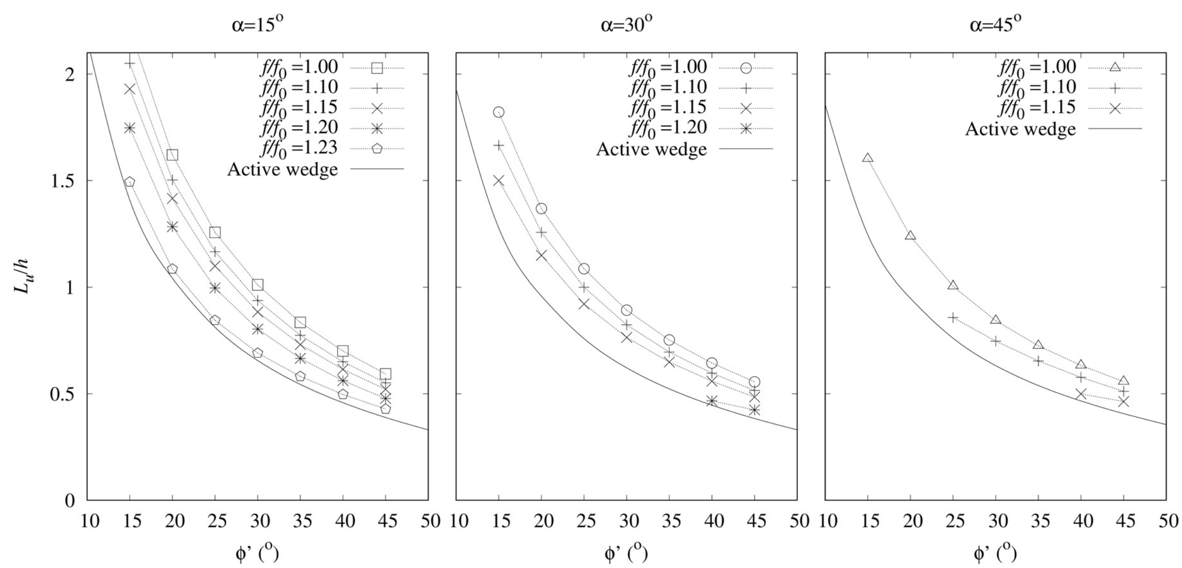

Figure 7 - Values of L_u/h as a function of the soil friction angle, φ', for different ratios f/f_0, different anchor inclinations, for *a/h* = 0.2 and δ/φ' = 2/3.

emphasized in this representation, as is the fact that beyond a certain f/f_0 ratio results can not be obtained.

5. Application of the Finite Element Method

5.1. Introduction

Results presented in the previous section highlighted the effectiveness of the increase of the embedded length of single-anchored retaining walls on the needed anchor length to ensure the overall stability. This was shown using a classical method, Broms' method, which had the versatility to provide these conclusions, which seem logical, but also showed some limitations beyond a certain value of the embedded length. Therefore, a finite element approach was also used for comparison with the limit equilibrium results and for further extending the study of the role of the embedded length of the wall on the overall stability of single-anchored retaining walls.

5.2. Description of the case study

The geometry of the case study presented in section 3 was modelled using the finite element program (Plaxis, 2014). A plane strain two-dimensional model was used. A total excavation depth of 10 m was assumed and an embedded length equal to 3.7 m was considered. The anchor head is at 2 m depth and the anchor is inclined at 15°. The anchor length L_u is 12.45 m; a bond length of 5 m was considered in the calculations and therefore a free length of 9.95 m was used.

The soil was modelled using the Hardening Soil Model (Schanz *et al.*, 1999). This model is based on the hyperbolic relationship between strains and stresses, but is elastoplastic. The yield surface of the model is not fixed in the principal stress space; it can expand due to plastic straining (hardening). The model uses compression hardening to model the evolution of plastic strains due to primary compression, and shear hardening for the plastic strains due to primary deviatoric loading. It uses the theory of plasticity, includes soil dilatancy and a yield cap (Plaxis, 2014).

The model uses three input stiffnesses: the secant triaxial loading stiffness to half of the strength, E_{50}, the triaxial unloading and reloading stifness, E_{ur}, and the oedometer loading stiffness, E_{oed}. These stiffnesses depend on the stress state according to the following equations:

$$E_{50} = E_{50}^{ref}\left(\frac{c'\cos\phi' + \sigma_3'\sin\phi'}{c'\cos\phi' + p^{ref}\sin\phi'}\right)^m \tag{8}$$

$$E_{ur} = E_{ur}^{ref}\left(\frac{c'\cos\phi' + \sigma_3'\sin\phi'}{c'\cos\phi' + p^{ref}\sin\phi'}\right)^m \tag{9}$$

$$E_{oed} = E_{oed}^{ref}\left(\frac{c'\cos\phi' + \sigma_3'\sin\phi'}{c'\cos\phi' + p^{ref}\sin\phi'}\right)^m \tag{10}$$

where ϕ' is the friction angle, c' is the effective cohesion, m is an exponent that expresses the dependence of the soil stiffness on the stress state in the soil, p^{ref} is an isotropic reference stress, usually taken equal to 100 kPa, σ'_1 is the major principal stress and σ'_3 is the minor principal stress. As a default setting, the program considers $E_{ur}^{ref} = 3E_{50}^{ref}$ and $E_{oed} = E_{50}$.

The case study considers an excavation in a homogeneous material, a dry sandy soil. The moist unit weight was set to 20 kN/m^3. A friction angle equal to 30° and a soil dilatancy equal to 0 were adopted. The stiffness parameters adopted intended to model a loose to medium compact sand and were: $E_{50} = E_{oed} = 15000$ kPa and $E_{ur} = 45000$ kPa. Coefficient m was taken equal to 0.5. The at rest earth pressure coefficient, K_0, was considered equal to 0.5.

The wall was modelled using plate elements, considering elastic behavior, with a bending stiffness, *EI*, of 1 x 10^6 kNm^2/m and a null Poisson's ratio, due to the plane strain assumption. The interface between the wall and the soil was simulated using joint elements, on both sides of the wall. The strength and stiffness properties of these elements are defined by the strength reduction factor, $R_{inter} = \tan\delta/\tan\phi'$ (Plaxis, 2014), set as 0.63, which corresponds to a δ/ϕ' ratio of 2/3.

The anchor level was modelled by a combination of a node-to-node anchor (free length) and a geogrid (bond length). The material of node-to-node anchor was assumed linear elastic with a stiffness, *EA*, equal to 56000 kN/m. The bond length was considered linear elastic also, with stiffness equal to 471200 kN/m. The anchor force is equal to 236.8 kN/m (the value determined in section 3).

The calculation consists of an initial stage plus seven construction stages. In stage 0 the initial stresses are generated; in stage 1, the wall is activated (plate and joint elements); in stage 2, the first 3 m of the soil are excavated; in stage 3 the level of anchors is installed and pre-stressed; in the next stages the soil is excavated down to 6 m (stage 4), 8 m (stage 5) and 10 m (final excavation stage). In stage 7 a safety analysis is performed using the c - ϕ reduction feature of the f.e. program, which allows determining the value of ϕ' that causes failure of the soil. The additional displacements that are generated in this stage do not have a physical meaning, but the incremental displacements and the incremental shear strains give an indication of the likely failure mechanism.

5.3. Results

Results obtained in the calculation for the displacements of the wall and of the surface of the supported soil are represented in Fig. 8, for different stages, until the final excavation. Results for the c - ϕ reduction stage are not represented. It can be observed that the initial 3 m excavation causes very small displacements and the effect of pre-stressing the anchor level is clearly seen in the wall displacements and also on the swelling of the soil surface, which is due to the anchor bond and the effect of the anchor force. Subsequent excavation stages cause an increase of the displacements. For the final excavation stage, displacements increase significantly, the horizontal displacements of the wall reaching 0.3% of the total height and the settlements of the surface of the supported soil about half that value.

Figure 9 shows the anchor load changes at each stage. Each excavation stage after anchor activation causes an increase in the anchor load, reaching a maximum of about 18% at the final excavation stage.

In stage 7, after modelling the 10 m excavation, a c - ϕ reduction analysis was performed. The determined value of ϕ' at collapse was 23.85° and the failure mechanism can be inferred from the total displacements presented in Fig. 10. The failure mechanism clearly involves the anchor, showing a typical overall stability mechanism. A passive wedge can be seen in front of the embedded length of the wall.

A comparison with the Brom's mechanism that had been obtained in section 4.2. (Fig. 3) and which is superposed to the one obtained from the numerical calculations shows a relatively good agreement; the main differences are (1) the fact (expected in two-dimensional analysis) that the mechanism from f.e.m. extends to the end of the bond length and does not stop at L_u and (2) the fact that there is a curved shape in the mechanism between the wall toe and

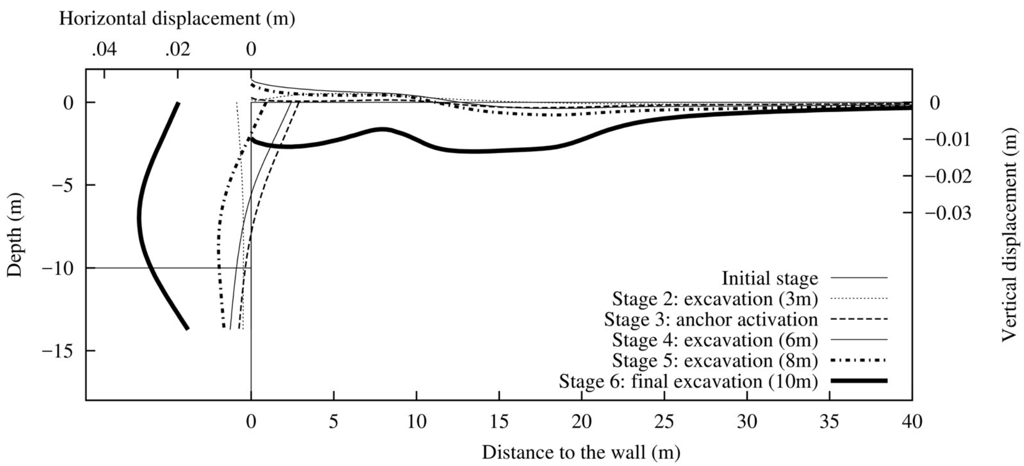

Figure 8 - Horizontal displacements of the wall and settlements of the surface of the supported soil obtained for the numerical case study.

the anchor, which is more realistic (Littlejohn, 1972), whereas Broms' method uses a rectilinear failure surface.

5.4. Parametric analysis

The procedure described in the previous section using the finite element program Plaxis was then repeated for different values of the embedded length ratio, f/h, and for different anchor length ratios, L_u/h. Four ratios f/h (0.31, 0.37, 0.43 and 0.55) were tested, for anchor length ratios L_u/h between 0.63 and 2.00. For all calculations the soil friction angle in the collapse was determined using Plaxis' c - ϕ reduction feature. The results obtained are shown in Fig. 11, where values obtained from Broms' method are also represented.

It can be seen in Fig. 11 that for constant embedded length, greater soil friction angles lead to the need for shorter anchor lengths. This main conclusion was expected and can be drawn from both the numerical results, represented by the points, and Broms' method, represented by the lines. The lines representing results of Broms' method have two zones: a solid line, for cases where f is greater or

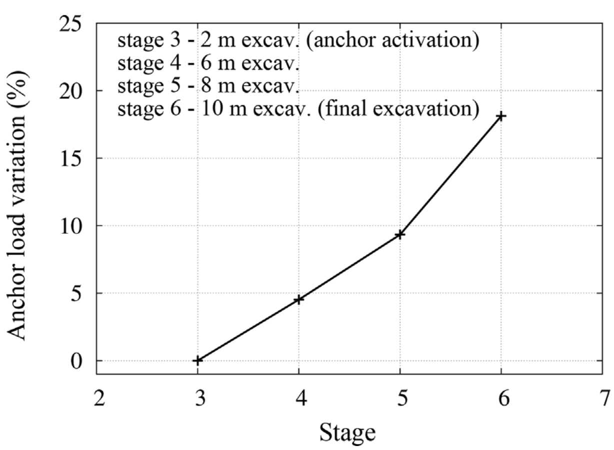

Figure 9 - Anchor load changes obtained for the numerical case study.

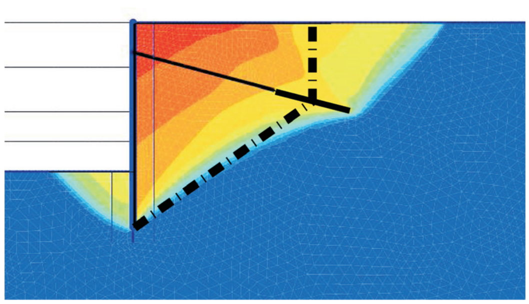

Figure 10 - Failure mechanism inferred from the graphic representation of the total displacements at the c - ϕ reduction stage. Comparison with the mechanism using Broms' method.

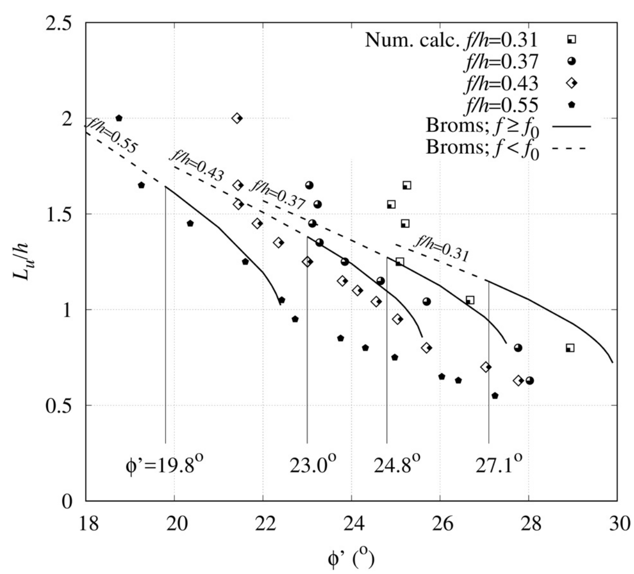

Figure 11 - Limit values of L_u/h as a function of the soil friction angle, ϕ' obtained in the numerical calculations, for different embedded length ratios, f/h; comparison with the results from Broms' method.

equal to f_0 and a dotted line, for f less than f_0. For example, for ϕ' = 24.8°, the ratio f_0/h (the one corresponding to the limit case, as seen in section 3), is 0.37 and so this value of the friction angle separates the dotted line from the solid line for this embedded length ratio. Also, the corresponding value of L_u/h is 1.245, as seen in section 4.2. The other values of these limit soil friction angles are indicated in the figure for the other embedded length ratios. If the numerical results were exactly the same as the analytical calculations, there should be no points to the left of these vertical lines, because the equilibrium of the wall would not be possible for friction angles lower than that limit value.

Naturally, finite element calculations do not correspond exactly to the limit equilibrium model and there are points to the left of those vertical lines, as in the case study of the previous section. But it can also be seen that there is a limit of friction angles (lower than the limit value from limit equilibrium) below which there are no results. This can be seen, for example, for *f*/*h* = 0.31; the limit friction angle from limit equilibrium calculations is 27.1°, but the limit friction angle from the numerical calculations seems to be around 25°. The points, representing the numerical calculations, are thereafter aligned vertically, which means that beyond a certain value of the anchor length L_u/h the friction angle corresponding to failure does not change.

These results can be understood by analysing the mechanisms involved. Some of those mechanisms are represented in Fig. 12. From this figure it can be seen that for a given *f*/*h*, up to a certain anchor length ratio L_u/h, the mechanisms can be recognized as typical overall stability mechanisms. It can also be seen that for these overall stability cases, the mechanisms involve a larger volume of soil for longer anchor lengths. These larger volumes of soil correspond, as has been seen from Fig. 11, to lower soil friction angles at collapse, or, as stated, lower soil friction angles need longer anchors to ensure overall stability. But after a certain anchor length, the mechanisms change and seem to become much simpler, with typical active and passive wedges behind and in front of the wall, respectively (in fact in some cases some transitional mechanisms exist between the two - overall and active/passive). These simpler mechanisms correspond to the condition of the stability of the wall and are no longer dependent on anchor length and therefore correspond to the numerical limit of the soil friction angle mentioned before.

Results presented in Fig. 11, although interesting, can not be used directly either to compare or to complete the type of information that was shown in Fig. 6. To do so, part of the results from Fig. 11, for a chosen value of the soil friction angle (for a certain vertical line) must be repre-

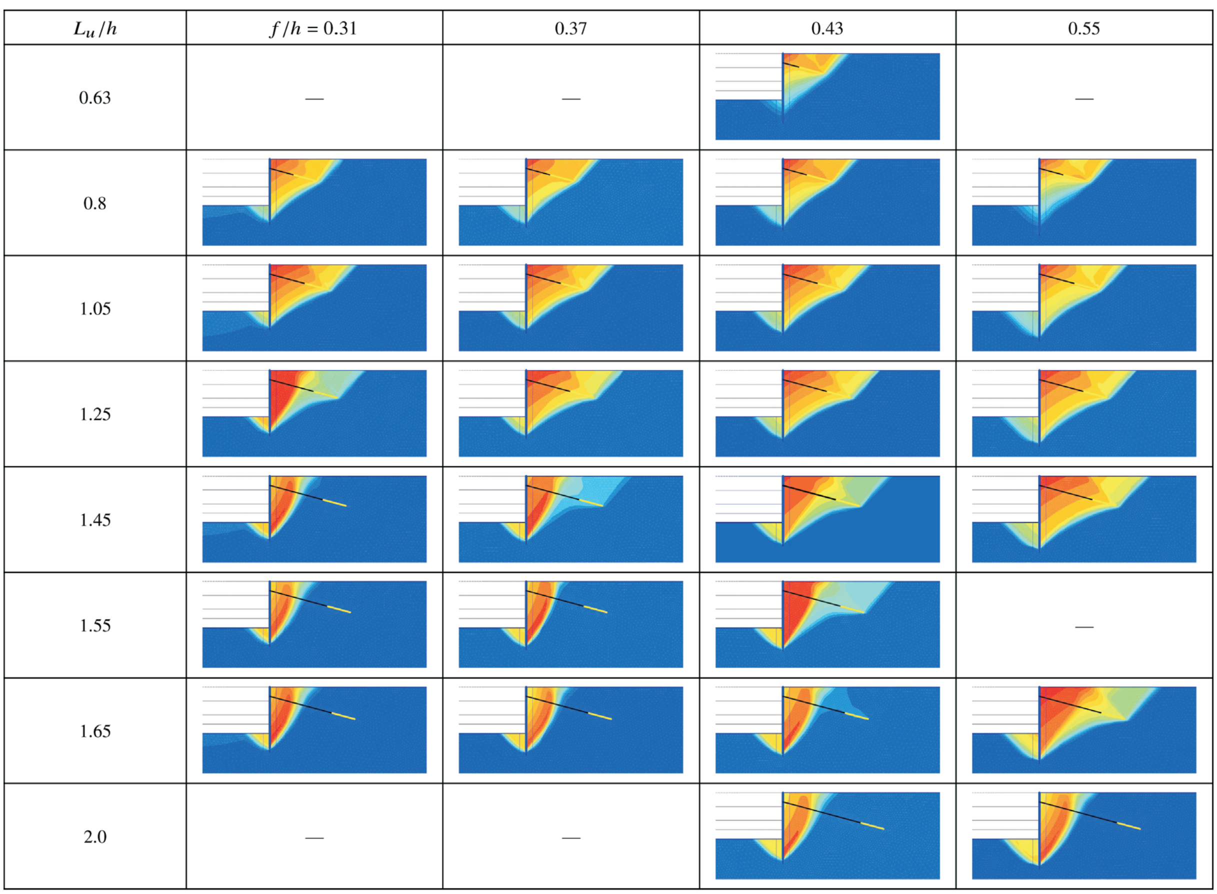

Figure 12 - Mechanisms obtained for most results presented in Fig. 11.

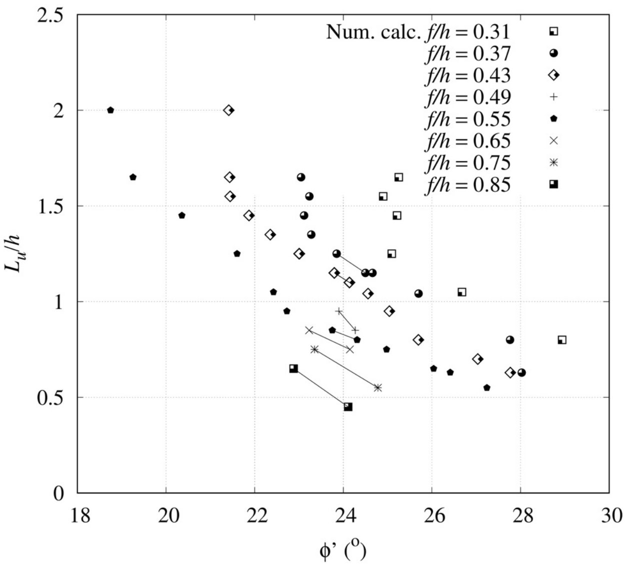

Figure 13 - Limit values of L_u/h as a function of the soil friction angle, ϕ' obtained in the numerical calculations, for different embedded length ratios, *f/h*; points used for interpolation for determining L_u/h for ϕ' = 24° are linked by a solid line.

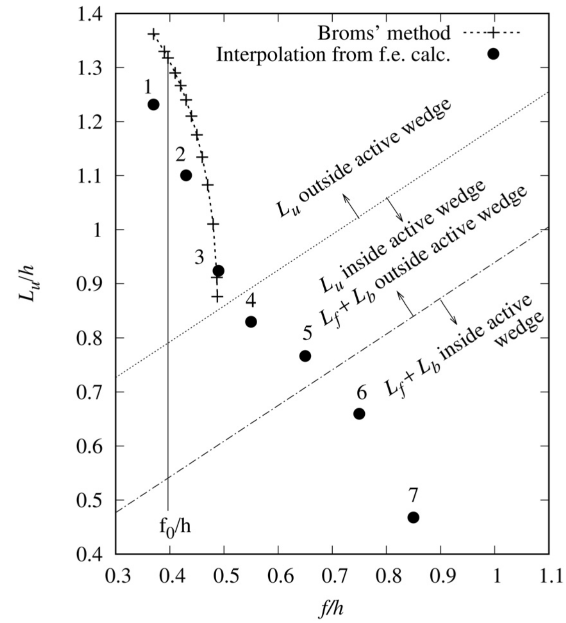

Figure 14 - Limit values of L_u/h obtained by interpolating results determined numerically (as represented in Fig. 13), as a function of *f/h*, for ϕ' = 24°, α = 15°, *a/h* = 0.2 and δ/ϕ' = 2/3.

sented in the same way as in Fig. 6. Taking as an example the value of ϕ' = 24°, a vertical line in Fig. 11 can be drawn and the points on that line or close to it can be used, either directly or by interpolating between two close values of the friction angle in such graphic. As can be seen from Fig. 11, few points would be provided in this way and so some more calculations were needed, using different values of *f/h* and different values of L_u/h and finding collapse values of the friction angle close to 24°. The values of L_u/h were determined by interpolating between those below that value and above it, for the same *f/h* ratio. The points used are represented in Fig. 13, linked by a solid line. This procedure is, of course, fastidious and can not be done systematically for different friction angles. But the case for ϕ' = 24° could be obtained that way and the results are represented in Fig. 14.

Figure 14 also shows the results obtained from Broms' method for the same friction angle, which allows comparison with the numerical results for the range of *f/h* for which Broms' method has solution. It can be seen that the significant decrease of the needed anchor length for small increases of the embedded length that had been observed previously is also present in the numerical calculations. In fact, points 1, 2 and 3 show this behavior, and the values of L_u/h obtained from the numerical calculations are quite similar to the ones obtained from Broms' method. For greater values of *f/h*, as seen before, Broms' method gives no solution (L_u is no longer outside the active wedge) and, as seen, this was part of the reasons for performing the numerical calculations. Numerical results were obtained and continue to show a decrease of the needed anchor length with increasing embedded length. This, however, happens with a significant change in the rate of the increase, with two different zones. In fact, points 4 and 5 show a much lower decrease of L_u/h with the increase of *f/h*; this rate seems to increase after point 5, with points 6 and 7.

The reason for this change seems to be related to the location of the bond length relatively to the active wedge. In fact, it was previously seen that Broms' method had a solution as long as the anchor length L_u was outside the active wedge. There are, therefore, no points obtained from this method below the line that represents the combination of *f/h* and L_u/h where L_u is at the failure surface of the active wedge. In the numerical calculations, however, the bond length to the right of L_u will also play some role in the equilibrium. And so it can be seen that this change in the rate of decreasing L_u/h with *f/h* happens almost exactly when the full anchor length ($L_f + L_b$, *i.e.*, $L_u + L_b/2$) is inside the active wedge.

For *f/h* ratios greater than around 0.85, results from the numerical calculations give collapse values of ϕ' less than 24°. This is expected, as *f/h* = 1.18 is the needed embedded length ratio for a cantilever wall for ϕ' = 24°, using, again, Frank *et al.* (2004) method and a coefficient of 1.2 for the embedded length, which means that for such value of *f/h* the anchor is no longer needed, the f.e.m. leading to a lower value.

It should also be mentioned that all numerical calculations used to obtain Fig. 14 were performed using a total excavation depth of 10 m and a bond length L_b = 5 m. This means that, for some of the lower values of L_u/h ratio adopted in the calculations used for the interpolations, some very small values of L_f had to be used. These values would not be used in practice, although they make sense in

Point in Fig. 14	f/h	L_u/h	"Left" mechanism ($\phi' < 24^o$)	"Right" mechanism ($\phi' > 24^o$)	Broms' mechanism
1	0.37	1.2315	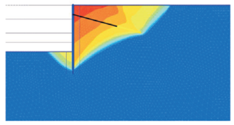 L_u/h = 1.25; ϕ' = 23.85^o	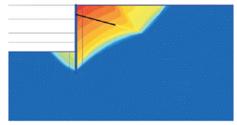 L_u/h = 1.15; ϕ' = 24.66^o	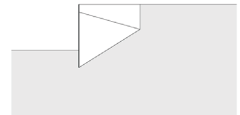 L_u/h = 1.362; ϕ' = 24^o
2	0.43	1.1003	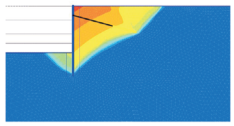 L_u/h = 1.15; ϕ' = 23.80^o	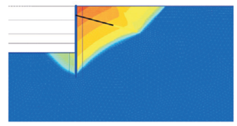 L_u/h = 1.10; ϕ' = 24.14^o	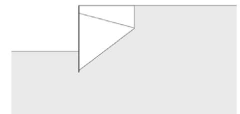 L_u/h = 1.241; ϕ' = 24^o
3	0.49	0.9238	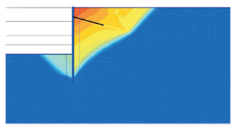 L_u/h = 0.95; ϕ' = 23.90^o	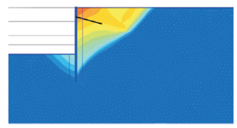 L_u/h = 0.85; ϕ' = 24.27^o	—
4	0.55	0.8298	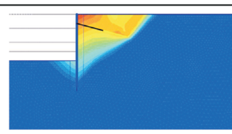 L_u/h = 0.85; ϕ' = 23.75^o	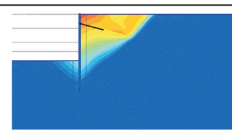 L_u/h = 0.8; ϕ' = 24.31^o	—
5	0.65	0.7665	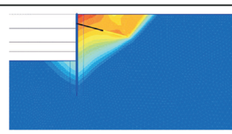 L_u/h = 0.85; ϕ' = 23.23^o	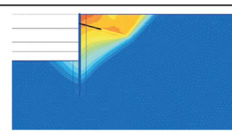 L_u/h = 0.75; ϕ' = 24.15^o	—
6	0.75	0.6596	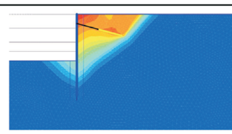 L_u/h = 0.75; ϕ' = 23.35^o	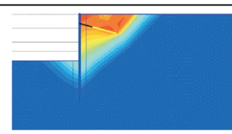 L_u/h = 0.55; ϕ' = 24.78^o	—
7	0.85	0.4678	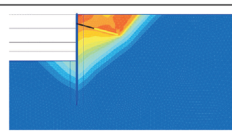 L_u/h = 0.65; ϕ' = 22.88^o	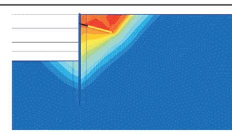 L_u/h = 0.45; ϕ' = 24.11^o	—

Figure 15 - Mechanisms obtained for results presented in Fig. 14 (and results presented in Fig. 13 for interpolation for ϕ' = 24°.

the perspective of the ratios L_u/h if greater values of h were used.

The mechanisms corresponding to the numerical results presented in Fig. 14 are represented in Fig. 15. As the points from Fig. 14 result from interpolation between two numerical calculations, the mechanisms included in Fig. 15 are shown for the two calculations, one on the "left" ($\phi' < 24°$) and the other on the "right" ($\phi' > 24°$). It can be seen that for the same f/h the two mechanisms are quite similar. It can also be observed that as f/h increases the mechanism becomes less typical of the overall stability and more triangular and rotational. The transition between the typical overall stability mechanisms and the triangular seems to correspond to cases 5 and 6.

The main result from these analyses seems to be that a decrease in the needed anchor length with increasing embedded length can indeed be obtained outside the range of validity of Broms' method. However, although possible from a limit state point of view, such solutions can only be practical if reasonable results are also obtained in a serviceability perspective. Such perspective needs to be verified by the designer for each particular case, but nevertheless the solutions for the case studied above can be a guide, if not for specific cases, at least as a way of evaluating if the study of such solutions can make sense.

To do so, results of the displacements obtained for each solution (the result that lead to the collapse friction angle closest to 24° was used) are represented in Fig. 16. Each solution is identified by a different line in this figure and the

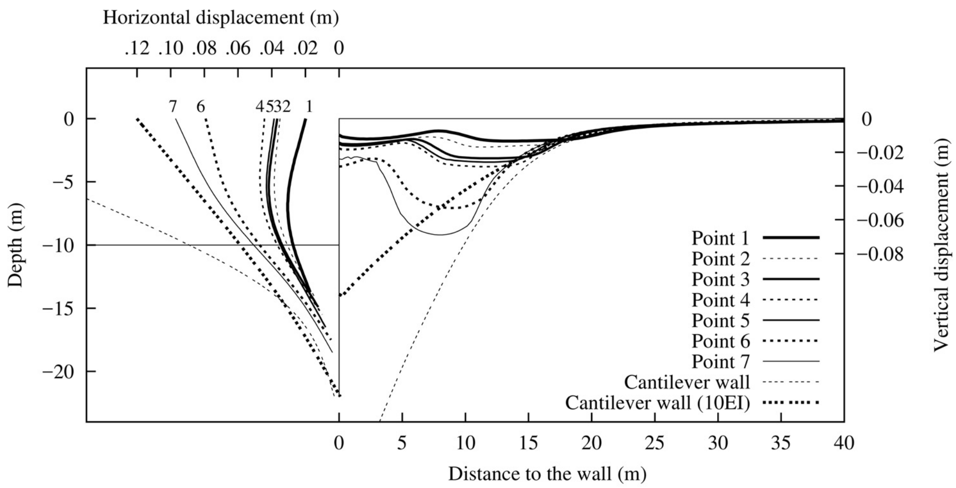

Figure 16 - Settlements and horizontal displacements of the wall for all construction stages for the cases of the points in Fig. 14.

horizontal displacements are also identified by the number corresponding to the points in Fig. 14. Analysis of this figure shows that: (1) the smallest displacements are obtained for case 1, for which no reduction in L_u was performed in exchange for an increase in f; (2) in general, displacements are greater for greater f_0 (and shorter L_u); (3) this trend is not exact for cases 4 and 5; displacements obtained for case 4 are slightly greater than the ones for case 3; (4) cases 2 to 5 show quite similar displacements; they correspond to cases where the bond length is interfering with the active wedges; (5) displacements for cases 6 and 7 are considerably greater than the displacements obtained for the other cases, with maximum horizontal displacements that seem unreasonable, as well as the settlements of the supported soil.

This last remark needs, however, some additional comment. In fact, the stiffness of the wall was kept constant in all calculations, which was considered suitable for comparison purposes. It should be noticed, however, that longer embedded lengths and shorter anchor lengths make the wall closer in its behavior to a cantilever wall. And if a cantilever wall was used for the same situation (a 10 m excavation in the same soil conditions), displacements would indeed be extremely large, as is also represented in Fig. 16, assuming elastic behavior of the wall. A significant part of these displacements are due to the flexibility of the wall, which means that a cantilever wall solution for this situation would need a more rigid structure. This case is also represented in Fig. 16 (marked as 10*EI*, because ten times the flexural stiffness of the previous calculations was assumed) and it can be observed that the displacements are much lower. So, back to comment (5) in the previous paragraph, it seems reasonable, in face of a particular design situation, to study the possibility of combining an increase in f_0 (and the correspondent decrease in L_u) with an increase in the flexural stiffness of the wall, which would to some extent reduce the displacements.

6. Conclusions

The overall stability of single-anchored retaining walls is an important stability verification that can be performed, in most situations, using Broms' method, a classical limit equilibrium method. Its simplicity and versatility allow the analysis of different geometrical and mechanical configurations. One of the parameters involved is the embedded length. A series of analyses using Broms' method showed that a small increase in the embedded length could lead to a significant decrease in the anchor length, which could be useful for economical or technical reasons, in particular in an urban environment, where intalling long anchors may not be possible.

Limitations of Broms' method do not allow the effect to be analysed for significant increases of the embedded length. For long embedded lengths the approach is not possible and a series of finite element calculations was performed. The procedure involved in this approach does not allow a systematic analysis of the problem for a wide range of cases, but it was used for one situation, as a way to evaluate if the increase in the embedded length could indeed be used for reducing anchor length.

Results of those analyses showed that such approach is possible and effective from an overall stability point of view, at a cost of some increase in the displacements, which can most probably be reduced by the increase of the flexural stiffness of the wall.

References

Broms, B.B. (1968). Swedish tieback system for sheet pile walls. Proc. 3rd Budapest Conf. Soil Mech. Found. Eng, pp. 391-403.

Costet, J. & Sanglerat, G. (1975). Cours pratique de Mécanique des Sols, Tome 2. Dunod, Paris, 352 p. In French.

Coulomb, C.A. (1776). Essai sur une application des règles des maximis et minimis à quelques problèmes de statique relatifs à l'architecture. Mem. Acad. Roy., 7, 38 p. In French.

Elton, D.J. & Whitbeck, J.E. (1997). Tieback design and construction. Final Report to the Alabama Highway Research Center. Technical report. Auburn University, Auburn, 72 p.

EN 1997-1 (2004). Eurocode 7, Geotechnical Design, Part 1: General Rules. CEN, European Committee for Standardization, Brussels.

Frank, R.; Bauduin, C.; Driscoll, R.; Kavvadas, M.; Ovesen, N.K.; Orr, T. & Schuppener, B. (2004). Designer's Guide to EN 1997-1 - Eurocode 7: Geotechnical Design - General Rules. Thomas Telford, London, 216 p.

Guerra, N.M.C.; Santos Josefino, C. & Antão, A.N. (2016). Overall stability of anchored retaining structures: revisiting Broms' method. In Lisyuk, M., Ulitsky, V. & Choudhury, D. (eds). Proceedings of two Seminars of TC207 ISSMGE in 2015. Soil-structure Interaction and Retaining Walls. Edinburgh and Pune. TC207, ISSMGE, pp. 25-32.

Hanna, T.H. (1982). Foundations in tension - ground anchors. McGraw-Hill, New York, 570 p.

Jelinek, R. & Ostermayer, H. (1967). Zur Berechnung von Fangedammen und verankerten Stützwänden. Die Bautechnik, 44(6):167-171;203-207. In German.

Kérisel, J. & Absi, E. (1990). Active and Passive Earth Pressure Tables. 3rd ed. Balkema, Rotterdam, 220 p.

Kranz, E. (1953). Über die Verankerung von Spundwänder. Wilhelm Ernst & Sohn, Berlin, 53 p. In German.

Littlejohn, G.S. (1972). Anchored diaphragm walls in sand. Ground Engineering, 5(1):12-17.

Matos Fernandes, M. (1990). Earth Retaining Structures. FEUP, Porto. In Portuguese.

Müller-Breslau, H. (1906). Erddruck auf Stützmauern. Kroener, Stuttgart. In German.

Plaxis (2014). Plaxis 2D Manual. Brinkgreve *et al.* (eds). Delft.

Puller, M. (1996). Deep excavations. A practical manual. Thomas Telford, London, 448 p.

Ranke, A. & Ostermayer, H. (1968). Beitrag zur Stabilitätsuntersuchung mehrfach verankerter Baugrubenumschließungen. Die Bautechnik, 45(10):341-350. In German.

Santos Josefino, C.; Guerra, N.M.C. & Antão, A.N. (2014). Review of Kranz's and Brom's methods applied to single anchored walls: preliminary results. In Proceedings of the 14th National Geotechnical Conference, Covilhã, UBI, April 6-9. Published in CD. In Portuguese.

Schanz, T.; Vermeer, P. & Bonnier, P. (1999). The hardening-soil model: formulation and verification. In: Beyond 2000 in Computational Geotechnics. Balkema, Rotterdam, pp. 281-290.

Schnabel Foundation Company (1996). Draft final report - ground anchor walls: Research results and recommendations. Technical report, US Department of Transportation, Federal Highway Admnistration.

A Sole Empirical Correlation Expressing Strength of Fine-Grained Soils - Lime Mixtures

N.C. Consoli, E. Ibraim, A. Diambra, L. Festugato, S.F.V. Marques

Abstract. This paper advances understanding of the key parameters controlling unconfined compressive strength (q_u) of lime stabilized fine-grained soils by considering distinct specimen porosities (η), different lime types and contents and several curing temperatures and time periods. A sole empirical relationship is proposed establishing the normalized unconfined compression strength for lime stabilized fine-grained materials considering all porosities, lime contents, curing temperatures and curing periods studied. From a practical point of view, this means that a very limited number of unconfined compression tests on specific lime stabilized fine-grained material specimens molded with a given lime type and amount, porosity, moisture content and cured for a given time period at a particular temperature, should be sufficient to estimate the strength for an entire range of porosities and lime contents at any given condition. Examples of the practicality of the proposed relationship are presented.
Keywords: normalization, porosity, lime, strength, fine grained soils, porosity/lime index.

1. Introduction

Previous studies of fine-grained materials-lime mixtures (Consoli *et al.*, 2011, 2014a,b and 2015) have shown that their behavior is complex, and affected by many factors, such as grain size distribution of the soil, lime type and content, molding moisture content, porosity of the material, and curing temperature and time period. Consoli *et al.* (2009) were the first to establish a unique dosage methodology based on rational criteria where the porosity/lime index plays a fundamental role in the assessment of the target unconfined compressive strength. This study explores the influence of the amount of lime and the porosity on the unconfined compressive strength (q_u) of various fine-grained materials. A normalization was searched dividing every single strength value (for each material studied) by the unconfined compressive strength corresponding to a specific porosity/lime index, as a result of which a unique power law function was obtained quantifying the influence of the amounts of lime, porosity, curing time and temperature in the assessment of q_u of fine-grained materials-lime mixtures. From a practical point of view, this means that carrying out a limited number of unconfined compression tests on specimens of the studied fine-grained materials molded with lime and cured for any time period, should allow the prediction of the unconfined compressive strength for an entire range of porosities and lime contents.

2. Experimental Program

The experimental program has been carried out in two parts. First, the properties of the several fine-grained materials were characterized. Then a number of unconfined compression tests were carried out for fine-grained materials - lime blends considering different amounts of lime, up to five dry unit weights varying from low to high density values, up to four moisture contents, curing temperatures and distinct curing time periods (from 1 to 360 days of curing).

2.1. Materials

Several fine-grained materials with distinct characteristics were considered in the present research, such as non-plastic and low plasticity soils, as well as industrial by-products such as powdered rock obtained from a cutting rock place and coal fly ash from a coal thermoelectric power plant. The physical properties of the materials are presented in Table 1. Eight different individual fine-grained materials or combinations between them were used as host matrix: dispersive clay, clayey sand (BRS), BRS + 25% powdered rock, BRS + 12.5% coal fly ash, BRS + 25% coal fly ash, coal fly ash, clayey soil from Italy and sulphated clay from Paraguay. The percentages of powdered rock and coal fly ash are calculated by mass of the BRS soil.

Nilo Cesar Consoli, Ph.D., Full Professor, Departamento de Engenharia Civil, Universidade Federal do Rio Grande do Sul, Porto Alegre, RS, Brazil. E-mail: consoli@ufrgs.br.
Erdin Ibraim, Ph.D., Associate Professor, Department of Civil Engineering, University of Bristol, Bristol, UK. E-mail: erdin.ibraim@bristol.ac.uk.
Andrea Diambra, Ph.D., Associate Professor, Department of Civil Engineering, University of Bristol, Bristol, UK. E-mail: andrea.diambra@bristol.ac.uk.
Lucas Festugato, D.Sc., Associate Professor, Departamento de Engenharia Civil, Universidade Federal do Rio Grande do Sul, Porto Alegre, RS, Brazil. E-mail: lucas@ufrgs.br.
Sérgio Filipe Veloso Marques, D.Sc., Lecturer, Departamento de Engenharia Civil, Universidade Federal do Rio Grande do Sul, Porto Alegre, RS, Brazil. E-mail: smarques@ufrgs.br.
Submitted on November 19, 2016; Final Acceptance on June 27, 2017; Discussion open until December 29, 2017.

Table 1 - Physical properties of the soil samples.

Soil type	Dispersive clay	Clayey sand (BRS)	Powdered rock	Coal fly ash	Clayey soil from Italy	Sulphated clay from Paraguay
Liquid limit (%)	43	23	28	-	40	33
Plastic limit (%)	19	13	20	-	20	17
Plasticity index (%)	24	10	8	Non-plastic	20	16
Unit weight of solids - (γs_s) (kN/m^3)	27.4	26.4	33.3	21.6	26.7	26.9
Coarse sand (2.0 mm < diameter < 4.75 mm) (%)	-	-	-	1.0	-	-
Medium sand (0.425 mm < diameter < 2.0 mm) (%)	-	16.1	1.9	4.0	-	1.0
Fine sand (0.075mm < diameter < 0.425mm) (%)	7.0	45.5	38.4	15.0	3.0	14.0
Silt (0.002 mm < diameter < 0.075 mm) (%)	59.0	33.4	57.5	78.0	58.0	52.0
Clay (diameter < 0.002 mm) (%)	34.0	5.0	2.2	2.0	39.0	33.0
Mean particle diameter, D_{50} (mm)	0.005	0.12	0.03	0.015	0.012	0.06
USCS class	CL	SC	CL	ML	CL	CL

Quicklime [CaO - product of calcination of limestone, consists of the oxides of calcium], dolomitic and calcitic hydrated lime [$Ca(OH)_2$ - manufactured by treating quicklime with sufficient water to satisfy its chemical affinity for water, thereby converting the oxides to hydroxides] and calcitic carbide lime [$Ca(OH)_2$ - a by-product of the manufacture of acetylene gas] were used as binders. The combinations host material - binder used are presented in Table 2.

2.2. Methods

2.2.1. Molding and curing of specimens

For the unconfined compression tests, cylindrical specimens 50 mm in diameter and 100 mm high were used. Given a certain amount of fine-grained material (enough for molding a specimen), the amount of lime for each mixture was calculated based on the mass of dry fine-grained material. A target dry unit weight for a given specimen was then established through the dry mass of fine-grained materials-lime divided by the total volume of the specimen. As a general procedure, in order to keep the dry unit weight of the specimens constant with increasing lime content, an equivalent amount of the fine-grained material was replaced by lime. Porosity (η) is defined as the ratio of voids (in volume) over the total volume of the specimen and as shown by Eq. 1, it is a function of dry unit weight (γ_d) of the blend, lime content (L) and the unit weight of solids of host material (γs_s - see Table 1) and lime (γs_L - see Table 2) respectively

$$\eta = 100 - 100\left\{\left[\frac{\gamma_d}{1+\left(\frac{L}{100}\right)}\right]\left[\frac{1}{\gamma s_s} + \frac{\frac{L}{100}}{\gamma s_L}\right]\right\} \qquad (1)$$

After each fine-grained material and lime was weighed, both materials were mixed until the mixture acquired a uniform consistency. Tap water between 13 and 18% by dry mass of host fine-grained material was then added, continuing the mixing process until a homogeneous paste was created. The specimen was then constructed in three layers each layer being statically compacted inside a cylindrical split mold, so that each layer reached the prescribed dry unit weight. In the process, the top of each layer was slightly scarified. After the molding, the specimen was immediately extracted from the split mold and its weight, diameter and height measured with accuracies of about 0.01 g and 0.1 mm, respectively. The specimens were cured in a humid room at specific temperatures (see Table 2) and relative humidity above 95%. The specimens were considered suitable for testing if they met the following tolerances: (i) *Dry unit weight* (γ_d): degree of compaction between 99% and 101% (the degree of compaction being defined as the value obtained in the molding process divided by the target value of γ_d); and (ii) *Dimensions*: diameter to within ± 0.5 mm and height ± 1 mm.

2.2.2. Unconfined compression tests

Unconfined compression tests have been systematically used in most experimental programs reported in the literature in order to verify the effectiveness of the lime stabilization process or to explore the importance of influencing factors on the strength of reinforced soils. This test is largely used in practice for material strength characteriza-

Table 2 - Details of molding, curing and normalization data.

Soil type	Lime type	Unit weight of solids of lime γs_L (kN/m³)	Lime contents L (%)	Molding dry unit weight γ_d (kN/m³)	w (%)	Curing temperature (°C)	Curing periods (days)	Normalization Index (∇)	Average q_u (kPa) for normalization
Clayey sand (BRS)	Dolomitic hydrated lime	24.9	3, 5, 7, 9 and 11	16.0, 17.0, 18.0 and 18.8	14	23	90, 180 and 360	$\frac{\eta}{L_{iv}^{0.12}} = 30$	250.3, 267.5 and 580.7 kPa, respectively for 90, 180 and 360 days of curing
Dispersive clay	Dolomitic hydrated lime	26.0	3, 5 and 7	16.0, 17.5 and 19.0	13	21	7, 28 and 60	$\frac{\eta}{L_{iv}^{0.12}} = 30$	1070, 1535.4 and 2010.5 kPa, respectively for 7, 28 and 60 days of curing
BRS + 25% Powdered Rock	Dolomitic hydrated lime	24.9	3, 5, 7, 9 and 11	16.0, 17.0, 18.0 and 18.8	14	23	28, 90 and 360	$\frac{\eta}{L_{iv}^{0.12}} = 30$	444.4, 873.7 and 1685.6 kPa, respectively for 28, 90 and 360 days of curing
BRS + 12.5% Coal Fly Ash	Dolomitic hydrated lime	24.9	3, 5, 7 and 9	14.0, 15.0, 16.0 and 17.0	14	23	28, 60, 90, 180 and 360	$\frac{\eta}{L_{iv}^{0.12}} = 30$	1206.7, 1993.4, 2649.8, 3142.3 and 2449.9 kPa, respectively for 28, 60, 90, 180 and 360 days of curing
BRS + 25.0% Coal Fly Ash	Dolomitic hydrated lime	24.9	3, 5, 7 and 9	14.0, 15.0, 16.0 and 17.0	14	23	28, 60, 90, 180 and 360	$\frac{\eta}{L_{iv}^{0.12}} = 30$	403.5, 3631.9, 6166.2, 6728.7 and 7083.0 kPa, respectively for 28, 60, 90, 180 and 360 days of curing
Coal fly ash	Carbide lime	21.2	5, 10 and 15	11.0, 12.0 and 13.0	18	23, 40, 60 and 80	1, 3, 7 and 14	$\frac{\eta}{L_{iv}^{0.12}} = 30$	→ 1491.9 and 2383.0 kPa (23 °C) and 7 and 14 days of curing → 1397.3, 3341.8 and 10562.8 kPa (40 °C) and 1, 3 and 7 days of curing → 5005.9, 12216.1 and 26475.4 kPa (60 °C) and 1, 3 and 7 days of curing → 8852.6, 11540.8 and 14 970.2 kPa (80 °C) and 1, 3 and 7 days of curing
Clayey soil from Italy	Quicklime	33.7	2 to 4	16.0 to 18.0	Not known	23	7	$\frac{\eta}{L_{iv}^{0.12}} = 32.6$	870.0
Sulphated clay from Paraguay	Calcitic Lime	24.1	4, 6 and 8	14.5, 15.5 and 16.8	15	23	90 and 180	$\frac{\eta}{L_{iv}^{0.12}} = 23.6$ and $\frac{\eta}{L_{iv}^{0.12}} = 23.2$, respectively for 90 and 180 days of curing	1509 and 2534 kPa, respectively for 90 and 180 days of curing

tion. The tests presented in this study followed standard ASTM C39 (ASTM, 2010).

An automatic loading machine with maximum capacity of 50 kN and a proving ring with capacity of 10 kN and resolution of 0.005 kN were used for the unconfined compression tests. Before carrying out testing, the specimens were submerged in a water tank for 24 h for saturation to minimize suction (Consoli *et al.*, 2012). The water temperature was controlled and maintained at 23 °C ± 2 °C. Immediately before the test, the specimens were removed from the water tank and dried superficially with an absorbent cloth. Then, the unconfined compression test was carried out and the maximum load recorded. Because of the typical scatter of data for unconfined compression tests, for each point, three specimens were tested. The testing program was chosen in such a way as to isolate, separately, the influences of the lime content, dry unit weight and porosity/lime index. The specimen molding conditions (lime contents, dry unit weights, moisture content and curing time period and temperature) of all tested fine-grained material are presented in Table 2.

3. Results

3.1. Effect of the lime content, dry unit weight and porosity/lime index on compressive strength

The unconfined compressive strength (q_u) variation with lime content (L) for a dispersive clay treated with 3, 5 and 7% of hydrated lime, water content of 13% and 28 days of curing period is shown in Fig. 1. It can be seen that an increase of both lime content and dry unit weight produces an increase of q_u. Other four fine-grained materials (clayey sand (BRS), BRS + 25% powdered rock, BRS + 12.5% coal fly ash, BRS + 25.0% coal fly ash) treated with hydrated lime and cured over periods varying from 7 to 360 days and a coal fly ash material treated with calcitic carbide lime (Consoli *et al.*, 2014b) presented similar behavioral trends.

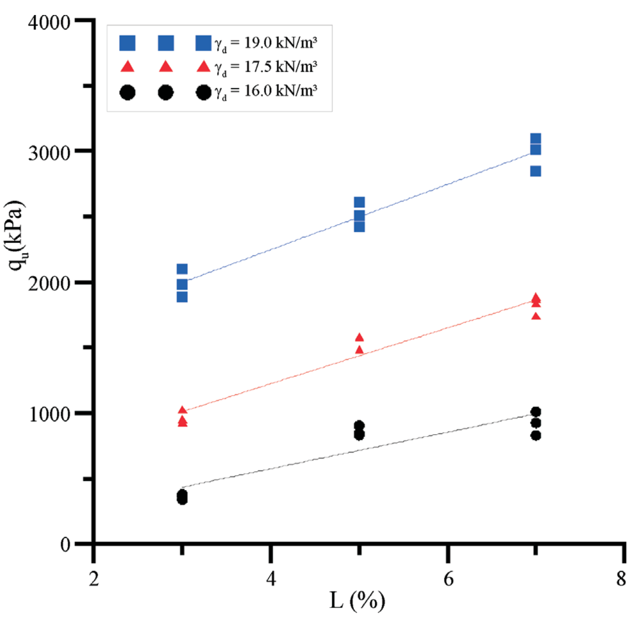

Figure 1 - Unconfined compressive strength (q_u) of a dispersive clay with hydrated lime content (L) for 28 days as curing period and 21 °C as curing temperature.

The typical unconfined compressive strength data shown in Figure 1, can further be presented as function of an adjusted porosity/lime index, $\eta/(L_{iv})^C$, [expressed as porosity (η) divided by the volumetric lime content (L_{iv}), the latter given as a percentage of lime volume regarding total volume (Consoli *et al.*, 2011)]:

$$q_u = A\left[\frac{\eta}{L_{iv}^c}\right]^{-B} \tag{2}$$

where C, A and B are material dependent parameters. Consoli *et al.* (2011) found that for the clayey sand soil (BRS) treated with hydrated lime contents between 3 and 11% and cured for 360 days at 23 °C temperature, the C coefficient is 0.12. A similar C = 0.12 value appears to provide the best fit exponent for all fine-grained materials treated with lime types studied herein, as well as for all curing temperatures and curing periods, as shown in Fig. 2.

3.2. Sole correlation determining strength

Dividing Eq. 2 by an arbitrary specific value of the unconfined compression strength, corresponding to a given value of the adjusted porosity/lime index, $\frac{\eta}{L_{iv}^{0.12}} = \nabla$, leads to:

$$\frac{q_u}{q_u\left\{\frac{\eta}{L_{iv}^{0.12}} = \nabla\right\}} = \frac{A\left[\frac{\eta}{L_{iv}^{0.12}}\right]^{-B}}{A[\nabla]^{-B}} = [\nabla]^B\left[\frac{\eta}{L_{iv}^{0.12}}\right]^{-B} \tag{3}$$

If a fixed $\left\{\frac{\eta}{L_{iv}^{0.12}}\right\} = \nabla = 30$ value is chosen, (any ∇ value could be selected, and ∇ = 30 covers all fine-grained materials - lime mixtures studied), then a sole function can be obtained through a normalization process of the experimental unconfined compressive strength (q_u) values of all the studied fine-grained materials - lime blends with respect to the corresponding specific value of q_u at $\left\{\frac{\eta}{L_{iv}^{0.12}}\right\} = \nabla = 30$, to give:

$$\frac{q_u}{q_u\left\{\frac{\eta}{L_{iv}^{0.12}} = 30\right\}} = 4.60\times10^5\left[\frac{\eta}{L_{iv}^{0.12}}\right]^{-3.84} \tag{4}$$

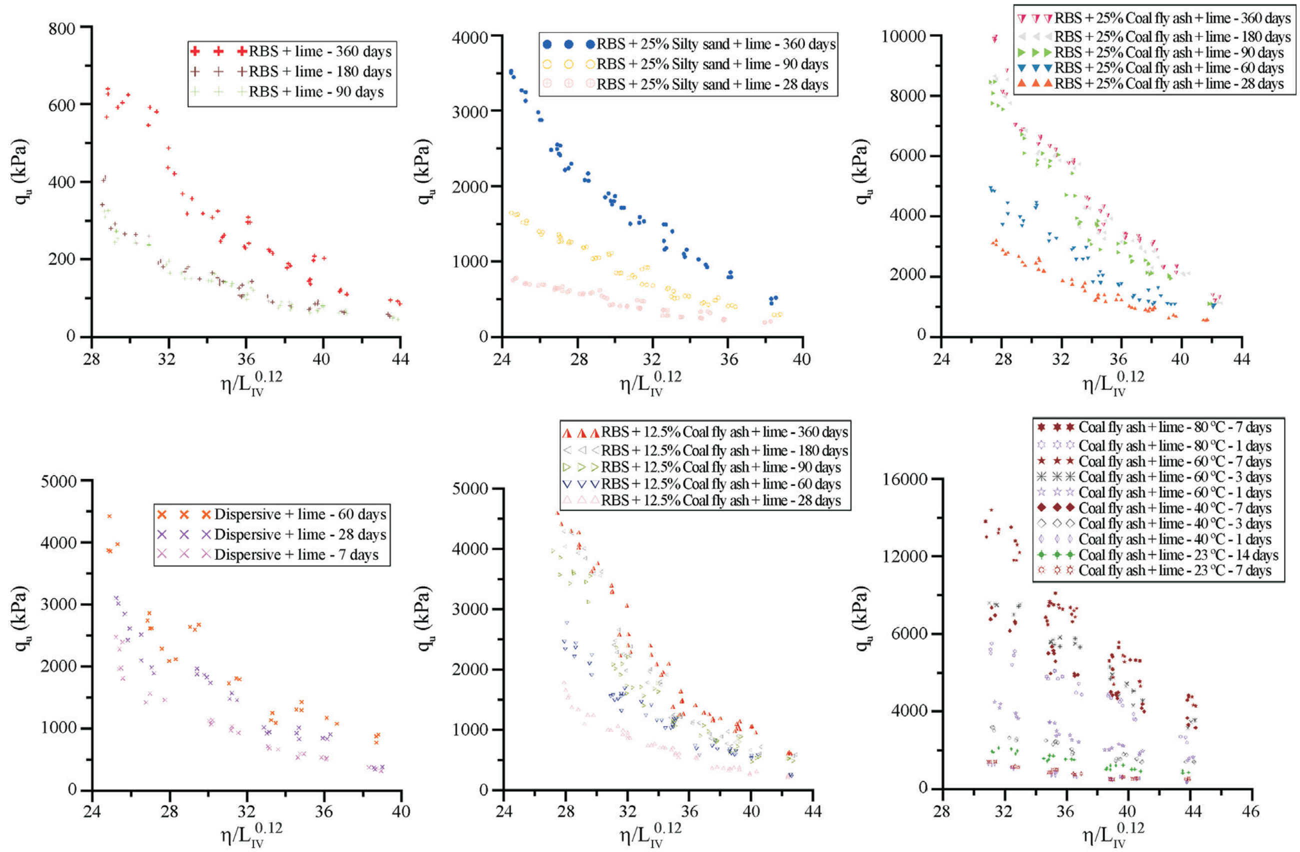

Figure 2 - Variation of unconfined compressive strength (q_u) with adjusted porosity/lime index for all studied fine-grained soils treated with distinct lime amounts and types considering distinct curing temperatures (varying from 21 °C to 80 °C) and time periods (varying from 1 to 360 days).

The last column of Table 2 presents the q_u values used for the normalization process for each material and curing periods, while Fig. 3 reassembles all the experimental results shown in Fig. 2, including also Eq. 4.

Inevitably it can be observed the scatter of data around Eq. 4, but from a practical point of view, the meaning of relations like those given by Eqs. 3 and 4 is that carrying out a limited number of tests (in reality three identical specimens are tested in order to obtain a good representativity) with a specific fine-grained material, a given lime type and any given curing temperature and period, one could predict the effect of varying binder content and porosity across a wide range.

The validation for this unique relationship establishing the compressive strength was done considering two distinct soils: a clayey soil from Italy (Consoli *et al.*, 2015) and a sulphated clay from Paraguay (Bittar, 2017). The physical properties of both soils were presented in Table 1. The former soil was treated with quicklime and the latter was treated with hydrated calcitic lime Curing time period was short (7 days) for the Italian soil and long (90 and 180 days) for the Paraguayan soil, validating the relationship use for distinct soils and a significant range of curing time periods.

Regarding the clayey soil from Italy, data were taken from the average of specimens with $\dfrac{\eta}{L_{iv}^{0.12}} = \nabla = 32.6$ and $q_u \left\{ \dfrac{\eta}{L_{iv}^{0.12}} = 32.6 \right\} = 870$ kPa (see Table 2 for details). Using the above values in Eq. 3, it results:

$$q_u\,(\text{kPa}) = 5.63 \times 10^8 \left[\frac{\eta}{L_{iv}^{0.12}} \right]^{-3.84} \tag{5}$$

Varying from 32.0 to 42.0 in Eq. 5, a curve is drawn in Fig. 4 and plotted together with lab-testing data points from Consoli *et al.* (2015) for clayey soil of low plasticity and quicklime blends under curing period of 7 days. It can be observed in Fig. 4 that the curve obtained using Eq. 5 is describing the laboratory testing data with good accuracy.

Concerning the sulphated clay from Paraguay, information was taken from the average of specimens with $\dfrac{\eta}{L_{iv}^{0.12}} = \nabla = 23.6$ for 90 days of curing and

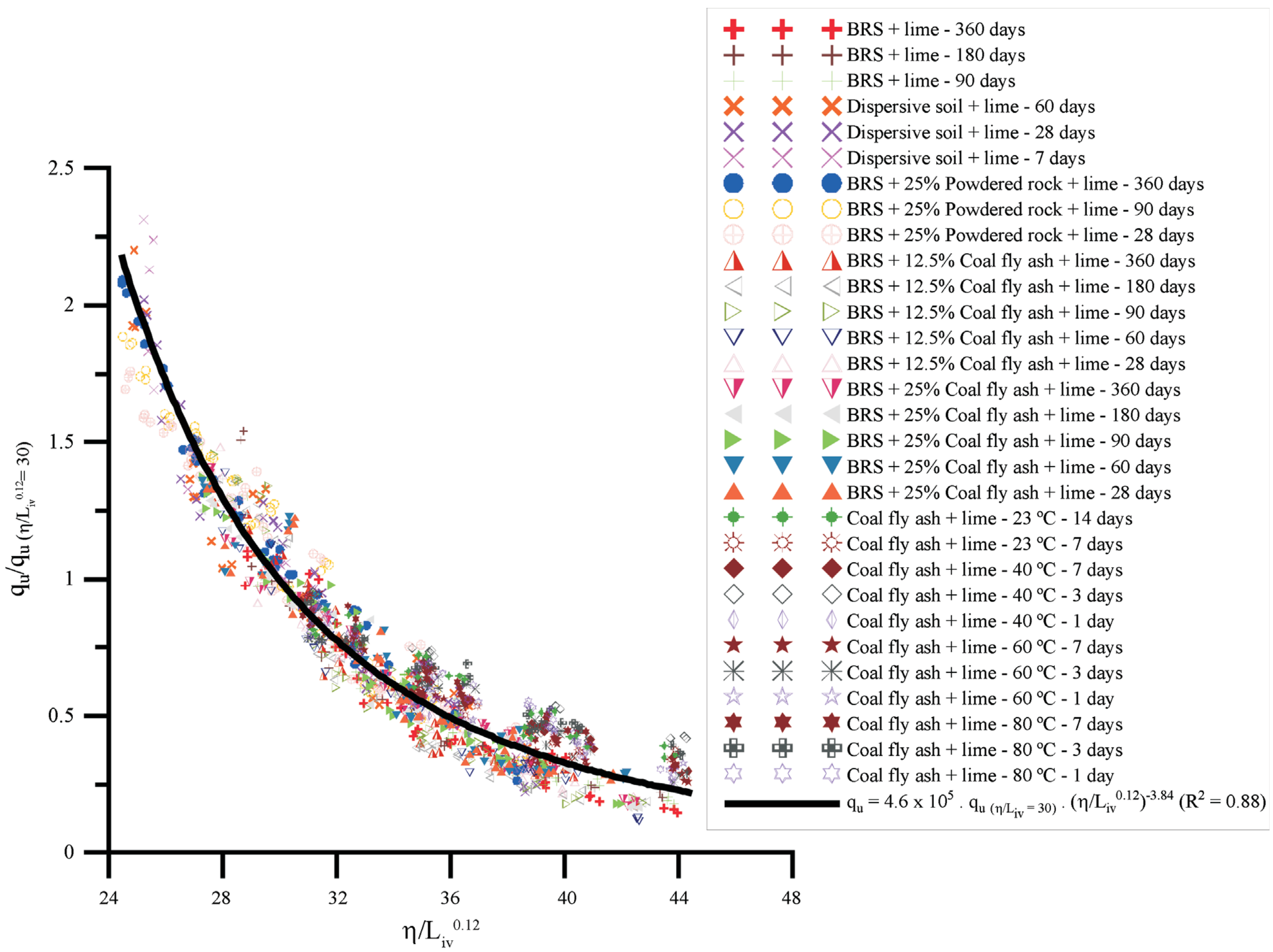

Figure 3 - Normalization of q_u (for the whole range of $\eta/L_{iv}^{0.12}$) dividing by q_u at $\eta/L_{iv}^{0.12}$ = 30 considering distinct curing temperatures (varying from 21 °C to 80 °C) and time periods (varying from 1 to 360 days).

$q_u\left\{\frac{\eta}{L_{iv}^{0.12}} = 23.6\right\} = 1509$ kPa and $\frac{\eta}{L_{iv}^{0.12}} = \nabla = 23.2$ for 180 days of curing and $q_u\left\{\frac{\eta}{L_{iv}^{0.12}} = 23.2\right\} = 2534$ kPa (see Table 2 for details). Using the above values in Eq. 3, it results:

$$q_u\,(\text{kPa}) = 2.80 \times 10^8 \left[\frac{\eta}{L_{iv}^{0.12}}\right]^{-3.84} \tag{6}$$

$$q_u\,(\text{kPa}) = 4.46 \times 10^8 \left[\frac{\eta}{L_{iv}^{0.12}}\right]^{-3.84} \tag{7}$$

Varying $\left[\frac{\eta}{L_{iv}^{0.12}}\right]^{-3.84}$ from 22.0 to 37.0 in Eqs. 6 and 7, respectively for 90 and 180 days of curing, curves were drawn in Fig. 5 together with lab-testing data points from Bittar (2017) for sulphated clay from Paraguay and hydrated calcitic lime blends. It can be observed in Fig. 5 that the curves obtained using Eqs. 6 and 7 are relating the laboratory testing data with sound accurateness.

4. Conclusions

From the data and analysis presented in this manuscript the following conclusions can be drawn:

- Taking advantage of the fact that an exclusive correlation shape expresses q_u *vs.* $\eta/(L_{iv})^{0.12}$, as well as of a normalization of the data by dividing the values of q_u by the value of strength of a specific $\eta/(L_{iv})^{0.12}$ [see Eq. 3] for all fine-grained materials-lime mixtures studied herein considering distinct moisture contents, porosities, amounts of lime, curing temperatures and periods studied, it was possible to establish and validate a sole relationship establishing strength of fine-grained soils with distinct characteristics (grain size distribution, plasticity index), distinct curing temperatures and curing periods up to 360 days, performing well in all studied conditions.

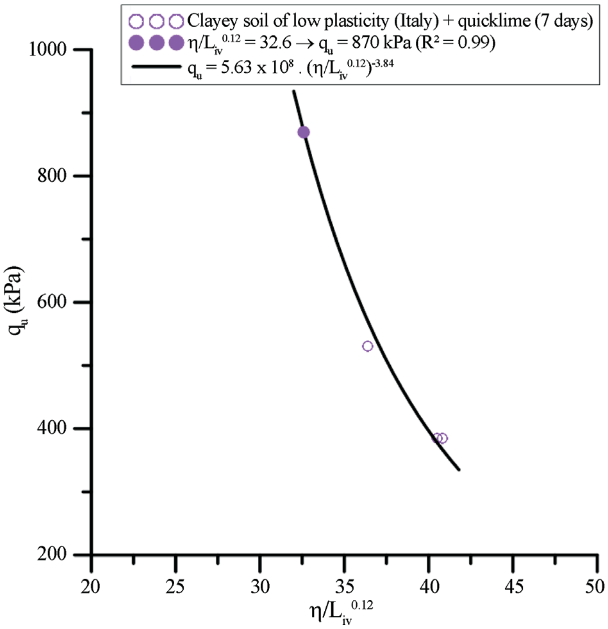

Figure 4 - Curve obtained using Eq. 6 and lab-testing data from Consoli *et al.* (2015) for clayey soil of low plasticity from Italy - quicklime mixtures under curing period of 7 days.

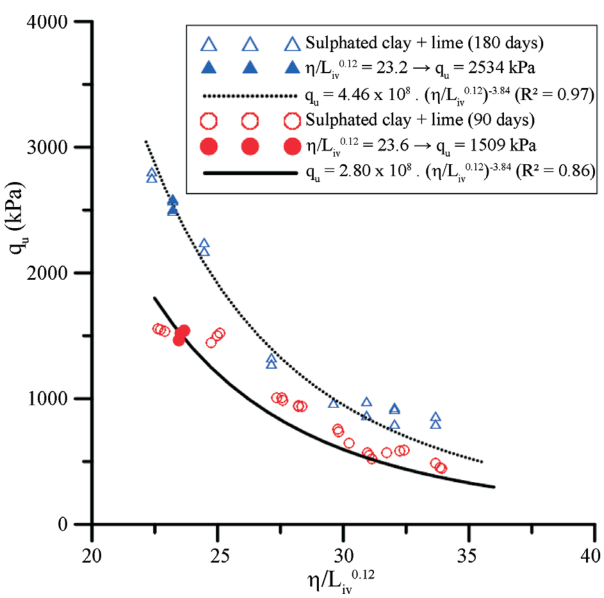

Figure 5 - Curve obtained using Eq. 6 and lab-testing data after Bittar (2017) for sulphated clay - hydrated lime mixtures for curing periods of 90 and 180 days.

- From a practical viewpoint, this means that carrying out only a limited number of unconfined compression tests (in reality three identical specimens, in order to have a better representation of the average q_u value) with a specimen molded with a specific binder and cured for a given time period, allows the establishment of an equation that controls the strength of a fine-grained soil-lime blend for distinct porosities and lime contents.

Acknowledgments

The authors wish to express their gratitude to Edital FAPERGS/CNPq 12/2014 - PRONEX (Project # 16/2551-0000469-2) for the financial support to the research group.

References

ASTM (2010). Standard Test Method for Compressive Strength of Cylindrical Concrete Specimens. ASTM C 39-10, West Conshohocken, Philadelphia.

Bittar, E. (2017). Field and Laboratory Study of the Mechanical Behavior of Sulphated Soil Stabilized with Lime. M.Sc. Dissertation, PPGEC-UFRGS, Porto Alegre, 232 p.

Consoli, N.C.; Lopes, L.S. Jr. & Heineck, K.S. (2009). Key parameters for the strength control of lime stabilized soils. Journal of Materials in Civil Engineering, 21(5):210-216.

Consoli, N.C.; Lopes Jr., L.S.; Prietto, P.D.M.; Festugato, L. & Cruz, R.C. (2011). Variables controlling stiffness and strength of lime-stabilized soils. Journal of Geotechnical and Geoenvironmental Engineering, 137(6):628-632.

Consoli, N.C.; da Fonseca, A.V.; Silva, S.R.; Cruz, R.C. & Fonini, A. (2012). Parameters controlling stiffness and strength of artificially cemented soils. Géotechnique, 62(2):177-183.

Consoli, N.C.; Lopes Jr., L.S., Consoli, B.S. & Festugato, L. (2014a). Mohr-Coulomb failure envelopes of lime-treated soils. Géotechnique, 64 (2):165-170.

Consoli, N.C.; Rocha, C.G. & Saldanha, R.B. (2014b). Coal fly ash - Carbide lime bricks: An environment friendly building product. Construction and Building Materials, 69:301-309.

Consoli, N.C.; Lopes Jr., L.S.; Consoli, B.S.; Festugato, L.; Di Sante, M.; Fratalocchi, E. & Mazzieri, F. (2015). Mohr-Coulomb failure envelopes of lime-treated soils (Discussion & Closure paper). Géotechnique, 65(10):866-868.

List of Symbols

D_{50}: mean effective diameter
L: lime content (expressed in relation to mass of dry soil)
L_{iv}: volumetric lime content (expressed in relation to the total specimen volume)
q_u: unconfined compressive strength
R^2: coefficient of determination
η: porosity
$\frac{\eta}{L_{iv}^{0.12}}$: adjusted porosity/lime index
γ_d: dry unit weight of the blend
γs_L: unit weight of lime
γs_s: unit weight of fine-grained material
w: moisture content

On the Durability and Strength of Compacted Coal Fly Ash-Carbide Lime Blends

N.C. Consoli, R.B. Saldanha, J.F. Novaes, H.C. Scheuermann Filho

Abstract. Present investigation intends to examine the mechanical behaviour of compacted coal fly ash - carbide lime mixes to assess their potential use as a sub-base/base material for low volume roads. This study plans to compute the impact of carbide lime content and dry density on the properties (durability and strength) of compacted coal fly ash - carbide lime blends. Its main significant addition to knowledge is quantifying the accumulated loss of mass (*ALM*) after wetting/drying cycles, tensile (q_t) and compressive strength (q_u) as a function of the porosity/lime index. A specific q_t/q_u matching 0.13 was established, being autonomous of the porosity/lime index. In addition, it is empirically revealed the existence of an exclusive relation connecting accumulated loss of mass divided by the number of wetting/drying cycles and porosity/lime index. This broadens the applicability of such index by demonstrating it controls endurance performance of compacted coal fly ash - lime blends.
Keywords: durability, coal fly ash, carbide lime, strength, porosity/lime index.

1. Introduction

In the last years the development of new geomaterials with the use of industrial by-products has been of concern to researchers. This can be seen as a positive process in which the premises for progress are closely related to the issue of environmental sustainability, a concept that intends to assure the conservation of natural resources that enables meeting current needs without compromising future generations (World Commission on Environment and Development 1987). In this context, the construction industry is an important cause of environmental impacts, since it consumes large amounts of natural resources and generates considerable quantities of waste. Hence, it is crucial an increase in the development and use of new materials and techniques capable of reducing those impacts, like the utilization of recycled waste.

An important industrial residue, which is responsible for pozzolanic reactions and, therefore, capable of generating cementing materials when properly stabilized with an alkaline activator, is the coal fly ash (*FA*) derived from the coal combustion in thermal power plants. Annually, about 750 Mt of this waste are generated in the whole world, however the average reutilization in this global perspective is only around 25% (Blissett & Rowson, 2012). Moreover, the *FA* can be stabilized with carbide lime, a by-product in the production process of acetylene gas (*e.g.* Consoli *et al.*, 2014; Arulrajah *et al.*, 2016, Saldanha & Consoli, 2016). Therefore, the use of these industrial residues makes it possible to decrease the use of natural resources in civil construction and prevents the allocation of them to landfills.

The mixture, in a wet process, of coal fly ash and carbide lime provides minerals, such as calcium silicate hydrate (*CSH*) and calcium aluminate hydrate (*CAH*), that crystallize and constitute the cementing by forming interparticle bonds (Massazza, 1998). Nevertheless, there are many factors that are able to interfere in the pozzolanic reactions originated in the mixture and compaction of these residues and, consequently, influence their mechanical properties. Thereby, it is necessary to assess variables for the main parameters which govern the development of these reactions, such as: amount of lime, porosity, curing period and temperature, and correlate these with the mechanical response of the *FA*-lime blends (Haque *et al.*, 2014; Rocha *et al.*, 2014; Dash & Hussain, 2015; Islam *et al.*, 2015; Saldanha & Consoli, 2016).

Strength tests are usually employed as a way to examine the influence of diverse variables on cemented materials behaviour. A logical dose procedure for coal fly ash - lime blends was created by Consoli *et al.* (2014) taking into consideration the porosity/lime index as a proper parameter to assess strength (q_u) of fly ash-carbide lime mixes. Yet, so far, no research has examined the applicability of the porosity/lime index (η/L_v) for compacted coal fly ash-lime mixes in terms of loss of mass after dry/wet cycles to check durability and tensile strength (q_t), as well as q_t/q_u. The target of

Nilo Cesar Consoli, Ph.D., Full Professor, Departamento de Engenharia Civil, Universidade Federal do Rio Grande do Sul, Porto Alegre, RS, Brazil. e-mail: consoli@ufrgs.br.
Rodrigo Beck Saldanha, Ph.D. Student, Departamento de Engenharia Civil, Universidade Federal do Rio Grande do Sul, Porto Alegre, RS, Brazil. e-mail: becksaldanha@yahoo.com.br.
Jéssica Flesch Novaes, M.Sc., Departamento de Engenharia Civil, Universidade Federal do Rio Grande do Sul, Porto Alegre, RS, Brazil. e-mail: jessicafleschn@gmail.com.
Hugo Carlos Scheuermann Filho, M.Sc. Student, Departamento de Engenharia Civil, Universidade Federal do Rio Grande do Sul, Porto Alegre, RS, Brazil. e-mail: hugocsf@gmail.com.
Submitted on January 13, 2017; Final Acceptance on July 5, 2017; Discussion open until December 29, 2017.

this study is to determine straight relations between η/L_v and accumulated loss of mass after wetting/drying cycles (durability), q_t and q_t/q_u for compacted coal fly ash-carbide lime mixes.

2. Background

Durability can be stated as the capability of a material to maintain stability and integrity over large periods of exposure to detrimental weathering (Dempsey & Thompson, 1968). Such property, as well as strength, is one of the important engineering properties of cemented mixes.

Previous studies have been carried out to evaluate the durability of soil-cement mixtures, most of them (*e.g.*, Starcher *et al.*, 2016, Jamshidi *et al.*, 2016) centered on two ASTM standards: wetting and drying (ASTM, 2015a) and freezing and thawing (ASTM, 2013).

Shihata & Baghdadi (2001) immersed sets of silty sand-cement specimens in saline water for different durations prior to running 12 wetting-drying cycles followed by brushing strokes. The authors found that soils with larger amounts of fines presented higher weight loss values in such tests. They also observed a close relationship between percent mass loss and reduction of unconfined compressive strength after the cycles.

Zhang & Tao (2008) performed durability tests in low plastic silty clay stabilized with cement. The authors observed that the mass loss decreased with the increase in cement contents, but increased with the increase of water-cement ratio.

Kelley (1988) and Cuisinier *et al.* (2012) showed qualitatively that the efficiency of lime treatment could be damaged by the alternation of wet/dry cycles in the long term. Such behaviour was also observed by Cuisinier *et al.* (2014). The latter authors also observed significant irreversible shrinkage strains at the end of the first cycle for lime treated clays. A dramatic decrease in yield stress brought by a loss of the lime cementation bonding was also evidenced after the first cycle.

Theivakularatnam & Gnanendran (2015) observed that the accelerated reaction of binders due to increasing temperature masked the detrimental effect of the wet-dry cycles.

However, there were no studies looking for the understanding of the key parameters that control durability of coal fly ash - lime blends and the analysis of the effect of such factors (*e.g.* porosity/lime index).

3. Experimental Program

The materials and methods used in present research are discussed below.

3.1. Materials

The coal fly ash characterization tests are displayed in Table 1. The fly ashes [type F according to ASTM (2015b)] utilized in the testing were taken from a thermal power plant disposal site situated in southern Brazil, being classified (ASTM, 2006) as low plasticity silt (ML). Surface area using nitrogen adsorption - BET method (ASTM, 2012) is 3.20 m^2/g. As a result of X-Ray Fluorescence Spectrometry (XRF) it was possible to identify the main components of the fly ash, among which stand out SiO_2 (64.8%), Al_2O_3 (20.4%), Fe_2O_3 (4.8%), and CaO (3.1%).

Table 1 - Physical properties of the coal fly ash sample.

Liquid limit (%)	-
Plastic limit (%)	-
Plasticity index (%)	Non-plastic
Specific gravity	2.17
Medium sand (0.2 mm < diameter < 0.6 mm) (%)	1.5
Fine sand (0.06 mm < diameter < 0.2 mm) (%)	12.9
Silt (0.002 mm < diameter < 0.06 mm) (%)	82.4
Clay (diameter < 0.002 mm) (%)	3.2
Mean particle diameter, D_{50} (mm)	0.02
USCS class	ML (low plasticity silt)

Carbide lime, a by-product of the production of acetylene gas, is a hydrated lime and was used throughout this research as the activator agent. Moreover, the determination of calcium and magnesium oxides (on a non-volatile basis) using the wet chemical analysis (ASTM, 2011) established 96% of calcium oxide, being then a calcitic lime. To ensure the occurrence of the pozzolanic reactions, the minimum lime content in the mixture was determined through the Initial Consumption of Lime Method (*ICL*) (Rogers *et al.*, 1997). For this study, a minimum quantity of 4% of carbide lime (based on the mass of dry coal fly ash) was found to stabilize the blends. So, based on such result, carbide lime contents of 5%, 8% and 11% were chosen for the present research. Carbide lime grains specific gravity is 2.12.

Distilled water was employed for characterization tests and moulding specimens for the mechanical tests.

3.2. Methods

3.2.1. Moulding and curing of specimens

For strength tests, cylindrical specimens with 50 mm diameter and 100 mm from top to bottom were employed. For durability (wetting and drying) tests, cylindrical specimens with 100 mm diameter and 120 mm from top to bottom were utilized. A designed dry unit weight for a particular specimen was then established as a result of the dry mass of coal fly ash-carbide lime inserted in the cylindrical mould divided by the total volume of the specimen. As exhibited in Eq. 1 (Saldanha & Consoli, 2016), porosity (η) is a function of dry density (γ_d) of the mix and carbide lime content (L). Each substance (fly ash and carbide lime) has a unit weight of solids (γs_{FA} and γs_L), which also requires to be pondered for computing porosity.

$$\eta = 100 - 100\left\{\left[\frac{\gamma_d}{1+\frac{L}{100}}\right]\left[\frac{1}{\gamma s_{FA}} + \frac{\frac{L}{100}}{\gamma s_L}\right]\right\} \tag{1}$$

Once the coal fly ash and carbide lime were weighed, they were blended till the mix attained uniformity. Moisture contents for the coal fly ash and carbide lime blends were then supplemented, remaining the mix procedure till a homogeneous paste was generated. Each specimen was then constructed in three layers, each layer being statically compacted inside a cylindrical split mold, so that each layer reached the prescribed dry unit weight. In the process, the top of each layer was slightly scarified. After the molding, the specimen was immediately extracted from the split mold and its weight, diameter and height measured with accuracies of about 0.01 g and 0.1 mm, respectively. The specimens were cured for 7 days in a moist chamber at 23 °C ± 2 °C and relative moisture of about 98%.

3.2.2. Unconfined compression and split tensile tests

Compression tests followed standard ASTM C 39 (ASTM, 2010) while tension tests obeyed standard ASTM C 496 (ASTM, 2011). Before testing, specimens were put underwater for 24 h to reduce suction (Consoli *et al.*, 2011). Compaction tests of coal fly ash - carbide lime blend (8% was the lime content used - based on the mass of dry coal fly ash) mix under standard, intermediate and modified energies (see Fig. 1) presented maximum dry unit weights and optimum moisture contents of 11.61 kN/m^3 and 31.5%, 11.96 kN/m^3 and 29.2% and 12.36 kN/m^3 and 27.6%, respectively. Specimens were moulded on top of the line formed by maximum dry unit weights and optimum moisture contents (at three distinct points) (see Fig. 1): 10.6 kN/m^3 and 36.6% (point 1), 11.6 kN/m^3 and 31.3% (point 2) and 12.6 kN/m^3 and 26.0% (point 3); carbide lime contents used were 5%, 8% and 11% and specimens were cured for 28 days. As for Portland cement, the amounts of water needed for lime-pozzolan reaction are minimum, and the Proctor optimum moisture content is more than enough to guarantee the necessary water amount.

3.2.3. Durability tests

Durability (wetting-drying cycles) tests of coal fly ash - carbide lime mixtures were completed according to standard ASTM D 559 (ASTM, 2015a). Specimens were moulded with the same variables as for strength tests. Test procedures determine mass losses produced by recurrent (12) wet-dry series. Every cycle begins by oven drying through 42 h at 71 °C ± 2 °C. Then, specimens are brushed a

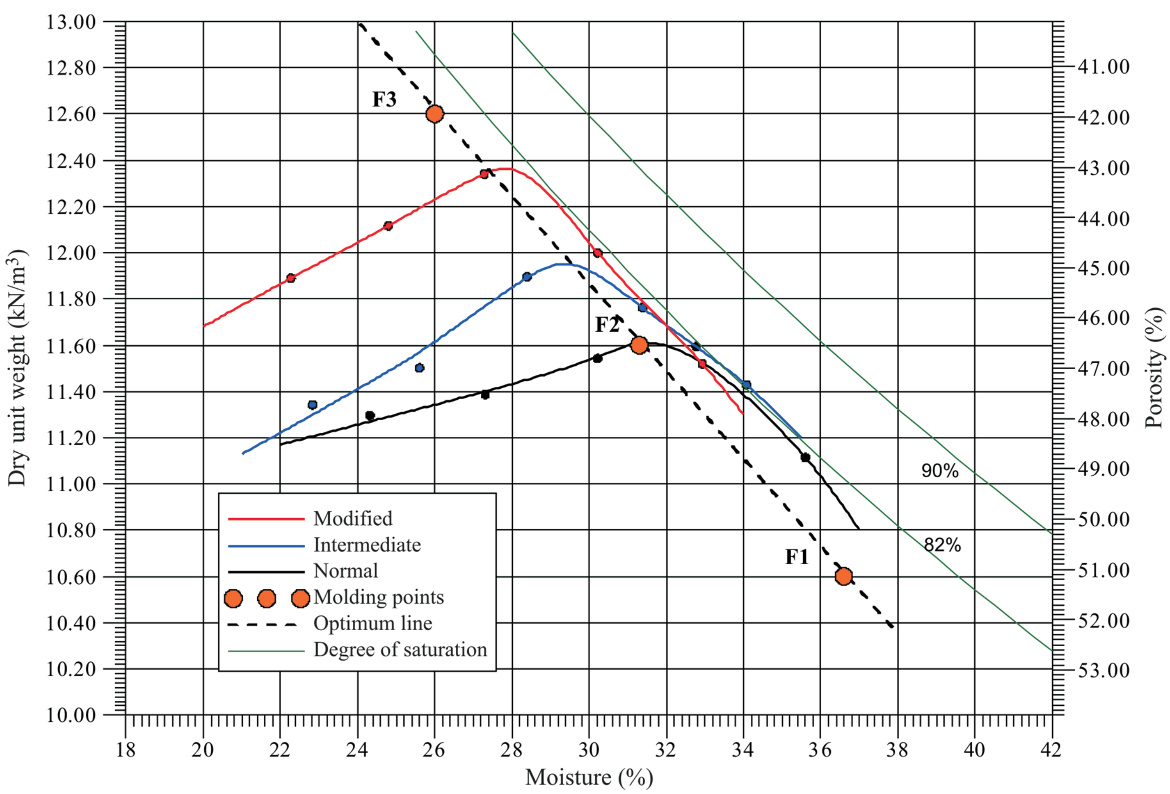

Figure 1 - Compaction test results, optimum compaction line and moulding points.

number of times using a force of approximately 15 N. Lastly, specimens are put underwater for 5 h at 23 °C ± 2 °C. It is important to point out that pozzolanic reactions are accelerated with temperature and so the 42 h at 71 °C during wetting and drying cycles can improve the material strength.

4. Results

4.1. Influence of the porosity/lime index on q_t and q_u

Figure 2 portrays q_t and q_u as a function of $\eta/(L_v)^{0.11}$ [stated as porosity (η) divided by the volumetric lime content (L_v), the latter expressed as a percentage of carbide lime volume to the total volume of the coal fly ash - carbide lime mixtures (Consoli *et al.*, 2014)] for the curing period studied (28 days). Fig. 2 indicates that the adjusted porosity/lime index is helpful in normalizing tensile and compressive strength results for coal fly ash - carbide lime mixtures. Fair correlations ($R^2 = 0.95$ and 0.91) can be perceived concerning q_t (Eq. 2) and q_u (Eq. 3) and $\eta/(L_v)^{0.11}$ for the coal fly ash - carbide lime mixtures studied.

$$q_t\ (\text{MPa}) = 0.30 \times 10^5 \left[\frac{\eta}{L_v^{0.11}}\right]^{-3.00} \quad (2)$$

$$q_u\ (\text{MPa}) = 2.32 \times 10^5 \left[\frac{\eta}{L_v^{0.11}}\right]^{-3.00} \quad (3)$$

The capability of the adjusted porosity/lime index to normalize strength of lime treated coal fly ash has been shown by Consoli *et al.* (2014, 2016). They have shown that rates of change of strength with porosity (η) and the inverse of the volumetric lime content ($1/L_v$) are as a rule not the same. Thus, the application of an exponent (as a directive around 0.11 - Consoli *et al.*, 2014, 2016; Saldanha & Consoli, 2016) to L_v is required for the rates of η and $1/L_v$ to be compatible.

By examining Fig. 2, as well as Eqs. 2 and 3, it can be seen that the tension and compression tests present rather similar trends. Plotting q_t *vs.* q_u of all tests carried out (see Fig. 3) it can be observed that q_t/q_u is a scalar (= 0.13) for the fly ash - carbide lime studied blend, being independent of porosity, carbide lime content, or porosity/lime index.

4.2. Influence of the carbide lime, porosity and porosity/lime index on durability (wetting and drying cycles) of compacted coal fly ash-carbide lime blends

Figure 4 shows compacted coal fly ash-carbide lime blends accumulated loss of mass (ALM) *vs.* adjusted porosity/lime index [$\eta/(L_v)^{0.11}$] after 3 [Eq. 4 - $R^2 = 0.91$], 6 [Eq. 5 - $R^2 = 0.92$], 9 [Eq. 6 - $R^2 = 0.92$] and 12 [Eq. 7 - $R^2 = 0.93$] wetting-drying cycles (during durability tests).

$$ALM(\%) = 1.26 \times 10^{-14} \left[\frac{\eta}{L_v^{0.11}}\right]^{8.30} \quad (4)$$

$$ALM(\%) = 2.48 \times 10^{-14} \left[\frac{\eta}{L_v^{0.11}}\right]^{8.30} \quad (5)$$

$$ALM(\%) = 3.20 \times 10^{-14} \left[\frac{\eta}{L_v^{0.11}}\right]^{8.30} \quad (6)$$

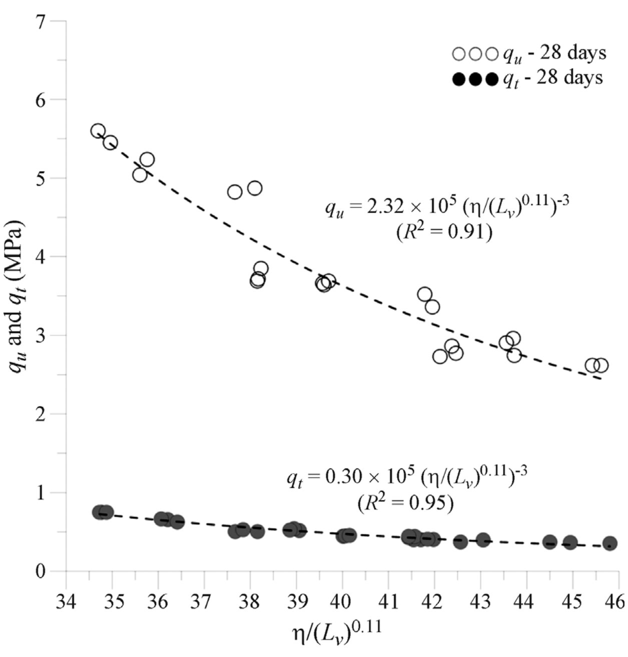

Figure 2 - Variation of split tensile strength (q_t) and unconfined compressive strength (q_u) with adjusted porosity/lime index for coal fly ash-carbide lime blends for 28 days of curing.

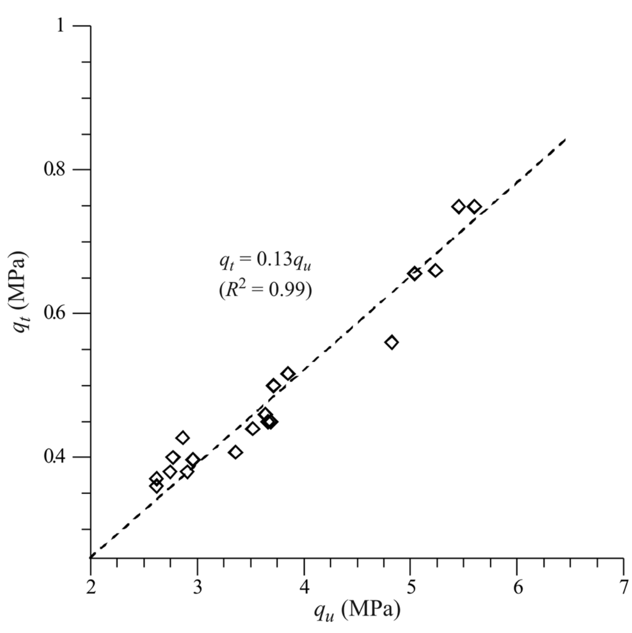

Figure 3 - Split tensile strength (q_t) *vs.* unconfined compressive strength (q_u) for 28 days of curing.

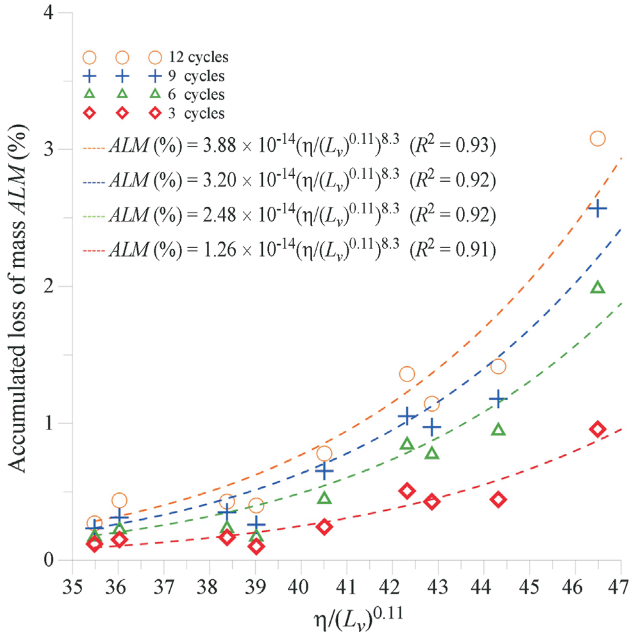

Figure 4 - Coal fly ash - carbide lime blends accumulated loss of mass *vs.* adjusted porosity/lime index after 3, 6, 9 and 12 wetting-drying cycles (during durability tests).

$$ALM(\%) = 3.88 \times 10^{-14} \left[\frac{\eta}{L_v^{0.11}} \right]^{8.30} \quad (7)$$

In order to further normalize the presented durability results, compacted coal fly ash - carbide lime blends accumulated loss of mass values for 3, 6, 9 and 12 cycles are divided by the number of cycles and plotted *vs.* adjusted porosity/lime index (see Fig. 5). A unique relationship

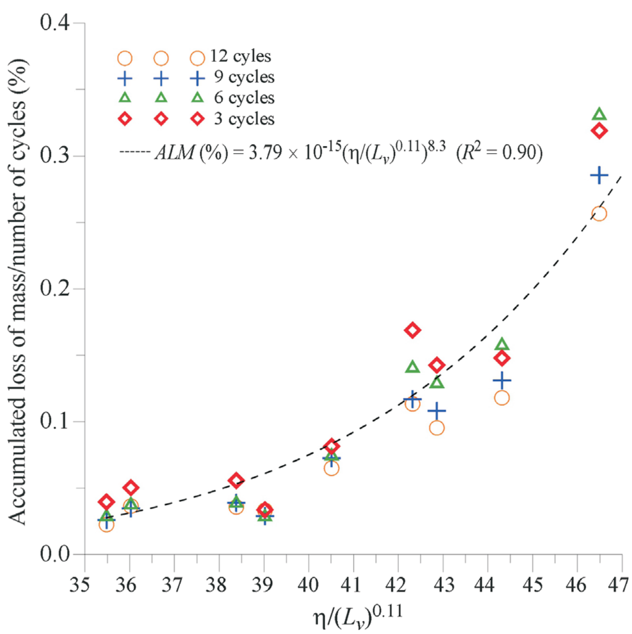

Figure 5 - Coal fly ash - carbide lime blends *ALM/NC vs.* adjusted porosity/lime index after wetting-drying cycles during durability tests.

(R^2 = 0.90) linking accumulated loss of mass divided by number of cycles (ALM/NC) and adjusted porosity/lime index $[\eta/(L_v)^{0.11}]$ after distinct wetting-drying cycles is found [see Eq. 8]. So, it can be seen, for the first time ever, that the porosity/lime index also controls the durability of compacted coal fly ash-carbide lime blends.

$$\frac{ALM}{NC}(\%) = 3.79 \times 10^{-15} \left[\frac{\eta}{L_v^{0.11}} \right]^{8.30} \quad (8)$$

Therefore, the porosity/lime index controls strength and endurance performance of the compacted coal fly ash-carbide lime blends.

5. Concluding Remarks

- From the studies developed in this document the following conclusions can be sketched:
- The accumulated loss of mass (*ALM*) (durability quantification) of individual wetting/drying cycles of compacted coal fly ash-carbide lime mixes were originally perceived in the present research to be directly associated with the adjusted porosity/lime index;
- An unique relationship linking accumulated loss of mass divided by number of cycles (*ALM/NC*) and adjusted porosity/lime index $[\eta/(L_v)^{0.11}]$ after distinct wetting-drying cycles is presented for the first time;
- The q_t/q_u ratio is distinctive (= 0.13) for the compacted coal fly ash-carbide lime assessed in the current study, being independent of the porosity/lime index;
- The porosity/lime index controls tensile and compressive strength, as well as endurance performance of the compacted coal fly ash-carbide lime blends. So, according to the strength and durability requirements, the earthwork designer can establish the adjusted porosity/lime index that fulfills the design needs. Lastly, distinct dry unit weights and carbide lime amounts can fulfill the project requirements.

Acknowledgments

The authors wish to express their gratitude to Edital FAPERGS/CNPq 12/2014 - PRONEX (Project # 16/2551-0000469-2) for the financial support to the research group.

References

Arulrajah, A.; Mohammadinia, A.; Phummiphan, I.; Horpibulsuk, S. & Samingthong, W. (2016). Stabilization of recycled demolition aggregates by geopolymers comprising calcium carbide residue, fly ash and slag precursors. Construction and Building Materials, 114:864-873.

ASTM (2006). Standard Classification of Soils for Engineering Purposes. ASTM D 2487, West Conshohocken, Philadelphia.

ASTM (2010). Standard Test Method for Compressive Strength of Cylindrical Concrete Specimens. ASTM C 39, West Conshohocken, Philadelphia.

ASTM (2011). Standard Test Method for Splitting Tensile Strength of Cylindrical Concrete Specimens. ASTM C 496, West Conshohocken, Philadelphia.

ASTM (2012). Standard Test Methods for Precipitated Silica-Surface Area by Single Point B.E.T. Nitrogen Adsorption. ASTM D5604, West Conshohocken, Philadelphia.

ASTM (2013) Standard Test Methods for Freezing and Thawing Compacted Soil-Cement Mixtures. ASTM D560, West Conshohocken, Philadelphia.

ASTM (2015a). Standard Test Methods for Wetting and Drying Compacted Soil-Cement Mixtures. ASTM D 559, West Conshohocken, Philadelphia.

ASTM (2015b). Standard Specification for Coal Fly Ash and Raw or Calcined Natural Pozzolan for Use in Concrete. ASTM C 618, West Conshohocken, Philadelphia.

Blissett, R.S. & Rowson, N.A. (2012). A review of the multi-component utilisation of coal fly ash. Fuel, 97(1):1-23 .

Consoli, N.C.; Dalla Rosa, A. & Saldanha, R.B. (2011). Variables governing strength of compacted soil-fly ash-lime mixtures. Journal Materials in Civil Engineering, 23(4): 432-440.

Consoli, N.C.; Rocha, C.G. & Saldanha, R.B. (2014). Coal fly ash-carbide lime bricks: An environment friendly building product. Construction and Building Materials, 69:301-309.

Consoli, N.C.; Quiñónez Samaniego, R.A.; Marques, S.F.V.; Venson, G.I.; Pasche, E. & González Velázquez, L.E. (2016). A single model establishing strength of dispersive clay treated with distinct binders. Canadian Geotechnical Journal, 53(12):2072-2079.

Cuisinier, O.; Gandille, D.; Robinet, A.; Stoltz, G.; Mehenni, A. & Robin, V. (2012). Long term behaviour of treated soils - case study of a lime and cement stabilized backfill. Proc. 3rd Int. Seminar on Earthworks. Technische Universität München, Berlin, pp. 189-200.

Cuisinier, O.; Stoltz, G. & Masrouri, F. (2014). Long term behavior of lime-treated clayey soil exposed to successive drying and wetting. Geo-Congress 2014 Technical Papers, American Society of Civil Engineers, Atlanta, pp. 4146-4155.

Dash, S.K. & Hussain, M. (2015). Influence of lime on shrinkage behavior of soils. Journal Materials in Civil Engineering, 27(12):04015041.

Dempsey, B.J. & Thompson, M.R. (1968). Durability Properties of Lime-Soil Mixtures. Highway Research Record 235, Highway Research Board, Washington, D.C., pp. 61-75.

Haque, A.; Tang, C.K.; Islam, S.; Ranjith, P.G. & Bui, H.H. (2014). Biochar sequestration in lime-slag treated synthetic soil: A green approach to ground improvement. Journal Materials in Civil Engineering, 26(12):1-5.

Islam, S.; Haque, A.; Wilson, S. & Ranjith, P. (2016). Time-dependent strength and mineralogy of lime-GGBS treated naturally occurring acid sulfate soils. Journal Materials in Civil Engineering, 28(1):04015077.

Jamshidi, R.J.; Lake, C.B.; Gunning, P. & Hills, C.D. (2016). Effect of freeze/thaw cycles on the performance and microstructure of cement-treated soils. Journal Materials in Civil Engineering, 28(12): 04016162.

Kelley, M. (1988). A long range durability study of lime stabilized bases at military posts in the southwest. Bulletin 328, National Lime Association, WSA, pp. 1-20.

Massazza, F. (1998). Pozzolana and pozzolanic cements. 4th ed. In: Lea-s Chemistry of Cement and Concrete, Peter C. Hewlett, ed., Arnold, pp. 471-635.

Rocha, C.G.; Consoli, N.C. & Johann, A.D.R. (2014). Greening stabilized rammed earth: devising more sustainable dosages based on strength controlling equations. Journal of Cleaner Production, 66:19-26.

Rogers, C.D.F.; Glendinning, S. & Roff, T.E.J. (1997). Lime modification of clay soils for construction expediency. Proceedings Institution of Civil Engineering - Geotechnical Engineering, 125(4):242-249.

Saldanha, R.B. & Consoli, N.C. (2016). Accelerated mix design of lime stabilized materials. Journal of Materials in Civil Engineering, 28(3):06015012.

Shihata, S.A. & Baghdadi, Z.A. (2001). Long-term strength and durability of soil cement. Journal Materials in Civil Engineering, 13(3):161-165.

Starcher, R.D.; Gassman, S.L. & Pierce, C.E. (2016). The durability of chemically treated soils subjected to cycles of wetting and drying. Geo-Chicago 2016:728-737.

Theivakularatnam, M. & Gnanendran, C.T. (2015). Durability of lightly stabilized granular material subjected to freeze-thaw and wet-dry cycles. Proc. IFCEE 2015, American Society of Civil Engineers,. San Antonio, pp. 1410-1419.

World Commission on Environment and Development (1987). Our Common Future. Oxford University Press, Oxford,.

Zhang, Z. & Tao, M. (2008). Durability of cement stabilized low plasticity soils. Journal of Geotechnical and Geoenvironmental Engineering, 134(2):203-213.

List of symbols

ALM: accumulated loss of mass

D_{50}: mean particle diameter

FA: coal fly ash

L: lime content (expressed in relation to mass of dry coal fly ash)

L_v: volumetric lime content (expressed in relation to the total specimen volume)

NC: number of wetting/drying cycles
q_u: unconfined compressive strength
R^2: coefficient of determination
η: porosity
η/L_v: porosity/lime index
γ_d: dry unit weight
γ_s: unit weight of solids
w: moisture content

Technical Note

Seepage Induced Consolidation Model Correlation with Index Properties

M. Janbaz, A. Maher, S. Janbaz

Abstract. Consolidation of soft sediments stored in the confined disposal facilities or mine tailing dams has challenged the scientists to come up with the best consolidation device for the past 50 years. Since the Terzaghi consolidation theory does not apply in soft sediments due to lack of permeability measurements and self-weight effect, the seepage-induced consolidation seems to be the best tool for soft sediments consolidation determination. Besides, index properties are easily obtained in any soil's laboratory and can be fast and accurate. Therefore, correlation of consolidation with index properties can help disposal facility designers to have a better perspective on the consolidation of similar sediments. This paper presents the result of seepage-induced consolidation test on six different soft soils and correlates their index properties with seepage-induced consolidation model. Finally, the correlation results are compared with the test data and similar correlations in the literature. The proposed correlation shows very satisfactory predictions to the laboratory test results.
Keywords: seepage, consolidation, index properties, soft sediments.

1. Introduction

Consolidation of soft sediments has challenged the geotechnical industry for more than five decades. Mine tailings, dredged sediments, and sludges are highly compressible in nature, and they can undergo consolidation under a very small range of stresses. This is an important matter since the available placement areas are decreasing while the production of soft sediments is increasing every day. Low density along with high water content cause self-weight consolidation settlement to be one of the most important parts of consolidation behavior of soft sediments. Due to the time-consuming nature of consolidation, the self-weight effect can significantly influence the design, management, and reclamation of disposal areas.

It is very critical to have a realistic understanding of the consolidation behavior of soft sediments. Consolidation settlement of these materials is important, as they may undergo significant volume change under the influence of relatively small stresses by their own weight or small surcharge. The consolidation process for these soils is highly nonlinear, as the soil compressibility and hydraulic conductivity may change by several orders of magnitude. Field monitoring and laboratory testing of soft sediments have led to significant improvement in their consolidation behavior prediction. Many scientific types of research, such as on Florida Phosphatic soft clays, have been conducted to shed more lights on the consolidation of high water content soft sediments (Abu-Hejleh *et al.*, 1996).

The main problem when dealing with soft sediment consolidation is the lack of competence of the traditional testing procedure. Classical consolidation tests cannot take into account the permeability characteristics of high water content soft sediments. Therefore, since 1979, different testing apparatuses, such as the Constant Rate of Strain Consolidometer (CRSC) by Carrier *et al.* (1983) or the Large Strain Controlled Rate of Strain Consolidation Tester (LSCRSC) by Cargill (1986), have been introduced for accurately predicting the soft sediments consolidation in the laboratory. The most accurate attempt, which overcame the shortcomings of the traditional test setup, *i.e.*, low range of stress, self-weight effect, and permeability measurement, is called seepage-induced consolidation that was introduced by Imai (1979) and later was simplified and improved by Znidarcic & Liu (1989). The advantages of this test method, which can take a week to be completed, are obtaining compressibility and hydraulic conductivity of the slurries in one test and testing under a small range of effective stresses. The minimum effective stress for the traditional test is about 50 kPa while this setup can provide about 0.1 kPa, which is more realistic when dealing with soft sediment self-weight consolidation.

The governing equation of finite strain consolidation of soft sediments, which can include the effect of self-weight and change in permeability and compressibility, was proposed by Gibson *et al.* (1967). Since then, many researchers have tried to introduce a setup that can accurately determine the consolidation behavior of soft sediments (Carrier *et al.*, 1983; Cargill, 1986; and Scott *et al.*, 1986). In some cases, some scientists have tried to propose mathematical approaches in material properties relationships to optimize the solution of the governing equation (Somogyi, 1979; and Cargill, 1983). According to Znidarcic *et al.* (1984), amongst all of the attempts, the proposed setup and

Masoud Janbaz, Ph.D., Post Doctoral Associate, Rutgers, The State University of New Jersey, New Brunswick, NJ, USA. e-mail: mj365@scarletmail.rutgers.edu.
Ali Maher, Ph.D., Professor, Rutgers, The State University of New Jersey, New Brunswick, NJ, USA. e-mail: mmaher@rci.rutgers.edu.
Saeed Janbaz, Ph.D. Student, University of Texas at Arlington, Arlington, TX, USA. e-mail: saeed.janbaz@mavs.uta.edu.
Submitted on January 31, 2017; Final Acceptance on July 14, 2017; Discussion open until December 29, 2017.

constitutive relationships, *i.e.* void ratio-effective stress (e - σ‘), and void ratio-permeability (e - k), by Znidarcic & Liu (1989) provide the best prediction.

The void ratio- compressibility equation was proposed by Liu & Znidarcic (1991) in Eq. 1 as:

$$e = A(\sigma' + Z)^B \tag{1}$$

and the void ratio-permeability equation is proposed by Somogyi (1979) in Eq. 2 as:

$$k = C \times e^D \tag{2}$$

In these equations, e is the void ratio, σ’ is the effective stress and k is the hydraulic conductivity. A, B, Z, C, and D are the model parameters which are used to predict the consolidation behavior for all stress levels.

The consolidation behavior model prediction depends on how accurate is the prediction of the model parameters, *i.e.* A, B, Z, C and D. In fact, laboratory test data help to find the model parameters and later the model parameters help to predict the consolidation behavior in the field. The first part of this article discusses the consolidation characteristics of six different clayey soils, prepared in the laboratory, and the second part correlates the index properties of the clays with the consolidation model parameters. Determining these model parameters from index properties can be very useful for the prediction of consolidation behavior of such soils. This can help storage facility designers to have better prediction of consolidation behavior of sediments, required time and settlement magnitude, with simple correlations with the index properties.

2. Materials and Methods

Six types of different soils include soft sediment sampled from Newark bay and five different types of clays which were purchased for the sake of providing different index properties. A total number of six samples were prepared for consolidation test. The Newark Bay sediment was prepared under its natural water content and the clay samples were prepared by adding required water to dry soil to reach 133 percent gravimetric moisture content. According to Estepho (2014), samples with 0.33 to 0.5 solid content, calculated by $\left(\frac{1}{1+w}\right)$, correspond to 100 to 230 percent moisture content (w) and are believed to be moist enough to act as soft sediment, which justified the moisture content of clay samples. The summary of soil and sediment sample tests are presented in Table 1.

2.1. Index properties

Natural water content (w_n), specific gravity of solids (G_s), Atterberg limits (LL, PL, and PI), and hydrometer test will provide the index properties of the soils. The grain size distribution of sediments is presented in Fig. 1.

The summary of index properties test results, including LL as liquid limit (%), PL as plastic limit (%), PI as plasticity index, w_n as natural moisture content (%), LI as liquidity index, G_S as specific gravity of solids and e_0 as initial void ratio in saturated state, is presented in Table 2.

Table 1 - Summary of samples and tests.

Type	Designation	Test type
Bay mud	BM	*Gs* (ASTM D854), Atterberg Limits (ASTM D4318), Natural water content (ASTM D2216), Hydrometer test (ASTM D422), Seepage Induced Consolidation (SICT)
Kaolin Red clay	KR	
Kaolin White clay	KW	
Sea clay	SC	
Moroccon clay	MC	
Rhassoul clay	RC	

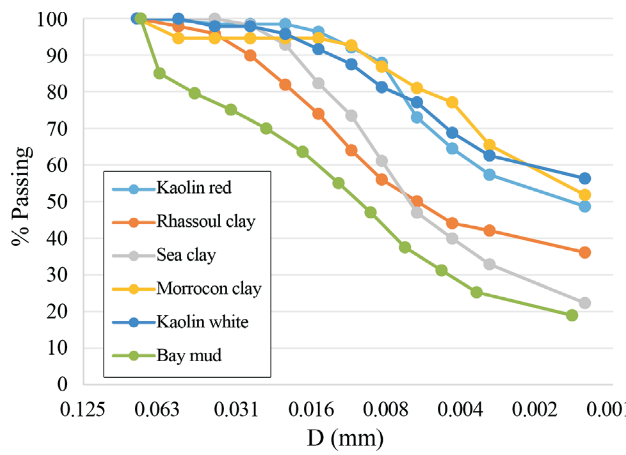

Figure 1 - Grain size distribution.

The range of plasticity index (PI) is 9 to 30, which covers a good range of plasticity indices in the Plasticity chart presented in Fig. 2.

Also, the specific gravity of solids (G_s) is in the range from 2.2 for Newark Bay sediment sample to 2.85 for Moroccon clay. The USCS classification indicates low to high plasticity organic clays.

2.2. Seepage induced consolidation test

The Seepage Induced Consolidation Test (SICT) has been used for over two decades to determine the consolidation characteristics of soft sediments, such as dredged sediments and mine tailings (Abu Hejleh & Znidarcic, 1994; Znidarcic *et al.*, 2011; Berilgen *et al.*, 2006; Pedroni & Aubertin, 2008; and Estepho, 2014). The efficient procedure of this test can result in permeability and compressibility relationships for the soft sediments which later are used to solve the governing equation of consolidation.

The SICT test consists of three stages. Different stages result in different void ratios measured in different stress levels. The first stage is sedimentation column test that provides the void ratio at zero effective stress. For this stage, a big batch of the desired sediment with specific water content was homogenized thoroughly with laboratory

Table 2 - Index properties test results.

	Kaolin Red	Rhassoul clay	Sea clay	Moroccon clay	Kaolin White	Bay mud
LL (%)	50	44	36	53	55	112
PL (%)	36	27	27	23	30	95
PI (%)	14	17	9	30	25	17
USCS Classification	OH	OL	OL	CH	OH	OH
w_n (%)	133	133	133	133	133	275
LI	6.9	6.2	11.8	3.7	4.1	10.6
G_s	2.42	2.6	2.8	2.85	2.7	2.2
e_0	3.21	3.45	3.72	3.79	3.59	6.05

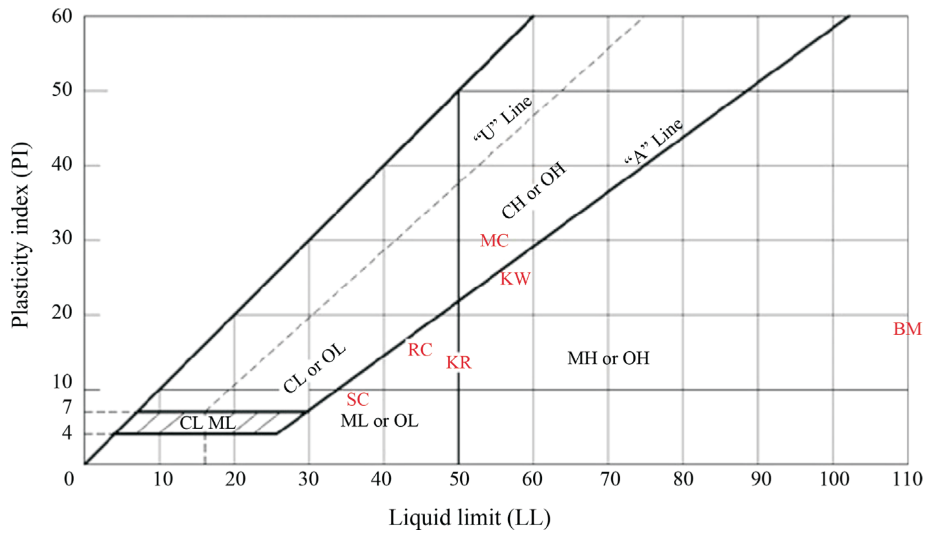

Figure 2 - Plasticity chart (Das, 2013).

mixer and then a representative sample was taken for the sedimentation column test. After homogenizing, the water content of the sample was measured to ensure the accuracy of initial water content. The second stage is consolidation under low effective stresses, created by seepage force and small surcharge (less than 1 kPa), and the last stage is consolidation under the desired surcharge load (10 kPa in this case). There are always intermediate stages, between the second and third stage of the test, based on the magnitude of the stress of interest. The first stage is the sedimentation column which is aside from the actual seepage test apparatus and may take weeks to be completed. Initially, the slurry is poured into a graduated cylinder and is left to settle down under its own weight (Fig. 3).

The average void ratio of the settled material is considered as zero stress void ratio e_0. The second and third stage are performed in the SICT device which is shown schematically in Fig. 4 and result in the two other void ratios for their corresponding effective stresses. The three void ratios are used to find the unknown compressibility model parameters (*A*, *B*, and *Z*) proposed by the Liu & Znidarcic (1991) model. The permeability of the sediment is also measured during the test in all void ratios that can be used to find the other two model parameters (*C* and *D*) proposed by Somogyi (1979).

The setup consists of the water reservoir to provide water to the system, sample chamber, and syringe pump to induce suction and initiate seepage force for consolidating sample. Also, the data acquisition system will record the axial deformation (read by LVDT), seepage rate, stresses and differential pressure between top and bottom of the sample.

3. Results

Figure 5 presents the test results for the six different types of soft sediments in this study. The nonlinear behavior of soft sediments under different effective stresses is presented in (a), while the variation of permeability for different void ratios is depicted in (b).

As expected in soft sediments, the variation of the void ratio in different test stages results in a nonlinear void ratio-effective stress relationship, which proves the incapa-

Figure 3 - Sedimentation column (RC).

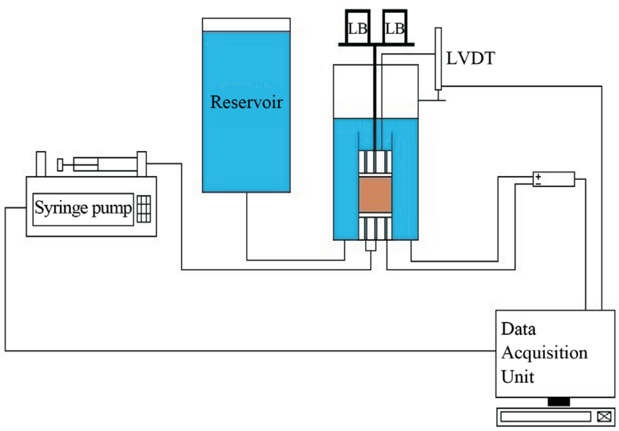

Figure 4 - Seepage induced consolidation apparatus.

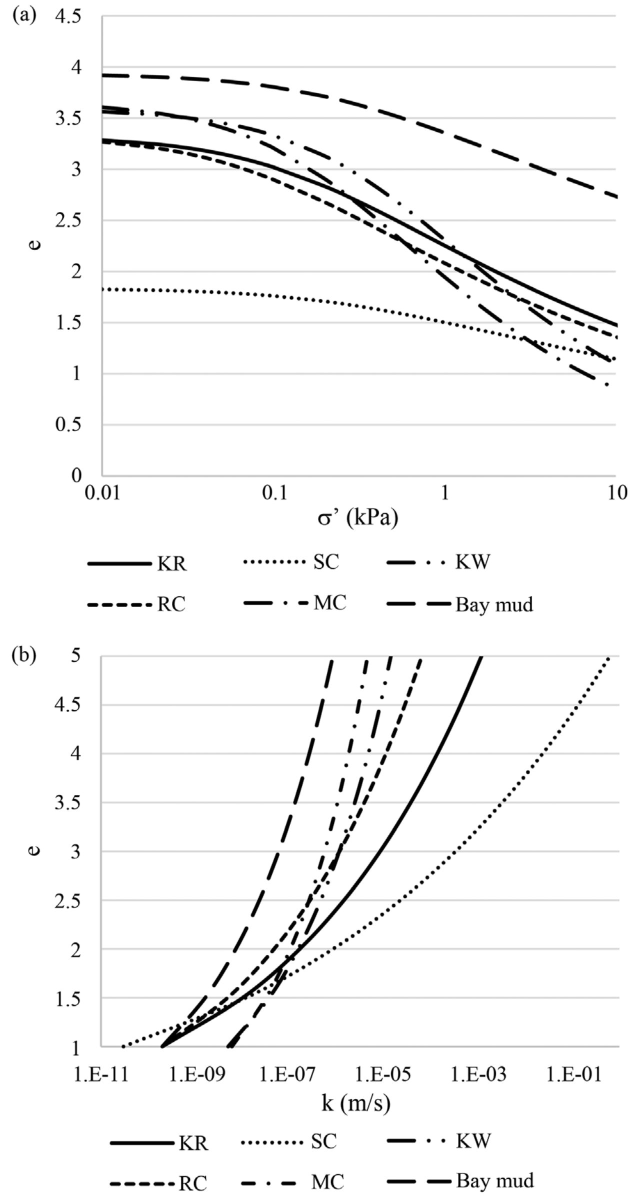

Figure 5 - (a) Effective stress-void ratio (b) void ratio-permeability.

bility of traditional consolidation testing in dealing with soft sediments. Furthermore, the proposed test setup can fully account for inducing small effective stresses on the soil sample which is a crucial part of the consolidation behavior of soft sediments.

The graphs in Fig. 5 present the consolidation model estimation from the test results. Figure 6 shows the actual test measurements for Red Kaolin Clay along with the fitted consolidation model.

Figure 6 shows that the precision of consolidation model estimation is satisfactory. In fact, in order to apply the consolidation model for effective stress void ratio with three unknowns (A, B and Z), three sets of test measurements are enough and the rest of the measured data are redundant, but all of the measurements are presented in Figs. 7 and 8 to ensure the accuracy of model predictions.

3.1. Prediction of model parameters with index properties

It is very practical to determine the model parameters (A, B, Z, C and D) from empirical relationships with index properties. Obtaining index properties is simple and fast while running a complete consolidation test for a soft sediment may take up to ten days. Soft sediment consolidation starts with very small effective stresses that are mostly induced by applying small hydraulic gradient between the two sides of the sample and will take a couple of days, depending on the permeability characteristics of the sediment to come into equilibrium. On the other hand, the index

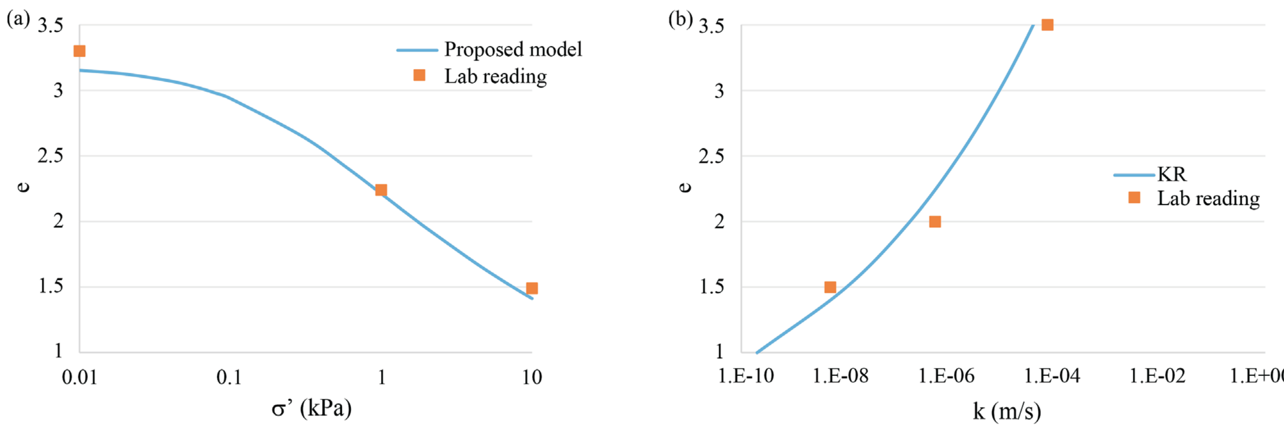

Figure 6 - Test data on Red Kaolin Clay (a) effective stress-void ratio (b) void ratio-permeability.

properties are straightforward and available in any soil's laboratory.

Berilgen *et al.* (2006), proposed their empirical relationships for the seepage-induced consolidation model based on their test results on three different clayey soils and used various published test results to verify their proposition. Based on their findings, the consolidation model parameters, *i.e.*, *A*, *B*, *Z*, *C* and *D* can be correlated with Atterberg limits, liquidity index, and initial void ratio. Table 3 shows their proposed equations for the correlation between abovementioned indices and consolidation model parameters.

In this study also the results of consolidation tests on different samples are statistically correlated with their index properties. The following equations (Eqs. 3 to 7) are presented for consolidation model parameters correlations. The best correlation is achieved based on statistical analysis and is optimized based on the regression coefficient (R^2) of the estimated results *vs.* actual test results.

Table 3 - Correlation equations proposed by Berilgen *et al.* (2006).

Compressibility Model	$A^* = 2.6 \times \exp(0.008 \times PI)$
	$B^* = (1 + e_0) \times [(0.008 \ln(PI)) - 0.054]$
	$Z^* = \exp(-5.51 - (4 \times \ln PI))$
Permeability Model	$C^* = (1 + e_0) \times \exp[1.97 - (3.91 \ln(LI))]$
	$D^* = 7.52 \times \exp[-(0.25 \times LI)]$

Table 4 - Model parameters predictions.

		KR	RC	Bay mud	MC	KW	Bay mud
Test data	A	2.31	2.11	1.55	2.12	2.65	3.42
	B	-0.19	-0.19	-0.13	-0.39	-0.37	-0.097
	Z	0.156	0.093	0.274	0.246	0.451	0.242
	C	2E-10	3E-10	6E-10	5E-10	3E-10	4E-17
	D	9.69	7.63	13.63	4.20	5.36	18.20
Model data	A'	2.30	2.28	1.52	2.27	2.40	3.26
	B'	-0.21	-0.24	-0.12	-0.39	-0.34	-0.14
	Z'	0.216	0.229	0.250	0.316	0.279	0.212
	C'	1.21E-09	2.66E-09	1.37E-09	2.97E-10	9.45E-10	1.03E-16
	D'	9.42	7.92	14.96	4.51	5.36	20.65
Berilgen Model	A*	3.00	3.07	2.88	3.41	3.27	3.07
	B*	-0.142	-0.140	-0.172	-0.128	-0.130	-0.221
	Z*	0.016	0.025	0.002	0.216	0.132	0.005
	C*	1.05E-07	4.84E-08	6.17E-07	5.00E-09	1.04E-08	4.84E-08
	D*	1.33	1.58	0.40	3.01	2.68	0.53

$$A' = \frac{2}{G_s}\log_{G_s} PI \quad (3)$$

$$B' = -\frac{PI}{20\times e_0} \quad (4)$$

$$Z' = \frac{1}{\log_{G_s} PI \times \log_{e_0} LI} \quad (5)$$

$$C' = \frac{1}{G_s \times PI \times (W_n^{e_0})} \quad (6)$$

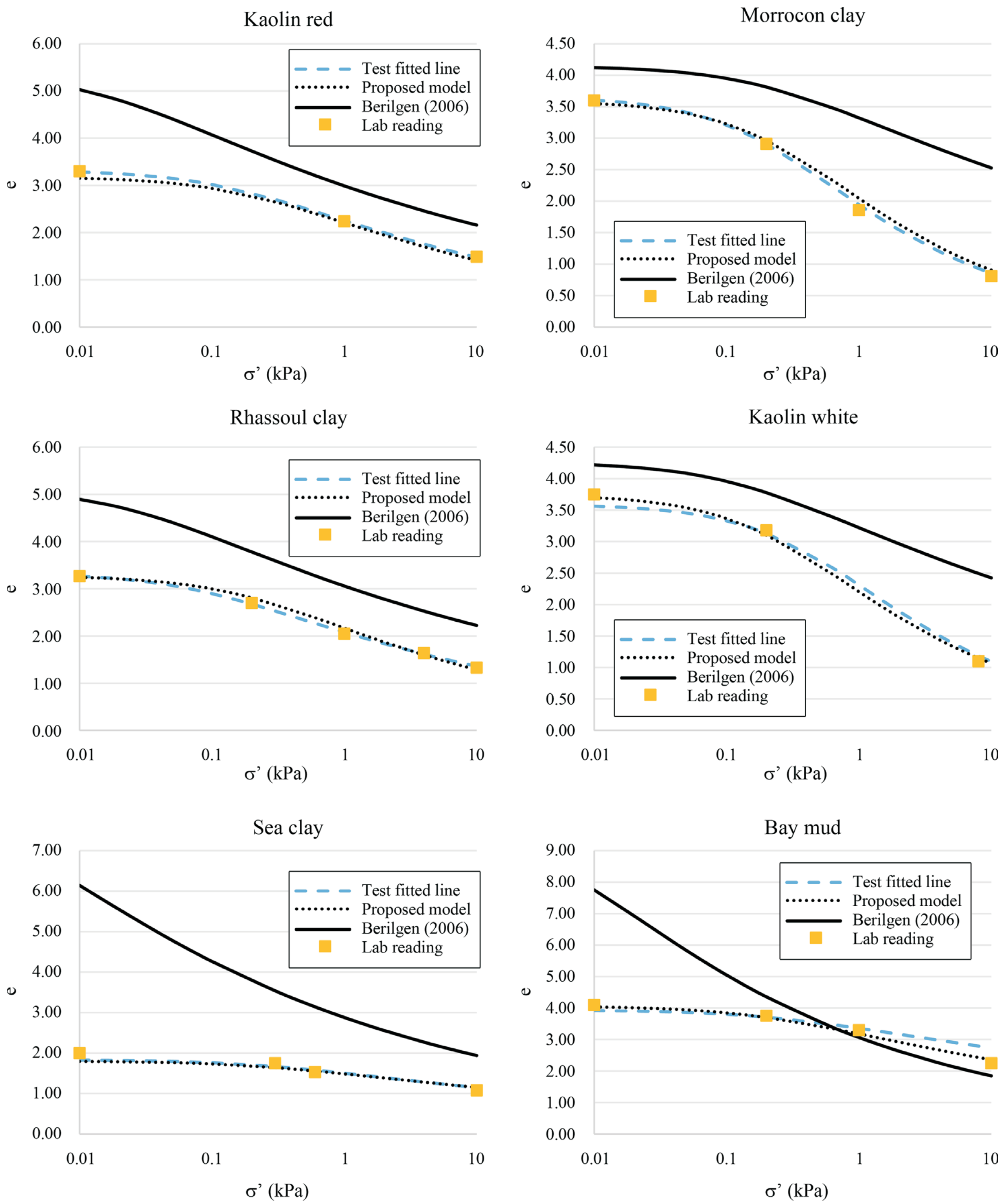

Figure 7 - Comparing test data with two correlating models (compressibility).

$$D' = LI \times \left(1 + \frac{PL}{100}\right) \quad (7)$$

It should be noted that the moisture content in the equations should be in percentage format rather than decimal, *i.e.* 133 should be used instead of 1.33 for 133% mois-

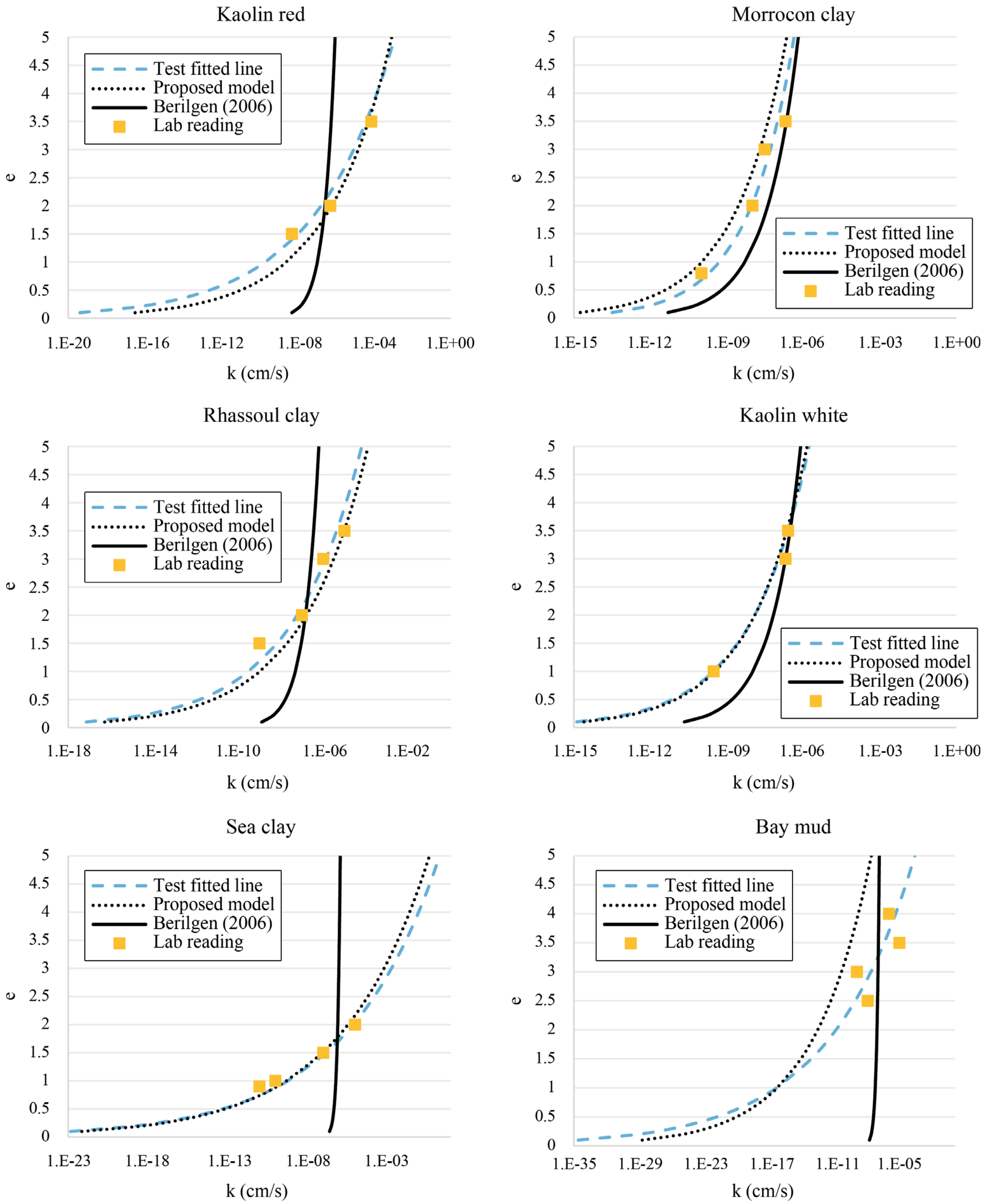

Figure 8 - Comparing test data with two correlating models (permeability).

ture content. The predictions' results are presented in Table 4 for a different type of sediments. Table 4 presents the results of test data from six seepage-induced consolidation tests, model data obtained from the proposed equations and Berilgen *et al.* (2006) correlation equations to compare with the proposed equations.

Figure 7 presents the graphical comparison between these three sets of data, *i.e.* test data, proposed correlation and Berilgen *et al.* (2006) correlation for compressibility equation and Fig. 8 presents the comparison of permeability data.

Figure 7 presents the test results for compressibility of the sediments and it proves that the soft sediments have very nonlinear behavior in a small range of effective stresses. The traditional consolidation test starts the effective stress at 50 kPa while most of the soft sediments undergo the majority of their consolidation in much smaller ranges of effective stresses compared to usual consolidation tests. Figure 8 also presents the nonlinear behavior of soft sediments in permeability measurements. The magnitude of permeability can change significantly with the void ratio in soft soil consolidation, which is neglected in infinitesimal strain consolidation theory. Both Figs. 7 and 8 represent the comparison between proposed equations and test results. This study's proposed correlations show satisfactory results compared to Berilgen *et al.* (2006) proposed correlations. Although the proposed correlations include more index properties in relatively complex format, the resulting approximation is very satisfactory.

4. Conclusions

The results of six seepage-induced consolidation tests are presented in this paper and the correlation between index properties and consolidation model parameters is investigated. Since obtaining the index properties is relatively quick and straightforward, the correlation between index properties and consolidation model parameters for soft sediments could help engineers to come up with good estimates about consolidation behavior of sediments in practice without performing the actual consolidation tests. However, it should be noted that using the correlation should not substitute the laboratory testing. The correlation can be used for initial estimation of consolidation of soft sediment retention ponds and the validity of them should be confirmed by performing an adequate number of laboratory consolidation tests for any specific case. The proposed correlations are compared with published correlations by Berilgen *et al.* (2006) and the results show better compatibility with proposed correlations when compared to Berilgen *et al.* (2006) correlation for the proposed six clays. The correlations proposed herein have a very good agreement with test results and can be used for similar sediments with similar index properties.

References

Abu-Hejleh, A.N. & Znidarcic, D. (1994). Estimation of the Consolidation Constitutive Relations. Computer Methods and Advances in Geomechanics. Siriwardane & Zaman (eds) Balkema, Rotterdam, pp. 499-504.

Abu-Hejleh, A.N.; Znidarcic, D. & Barnes, B.L. (1996). Consolidation characteristics of phosphatic clays. Journal of Geotechnical Engineering, 122(4):295-301.

Berilgen, S.A.; Berilgen, M.M. & Ozaydin, I.K. (2006). Compression and permeability relationships in high water content clays. Applied Clay Science, 31(3):249-261.

Cargill, K.W. (1983). Procedures for Prediction of Consolidation in Soft Fine-Grained Dredged Material. Technical Report D-83-1, U.S. Army Engineer Waterways Experiment Station, Vicksburg, 157 p.

Cargill, K.W. (1986). The Large Strain Consolidation Controlled Rate of Strain (LSCRS) Device for Consolidation Testing of Soft Fine-Grained Soils. Technical Report GL-86-13, U.S. Army Engineer Waterways Experiment Station, Vicksburg, 186 p.

Carrier, W.D.; Bromwell, L.G. & Somogyi, F. (1983). Design capacity of slurried mineral waste ponds. Journal of Geotechnical Engineering, ASCE, 109(5):699-716.

Das, B. (2013). Principles of Foundation Engineering. Cengage Learning Engineering, Boston, 897 p.

Estepho, M. (2014). Seepage Induced Consolidation Test: Characterization of Mature Fine Tailings. Master Thesis, University of British Columbia, Vancouver, 134 p.

Gibson, R.E.; England, G.L. & Hussey, M.J.L. (1967). The theory of one-dimensional consolidation of saturated clays, I. Finite nonlinear consolidation of thin homogeneous layers. Geotechnique, 17(3):261-273.

Imai, G. (1979). Development of a new consolidation test procedure using seepage force. Soils and Foundations, 19(3):45-60.

Liu, J.C. & Znidarcic, D. (1991). Modeling one-dimensional compression characteristics of soils. Journal of Geotechnical Engineering, ASCE, 117(1):162-169.

Pedroni, L. & Aubertin, M. (2008). Evaluation of sludge consolidation from hydraulic gradient tests conducted in large size columns. 61st Canadian Geotechnical Conference and 9th Joint CGS/IAH-CNC Groundwater Conference, Edmonton, Canada, pp. 769-776.

Scott, J.D.; Dusseault, M.B. & Carrier, W.D. (1986). Large-scale self-weight consolidation testing. ASTM Special Technical Publication, No. 892:500-515.

Somogyi, F. (1979). Analysis and Prediction of Phosphatic Clay Consolidation: Implementation Package. Tech. Report. Florida Phosphatic Clay Research Project, Lakeland, Florida.

Znidarcic, D.; Croce, P.; Pane, V.; Ko, H.Y.; Olsen, H.W. & Schiffman, R.L. (1984). The Theory of One-Dimensional Consolidation of Saturated Clays: III. Existing Testing Procedures and Analyses. Geotechnical Testing Journal, 7(3):123-133.

Znidarcic, D.; & Liu J.C. (1989). Consolidation characteristics determination for dredged materials. Proc. of 22nd Annual Dredging Seminar, Center for Dredging Studies, Texas A&M University, College Station, pp. 45-65.

Znidarcic, D.; Miller, R.; Van Zyl, D.; Fredlund, M. & Wells, S. (2011). Consolidation testing of oil sand fine tailings. Proc. Tailings and Mine Waste, Vancouver, BC, pp.251-257.

Case Studies

Behavior of Reinjectable and Prestressed Anchors in Soil Masses: Construction Case Study in Congonhas - Brazil

T.B. Porto, A.C.A. Torres, R.C. Gomes

Abstract.. The present work evaluates the behavior of 26 reinjectable and prestressed anchors executed during the construction of a ground anchored wall in the city of Congonhas, Minas Gerais, with the purpose of stabilizing a slope near a railway of MRS Logística. It refers to a 4.5-m high retaining wall, 30 m in length, and wall thickness of 0.25 m, with three anchors' lines, totalizing 36 anchors. The anchors were installed in a soil primarily composed of sandy silt with ore. The anchored length was 6.8 m. During the acceptance tests, significant differences in load capacity were verified, despite the geotechnical characteristics being alike. This work aims to analyze the behavior of anchorages, as well as the resistance gain through the increase of injection numbers, and finally the possible causes of the divergence in the results.
Keywords: anchors, reinjectable anchor, retaining wall, ground anchored wall, load capacity, slope stabilization.

1. Introduction

The use of a retaining wall system for stabilization of slopes is presented as a viable and economical technique for cases in which the re-sloping is impractical. Among the retaining wall techniques, the construction of reinforced concrete walls integrated with reinjectable and prestressed anchors is presented as the most suitable solution for great heights and restricted areas as hillside roads, canals and bridge abutments (Das *et al.*, 2016). This is due to its convenience, rapidity of execution, versatility, and safety. It ensures small deformation compared to other containment techniques, for example, soil nailing.

Despite the widespread use of this technique in Brazil, little research has been done on its implementation method. The knowledge and improvement of this technique mainly come from the experience of contractors, through the implementation and monitoring of the works (Porto, 2015).

Understanding the anchor-soil interface behavior is essential in order to determine the anchor pullout resistance and predict the deformation of the prestressed anchor system in working load terms (Liang & Feng, 2002). It is known, therefore, that the amplitude of anchor load is the factor that governs the performance of the retaining structure (Wang *et al.*, 2016).

Through experimental studies conducted in 2014 by Porto (2015), this research aims to analyze the behavior of anchorages performed in the construction of a retaining wall in Congonhas city, compare the results of acceptance tests on some anchors, and identify possible factors responsible for differences between readings of anchor load capacity.

2. Ground Anchored Wall

As established by NBR 5629 (ABNT, 2006), the execution process of an anchor wall starts by the vertical cut of the ground, followed by the execution of the inclined hole. The anchor system is installed and grout is inserted into the hole for its stabilization, from the deep end to the entry. Then, the first grout injection phase is performed and, after its cure, the second phase is injected and so on. In this work, the gravity grouting will be referred as "sheath" and the terms "first", "second" and "third injections" refer to pressurized injection phases as shown in Fig. 1. In the sequence of the executive process, the reinforced concrete wall is made. After concrete curing, the anchors are subject to proving, suitability or acceptance tests, according to NBR 5629 (ABNT, 2006), with the purpose of approving or rejecting the anchors through the evaluation of their geotechnical load capacity.

3. Acceptance Tests

In accordance to NBR 5629 (ABNT, 2006), acceptance tests were performed to control the anchors' behavior and load capacity. The test consists of measuring the head displacement of the anchors, using dial or strain gages while applying tensile loads measured by hydraulic pump-jack-manometer. This test should be done mandatorily in all anchors of a retaining wall. The acceptance test type A should be performed at least on 10% of anchors of a construction and type B on the rest. Test type A is performed on permanent anchors, whose stages of loading and unloading are: F_0; 0.3 F_t; 0.6 F_t; 0.8 F_t; 1.0 F_t; 1.2 F_t; 1.4 F_t; 1.6 F_t and 1.75 F_t, where F_0 is the initial load applied to the anchor through the hydraulic pump-jack-manometer set and corre-

Thiago Bomjardim Porto, Ph.D., Associate Professor, Departamento de Engenharia Civil, Pontifícia Universidade Católica de Minas Gerais, Belo Horizonte, MG, Brazil. e-mail: thiago@consmara.com.br.
Ana Clara dos Anjos Torres, Undergraduate Student, Departamento de Engenharia Civil, Pontifícia Universidade Católica de Minas Gerais, Belo Horizonte, MG, Brazil. e-mail: anaclara.torres@hotmail.com.
Romero Cesar Gomes, Ph.D., Full Professor, Departamento de Geotecnia, Universidade Federal de Ouro Preto, Ouro Preto, MG, Brazil. e-mail: romero@em.ufop.br.
Submitted on July 5, 2016; Final Acceptance on July 7, 2017; Discussion open until December 29, 2017.

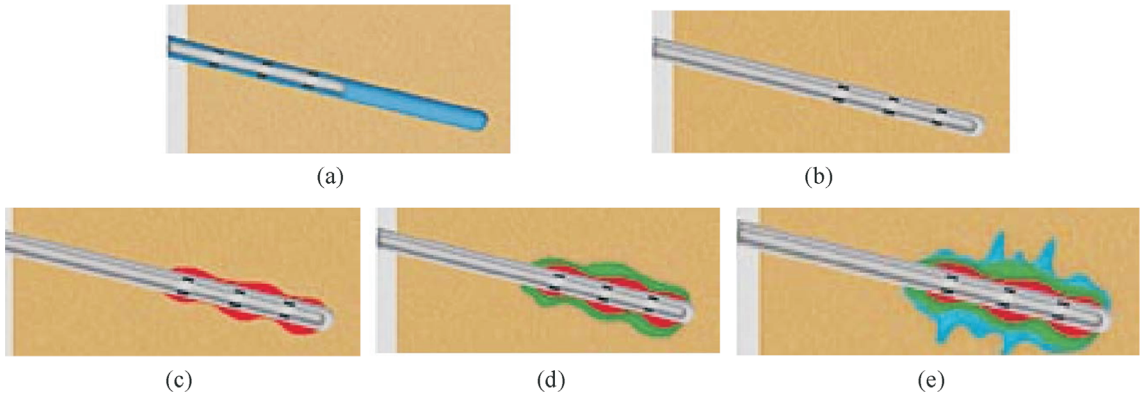

Figure 1 - (a) Drilling and anchor installation; (b) gravity grouting; (c) first injection phase; (d) second injection phase; (e) third injection phase, prestressing and anchor/structure connection (Zirlis *et al.*, 2015).

sponding to 10% of anchor yield strength. F_t is the working load or maximum load that can be applied for which the anchor provides the necessary safety against tendon yielding, anchored length pullout and creep deformations.

In other words, the working load corresponds to the geotechnical load to which the anchor is submitted and under which it should work. After performing full loading and unloading to F_0, the anchor is directly loaded from F_0 to 1.0 F_t. Test type B is performed on permanent anchors too, but stages of loading and unloading are F_0; 0.3 F_t; 0.6 F_t; 0.8 F_t; 1.0 F_t; 1.2 F_t and 1.4 F_t. The displacements that occur due to minor loads F_0 are not measured. Each load increment can only be applied after the stabilization of pressure reading obtained by the manometer (ABNT, 2006).

According to Xiao & Guo (2017), the anchor load is mainly influenced by six factors: the internal friction angle, soil cohesion, wall friction angle, surcharge on the ground surface, anchor dip angle, and depth from the anchor force action point on the wall to the ground surface.

In the acceptance test, the total stabilized displacement must be checked for the maximum load to which the anchor is submitted. Part of this displacement is attributed to elastic elongation of the anchor, in conjunction with permanent elongation. The elastic displacement is considered only from the unbonded part, while the permanent elongation comes from the bulb elongation.

The displacements limits are presented by NBR 5629 (ABNT, 2006) and Fig. 2 represents a typical test result of the acceptance type A. The lines are calculated using the following variables: displacement, acting force on the test, initial load, unbonded part length, grout bulb length, steel elasticity modulus and steel cross-sectional area.

4. Geotechnical Features and Design

The work at Congonhas corresponded to the construction of a ground anchored retaining wall for a slope. A railway is located at the slope crest, therefore the need for the retaining wall to provide greater stability to the ground (Fig. 3a). The phases of construction were: terrain cleaning, foundation, excavation, installation of formwork, reinforcement, and wall concreting. For the foundation, root piles were performed, with 2 m spacing and 15 cm diameter. Figure 3b shows the finished ground anchor wall. For this construction, the “sheath” was made by gravity, despite the injection of pressurized grout to increase the pullout resis-

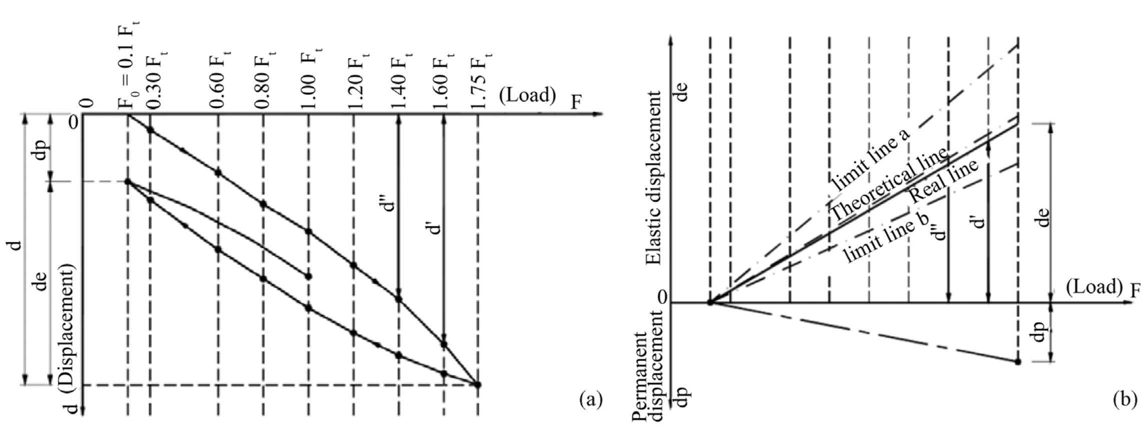

Figure 2 - Acceptance test Type A- a) loads x total displacements; b) breakdown between elastic and permanent displacement (ABNT, 2006).

Figure 3 - (a) View of the slope to be retained; (b) View of finished ground anchored wall (Porto, 2015).

tance by compression of soil due to cavity expansion (Seo *et al.*, 2012).

After the execution of the foundation, the ground was drilled and tendons were installed (CA 50 steel bars with 25° inclination), according to their location planned during design (Figs. 4, 5, 6 and 7). Then the sheath was made to replace the excavated soil. The next day, the first grout layer was injected (f_{ck} = 25 MPa and water/cement ratio = 0.5) with sufficient pressure to rupture the sheath in order to form the anchor bulb. After the minimum period of seven days after the final injection phase, the anchors were prestressed and tested by acceptance tests and, soon after, the anchor heads were concreted. The lengths of the free and anchored parts were hypothetically defined, using the technical expertise of the design engineer. From these lengths, and results of SPT tests, it was possible to estimate the average N_{SPT} for the location of the anchored part of each tendon. Consequently, the ground anchored wall was divided into three modules, each with three levels of anchors, as shown in Figs. 4, 5, 6 and 7.

The determination of the N_{SPT} at the bulb location is needed to calculate the rupture load of the anchors, which was obtained using mathematical extrapolation from the load data and displacement reached at the acceptance tests.

Four Standard Penetration Test boreholes were made near the slope, as illustrated in Fig. 8. Boreholes one and two had a soil composed basically of clay layers and sandy silt filled with coarse gravel and ore, fine to medium sand, moderately compact and coarse gravel with ore. The soil in the first two layers of boreholes three and four are similar to the ones in boreholes one and two, except for the third hole which is composed of sandy silt with ore, instead of gravel. The geotechnical soil profile and the traces are shown in Figs. 9 and 10. Once the bulbs of this construction had the correct length, it was necessary to evaluate the average N_{SPT} at the geometric center of the anchor bulb, in order to estimate the anchor load capacity (Table 1).

Table 2 presents some additional information on the anchors in the study. To estimate the bulb diameter it was considered an increase of 60% in the hole diameter.

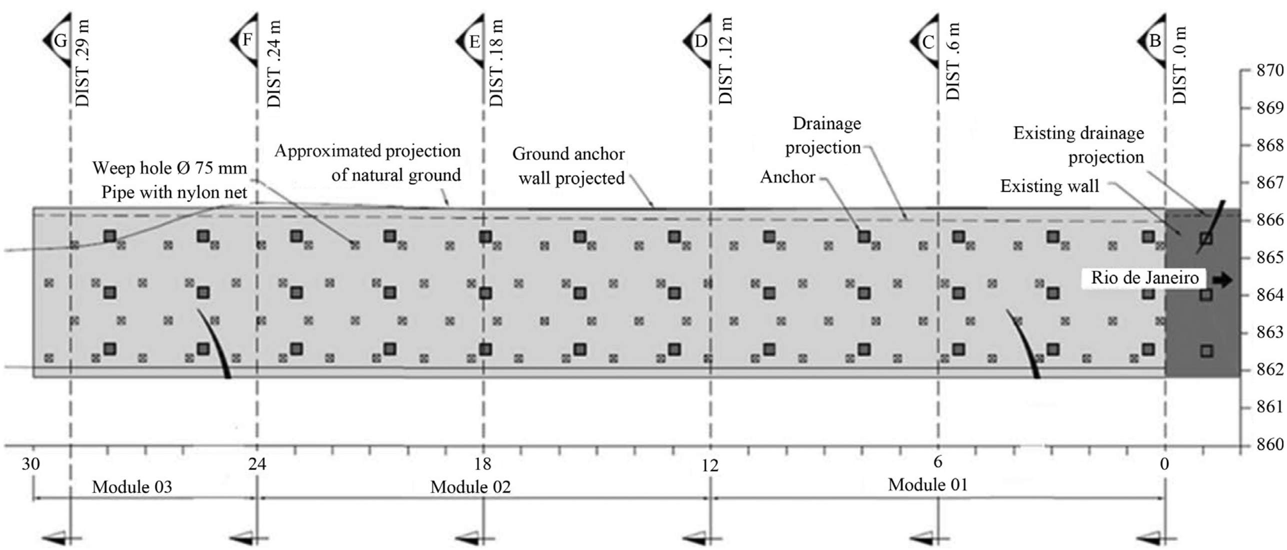

Figure 4 - Overall view of the ground anchored wall (Porto, 2015).

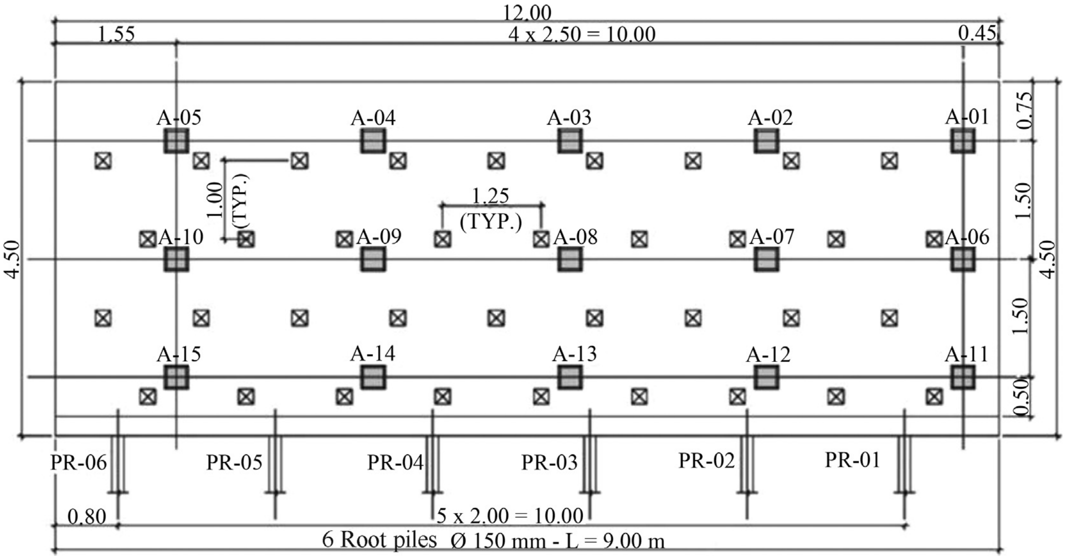

Figure 5 - Ground Anchored Wall - H = 4.50 m. Front view - Module 1 (Porto, 2015).

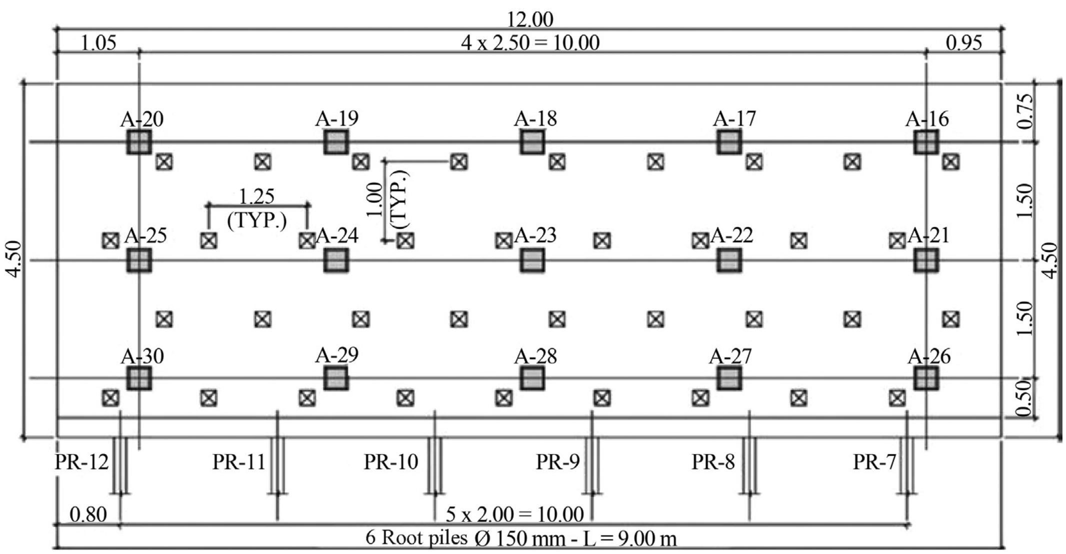

Figure 6 - Ground Anchored Wall - H = 4.50 m. Front view - Module 2 (Porto, 2015).

5. Test Methodology Used in Congonhas

According to Lee *et al.* (2012), the effect of pressurized grouting is more prominent in soil with N_{SPT} value less than 50 for an increase of bulb diameter and pullout resistance. To ensure this resistance gain, it is necessary that the injection procedure is from bottom to the surface (hole entry). However, the anchors in Congonhas were executed by pressurized injection from the entry (surface) to the bottom, hampering the control of injection pressure by the headline valve.

In total, 36 anchors were installed of which 26 were tested. The test load, according to NBR 5629 (ABNT, 2006) was 600kN and the working load was 340 kN. In the absence of physical rupture, a mathematical extrapolation was made, employing Van der Veen (1953) method. Technical control of the test anchors is shown in Table 3.

However, for unreported reasons, the tests did not reload the anchors to the working load during the last stage of the acceptance test. Consequently, the incorporation of the load was made at a later time.

6. Results and Discussion

The results of load capacity in the acceptance test were analyzed in terms of the following parameters: number of grout injections and quantity of cement bags per anchor.

Due to the innumerable variables that influence the anchors' behavior, such as anchor tilting angle, injected grout volume, bulb injection pressure, soil variability, an-

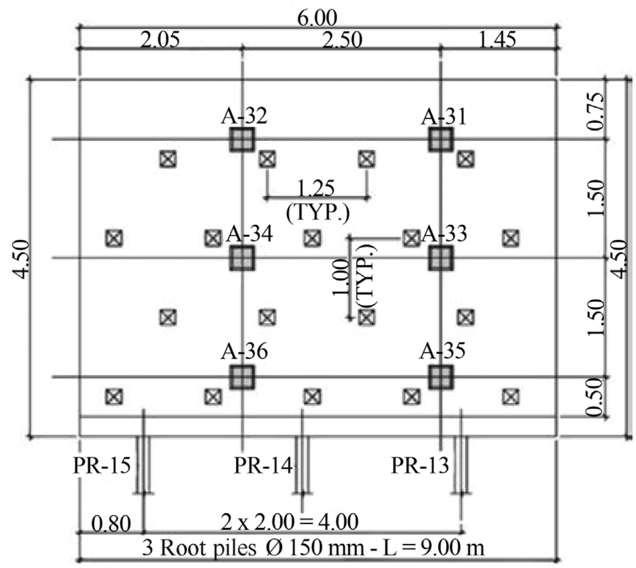

Figure 7 - Ground Anchored Wall - H = 4.50 m. Front view - Module 3 (Porto, 2015).

chor depth, among others, the comparative analysis was performed in terms of load capacity gain as a function of the average values obtained, since a unit analysis is often not representative from the statistical point of view regarding the average behavior of the anchors analyzed.

6.1. Physical rupture

Only three anchors were tested until physical rupture. Figure 11 shows the rupture load evolution as a function of the injections number. Briefly, there is a gain in load capac-

Table 2 - Additional information of the anchors (Porto, 2015).

	First line	Second line	Third line
Bulb length (m)	6.8	6.8	6.8
Total length (m)	26.0	23.0	20.0
Hole diameter (cm)	20	20	20
Bulb diameter (cm)	32	33	32

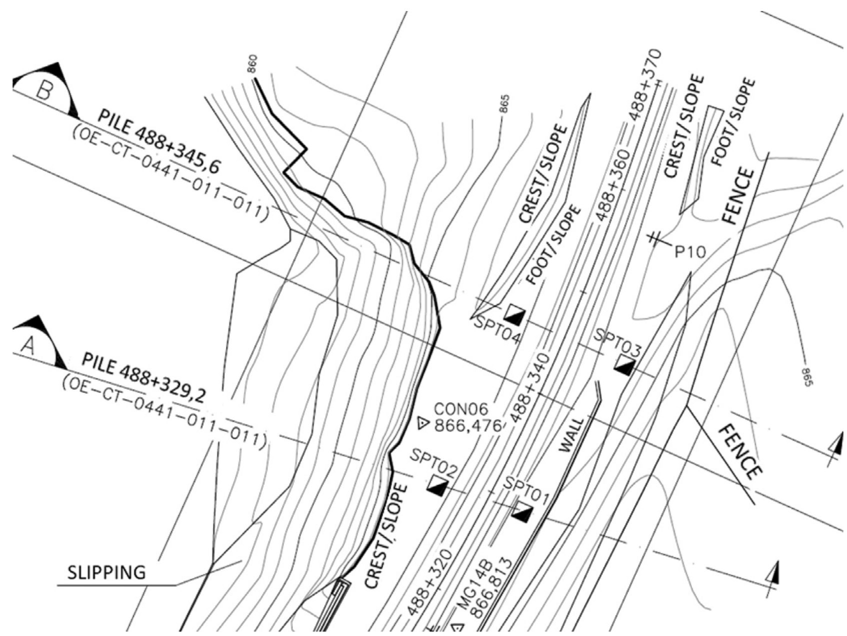

Figure 8 - Planialtimetric project representing sections and holes (Porto, 2015).

Table 1 - The relationship between the N_{SPT} average of the bulb and the type of soil (Porto, 2015).

Anchor	N_{SPT} average	Soil type	Bulb depth (m)
Line 1 - Module 1	13	Coarse gravel with ore	17.16
Line 2 - Module 1	13	Coarse gravel with ore	17.16
Line 3 - Module 1	13	Coarse gravel with ore	17.74
Line 1 - Module 2	11	Sandy silt with compressed ore	11.91
Line 2 - Module 2	11	Sandy silt with compressed ore	13.58
Line 3 - Module 2	11	Sandy silt with compressed ore	14.11
Line 1 - Module 3	13	Sandy silt with compressed ore	11.91
Line 2 - Module 3	11	Sandy silt with compressed ore	13.58
Line 3 - Module 3	11	Sandy silt with compressed ore	14.11

Table 3 - Anchors technical control (Porto, 2015).

Anchor number	Sheath date	Injections													Total length	
		V	1st phase date	V	OP	IP	2nd phase date	V	OP	IP	3rd phase date	V	OP	IP	Soil (m)	Rock (m)
1	18/08/14	11	25/08/14	8	1.5	1.1	27/08/01	4	1.9	1.7	28/08/14	5	1.5	1.0	20.0	3.0
2	19/08/14	11	25/08/14	8	1.4	1.0	27/08/14	4	1.8	1.6	28/08/14	2	2.5	2.2	20.2	2.8
3	25/08/14	8	27/08/14	8	1.4	1.0	28/08/14	4	1.7	1.5	02/09/14	3	2.8	2.5	22.0	4.0
4	25/08/14	8	27/08/14	8	1.4	1.0	28/08/14	4	1.8	1.5	02/09/14	3	2.8	2.5	22.1	3.9
5	25/08/14	10	27/08/14	8	1.5	1.0	28/08/14	4	1.8	1.5	02/09/14	3	2.5	2.2	22.3	3.7
6	11/08/14	12	12/08/14	4	1.3	1.2	02/09/14	4	2.0	1.5	03/09/14	4	2.5	2.2	20.7	2.3
7	12/08/14	12	13/08/14	4	1.5	1.2	02/09/14	4	2.0	1.5	03/09/14	4	2.5	2.2	21.0	2.0
8	15/08/14	11	18/08/14	8	1.3	1.0	02/09/14	7	1.8	1.5	03/09/14	4	2.5	2.0	20.0	3.0
9	22/08/14	8	25/08/14	8	1.5	1.0	02/09/14	5	1.8	1.5	02/09/14	4	2.8	2.4	22.6	3.4
10	15/08/14	11	25/08/14	11	1.3	1.0	02/09/14	4	1.5	1.3	03/09/14	4	2.5	2.2	19.5	3.5
11	15/09/14	6	16/09/14	8	1.8	1.5	22/09/14	7	2.0	1.7	—	—	—	—	18.1	1.9
12	15/09/14	6	16/09/14	9	1.8	1.5	26/09/14	8	2.0	1.7	—	—	—	—	17.4	2.6
13	12/09/14	5	16/09/14	8	1.8	1.5	22/09/14	7	2.0	1.7	—	—	—	—	17.6	2.4
14	12/09/14	5	16/09/14	8	2.0	1.5	22/09/14	7	2.5	1.8	—	—	—	—	17.9	2.1
15	12/09/14	11	16/09/14	7	2.0	1.5	22/09/14	5	2.0	1.7	—	—	—	—	18.1	1.9
16	26/08/14	8	27/08/14	8	1.7	1.3	28/08/14	4	1.8	1.5	02/09/14	3	2.5	2.0	22.0	4.0
17	26/08/14	8	27/08/14	8	1.7	1.3	28/08/14	4	1.8	1.4	02/09/14	3	2.5	2.2	21.9	4.1
18	22/08/14	8	27/08/14	8	1.5	1.0	28/08/14	8	1.8	1.5	02/09/14	3	2.5	2.0	22.2	3.8
19	18/08/14	11	27/08/14	8	1.3	1.0	28/08/14	4	1.8	1.6	02/09/14	4	1.5	1.3	22.1	3.9
20	22/08/14	8	27/08/14	8	1.3	1.0	28/08/14	8	1.8	1.4	02/09/14	7	2.5	2.2	22.5	3.5
21	13/08/14	14	25/08/14	9	1.0	0.8	02/09/14	8	1.8	1.5	03/09/14	3	2.5	2.0	20.8	2.2
22	14/08/14	11	15/08/14	8	1.0	0.8	02/09/14	7	1.8	1.6	03/09/14	4	2.5	2.2	20.2	2.8
23	14/08/14	11	15/08/14	8	1.3	1.0	02/09/14	4	1.9	1.7	03/09/14	4	2.5	2.2	20.0	3.0
24	14/08/14	11	15/08/14	8	1.3	1.0	02/09/14	5	1.9	1.7	03/09/14	3	1.5	2.0	19.9	3.1
25	15/08/14	11	18/08/14	8	1.6	1.0	02/09/14	5	1.8	1.6	03/09/14	3	2.5	2.0	19.6	3.4
26	12/09/14	4	16/09/14	9	1.8	1.5	24/09/14	7	1.0	1.7	—	—	—	—	18.0	2.0
27	12/09/14	4	16/09/14	9	1.9	1.7	24/09/14	7	2.0	1.8	—	—	—	—	17.2	2.8
28	12/09/14	4	16/09/14	9	1.8	1.5	24/09/14	8	2.0	1.8	—	—	—	—	17.8	2.2
29	12/09/14	5	16/09/14	9	1.8	1.4	24/09/14	8	2.0	1.8	—	—	—	—	18.5	1.5
30	12/09/14	5	16/09/14	9	1.8	1.5	24/09/14	7	2.0	1.7	—	—	—	—	18.2	1.8
31	27/08/14	8	02/09/14	8	1.3	1.0	03/09/14	4	1.8	1.6	24/09/14	3	2.6	2.3	21.8	4.2
32	27/08/14	8	02/09/14	8	1.8	1.3	03/09/14	3	2.0	1.8	04/09/14	2	2.6	2.3	22.1	3.9
33	13/08/14	14	14/08/14	4	1.3	1.0	02/09/14	4	1.8	1.5	03/09/14	5	2.0	1.7	20.9	2.1
34	13/08/14	14	14/08/14	4	1.3	1.0	02/09/14	4	1.8	1.5	03/09/14	3	2.5	2.0	20.5	2.5
35	12/09/14	8	16/09/14	8	1.8	1.5	24/09/14	5	2.0	1.8	—	1	—	—	17.8	2.2
36	12/09/14	6	16/09/14	8	1.8	1.4	24/09/14	7	2.0	1.7	—	—	—	—	17.9	2.1

V = Volume of injected grout into hole (cement bags) and water/cement = 0.5. OP = Opening Pressure (MPa). IP = Injection Pressure (MPa).

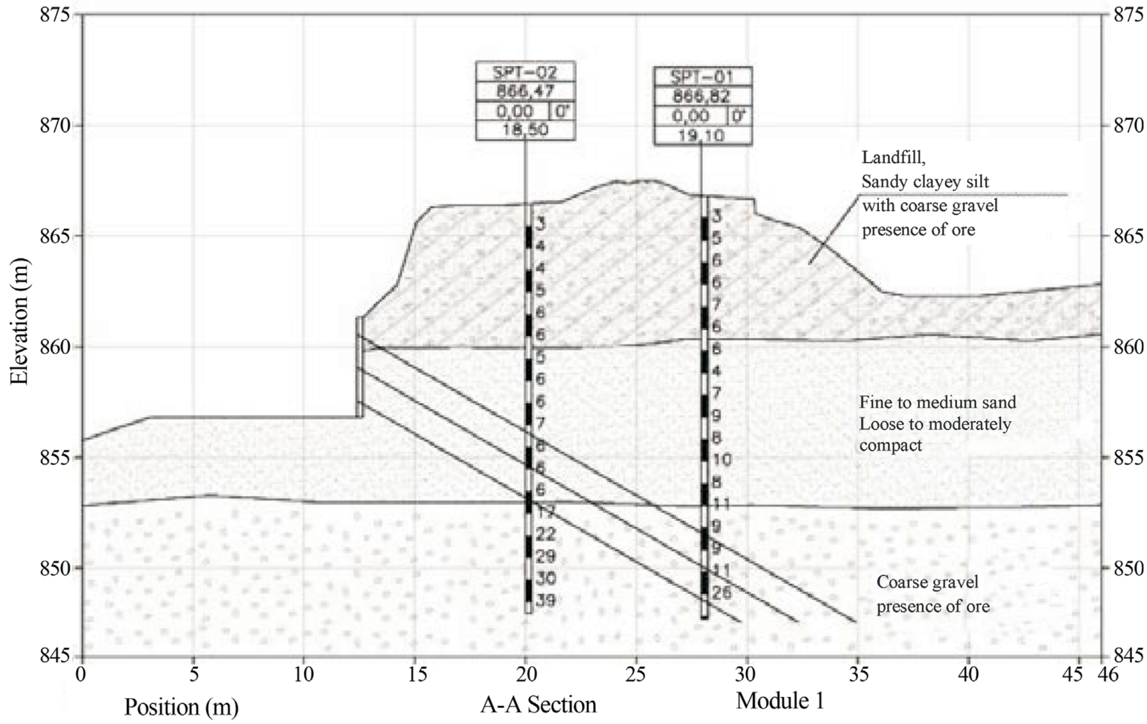

Figure 9 - Representation of anchors - Module 1, Lines 1, 2, 3 in the geotechnical profile (Porto, 2015).

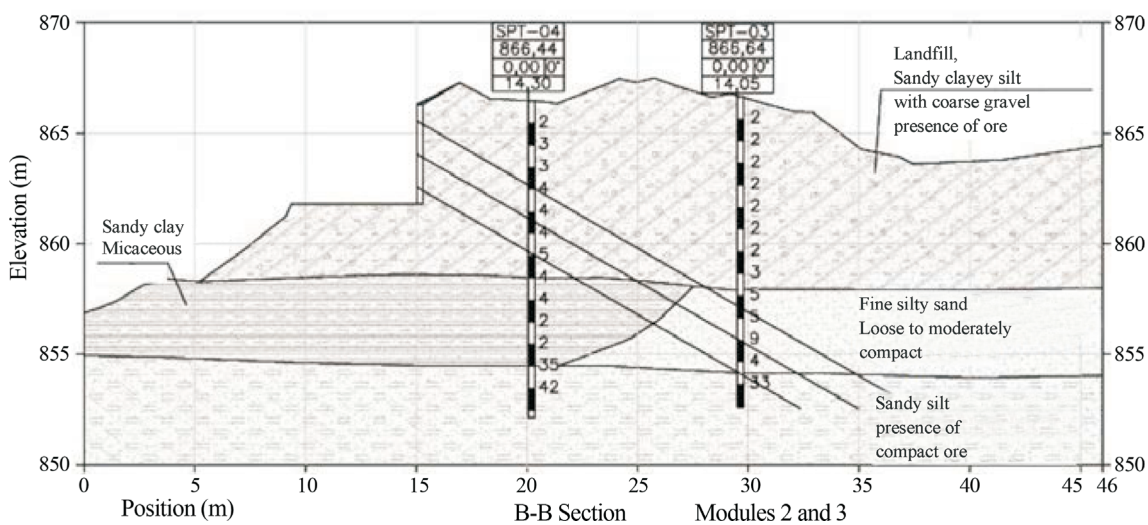

Figure 10 - Representation of anchors - Modules 2 and 3, lines 1, 2, 3 in the geotechnical profile (Porto, 2015).

ity as the grout injections number increases, as showed by average values presented in Fig. 11.

As discussed earlier, an increase in the geotechnical rupture load is observed as the number of injections increases (for the analyzed anchors). However, this increase does not show a trend. The A12 and A35 anchors presented a resistance gain of 35% from the sheath phase to the first injection phase. Nevertheless, the A27 anchor in the same phase achieved a 74% load gain, showing the great dispersion of results for the same soil type.

6.2. Theoretical rupture (mathematical extrapolation)

a) Anchors A02, A03, A05, A16, A17, A18, A19, A31 and A32 (first injection phase)

Geotechnical load capacity and the quantity of cement utilized in the first line in the first injection phase are shown in Fig. 12. For this group of tests, 896 kN was the average rupture load obtained, with 24% variability coefficient, 215 kN standard deviation and an average of 72 kN.

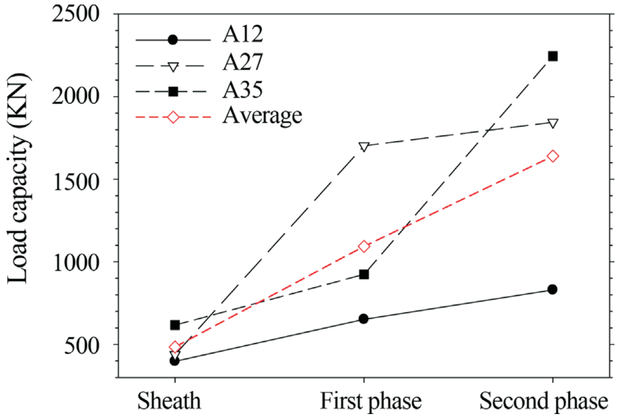

Figure 11 - Analysis of the influence of the injections number in load capacity (Porto, 2015).

Despite the geotechnical characteristics of the ground being very similar, there was a significant dispersion among the results. The load capacity data were obtained by mathematical extrapolation, from the acceptance tests results, as the anchors were not loaded to the limit of the geotechnical load.

b) Anchors A12, A27 and A35 (sheath)

In Fig. 13, the geotechnical load capacity and the quantity of cement utilized in the anchors' third line at the sheath stage are shown. It was obtained an average rupture load of 485 kN, with 24% variability coefficient, 116 kN standard deviation and an average of 67 kN.

It is important to note that the coefficient of variation is considered low, and therefore acceptable, when less or equal to 30% in a set of homogeneous data (Nogueira *et al.*, 2014), as achieved by our results.

c) Anchors A12, A27, A35 and A26 (first injection phase)

Figure 14 presents the geotechnical load capacity and the quantity of cement utilized in the anchors' third line, in the first injection phase. For this group of tests, an average rupture load of 1044 kN was obtained, with a 44% variability coefficient, 456 kN standard deviation and an average of 228 kN. Such results show a great dispersion in the measurements, especially for A27, despite the geotechnical ground conditions being very alike.

d) Anchors A11, A12, A14, A15, A26, A28, A29 and A35 (second injection phase)

Figure 15 presents the geotechnical load capacity and the quantity of cement utilized in the anchors' third line, in the second injection phase. For this group of tests, 1274 kN was the average rupture load obtained, with 44% variability coefficient, 561 kN standard deviation and average of 198 kN. It is noticed that there was a significant dispersion between the results obtained, especially for A35.

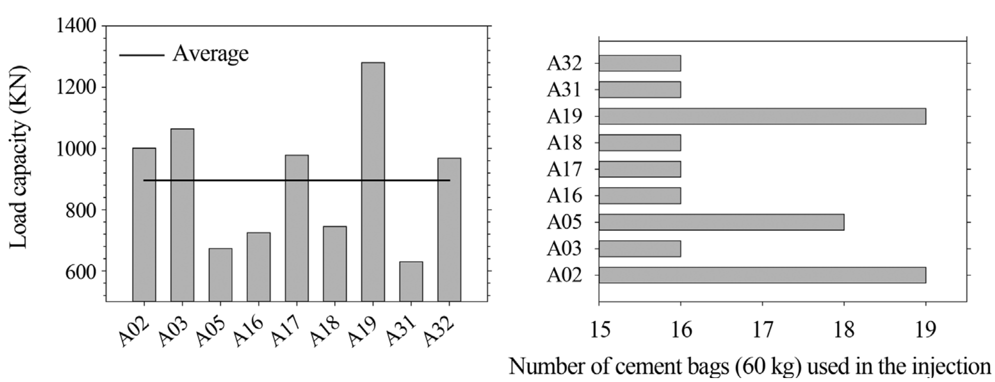

Figure 12 - First injection phase of the anchors' first line: a) Graph load capacity x tested anchor, b) Number of cement bags (60 kg) used (Porto, 2015).

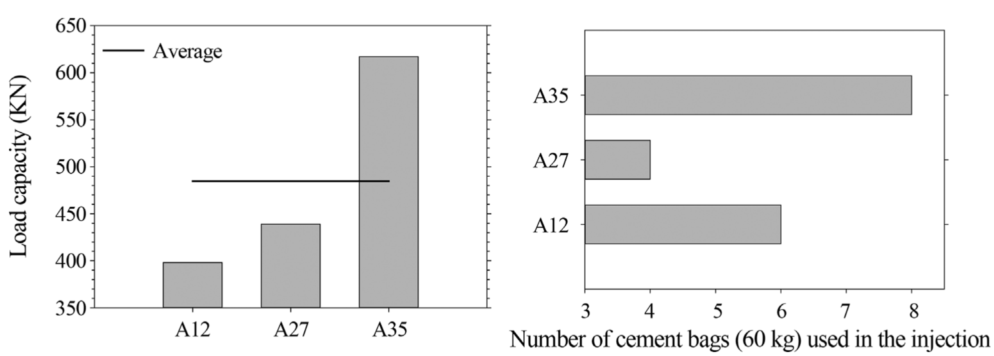

Figure 13 - Sheath of the anchors' third line: a) Graph load capacity x tested anchor, b) Number of cement bags (60 kg) used (Porto, 2015).

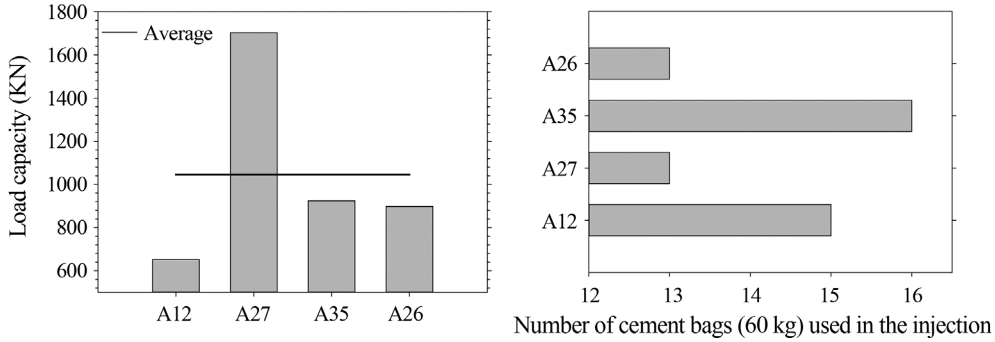

Figure 14 - First injection phase of the anchors' third line: a) Graph load capacity x tested anchor, b) Number of cement bags (60 kg) used (Porto, 2015).

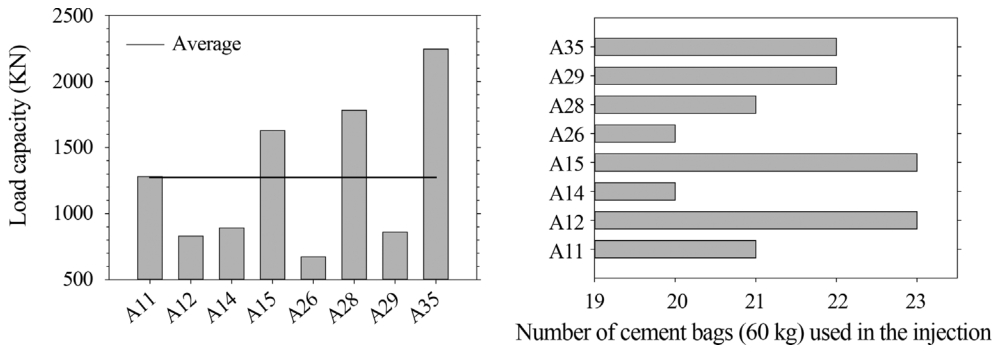

Figure 15 - Second injection phase of the anchors' third line: a) Graph Load Capacity x Tested Anchor, b) Number of cement bags (60 kg) used (Porto, 2015).

6.3. Final discussion

Evaluating the average load capacity values presented in Figs. 13, 14 and 15, it is possible to conclude that there is a significant gain in geotechnical load capacity in the first injection phase (125%) and a new gain of load capacity in the second injection phase, less significant than that of the first phase (50%).

In addition, analyzing the average load capacity shown in Figs. 12 and 14, it was observed an increase in the load capacity of 16.5% in the anchors' third line, in relation to the first line. This fact is possibly due to the fact that the anchors are anchored in a more resistant region of the geotechnical mass.

An increase in the geotechnical load capacity was expected as the amount of cement bag per anchor increased, since, in theory, the diameter of the bulb would increase and, therefore, there would be an increase in the contact between the soil and the bulb. This expectation was not verified in most of the analyzed cases, Figs. 12, 13, 14 e 15. This fact has a number of plausible justifications, for instance: (a) error in the measurement of the quantity of cement bags in the work. Anchorage works are quite dynamic, and the pumping of grout is quite fast. A slight lack of attention of the operator may cause errors in the quantity injected; (b) Loss of grout through soil voids. This fact is common in soft soils or regions with fractured rocks or boulders. Thus, the results presented in terms of quantity of cement bags in the work are inconclusive. However, it is expected that this work will be used as an analysis guideline for future works.

7. Conclusion

Through the analysis of the influence of grout injection numbers on load capacity, this study evidenced the dispersion of results in terms of load capacity for the same soil type.

To explain these divergent results, it is considered that the bulb diameters have different values, due to the lack of systematic injection control by headline valve and consequently, poor bulb structural control. This fact explains the different load capacity readings. Another reason for the difference of load capacity between the A35 (Fig. 15), for instance, and the other anchors of the third line in the second injection phase would be, probably, the fact that the A35 anchor reached a soil region more resistant than those reached by other anchors (such as boulder or fractured rock). The same occurred with anchor A27 (Fig. 14), whose result was discrepant in relation to anchors A12, A26, and A35 in the first injection phase.

Therefore, it is advisable that the anchorages should be performed with injection control by headline valve, injecting grout from the bottom to the hole entry, thereby the bulbs tend to be more uniform. Further research must be done in order to study the anchors' behavior, as well as to further analyze the factors that influence their load capacity in order to obtain a more comprehensive database to facilitate the implementation and improve the quality control of retaining wall construction, providing a more economical and safe construction.

Acknowledgments

Thanks to Alberto Zirlis, of Solotrat, for the indirect support to this research and to Consmara Engenharia for technical material about reinjectable and prestressed anchors.

References

ABNT (2006). Execução de Tirantes Ancorados no Terreno - NBR 5629. ABNT, Rio de Janeiro, RJ, Brazil, 24 p.

Das, M.; Purohit, S. & Das, S. (2016). Multi-objective optimization of reinforced cement concrete retaining wall. Indian Geotechnical Journal, 46(4):354-368.

Lee, S.W.; Kim, T.S.; Sim, B.K.; Kim, J.S. & Lee, I.M. (2012). Effect of pressurized grouting on pullout resistance and group efficiency of compression ground anchor. Canadian Geotechnical Journal, 49(8):939-953.

Liang, R. & Feng, Y.L. (2002). Development and application of anchor soil interface models. Soils and Foundations, 42(2):59-70.

Nogueira, M.L.G.; Gontijo, R.; Gomes, A.; Fonseca, J.A.; Bogutchi, T.F.; Neves, O.F. & Ribeiro, E.A.R.L. (2014). Laboratório de Estatística. 4th ed. Fumarc, Belo Horizonte, 234 p.

Porto, T.B. (2015). Ancoragens em Solos: Comportamento Geotécnico e Metodologia via Web para Previsão e Controle. PhD Dissertation, Department of Geotechnics, Universidade Federal de Ouro Preto, Ouro Preto, 224 p.

Seo, J.H.; Jeong, K.H.; Choi, K.H. & Lee, I.M. (2012). Pullout resistance increase of soil nailing induced by pressurized grouting. Journal of Geotechnical and Geoenvironmental Engineering, 138(5):604-613.

Van Der Veen (1953). The bearing capacity of a pile. Proc. Third Int. Conference on Soil Mechanics and Foundation Engineering, Zurich, v. 2, pp. 84-90.

Xiao, S. & Guo, W.D. (2017). Limit analysis of ground anchor forces. Geotechnical Engineering, 170(2):175-186.

Wang, H.; Cheng, J.; Guo, Y. & Gao, X. (2016). Failure mechanism of soil nail- prestressed anchor composite retaining structure. Geotechnical and Geological Engineering, 34(6):1889-1898.

Zirlis, A.C.; Pitta, C.A. & Souza, G.J.T. (2015). Manual Solotrat. Solotrat, São Paulo, 31 p.

Three-Dimensional Geostatistical Estimation of Soil Units: A Case Study From Capitão Pocinho, Pará, Brazil

J.C.B. Queiroz, T.O. Vieira, P.P. Araujo, F.A. Matos, M.M. Amin, C.W. Salame

Abstract. Lithology volumetric estimation was performed from samples of drills using three-dimensional geostatistical techniques. Monte Carlo simulations were performed to test the accuracy and influencing factors. Next, procedures were applied to a case study related to the environment. The simulation results show that estimates obtained via block Kriging can be relatively accurate. The case study in this research was challenging, given the quantitative limitations of information collected in the area. However, block Kriging proved to be consistent and feasible, and observed the model's assumptions. It also offers the advantage that, after obtaining data from the drills, all necessary computational tools are available for free. A computer code was developed in the R program for mapping 3D and calculation of volumes of lithology. These results open precedents for future research using other geostatistical techniques, such as Indicator Simulation, Spatio-temporal Analysis, or even co-Kriging, correlating the lithologies with variables related to environmental contamination by pollutants. In the study area, the lithological profiles of piezometer wells revealed that the vadose zone was composed predominantly of sandy-clay material. The soil classified as sandy clay may have been associated with free aquifers. This sandy-clay material totaled around 2.67% of the study area, with a volume of approximately 596 240 m^3. The classified material, such as silty clayed sand and sand, which seemed to predominate in the saturated zone, represented about 14.31% and 13.1%, respectively. In this case, the volume estimated for each lithology was around 3 189 280 m^3 and 2 916 384 m^3, respectively. The highest prevalence was sandy clay with 61.8% of the region's volume, which is about 13 795 264 m^3. Finally, the silty sand represented about 8.2% of the total, with an estimated volume of 1 836 672 m^3.

Keywords: lithology, Monte Carlo simulation, block Kriging.

1. Introduction

The use of geostatistical modeling in geological studies has become increasingly common due to the accuracy of estimates provided and measurements of the uncertainties associated with these estimates. Nevertheless, taking into account only the analysis of categorized or categorical variables, in the case of lithologies (soil types), there are few studies involving geostatistical techniques. In the specific case of applying Kriging to estimate lithologies, Rosenbaum, Rosen & Gustafson (1997 apud Oliveira & Rocha, 2011) probably conducted the first study on this issue.

Most studies involving a geostatistical approach to geological variables have comprised estimates of mineral resources and reserves for economic viability plans in mineral exploration. This is justifiable, since the theory of regionalized variables and Kriging were formulated, by Krige and Matheron (Matheron, 1982) in the 1950s, with these objectives in mind. However, in recent decades, geostatistical modeling methodology has also become applicable in analyses aimed at estimating and minimizing environmental impacts caused by the exploitation of natural and mineral resources.

One of the primary environmental concerns for authorities and the population of most industrialized countries pertain to the contamination and pollution of drinking water reservoirs, as this may result in serious public health problems. According to Queiroz (2003), groundwater pollution is more worrying than surface water pollution, as the former water type does not renew as quickly as the latter. The vulnerability of groundwater to contamination by pollutants depends on several factors, among which are the presences of ground lithology in the aquifer.

Several consolidated methods for assessing the vulnerability of aquifers to pollution, such as GOD, DRASTIC, and SINTACS, consider the lithology as a factor of influence, with fairly significant weights (Aller *et al.*, 1987). Thus, three-dimensional (3D) mapping of lithologies reveals important information about their format and their locations in the area studied. Oliveira (2008) demonstrated the use of a Kriging indicator in creating geological models based on estimates of lithologies.

Joaquim Carlos Barbosa Queiroz, D.Sc., Associate Professor, Instituto de Geociencias, Universidade Federal do Pará, Belém, PA, Brazil. e-mail: joaquimqz@gmail.com.
Tiago de Oliveira Vieira, M.Sc., Instituto Federal de Educação, Ciência e Tecnologia do Pará, Belém, PA, Brazil. e-mail: tiagovieira7@yahoo.com.br.
Paulo Pontes Araujo, D.Sc., Companhia de Pesquisa de Recursos Minerais de Belém, Departamento de Hidrologia e Gestão Territorial, Belém, PA, Brazil. e-mail: hg.paulo.pontes@gmail.com.
Francisco de Assis Matos, D.Sc., Associate Professor, Instituto de Geociencias, Universidade Federal do Pará, Belém, PA, Brazil. e-mail: famatos@ufpa.br.
Mario Miguel Amin, D.Sc., Associate Professor, Nucleus for Amazon Research, Federal University of Para, Brazil, 66075-110, Belém, PA, Brazil. marioamin@gmail.com.
Camil Wadih Salame, Ph.D. Student, Instituto de Geociencias, Universidade Federal do Pará, Belém, PA, Brazil. e-mail: camilsalame@yahoo.com.br.
Submitted on November 28, 2016; Final Acceptance on June 24, 2017; Discussion open until December 29, 2017.

Analyses of this type are generally intended to associate certain lithologies with the presence of substances or materials of interest, such as minerals, gas, and oil. This principle of relationship between lithology and certain objects can be seen as analogous to vulnerability studies and the measurement of environmental impacts, which can relate lithologies in the region with potential pollutants, such as nitrate, ammonia, etc.

The purpose of this study is to analyze the applicability of geostatistics, highlighting Kriging combined with a 3D block model (block Kriging) and the volumetric estimate of lithology with drill samples. Thus, in order to assess the methodology regarding volumetric estimates for underground objects, Monte Carlo non-conditional simulations were used. Then, 3D geostatistical modeling techniques were applied using actual sample surveys for mapping the lithologies in the studied area. Finally, volumetric estimates were conducted for rock types found in the study area, particularly materials that made up the potentiometric surface, using the proposed methodology.

2. The Study Area

The study area is located on the river Capitão Pocinho, next to its springs, in the Citropar I and Citropar II farms, and in the village of Capitão Pocinho. Both sites are in Capitão Poço County, in the northeastern region of Pará, Brazil (Fig. 1). According to Araújo (2011), the area has an urban-rural setting, with a land area of approximately 1.2 km^2, and is located 160 km from the state's capital (Belém-PA). Its geographical coordinates are 1°49'58.9" S and 1°49'22.4" S, and 53°12'7" W and 53°11'27" W. Figure 1 shows a map of the State of Pará, with the location of Capitão Poço County and the satellite image of the study area with the location of monitoring wells.

The geology of the study area is predominantly composed of tertiary sediments of the Barreiras and Post-Barreiras Group, and alluvial quaternary sediments. The Barreiras Group consists of yellow-reddish, medium-to-coarse sandstones, with poorly sorted pebbles that are friable and rusty; cream-yellow sandstones with a fine average particle size; well-selected, compact, white mudstone levels of iron oxide stains; and black-gray mudstone.

The Post-Barreiras unit consists of sandy clay, unconsolidated sediments, with little levels of ferruginous sandstone pebbles. The recent sediments are unconsolidated, typical of organic clays with plant debris and bioturbation, and layered with silts and fine sands, with thicknesses ranging from millimetric to centimetric. These deposits occur along the major rivers and smaller tributaries, being in greater proportion in the vicinity of artificial dams, which form floodplains. The hydrogeological profile of the study area is shown in Fig. 2, which also shows the presence of suspended unconfined aquifers.

3. Material and Methods

Information on the lithology of the study area was collected via 15 monitoring wells, with a motorized mechanical probe MB1 (Honda engine 01 HP) coupled to an

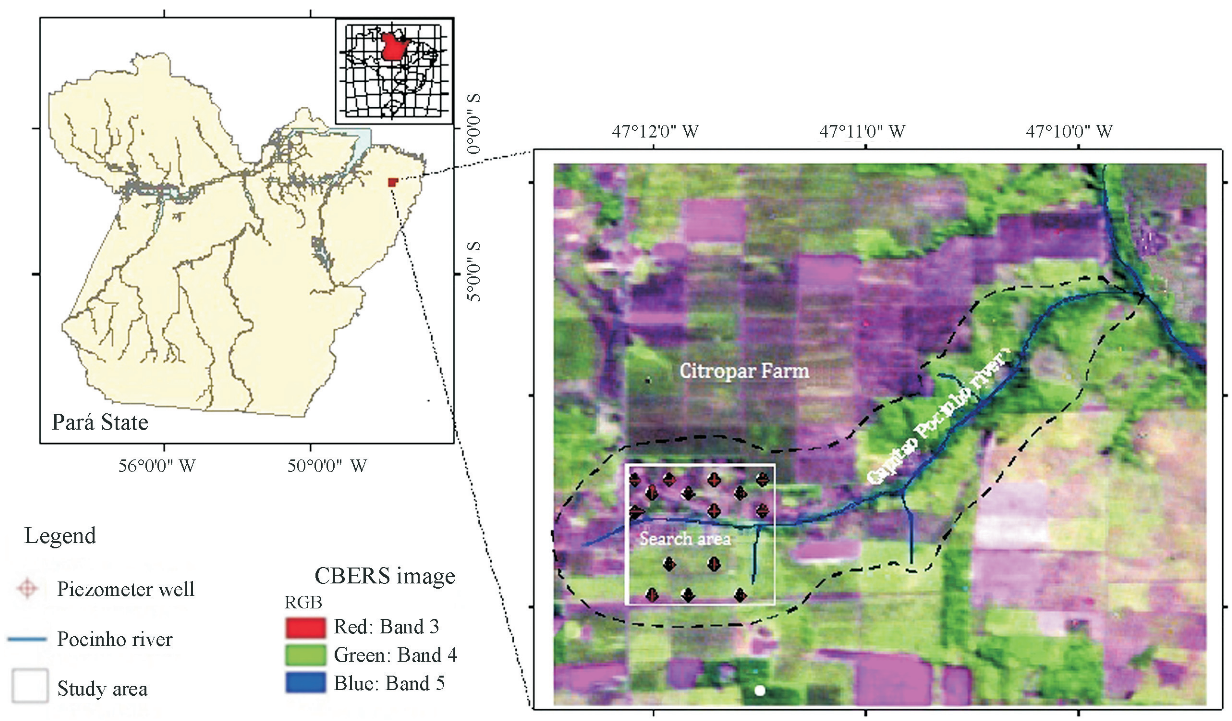

Figure 1 - Geographical location of Capitão Poço County, including a satellite image of the study area and location of monitoring wells (extracted from Araújo, 2011).

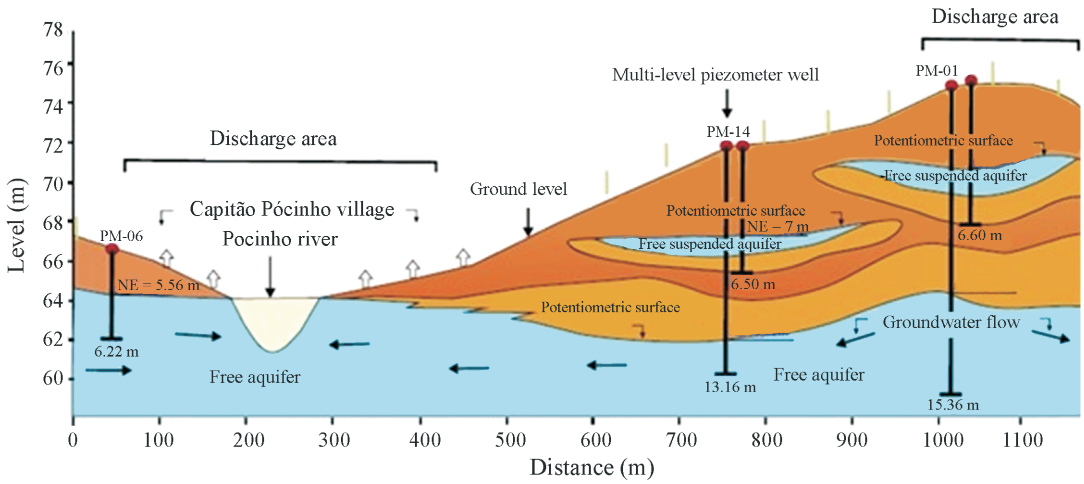

Figure 2 - Hydrogeological profile across the channel of the Capitão Pocinho River, on the north-south axis (extracted from Araújo, 2011).

excavator auger with a four-inch diameter. Samples were collected every meter drilled in the 15 wells within the study area, or when there was a change in lithotype. This material was homogenized, divide into quarters, packed in polypropylene bags (NBR 7181), and sent for sieve analysis (Araújo, 2011).

The lithology attribute in areas not sampled can be estimated through the application of geostatistical methods. Kriging is a generic geostatistical name adopted for a family of regression algorithms based on least squares using a linear regression estimator $Z^*(\mathbf{u})$ given by:

$$Z^*(\mathbf{u}) - m(\mathbf{u}) = \sum_{\alpha=1}^{n(\mathbf{u})} \lambda_\alpha(\mathbf{u})[Z(\mathbf{u}_\alpha) - m(\mathbf{u}_\alpha)] \quad (1)$$

where $\lambda_a(\mathbf{u})$ is the weight assigned to each observed value $Z(\mathbf{u}_\alpha)$ located within a particular neighborhood $Z^*(\mathbf{u})$ centered on $\mathbf{u}$ location. The weights $\lambda_a(\mathbf{u})$ are chosen to minimize the estimation or variance error $\sigma_E^2(\mathbf{u}) = Var[Z^*(\mathbf{u}) - Z(\mathbf{u})]$ under the condition of a non-bias estimator. These weights are obtained by solving a system of linear equations known as the Kriging system.

A detailed presentation of the mathematics involved in these equations can be found in geostatistical textbooks such as those by Isaaks & Srivastava (1989) and Goovaerts (1997). The differences between the various types of Kriging reside in the model considered for the tendency $m(\mathbf{u})$ in Eq. 1. Simple Kriging (SK) considers the average $m(\mathbf{u})$ that is known and constant throughout the study area, while the ordinary kriging limits the average stationary domain in the local neighborhood $W(\mathbf{u})$ and wherein, unlike SK, the average is unknown (Goovaerts, 1997). Uncertainty can be modeled on the unknown value $z(\mathbf{u})$ from the conditional cumulative distribution function (ccdf), $F(\mathbf{u};z|(n))$.

The value of this function is determined by a number of cut-off values z_k discretizing the variation range of z:

$$F(\mathbf{u}; z_k | (n)) = Prob\{Z(\mathbf{u}) \le z_k)|(n)\} \quad k = 1, \ldots K \quad (2)$$

Nonparametric geostatistical estimation of the conditional cumulative distribution function values is based on the interpretation of conditional probability (Eq. 2). As the conditional expected value of a variable indicator $I(\mathbf{u};z_k)$ based on n observed data,

$$F(\mathbf{u}; z_k | (n)) = E\{I(\mathbf{u}) \le z_k)|(n)\} \quad (3)$$

where $I(\mathbf{u};z_k) = 1$ if $Z(\mathbf{u}) \le z_k$ and zero otherwise. The values of ccfd are estimated by ordinary Kriging of transformed indicative data. In the case of qualitative data, the information is related to a categorical attribute such as type of lithology, with two categories. In this case,

$$I(\mathbf{u}_\alpha; z_{cat}) = \begin{cases} 1 & if\ z(\mathbf{u}_i) = z_{cat} \\ 0 & otherwise \end{cases} \quad (4)$$

where $\alpha = 1, \ldots, N$ (number of observations).

Thus, $I(\mathbf{u}_\alpha;z_{cat})$ is the variable indicator of zcat category. Implementing the indicator approach involves choosing the set of cutting values, K, so that the range of values of variable z is divided into $K + 1$ classes with approximately equal frequencies. For each cutoff value z_k, indicative experimental semivariograms data is calculated, given by (Goovaerts, 1997).

$$\hat{\gamma}_I(\mathbf{h}; z_k) = \frac{1}{2N(\mathbf{h})} \sum_{\alpha=1}^{N(\mathbf{h})} [i(\mathbf{u}_\alpha; z_k) - i(\mathbf{u}_\alpha + \mathbf{h}; z_k)]^2 \quad (5)$$

where $N(\mathbf{h})$ is the number of data pairs within a given class separated by vector $\mathbf{h}$ (distance and direction). The higher the value of $\hat{\gamma}_I(\mathbf{h}; z_k)$, the less connected in space are the values of a given category.

The semivariogram is the main geostatistical tool for spatial variability analysis, and the main objective is to quantify the spatial variability of available samples in order to detect any spatial relationship. Although many applications of semivariogram analysis are limited to two dimensions, the analysis can be readily extended to 3D. Matheron (1982) deduced a theoretical relationship to $\gamma(\mathbf{h})$. One of the most-used semivariogram models is referred to as the spherical model, and is expressed mathematically, in general terms, as

$$\gamma(\mathbf{h}) = \begin{cases} C_0 + C\left(\dfrac{3a}{2\mathbf{h}} - \dfrac{a^3}{2\mathbf{h}^3}\right) & to\ 0 < \mathbf{h} < a \\ C_0 + C \quad to\ \mathbf{h} \geq a \end{cases} \tag{6}$$

where C_0 is the inherent random variability of the samples at zero distance, referred to as the nugget effect. The distance at which the samples become independent of one another is represented by a, referred to as range. The constant semivariance where the values of $\gamma(\mathbf{h})$ are leveled at distances greater than a is represented by sill ($C_0 + C$), where C is referred to as spatial variance or semivariogram.

This model's parameters are determined interactively through fitting of theoretical models to the analysis' results of the semivariogram sample. The resulting model, assuming that the samples are representative, is a measure of spatial variability of the variable under study.

Since the uncertainty about the unsampled value has been modeled using an indicative approximation, an estimate of this unknown value can be obtained from the conditional cumulative distribution function. The mean estimated conditional distribution, known as the *E*-type of $z(\mathbf{u})$, is defined as,

$$z(\mathbf{u})^*_E \approx \sum_{k=1}^{K+1} z'_k \left[F^*(\mathbf{u}; z_k|(n)) - F^*(\mathbf{u}; z_{k-1}|(n))\right] \tag{7}$$

while the conditional variance of the conditional cumulative distribution is obtained by,

$$\begin{aligned} \sigma^2(\mathbf{u}) &\approx \sum_{k=1}^{K+1} [z'_k - z(\mathbf{u})^*_E]^2 \\ &\times [F^*(\mathbf{u}; z_k|(n)) - F^*(\mathbf{u}; z_{k-1}|(n))] \end{aligned} \tag{8}$$

where z_k, $k = 1, \ldots K$ are the cutting values that discretize the variation band of z, and the z'_k value is the mean of the ($z_{k-1} - z_k$), which depends on the interpolation model used within classes. For example, for the linear model z'_k = ($z_{k-1} + z_k$)/2.

To estimate values for 3D regions, block Kriging is used. The blocks are subdivisions of a larger block that encompasses the entire area of study. According to Catarino (2009), the size of the blocks can be uniform or may be variable, considering factors such as the spacing between the boreholes.

Analyses were performed using gstat software implemented in the R environment (R Development Core Team , 2005). The procedures were performed in sequential steps, including, in this case, data validation of boreholes, exploratory analysis, construction of the experimental semivariogram, and semivariogram modeling, determination of the support (block size), application of block Kriging and visualization (mapping) in three dimensions, and finally estimation of the volume of lithology (Isaaks & Srivastava, 1989). The volume of the determined lithology of interest or any of the K classes are estimated by,

$$\hat{V}(z_k) = \sum_b^B \{I[\hat{z}^*_V(\mathbf{u}_b; z_k)] \times V(\mathbf{u}_b)\} \tag{9}$$

where $\hat{z}^*_V(\mathbf{u}_b; z_k)$ is estimated by block Kriging for block b and V($\mathbf{u}_b$) is the block's b volume, while, as per Isaaks & Srivastava (1989)

$$I[\hat{z}^*_V(\mathbf{u}_b; z_k)] = \begin{cases} 1,\ if\ z^*_V(\mathbf{u}_b; z_k) \\ \quad = \max[(z^*_V(\mathbf{u}_b; z_1), z^*_V(\mathbf{u}_b; z_2), \ldots, \\ \quad z^*_V(\mathbf{u}_b; z_K)] \\ 0,\ otherside \end{cases} \tag{10}$$

4. Analysis and Discussion of Results

To verify the consistency of the proposed methodology, an empirical method of measurement of errors through Monte Carlo simulation was developed. This simulation includes all stages of the volume estimation process, from drilling sampling, through the geostatistical methods, and finally the volume estimation, since the objective is to detect problems that may occur in the use of geostatistics in borehole studies.

The computational implementations were all subsidized using free software, *i.e.*, the graph and statistical environment R (version 2.15.2) used in implementing the simulation and its application to the collected data, with the addition of gstat packages (variogram, Kriging, and inverse distance weighting [IDW]), lattices (three-dimensional maps), and rgl (iterative graphics).

During the simulation process, a sphere was initially generated, which is the basic shape from which to estimate the volume. Even though a spherical shape is unlikely in lithological materials, this form was adopted as it is a closed and defined geometric shape, which enables accurate calculation of the estimate deviation. The radius of the sphere is defined as 30 m centered on a cube with a thickness (x), width (y) and depth/height (z) equal to 100 m, representing the entire area of study. Next, 15 points were randomly selected in the plane of the x and y axes, representing the possible monitoring wells. A binary variable was created that took the value 1 if the point belonged to the sphere and zero otherwise. This enabled simulation of what happens in practice in drilling studies. For realization of the block Kriging, the block support was initially set at 10 x 10 x 10 m^3. In this case, the area of study (100 x 100 x 100 m^3) was divided into 1,000 regular sub-blocks. The variogram model used to calculate the Kriging should be set to whatever the sample is (Taylor *et al.*, 2001). The results enabled estimation of the volume, based on Eq. 9 and the absolute relative error given by:

$$\varepsilon = \frac{|\hat{V} - V|}{V} \tag{11}$$

where $\hat{V}$ is the estimated volume and V is the actual volume of the sphere, such as $V = \frac{4}{3}\pi r^3$. Since the radius, r, of the sphere is 30 m, V ≈ 113097.3 m^3. Volumes were estimated considering blocks with support of 5 x 5 x 5 m^3 and block supports of 2.5 x 2.5 x 2.5 m^3. The above procedures were repeated 2000 times and the average of the errors calculated. Then, volumes for random samples of 30, 60, and 120 wells were estimated. Thus, the influence of the size of the support and the number of samples in the volume estimates could be evaluated using geostatistical techniques. The results are shown in Table 1 and Fig. 3.

The results of the sample simulations indicate that block Kriging can provide satisfactory results for estimated volumes. The results show that the accuracy of the estimate increases when the number of samples is increased. Decreased values of errors can be related to the kriging smoothing effect that is increased when the block support becomes smaller.

Table 1 - Mean absolute relative errors (m^3).

Number of wells	Support		
	10 x 10 x 10	5 x 5 x 5	2.5 x 2.5 x 2.5
15	0.24448	0.23863	0.23448
30	0.15398	0.14710	0.14149
60	0.09549	0.08650	0.08073
120	0.05727	0.05066	0.04560

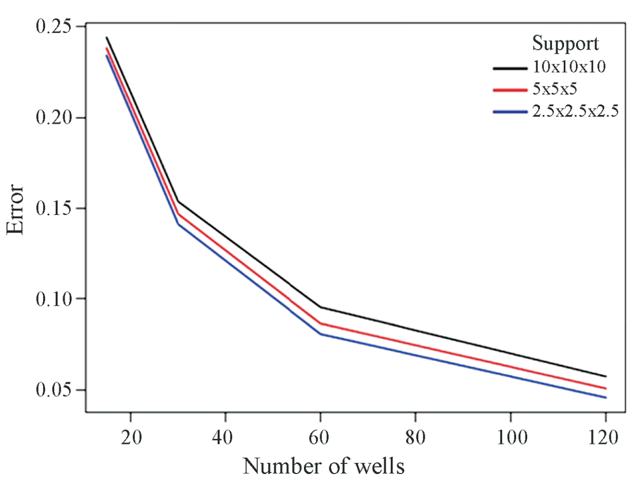

Figure 3 - Mean of the relative absolute error in relation to the number of wells sampled by support blocks.

The results of the particle size analysis for the samples collected in the monitoring wells revealed the existence of five classes of materials: sand, clayey sand, silty sand, silty clayey sand, and sandy clay. These materials form the Barreiras unconfined aquifer and match the geological model shown in Fig. 2. The distribution of the five lithologies in 3D space is shown in Fig. 4.

To calculate the semivariogram indicators of each lithology, certain considerations were necessary, such as the scale of difference between the axes. In this case, it is known that the maximum distance between sampling points on the axes UTM-N(x) and UTM-E(y) was approximately 1014 and 1110 m, respectively, whereas for the axis of coordinates (z) the distance was 30 m. Therefore, the parameters used for calculating the semivariogram had to be different to the axis of coordinates in relation to UTM-N and UTM-E. In this case, the values of the x and y axes were divided by 100. Table 2 shows the parameters used in calculating the semivariogram indicators of all lithologies, by direction.

Figure 5 shows the graphs of the experimental semivariogram indicators and adjusted models for each of the lithologies found in the study area. Because the amount of boreholes was relatively low, it was not possible to perform analysis of the anisotropy in the study area. Besides the ad-

Table 2 - Parameters used to calculate the experimental semivariogram.

Direction	Number of steps	Steps (m)	Tolerance (m)
UTM-N	15	0.60	0.3
UTM-E	15	0.60	0.3
Elevation (z)	15	0.60	0.3

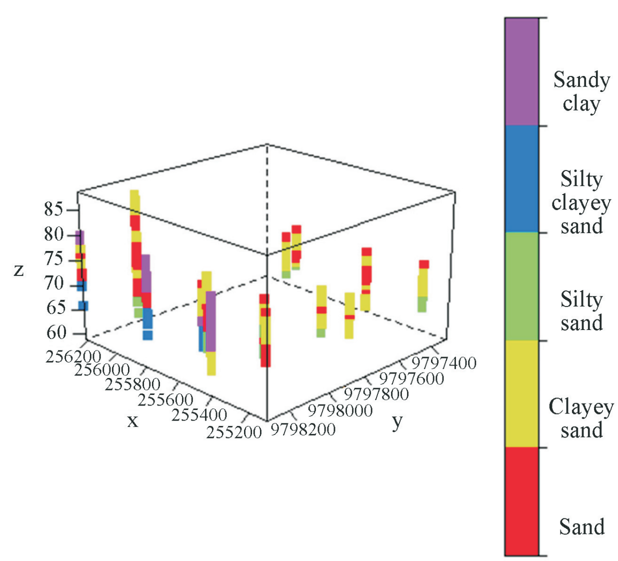

Figure 4 - 3D view of the results obtained from the drilling sampling.

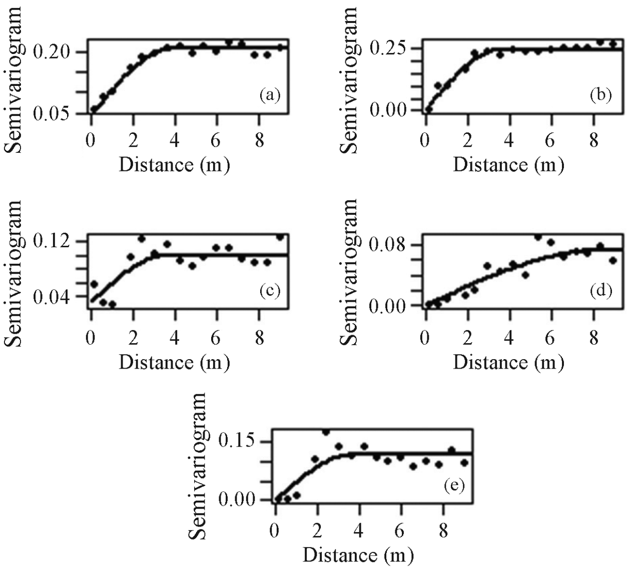

Figure 5 - Experimental variograms and models adjusted for (a) sand, (b) clayey sand, (c) silty sand, (d) silty clayey sand, and (e) sandy clay.

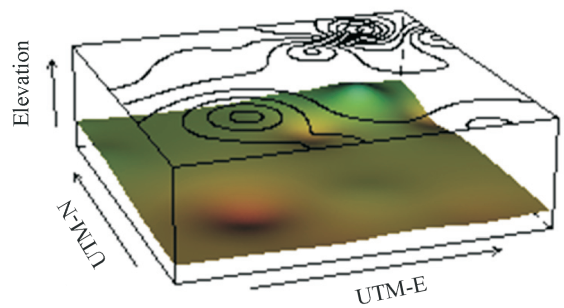

Figure 6 - Contour map of estimated surface area under study.

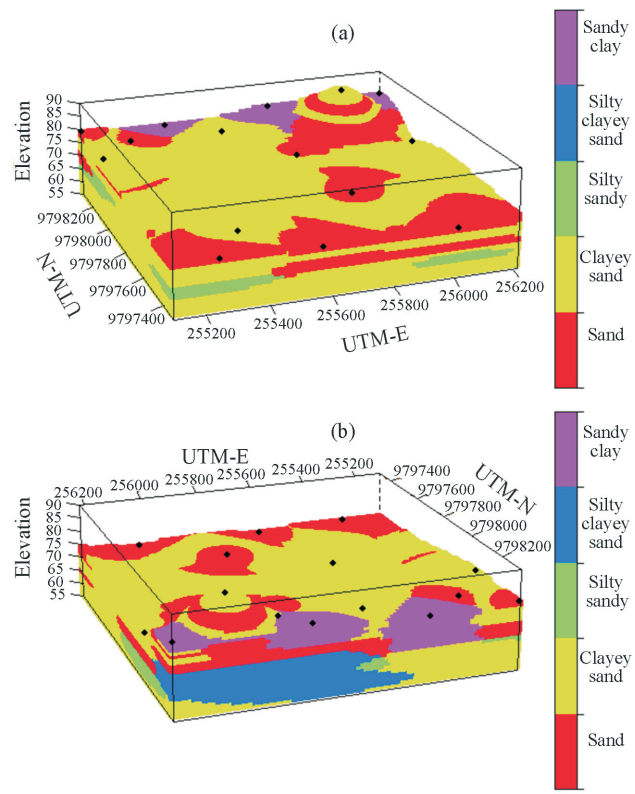

Figure 7 - Map of the distribution of lithologies in the outer region of the study area at NE (above) and SW (below) perspectives.

vantage that Kriging does not require a normality of variables assumption, the semivariogram usually presents simpler structures and is easy to model. The maximum ranges varied from about 3.5 to 4.5 m, except with respect to the lithology classified as silty clayey sand, which presented a range of around 8.6 m.

There are several methods for supporting the setting of a block model. Based on the results of the simulation, in order to improve the mapping and estimate the volume of lithologies, the largest possible number of blocks was used, with limitations on computational resources observed. Thus, the support adopted in Kriging interpolation of blocks was 4 x 4 x 1 m, totaling 2 410 260 blocks (Table 3), following the criteria shown in Table 1.

Due to the small number of sampling points (15 sampling points with information on the maximum elevation of boreholes), the study area estimate of the surface was obtained via interpolation using the method of IDW (Fig. 6). Thus, it was possible to remove from the interpolating mesh the blocks located above the estimate's surface. Following removal of these blocks, 1 395 865 blocks remained.

For easy viewing, the results of the block Kriging in the study area were presented in two different perspectives. Fig. 7 shows a map of the distribution of lithologies in the outer region of the study area, and Fig. 8 the distribution map of lithologies in the inner region, with a "slice" removed. Table 4 shows the estimated volumes for each lithology. A study by Araújo (2011) showed that in the lithological profiles of piezometer wells, the vadose zone consists primarily of sandy-clay material.

Table 3 - Parameters used for determining the support blocks.

Direction	Minimum (m)	Maximum (m)	Blocks distance (m)	Steps
UTM-E	255102	256214	4	278
UTM-N	9797302	9798318	4	255
Elevation	56	90	1	34

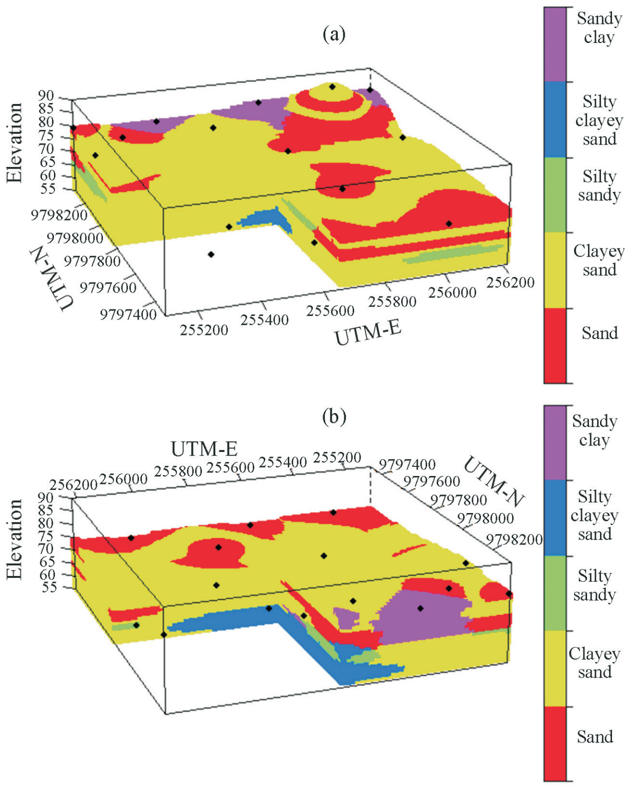

Figure 8 - Map of the distribution of lithologies in the inner region of the study area at NE (above) and SW (below) perspectives.

The vadose (or unsaturated) zone is the part of the ground that is partially filled with water. It can be seen from Figs. 7 and 8 that the soil classified as sandy clay may be related to unconfined aquifers shown in the model of the hydrological profile presented in Fig. 2. These results coincide with and reinforce the potentiometric analysis of headwaters of the watershed of the Capitão Pocinho river conducted by Araújo (2011). This sandy-clay material totals around 2.7% of the study area, with a volume of approximately 596240 m^3 (Table 4).

The materials classified as silty clayey sand and silty sand seem to predominate in the saturated zone, at about 14.3% and 8.2%, respectively. In this case, the volume estimated for each lithology was around 3189280 m^3 and 1836672 m^3, respectively. The highest prevalence was clayey sand, with 61.8% of the volume of the region, which equates to about 13795264 m^3. Finally, the sand represents approximately 6.1% of the total, with an estimated volume of 2916384 m^3 (Table 4).

Table 4 - Results of the volumetric estimate of lithology.

Material	Number of blocks	Volume (m^3)	Proportion (%)
Sand	182 274	2 916 384	13.1
Clayey sand	862 204	13 795 264	61.8
Silty sand	114 792	1 836 672	8.2
Silty clayey sand	199 330	3 189 280	14.3
Sandy clay	37 265	596 240	2.7

5. Conclusions

The use of 3D models as an additional instrument in environmental studies has had little application to date, probably due to the degree of complexity that comes with these models. However, the current study has shown how use of these models can enrich environmental assessments, and make them more accurate and attractive. An example of this would be the study of groundwater resources management, in which estimates of volumes of soil and aquifer material can improve the accuracy of calculations of the vulnerability index, since the potential for groundwater contamination is directly related to the compounds' physical and chemical characteristics, as well as the specific environmental characteristics of the type of soil, vadose zone material, aquifer material, and so on.

The 3D knowledge of the geological characteristics that conduct aquifer groundwater can contribute substantially to understanding of the variation of hydraulic parameters in complex media. One of the difficulties that will need to be overcome is the use of 3D geostatistical techniques in groundwater regions that involve some oscillation in the static level in monitoring wells at certain times of the year. A suggested alternative is joint space–time analysis, where the seasonality of the rainy periods could be included in the model. The number of wells compared to the scope of the study area is a limiting factor in the current study. Future research should use larger amounts of information, which would make possible extremely concise variogram analysis, including anisotropy verification, and thus lithological mapping and more accurate volumetric estimates.

Obviously, lithological mapping by itself may not definitively contribute to solving certain environmental issues; however, when combined with other variables, as indicated in the literature, important conclusions can be reached with respect to environmental issues. Therefore, after analyzing the results of the current study, it is also recommended that future researchers verify other techniques developed in the framework of geostatistics, such as indicator simulation and co-Kriging, correlating the types of lithologies with the incidence of environmentally harmful substances, and especially underground aquifers.

References

Aller, L.; Bennett, T.; Lehr, J.H.; Pretty, R.J. & Hackett, G. (1987). DRASTIC: A standardized system for evaluating ground water pollution potential using hydrogeologic settings. EPA-600/2-87-035.

Araújo, P.P. de (2011). Avaliação dos Compostos Nitrogenados no Aquífero Livre em Agroecossistemas de Citros no Alto Rio Capitão Pocinho, Amazônia Oriental. Tese de Doutorado em Ciências Agrárias _ Universidade Federal Rural da Amazônia e Empresa 364 Brasileira de Pesquisa Agropecuária, Belém 175 pp.

Catarino, B.M.P. (2009). Modelação Tridimensional de uma Jazida Mineral Prospectada por Sondagens e Objectivando a sua Exploração a Céu Aberto. Mestrado em Engenharia Geológica e de Minas _ Universidade Técnica de Lisboa, Lisboa.101 pp

Goovaerts, P. (1997). Geostatistics for Natural Resources Evaluation. New York: Oxford University Press. (Applied Geostatistics Series).

Isaaks, E.H. & Srivastava, R.M. (1989). An Introduction to Applied Geostatistics. New York: Oxford University Press.

Matheron, G. (1982). Pour unites analyse krigeante you give données régionalisées. Rep. N-732, center of Géostatistique, Fontanebleaus, France.

NBR 7181 – ABNT – “Solo – Análise granulométrica – procedimento”. Rio de Janeiro: 1984a. 13p.

Oliveira, S.B de (2008). Estudos Geoestatísticos Aplicados a um Depósito Magmático de NI-CU. Mestrado em Geociências (Recursos Minerais e Hidrogeologia). Universidade de São Paulo, São Paulo, 94 pp.

Oliveira, S.B. & Rocha, M.M. da (2011). Krigagem indicadora aplicada aos litotipos de depósito de ni-cu de americano do Brasil, go. Revista do Instituto de Geociências da USP,11(2): 123-134.

Queiroz, J.C.B. (2003). Utilização da Geoestatística na Quantificação do Risco de Contaminação por Metais Pesados, na Área Portuária de Santana, Amapá. Doutorado em Geociências , Universidade Estadual Paulista, Rio Claro, 170 pp.

R Development Core Team (2005). R: A language and environment for statistical computing. R Foundation for Statistical Computing, Vienna, Austria. URL http://www.R-project.org.

Rosenbaum, M.S.; Rosen, L. & Gustafson, G. (1997). Probabilistic model for estimating lithology. Engineering Geology, 47(1):43-55.

Taylor, G.; Kudowor, A.Y.T. & Fairbairn, D. (2001). Empirical method of error analysis in volume estimation: Monte carlo simulation under kriging and triangulation. Journal of Surveying Engineering, 127(2):59-77.

List of Symbols

DRASTIC: **D**epth to water, net **R**echarge, **A**quifer media, **S**oil media, **T**opography, **I**mpact of the vadose zone, and hydraulic **C**onductivity of the aquifer.

GOD: **G**roundwater occurrence, **O**verall lithology of aquifer or aquitard and **D**epth to groundwater table.

IDW: Inverse Distance Weighting

SINTACS: groundwater table depth from **S**urface, actual **I**nfiltration, self-depuration effect u**N**saturated zone, overburden **T**ype, hydrogeological characteristics of the **A**quifer, hydraulic **C**onductivity and topographical **S**urface slope.

Discussion

Soils and Rocks
v. 40, n. 2

Discussion

An Evaluation of the Shaft Resistance of Piles Embedded in Gneissic Rock

Discussion by:
Frederico Falconi,
Consultant, ZF & Engenheiros Associados, e-mail: fred@zfsolos.com.br

The writer would like to offer some comments addressed to the authors of "An Evaluation of the Shaft Resistance of Piles Embedded in Gneissic Rock".

The authors state that the pile base contribution is not considered. Actually, in practice, it is quite usual to take advantage of the toe resistance, provided proper base clean-up can be ensured. Given that the authors have conducted many dynamic load tests, and analyzed them with CAPWAP C, the presentation of such analyses would be of great help to clarify the contribution of shaft and toe resistances (both soil and rock).

The authors might consider writing a paper that reports and discusses, for each of the 5 typical profiles shown in Figs. 13 to 17, the complete results of dynamic load tests, focusing on the contributions from both soil and rock to the ultimate toe and shaft pile resistance.

Specimens for laboratory compression tests on rocks are usually obtained from essentially sound rock fragments. Do the authors believe that this could be the reason for the very limited range of q_u shown in Table 3, as compared to the results presented in Table 2? The correlation between q_u and RQD is quite low for the experimental data of Table 3.

Equation 7, for maximum mobilized shear stress, was derived from Eq. 6, in which the multiplier for RQD is 0.6. Given that the observed average multiplier was 0.8 to 0.9 (Figs. 11 and 12), Eq. 7 seems to be overly conservative as compared to other equations proposed elsewhere for weak rocks.

On page 19 the authors report a displacement of 2 mm for E111, Block 16. In Table 4, and in the figures, that displacement is 4.7 mm.

The statement that NBR 13208, dated 2007, follows the more recent ASTM D4945 (2012) goes against common sense.

Article by E.L. Juvencio *et al.*, published in Soils and Rocks, 40(1):61-74 (2017), e-mail: erisvaldo.lima@gmail.com.

Closure by authors

The authors would like to thank the discusser for his valuable comments, and will try to respond to all the questions raised.

1. It is generally accepted that the base resistance of piles in rock is considered only if the borehole is completely cleared of debris prior to concrete pouring. If the design is completed before any bidding and contractor selection, it is on the safe side to disregard such resistance. However, if the selected pilling contractor has the means and can assure a proper bottom clean-up, the design engineer can consider the contribution of base resistance, resulting in reduction in the foundation cost.

A detailed presentation of the dynamic tests - with observed shaft and base resistances - can be found in the DSc thesis of the senior author (reference in the paper). In these tests, a contribution of base resistance was definitely observed. On average, the mobilized base loads were 9% of the total mobilized load, but with considerable variation between tests. This variation was due to different load mobilization levels but may also be due to different borehole clearing processes. It should be kept in mind that two processes of debris removal were used: (a) by water circulation ("wet" boring) and (b) by compressed-air ("dry" boring). The latter method is efficient only up to a certain depth.

2. The authors accept the suggestion to present a further paper exploring the contribution of both base resistance and shaft friction in the saprolitic soil.

3. Juvencio's (2015) selection of specimens for laboratory tests was made after the examination of many boxes of samples (there was practically one boring per column of each bridge), with a wide range of RQDs. As expected, test results indicated a wide range of q_u: 14-90 MPa (Table 2). The testing program for the Rio de Janeiro Harbour Improvement (Table 3), on the other hand, used specimens with higher RQDs and, consequently, q_u were in a more tight - and higher - range: 50-90 MPa. The two sets of test results were put together in Fig. 12, and the observed scatter was not too severe, leading to the correlation (on the safe side) of Eq. (5).

4. The authors agree - and this was clearly stated in the paper - that Eq. (7), for maximum mobilized shear stress, is conservative. It is of avail, as mentioned in the paper, when there is no laboratory testing and only RQD values are available.

5. The maximum displacement of E111, Block 16, mentioned in the text, 2 mm, is incorrect. The right value is 4.7 mm, as shown in Table 4 and Fig. 18. This does not change the understanding that the maximum mobilized load was far from failure.

6. The American standard ASTM D4945 was first published in 1989, and served as basis for other national standards, such as the Brazilian standard NBR 13208. When referring to the American standard, the authors used the lastest version of 2012. The correct expression in the paper should be that NBR 13208 *is in accordance* with ASTM D4945.

SOILS and ROCKS
An International Journal of Geotechnical and Geoenvironmental Engineering
Publication of
ABMS - Brazilian Association for Soil Mechanics and Geotechnical Engineering
SPG - Portuguese Geotechnical Society
Volume 40, N. 2, May-August 2017

Author index

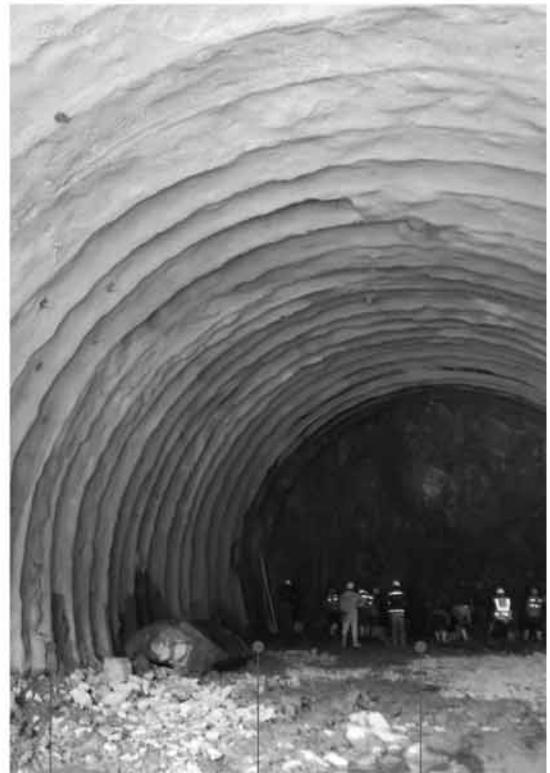

Conheça mais:
www.geobrugg.com/pt/taludes

Safety is our nature

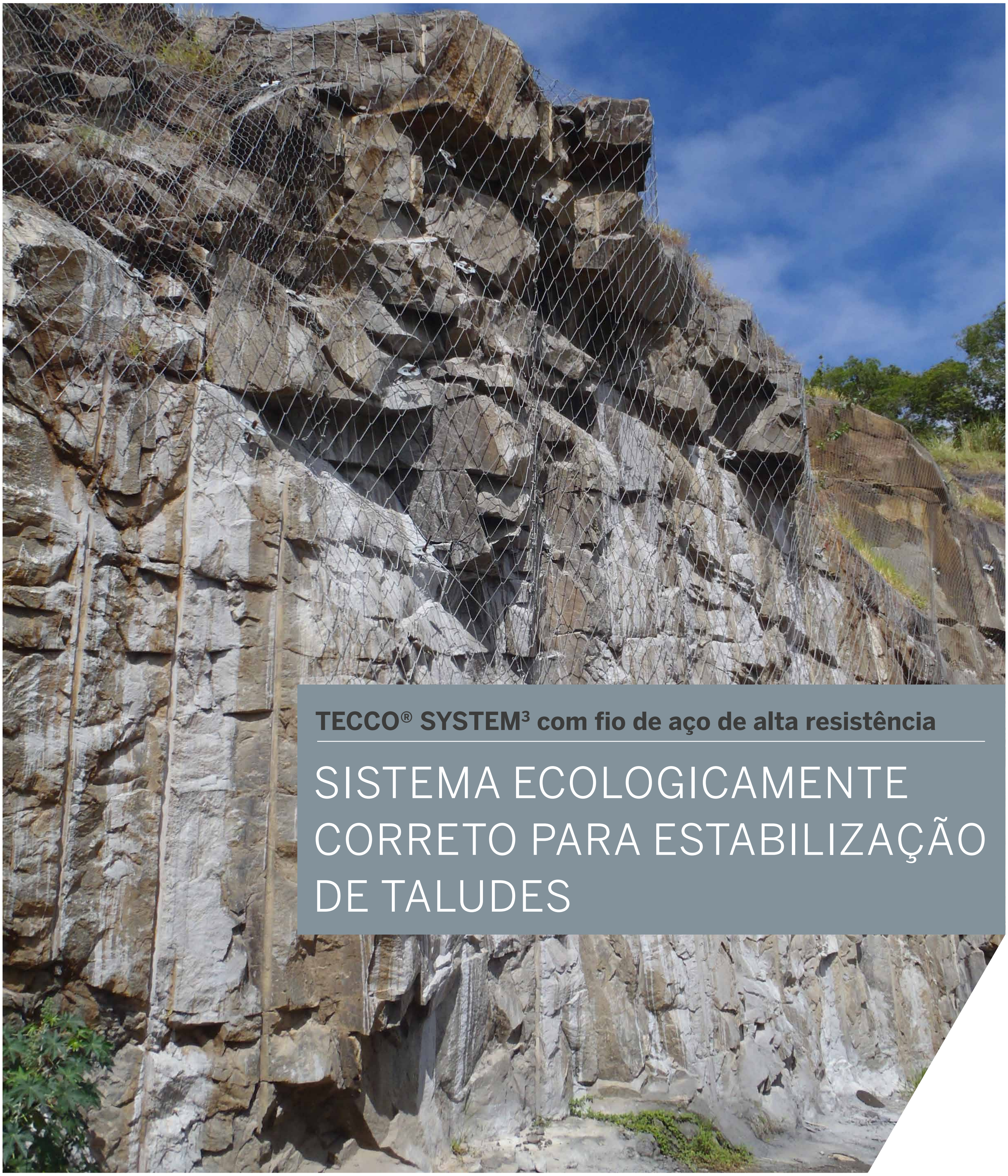

TECCO® SYSTEM³ com fio de aço de alta resistência

SISTEMA ECOLOGICAMENTE CORRETO PARA ESTABILIZAÇÃO DE TALUDES

Geobrugg AG | Rua Visconde de Pirajá, 82 sl.606 | 22410-003 - Rio de Janeiro, Brasil | Phone + 55 21 3624 1449 | www.geobrugg.com | info@geobrugg.com


A strong, lasting connection.

Instructions for Submission of Manuscripts

Category of the Papers

Soils and Rocks is the international scientific journal edited by the Brazilian Association for Soil Mechanics and Geotechnical Engineering (ABMS) and the Portuguese Geotechnical Society (SPG). The aim of the journal is to publish (in English) original research and technical works on all geotechnical branches.

According to its content the accepted paper is classified in one of the following categories: Article paper, Technical Note, Case Study or Discussion. An article paper is an extensive and conclusive dissertation about a geotechnical topic. A paper is considered as a technical note if it gives a short description of ongoing studies, comprising partial results and/or particular aspects of the investigation. A case study is a report of unusual problems found during the design, construction or the performance of geotechnical projects. A case study is also considered as the report of an unusual solution given to an ordinary problem. The discussions about published papers, case studies and technical notes are made in the Discussions Section.

When submitting a manuscript for review, the authors should indicate the category of the manuscript, and is also understood that they:

a) assume full responsibility for the contents and accuracy of the information in the paper;

b) assure that the paper has not been previously published, and is not being submitted to any other periodical for publication.

Manuscript Instructions

Manuscripts must be written in English. The text is to be typed in a word processor (preferably MS Word), **single column**, using ISO A4 page size, left, right, top, and bottom margins of 25 mm, Times New Roman 12 font, and line spacing of 1.5. All lines and pages should be numbered. The text should be written in the third person.

The first page of the manuscript must include the title of the paper followed by the names of the authors with the abbreviation of the most relevant academic title. The affiliation, address and e-mail must appear below each author´s name. An abstract of 200 words follows after the author´s names. A list with up to six keywords at the end of the abstract is required.

Although variations on the sequence and title of each section are possible, it is suggested that the text contains the following sections: Introduction, Material and Methods, Results, Discussions, Conclusions, Acknowledgements, References and List of Symbols. A brief description of each section is given next.

Introduction: This section should indicate the state of the art of the problem under evaluation, a description of the problem and the methods undertaken. The objective of the work should be clearly presented at the end of the section.

Materials and Methods: This section should include all information needed to the reproduction of the presented work by other researchers.

Results: In this section the data of the investigation should be presented in a clear and concise way. Figures and tables should not repeat the same information.

Discussion: The analyses of the results should be described in this section.

Conclusions: The content of this section should be based on the data and on the discussions presented.

Acknowledgenments: If necessary, concise acknowledgements should be presented in this section.

References: References to other published sources must be made in the text by the last name(s) of the author(s), followed by the year of publication, similarly to one of the two possibilities below:

…while Silva & Pereira (1987) observed that resistance depended on soil density… or *It was observed that resistance depended on soil density (Silva & Pereira, 1987).*

In the case of three or more authors, the reduced format must be used, *e.g.*: Silva *et al.* (1982) or (Silva *et al.*, 1982). Two or more citations belonging to the same author(s) and published in the same year are to be distinguished with small letters, *e.g.*: (Silva, 1975a, b, c.). Standards must be cited in the text by the initials of the entity and the year of publication, *e.g.*: ABNT (1996), ASTM (2003).

Full references shall be listed alphabetically at the end of the text by the first author´s last name. Several references belonging to the same author shall be cited chronologically. Some examples are listed next:

Papers: Bishop, A.W. & Blight, G.E. (1963). Some aspects of effective stress in saturated and unsaturated soils. Geotechnique, 13(2):177-197.

Books: Lambe, T.W. & Whitman, R.V. (1979). Soil Mechanics, SI Version. John Wiley & Sons, New York, 553 p.

Book with editors: Sharma, H.D.; Dukes, M.T. & Olsen, D.M. (1990). Field measurements of dynamic moduli and Poisson's ratios of refuse and underlying soils at a landfill site. Landva, A. & Knowles, G.D. (eds), Geotechnics of Waste Fills - Theory and Practice, American Society for Testing and Materials - STP 1070, Philadelphia, pp. 57-70.

Proceedings (printed matter or CD-ROM): Jamiolkowski, M.; Ladd, C.C.; Germaine, J.T. & Lancellotta, R. (1985). New developments in field and laboratory testing of soils. Proc. 11th Int. Conf. on Soil Mech. and Found. Engn., ISSMFE, San Francisco, v. 1, pp. 57-153. (specify if CD ROM).

Thesis and dissertations: Lee, K.L. (1965). Triaxial Compressive Strength of Saturated Sands Under Seismic Loading Conditions. PhD Dissertation, Department of Civil Engineering, University of California, Berkeley, 521 p.

Standards: ASTM (2003). Standard Test Method for Particle Size Analysis of Soils - D 422-63. ASTM International, West Conshohocken, Pennsylvania, USA, 8 p.

Internet references: Soils and Rocks available at http://www.abms.com.br and downloaded on August 6th 2003.

On line first publications must also bring the digital object identifier (DOI) at the end.

Figures shall be either computer generated or drawn with India ink on tracing paper. Computer generated figures must be accompanied by the corresponding digital file (.tif, .jpg, .pcx, etc.). All figures (graphs, line drawings, photographs, etc.) shall be numbered consecutively and have a caption consisting of the figure number and a brief title or description of the figure. This number should be used when referring to the figure in text. Photographs should be black and white, sharp, high contrasted and printed on glossy paper.

Tables shall be numbered consecutively in Arabic and have a caption consisting of the table number and a brief title. This number should be used when referring to the table in the text. Units should be indicated in the first line of the table, below the title of each column. Acronyms should be avoided. When applicable, the units should come right below the corresponding column heading. Additional comments can be placed as footnotes.

Equations shall appear isolated in a single line of the text. Numbers identifying equations must be flushed with the right margin. International System (SI) units must be used. The definitions of the symbols used in the equations must appear in the List of Symbols. It is recommended that the symbols used are in accordance with Lexicon in 8 Languages, ISSMFE (1981) and the ISRM List of Symbols.

The text of the submitted manuscript (including figures, tables and references) intended to be published as an article paper or a case history should not contain more than 30 pages, formatted according to the instructions mentioned above. Technical notes and discussions should have no more than 15 and 8 pages, respectively. Longer manuscripts may be exceptionally accepted if the authors provide proper explanation for the need of the required extra space in a cover letter.

Discussion

Discussions must be written in English. The first page of a discussion should contain:

The title of the paper under discussion;

Name of the author(s) of the discussion, followed by their position, affiliation, address and e-mail. The author(s) of the discussion should refer to himself (herself/themselves) as the reader(s) and to the author(s) of the paper as the author(s).

Figures, tables and equations should be numbered following the same sequence of the original paper. All instructions previously mentioned for the preparation of article papers, case studies and technical notes also apply to the preparation of discussions.

Editorial Review

Each paper will be evaluated by reviewers selected by the editors according to the subject of the paper. The authors will be informed about the results of the review process. If the paper is accepted, the authors will be required to submit a version of the revised manuscript with the suggested modifications. If the manuscript is rejected for publication, the authors will be informed about the reasons for rejection. In any situation comprising modification of the original text, classification of the manuscript in a category different from that proposed by the authors, or rejection, the authors can reply presenting their reasons for disagreeing with the reviewer comments.

Submission

The author(s) must upload a digital file of the manuscript to the Soils and Rocks website.

Follow Up

The online management system will provide a password to the corresponding author, which will enable him/her to follow the reviewing process of the submitted manuscript at the Soils and Rocks website.

Volume 40, N. 2, May-August 2017

Table of Contents